Precipitation in the high strength AA7449 aluminium alloy: implications on internal stresses on different length scales

THÈSE N^{O} 6525 (2015)

PRÉSENTÉE LE 19 JUIN 2015
À LA FACULTÉ DES SCIENCES ET TECHNIQUES DE L'INGÉNIEUR
LABORATOIRE DE SIMULATION DES MATÉRIAUX
PROGRAMME DOCTORAL EN SCIENCE ET GÉNIE DES MATÉRIAUX

ÉCOLE POLYTECHNIQUE FÉDÉRALE DE LAUSANNE

POUR L'OBTENTION DU GRADE DE DOCTEUR ÈS SCIENCES

PAR

Patrick SCHLOTH

acceptée sur proposition du jury:

Prof. D. Damjanovic, président du jury
Prof. H. Van Swygenhoven, Dr J.-M. Drezet, directeurs de thèse
Prof. L. Delannay, rapporteur
Prof. G. Eggeler, rapporteur
Prof. R. Logé, rapporteur

ÉCOLE POLYTECHNIQUE
FÉDÉRALE DE LAUSANNE

Suisse
2015

Acknowledgements

This project is funded by the Competence Center for Materials Science and Technology (http://www.ccmx.ch/) in the frame of the work entitled “Measurements and modelling of residual stress during quenching of thick heat treatable aluminium components in relation to their microstructure” involving EPF Lausanne, PSI Villigen, Univ. de Bretagne Sud Lorient, Constellium CRV and ABB Turbo Systems Ltd..

I would like to thank several people who helped me in different ways to accomplish this thesis over the past 4 years:

- My supervisors Prof. Helena Van Swygenhoven (MSS, PSI) and Prof. Jean-Marie Drezet (LSMX, EPFL) for giving the the opportunity to perform this thesis at EPFL and in an interessting project. I would like to thank Prof. Helena Van Swygenhoven for the trust she had in me and for her support during the four years. Further, I would like to thank Prof. Jean-Marie Drezet for his encouragement and his help during the thesis and for allowing me to colloborate with Prof. Alexis Deschamps and Prof. Charles-André Gandin.

- The members of my thesis jury: Prof. Roland Logé (EPFL), Prof. Gunther Eggeler (Ruhr University Bochum) and Prof. Laurent Delannay (Catholic University of Louvain) for the time and effort they spent to read and review my thesis. I am also thanksful to Prof. Dragan Damjanovic (EPFL) who was the president of the Jury.

- Prof. Michel Rappaz (EPFL) for welcoming me in his laboratory (LSMX) and later accepting my change to PSI for private reasons.

- Prof. Alexis Deschamps (INPG, Grenoble) for fruitful and motivating discussions about small-angle scattering and the metallurgy of heat treatable aluminium alloys and for inviting me to his laboratory to perform several experiments.

- Prof. Charles-André Gandin for allowing me to use his precipitation model and for interessting discussions.
- The members of the CCMX project for a nice and constructive atmosphere during the project meetings. Special thanks to Dr. Julia Wagner for correcting my beamtime proposals and for her support during several beamtimes and to Dr. Christophe Sigli for his valuable comments on precipitation modeling.
- The beamline scientists Vadim Davydov (POLDI, PSI), Frederic de Geuser (SIMAP, INPG), Andreas Menzel (cSAXS, PSI), Thomas Buslaps (ID15B, ESRF), Julie Fife (TOMCAT, PSI), Joachim Kohlbrecher (SANS-I, PSI) and Weimin Gan (Stress-Spec, FRMII) for their help and showing me how to use their beamlines.
- Prof. Andreas Mortensen (LMM, EPFL) for allowing me to use his laboratory equipment and his critical questions during my EDMX exams and Dr. Ludger Weber (LMM, EPFL) for introducing me to the LMM equipment and his help at the beginning of my PhD.
- The ATMX workshop of the EPFL for all the great and quick machining work.
- Anne Roy (LSMX, EPFL) for all her quick and kind help with the administrative work
- My colleaques at LSMX (EPFL) and MSS (PSI) for the nice atmosphere and the irreplaceable important coffee breaks
- My girlfriend Lysiann, my friends and my family for their constant support in times when things were not easy, for making me smile and getting my mind out of work.

Lausanne, 23 February 2015 P. S.

Abstract

Al-Zn-Mg(-Cu) (AA7xxx) alloys are widely used structural materials owing to their excellent mechanical properties and low corrosion susceptibility. The high strength of these materials is obtained by the formation of secondary phases, e.g. precipitation.

This present thesis aims at contributing to the understanding of the influence of precipitation in the high strength AA7449 alloy on the internal stress formation at different length scales. Two different cases are studied in this thesis. In the first case, the influence of precipitation during quench on macroscopic residual stresses is studied in an industrial 75 mm AA7449 thick plate. For some investigations the behaviour of the AA7449 alloy is compared with the medium strength AA7040 alloy. In the second case, the influence of different precipitation states on the internal strain formation is investigated at the microstructural length scale.

For the first case, in situ small angle X-ray scattering evidenced that during quenching the heterogeneous η phase forms at high temperatures in contrast to homogeneous GP(I) zones, which form at low temperatures. The η formation is influenced by the cooling conditions but also by macrosegregation that is present in thick plates. Yet, the volume fraction of η precipitates is very low and has a negligible effect on the macroscopic residual stresses in thick plates.

The homogeneous GP(I) zones form during quench with radii in the subnanometre range. Their formation is strongly influenced by excess vacancies. Fast cooling rates can lead to higher radius and volume fraction of GP(I) zones compared to slower cooling. The GP(I) zone formation increases the yield strength during quench and is responsible for the observed high macroscopic residual stresses in industrial thick plates. Therefore, the GP(I) zone formation during quench needs to be taken into account in macroscopic finite element residual stress simulations by using precipitation modelling.

The GP(I) zone formation during quench is simulated by using a thermodynamic based Eulerian multi-class model. Therefore, a thermodynamic description for GP(I) zones is derived from reversion heat treatments by using the solubility

product. The influence of excess vacancies is taken into account by adapted effective diffusion coefficients. This simplified approach allows reproducing reasonably well the measured GP(I) zone formation during rapid coolings. In addition, the simulated as-quenched surface yield strength of two AA7449 plates compare well with experimental results reported in literature. The coupling of the precipitation model with finite element residual stress calculations (performed by the other PhD student in this project) allows predicting very well the measured residual stress profiles in two AA7449 thick plates.

For the second case, in situ mechanical testing during tensile deformation using X-rays and neutrons evidence that the presence of different precipitate types change the internal strain formation in the aluminium matrix at the microstructural length scale. The presence of small shearable GP(I) zones leads to an internal strain formation that is dominated by the intergranular strains of the aluminium matrix. When large unshearable η precipitates are embedded in the aluminium matrix the interphase strains clearly dominate the internal strain formation. In the case of a mixture of shearable and unshearable η' and η precipitates, the internal strain formation is influenced by both intergranular and interphase strains. Further, it is shown that the η phase has a higher elastic modulus than the aluminium matrix and shows an anisotropic behaviour in the elastic and plastic regime during deformation.
In addition, it is pointed out that the internal strain formation at the microstructural length scale can have a significant effect on macroscopic residual stress measurements performed by XRD when the plastically deformed sample contains larger η' and η precipitates.

Key words: Al-Zn-Mg-Cu alloys, Precipitation, Quenching, Vacancies, Guinier-Preston zones, Early precipitation, Small-angle scattering, Precipitation modelling, X-ray and neutron diffraction; Residual macroscopic stresses, Residual intergranular and interphase strain

Résumé

Les alliages d'aluminium de la série 7xxx (Al-Zn-Mg (-Cu)) sont principalement utilisés dans des applications aéronautiques en raison de leurs excellentes propriétés mécaniques et une faible sensibilité à la corrosion. La résistance mécanique élevée de ces matériaux est obtenue par la formation de phases secondaires, par exemple la précipitation.

Cette thèse vise à contribuer à la compréhension de l'influence de la précipitation dans l'alliage AA7449 sur la formation des contraintes internes à différentes échelles. Deux cas sont étudiés dans cette thèse. Dans le premier cas, l'influence de la précipitation au cours de la trempe sur les contraintes résiduelles macroscopiques est étudiée pour une tôle industrielle de 75 mm d'épaisseur en alliage AA7449. Pour certaines investigations, le comportement de l'alliage AA7449 est comparé à celui de l'alliage AA7040. Dans le second cas, l'influence de différents états de précipitation sur la formation des contraintes internes est étudiée à l'échelle de la microstructure.

Pour le premier cas, l'expérience in situ de diffusion centrale des rayons X aux petits angles à mis en évidence la formation de précipités hétérogènes de phase η à haute température et la formation de zones GP(I) à basse température. La formation de η est influencée par les conditions de refroidissement, mais également par la macroségrégation présente dans des tôles épaisses. Cependant, la fraction volumique de phase η est très faible et a un effet négligeable sur les contraintes résiduelles macroscopiques dans des tôles épaisses trempée à l'eau froide.

Les zones GP(I) homogènes se forment pendant trempe avec un rayon de l'ordre du sub-nanomètre. Leur formation est fortement influencée par les lacunes en sursaturation. Les refroidissements rapides conduisent à des rayons et fractions volumiques de zones GP(I) plus élevés que ceux mesurés lors de refroidissements plus lents. La formation des zones GP(I) augmente la limite d'élasticité lors de la trempe et est responsable des fortes contraintes résiduelles macroscopiques observés dans les plaques industrielles épaisses. Par conséquent, la formation des zones GP (I) au cours de la trempe doit être prise en compte dans la modélisation par

éléments finis des contraintes résiduelles macroscopiques à l'aide de la modélisation de la précipitation.
La formation des zones GP(I) pendant trempe est simulée en utilisant un modèle thermodynamique de précipitation basé sur une approche Eulérienne multi-classes. Par conséquent, une description thermodynamique des zones GP(I) est établie en utilisant le produit de solubilité. L'influence des lacunes en sursaturation est prise en compte en adaptant le terme pré-exponentiel et l'activation d'énergie des coefficients de diffusion. Cette approche simplifiée permet de reproduire de manière satisfaisante les mesures de cinétique de formation des zones GP(I) pendant des refroidissements rapides. En outre, la limite d'élasticité simulée en surface de deux tôles industrielles en alliage AA7449 est en bon accord avec les résultats expérimentaux rapportés dans la littérature. Le couplage du modèle de précipitation avec le modèle par éléments finis (effectué par un autre doctorant dans le cadre de ce projet) permet de prédire des profils de contraintes résiduelles en excellent accord avec les profils mesurés dans deux tôles épaisses de l'alliage AA7449.

Dans le second cas, des essais de traction in situ sous rayons X ou neutrons, permettant la mesure des déformations élastiques, ont montré que la présence de différents types de précipités change la formation des contraintes internes dans la matrice d'aluminium à l'échelle de la microstructure. La présence de zones GP(I), fin précipités cisaillables, conduit à une formation de contraintes internes dominée par la déformation intergranulaire. Dans le cas de gros précipités non-cisaillables η, la formation des contraintes internes est dominée par les incompatibilités de déformation inter-phases. Lorsque des précipités cisaillables et non-cisaillables de phase η' et η coexistent dans la matrice d'aluminium, la formation des contraintes internes est influencée par les déformations intergranulaires et inter-phases. Par ailleurs, il est démontré que la phase η a un module d'élasticité plus élevé que la matrice d'aluminium et présente un comportement anisotrope en régimes élastique et plastique lors de la déformation.
En outre, il est souligné que la formation de contraintes internes à l'échelle de la microstructure peut avoir un effet significatif sur les mesures de contraintes résiduelles macroscopiques effectuées par DRX lorsque l'échantillon déformé plastiquement contient de gros précipités de phase η' et η.

Mots clés : Alliages d'aluminium de la série 7xxx (Al-Zn-Mg-Cu), Précipitation, trempe, lacunes en sursaturation, zones GP(I), précipitation, diffusion des rayons X aux petits angles, diffraction des neutrons et des rayons X, modélisation de la précipitation, contraintes résiduelles macroscopiques, contraintes intergranulaire

et d'interphase microscopiques

Zusammenfassung

Al-Zn-Mg(-Cu) (AA7xxx) Legierungen werden aufgrund ihrer exzellenten mechanischen Eigenschaften und geringer Korrosionsneigung bevorzugt als Strukturmaterialien eingesetzt. Die Hochfestigkeit dieser Legierungen wird durch die Bildung von Sekundärphasen, so genannten Ausscheidungen, erreicht.

Die vorliegende Doktorarbeit beschreibt den Einfluss von Ausscheidungen auf die Ausbildung von Eigenspannungen auf verschiedenen Längenskalen in der hochfesten AA7449 Legierungen. Zwei Fälle werden in dieser Arbeit untersucht. Ein Fall untersucht den Einfluss der Ausscheidungsbildung während dem Abschrecken einer 75 mm dicken AA7449 Platte auf die makroskopischen Eigenspannungen untersucht. In einigen Untersuchungen wird das Verhalten der AA7449 Legierung mit der mittelfesten AA7040 Legierung verglichen. Der andere Fall beschreibt den Einfluss von verschiedenen Ausscheidungsarten auf die Eigenspannungsausbildung auf der mikroskopischen Längenskala untersucht.

In ersten Fall wird gezeigt, dass sich während dem Abschrecken bei hohen Temperaturen die heterogene η Phase bildet, im Gegensatz zu homogenen GP(I) Zonen, die bei tieferen Temperaturen ausscheiden. Die Ausbildung der η Phase wird von den Abkühlungsbedingungen, aber auch von Makroseigerungen, in den dicken Platten beeinflusst. Der Volumenanteil der η Phase ist jedoch sehr gering und hat einen vernachlässigbar kleinen Einfluss auf die makroskopischen Eigenspannungen der untersuchten dicken Platten.

Die homogenen GP(I) Zonen, die sich während dem Abschrecken ausbilden, haben Radien im sub-nanometer Bereich. Ihre Bildung wird sehr stark von der Leerstellenkonzentration beeinflusst. Ein schnelles Abkühlen kann, im Vergleich zu langsameren Abkühlungsraten, zu einer Ausbildung von GP(I) Zonen mit einem höheren Volumenanteil und Radius führen. Die sich bildenden GP(I) Zonen erhöhen die Streckgrenze des Materials während dem Abschreckens und sind deshalb für die gemessenen hohen makroskopischen Eigenspannungen in den dicken industriellen Platten verantwortlich. Infolgedessen muss die Ausbildung der GP(I) Zonen während des Abschreckens in den makroskopischen Finite Elemente Simulationen

durch ein Ausscheidungsmodel berücksichtigt werden.
Die GP(I) Zonen Bildung während des Abschreckens wird mit Hilfe von einem thermodynamisch basierten Eulerian Multiklassen Ausscheidungsmodel simuliert. Dafür wurde mit Hilfe des Löslichkeitproduktes eine thermodynamische Beschreibung für die GP(I) Zonen entwickelt, die auf Umkehrwärmebehandlungen basiert. Der Einfluss von übersättigten Leerstellen wird durch adaptierte effektive Diffusionsparameter berücksichtigt. Dieser vereinfachte Modellierungsansatz erlaubt es, die gemessene Bildung von GP(I) Zonen während dem schnellen Abkühlens gut zu reproduzieren. Des Weiteren stimmen die simulierten Streckgrenzen an der Oberfläche von zwei AA7449 Platten sehr gut mit experimentellen Messungen überein, die in der Literatur angegeben wurden. Die Kopplung des Ausscheidungsmodels mit den makroskopischen Finite Elemente Eigenspannungsberechnungen (die von den anderen Doktoranden in dem Projekt durchgeführt wurden) erlaubt es die in zwei dicken AA7449 Platten gemessenen Eigenspannungsprofile gut vorherzusagen.

In dem zweiten Fall konnte mittels in situ mechanischen Versuchen während Zugverformung unter Röntgen- und Neutronenbeugung eine Veränderung der Eigenspannungsausbildung in der Aluminium matrix nachgewiesen werden, wenn verschiedene Ausscheidungstypen im Material vorhanden sind. Kleine scherbare GP(I) Zonen führen zu einer Eigenspannungsausbildung, die im wesentlichen von der Lastumverteilung zwischen den verschiedenen Kornorientierungen des Aluminiums beeinflusst wird. Wenn grosse nicht-scherbare η Ausscheidungen in der Aluminiummatrix vorliegen, wird die Eigendehnungsausbildung von der Lastumverteilung zwischen den beiden Phasen bestimmt. ImFall von scherbaren η' und nicht-scherbaren η Ausscheidungen wird die Eigendehungsausbildung sowohl von der Lastumverteilung zwischen den verschiedenen Kornorientierungen des Aluminiums als auch von der Lastumverteilung zwischen den beiden Phasen beeinflusst. Des Weiteren konnte gezeigt werden, dass die η Phase einen höheren Elastizitätsmodul als Aluminium hat und dassdie η Phase ein anisotropes Verhalten im elastischen und plastischen Verformungsbereich aufweist.
Ausserdem wurde aufgezeigt, dass die Ausbildung der Eigendehnungen auf der mikroskopischen Längenskala einen grossen Einfluss auf die Messung von makroskopischen Eigenspannungsmessungen haben kann, wenn (i) grosse η' and η Ausscheidungen vorliegen, (ii) ein erhöhter Grad an plastischer Verformung vorliegt und (iii) Röntgenbeugung benutzt wird.

Stichwörter: Al-Zn-Mg(-Cu) Legierungen, Ausscheidungsbildung, Abschrecken, Leerstellen, Guinier-Preston Zonen, frühe Ausscheidungsbildung, Kleinwinkelstreuung, Ausscheidungsmodellierung, Röntgen- und Neutronenbeugung, Makroskopische Eigenspannungen, Eigendehungen zwischen den Phasen und zwischen den Kornorientierungen

Contents

Acknowledgements **i**

Abstract **iii**

1 Introduction **1**

1.1 Objectives of the thesis . . . 3

1.2 Structure of the thesis . . . 5

2 Literature review **7**

2.1 Heat treatable Al-Zn-Mg (-Cu) Aluminium alloys . . . 8

2.2 Processing of 7xxx Aluminium alloys . . . 8

2.3 Precipitation in 7xxx Aluminium alloys . . . 12

2.4 Precipitation during quench in 7xxx alloys . . . 16

2.5 Thermodynamics of precipitation . . . 19

2.6 Strengthening mechanism . . . 24

2.7 Internal stresses . . . 28

2.7.1 Macroscopic residual stresses in large AA7xxx components . 28

2.7.2 Intergranular and interphase microstresses . . . 31

3 Experimental and numerical methods **35**

3.1 Materials and heat treatments . . . 36

3.2 Electron microscopy . . . 37

3.3 Differential scanning calorimetry . . . 38

3.4 Small angle scattering . . . 39

3.4.1 Scattering theory . . . 39

3.4.2 SAS experiments . . . 41

3.4.3 Data treatment . . . 44

3.4.4 Data analysis . . . 46

3.4.5 Considerations about the accuracy of SAS analysis . . . 52

3.5 Precipitation modelling . . . 55

3.5.1 Calculation of the cooling conditions in the plates 55
3.5.2 Thermodynamic description of phases 55
3.5.3 Precipitation model 57
3.5.4 The influence of excess vacancies on diffusion 60
3.6 Yield strength model 63
3.7 In-situ mechanical testing using diffraction 64
3.7.1 Diffraction 64
3.7.2 Diffraction experiments 66
3.7.3 Data treatment and analysis 67

4 As-quenched microstructure and precipitation during quench 71
4.1 Characterisation of the plate microstructure after quench 72
4.1.1 Characterisation of the homogeneous precipitates after quench 74
4.1.2 Characterisation of the heterogeneous precipitates after quench 76
4.2 Characterisation of homogeneous precipitation during rapid cooling 82
4.3 Characterisation of heterogeneous precipitation during cooling . . . 89
4.4 Comparison of AA7449 and AA7040 92
4.5 Continuous cooling precipitation diagram - AA7449 95
4.6 Implications for macroscopic residual streses 96
4.7 Summary 99

5 Reversion heat treatments 103
5.1 Nature of the quench-induced homogeneous phase 104
5.2 Thermodynamic description of GP(I) zones 110
5.3 Activation energy of GP(I) zone formation and dissolution 115
5.4 Summary 116

6 Precipitation modeling during rapid cooling 119
6.1 GP(I) zones formation during rapid cooling of AA7449 120
6.2 GP(I) zone formation during rapid cooling of AA7040 128
6.3 Application to quenching of a 75 mm AA7449 thick plate 132
6.4 Application to the surface cooling of different thick plates 137
6.5 Summary 139

7 Influence of precipitation on internal stresses formation 143
7.1 Microstructures 144
7.2 Neutron diffraction 146
7.3 X-ray diffraction 150

7.4 Comparison of aluminium lattice strain evolution for the three microstructures . . . 155
7.5 Summary . . . 159

8 Conclusions and outlook 161
8.1 Conclusions . . . 161
8.2 Outlook . . . 165

A Chemical composition of GP zones, η' and η 167

B Diffraction elastic constants 171

C Lattice strain evolution during loading and residual lattice strain 173

Bibliography 190

Acronyms 191

List of symbols 193

List of figures 196

List of tables 206

Curriculum vitae 209

1 Introduction

Aluminium alloys (AA) are widely used as structural components owing to their high specific strength, low corrosion susceptibility and high damage tolerance. In the aircraft industry, heat treatable aluminium alloys are still the dominating structural materials in spite of growing importance of fiber reinforced materials. The age-hardenable Al-Zn-Mg-Cu (AA7xxx) alloys, such as the high strength AA7449 and medium strength AA7040, are commonly used in the fuselage and wings.

The fabrication of AA7xxx aluminium alloys requires a number of thermo-mechanical steps such as age-hardening treatment, which allows tailoring the mechanical properties of these alloys. The quenching step of the age-hardening treatment, induces high internal stresses that usually emerge over macroscopic distances in the parts, so called type-I or macro-stresses. Different processes can be applied to reduce the residual stresses such as stretching that is commonly used for plates. For complex geometries as in the case of forgings stress relief is not always possible. Yet, residual stresses cannot be removed completely and part distortions can still occur [1, 2], which make final shape corrections necessary, thereby increasing the manufacturing time cycle and costs [3].

Therefore, it is of great industrial interest to simulate the residual stress formation during the processing of industrial components as part of through process modelling. Numerical simulation tools such as the finite element method (FEM) are commonly applied [4, 5]. The formation of residual stresses during quench needs to be well predicted in order to simulate the redistribution of residual stresses during stress relief treatments and/or during machining. Eventually, the mechanical properties during service and lifetime can be predicted by knowing the residual stresses in the final manufactured part, which is a superposition of the residual and service stresses.

The demand for larger structural parts, e.g. in the case of the A380 aircraft, leads to new challenges for manufacturing. One major concern that arises due to the processing of large industrial Aluminium components such as plates and forgings is related to the quenching step.
One the one side, residual stresses result from thermal strain and inhomogeneous plastic strain near the surface of the quenched parts and originate from thermal gradients. Therefore, the residual stresses will be larger in larger parts because of the higher thermal gradients between the surface and the center [6].
On the other side, it was evidenced that the lower cooling rates in larger products can lead also to material property variations due to quench-induced precipitation [7]. Godard found that precipitates form at high but also at low temperatures during quench in thick plates, which yield both a softening and hardening effect, respectively. Godard simulated the quench-induced precipitation and linked it with a thermo-mechanical model in order to investigate the influence of precipitation on residual stress predictions. In the case of a 400 mm AA7010 thick plate the influence was small. In contrast, Chobaut et al. stated that the residual stress formation during quench in thick AA7449 plates cannot be predicted well, when the influence of precipitation on the mechanical properties is not considered [8].

Several studies focused on quench-induced precipitation. The heterogeneous formation of the coarse equilibrium η phase was evidenced at high temperatures during quench, predominantly on grain boundaries and dispersoids [9, 10]. The formation of the η phase has a detrimental effect on the final mechanical properties [10, 11, 12] and decreases the yield strength during quench [13]. Only few studies dealt with the simulation of heterogeneous precipitation during quench [7, 14].
The homogeneous precipitation during quench was little investigated since the temperature changes during quench are rapid and the decomposition after quench (natural aging) occurs instantly. Zhang et al. evidenced low temperature precipitation during fast cooling by using DSC between 250-150°C, which they ascribed to the η' phase [15]. An attempt to simulate quench-induced homogeneous precipitation was proposed so far only by Godard but he could not verify his results against experimental findings [7].

1.1 Objectives of the thesis

This PhD thesis is part of a CCMX project[1], which focusses on the measurements and simulations of quench-induced residual stresses in large industrial components made of heat treatable aluminium alloys. The main goal is better understand and model the residual stress build-up during quench in large industrial components by taking into account the change in microstructure. In more details, a multi-scale modelling approach is foreseen, which allows implementing the simulation of the precipitation during quench on the microstructural scale in a macroscopic finite element model for the residual stress generation.

The present PhD thesis features three distinct objectives, which concern the influence of precipitation in the high strength AA7449 alloy on the internal stress formation at different length scale.

On the macroscopic scale:

1. The quench-induced precipitation is characterised in two AA7xxx thick plates (a 75 mm AA7449 thick plate and to some extent also a 140 mm AA7040 thick plate). The formation of different types of precipitates is investigated in the as-quenched state but more importantly also in situ during coolings. The influence of the different precipitation types on the macroscopic residual stresses is outlined.

2. Based on the experimental findings a modelling approach is presented, which allows accounting for the major precipitation effect on the residual stress formation. The precipitation model uses a thermodynamic description for the homogeneous quench-induced precipitates that is derived from dissolution heat treatments and takes into account the influence of excess vacanies on the diffusion.

---

[1] This project is funded by the Competence Center for Materials Science and Technology (http://www.ccmx.ch/) in the frame of the work entitled “Measurements and modelling of residual stress during quenching of thick heat treatable aluminium components in relation to their microstructure” involving EPF Lausanne, PSI Villigen, Univ. de Bretagne Sud Lorient, Constellium CRV and ABB Turbo Systems Ltd..

On the microscopic scale:

3. The influence of different precipitation types on the internal stress formation in the aluminium matrix is investigated at the microscopic length scale (so called type-II or micro-stresses) by in situ mechanical testing. The impact of the type-II stresses on macroscopic residual stress measurements is discussed in AA7xxx alloys.

1.2 Structure of the thesis

This thesis is divided into eight chapters:

- Chapter 2 provides an introduction to Al-Zn-Mg(-Cu) alloys and a review of precipitation and quench-induced precipitation in these alloys. Further, basic thermodynamics concepts are recalled to describe precipitation and the state of the art to simulate precipitation microstructures in AA7xxx alloys is discussed. A short overview on strengthening mechanisms is given and an overview is provides on internal stresses on different length scales.
- Chapter 3 presents the investigated materials and the heat treatment parameters. Further, the experimental and numerical methods used in this thesis are described in more detail.
- Chapter 4 focuses on the characterisation of the quench-induced precipitation in a 75 mm AA7449 industrial thick plates after quench and during rapid coolings. The impact of the quench-induced precipitation on macroscopic residual stresses in thick plates is emphasized. In addition, for some experiments, the differences between the AA7449 alloy and the AA7040 are highlighted.
- Chapter 5 gives insight on the nature of the quench-induced homogeneous phase and provides a thermodynamic description for GP(I) zones by using the solubility product. In addition, the influence of excess vacancies on the activation energy of GP(I) zone formation is evidenced.
- Chapter 6 presents a precipitation modelling approach to account for the major effect of quench-induced precipitation the investigated thick plates. The modelling parameters are calibrated with experimental results and applied to the quenching in thick plates.
- Chapter 7 investigates the influence of different precipitation types on the internal strain formation in the aluminium matrix and discusses their influence on macroscopic residual stresses
- Chapter 8 summarizes the main findings of the thesis and proposes some starting points for future work.

2 Literature review

This chapter presents a short literature review in seven section on topics that are relevant to this thesis. A short introduction is given to heat treatable Al-Zn-Mg-(Cu) alloys (Section 2.1), their processing (Section 2.2) and precipitation phenomena (Section 2.3). Section 2.4 focuses on the precipitation during quench and Section 2.5 provides basic information about the thermodynamics of precipitation and the state of the art of precipitation modelling. Section 2.6 presents an overview of different strengthening mechanism and Section 2.7 gives an introduction to internal stresses.

2.1 Heat treatable Al-Zn-Mg (-Cu) Aluminium alloys

The Al-Zn-Mg-Cu (AA7xxx) alloys are widely used as structural components for aerospace applications owing to their excellent mechanical properties and corrosion resistance as shown in Figure 2.1. The high strength AA7449 alloy is used for upper wing structures and shows high strength due to an increased zinc content.This alloy is typically used in the overaged T7X51 temper, which features a reduced yield strength compared to the peak aged T651 temper, but in return shows a significantly improved corrosion resistance [3, 16].The AA7040 was developed for ultra-thick plate applications such as spars and other structural components, since it is less quench sensitive due to a lower solute content [16, 17].

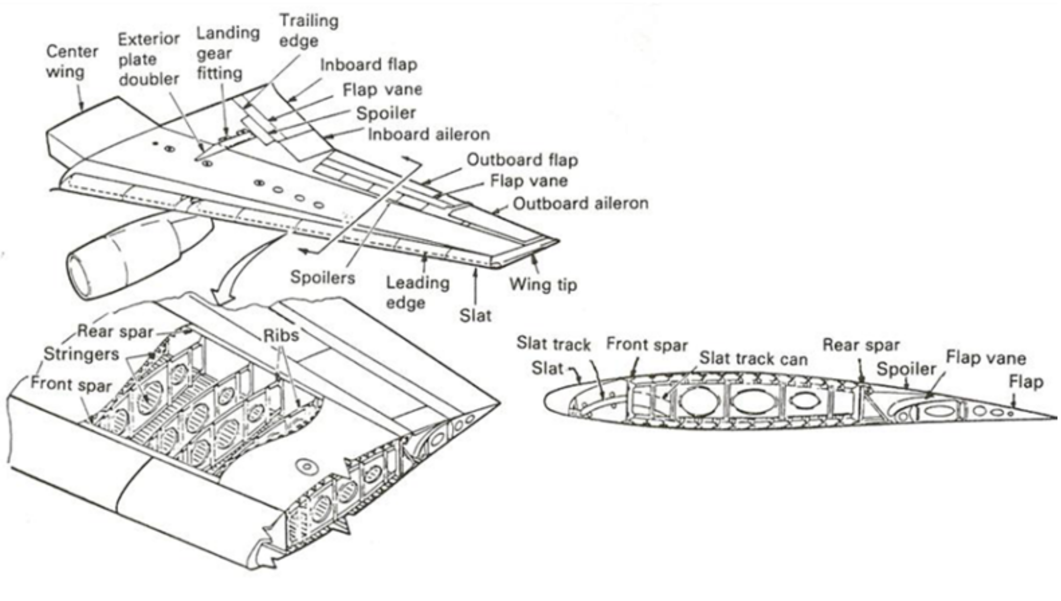
Center wing
Exterior plate doubler
Landing gear fitting
Trailing edge
Inboard flap
Flap vane
Spoiler
Inboard aileron
Outboard flap
Flap vane
Outboard aileron
Spoilers
Leading edge
Slat
Wing tip
Rear spar
Stringers
Front spar
Ribs
Slat track
Slat
Front spar
Slat track can
Rear spar
Spoiler
Flap vane
Flap

Figure 2.1: Application of AA7xxx alloys in aerospace industry.

2.2 Processing of 7xxx Aluminium alloys

AA7xxx aluminium alloys are commonly processed in plates and undergo a complex thermo-mechanical processing route as schematically shown in Figure 2.2. The processing route can be described by two main stages, the primary process and the age hardening treatment, respectively.

Primary processing of 7xxx

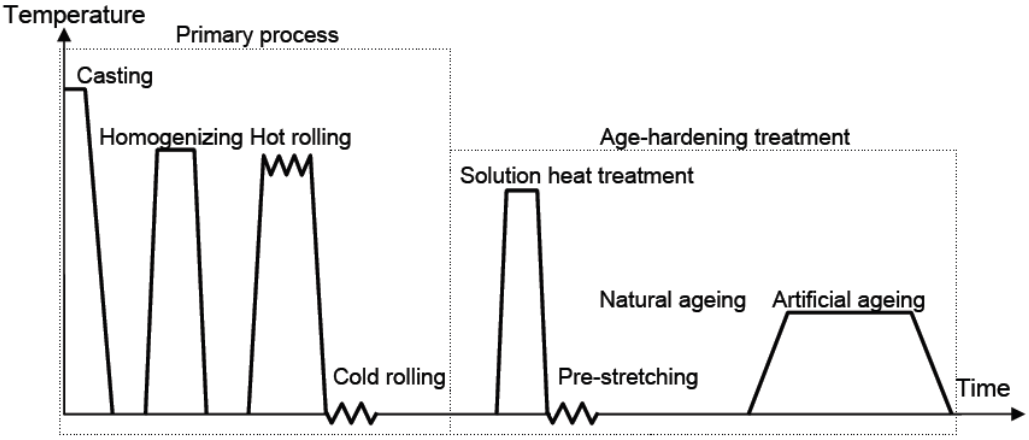

Figure 2.2: Typical thermomechanical treatment for 7xxx aluminium alloys (taken from [18]).

The primary processing features casting, homogenization, hot and cold rolling. These processing steps control the materials composition and grain structure. The rolling processes induce crystallographic texture that differs through the plate thickness [19, 20, 21]. In addition, secondary phases such as intermetallic phases and dispersoids form during casting and homogenization. Coarse intermetallic phases form due to impurities e.g. Fe and Si. A large amount of these phases is detrimental and should be avoided. On the one hand, they decrease the formability and fracture toughness and one the other hand they decrease the solute content (e.g. Cu and Mg) and therefore the maximum hardening potential [22, 23, 11, 24, 25]. Further, small amount of transition elements such as Cr or Zr are added to the alloy in order to form dispersoids. They usually form during homogenization with sizes in the range of 10-50 nm [26, 27]. The dispersoids do not evolve during the subsequent heat treatment as they feature slow diffusing elements and they are rather thermally stable. The formation of dispersoids is beneficial as they inhibit recrystallization by Zener pinning [28, 18, 29]. The effectiveness depends on their size, spacing and distribution. Zr is also a peritectic element, which can lead to Zr segregation at the dendrite cores during solidification. This explains the observed inhomogeneous distribution of the Al3Zr dispersoids in the microstructure [30].

Secondary processing - age hardening heat treatment

The secondary processing contains the age hardening treatment, which is applied to tailor the mechanical properties, but also the corrosion properties of the final product by creating a specific precipitation microstructure. The secondary processing features the solutionizing heat treatment (SHT), quenching, stretching and aging treatment.

The solution heat treatment is carried out above the solvus temperature in the α region to dissolve the secondary θ phases and obtain a homogeneously distributed solid solution (step 1 in Figure 2.3). After the solutionizing treatment, the material is rapidly quenched in cold water. Due to the decreasing solid solubility with decreasing temperature a supersaturated solid solution is obtained at room temperature when the quench is fast enough to prevent any atom diffusion (step 2 in Figure 2.3). The retained supersaturated solid solution is crucial to obtain a maximum hardening potential. The quench or cooling rate is a critical factor as it influences the vacancy concentration (section 3.5.4), quench-induced precipitation (section 2.4) and residual stress (RS) formation (section 2.7.1). The stretching step is performed directly after quenching in order to reduce residual stresses in the plate, typically by a factor 10 [3]. This helps to minimize the part distortion during machining. After stretching the material is kept for several days at room temperature. This step is characterised by the formation of very small coherent precipitates (Guinier Preston zones) and is called natural aging (NA). Finally, the multi-step artificial aging is performed to create homogeneously distributed precipitates in the material, which strengthen the material due to precipitation hardening (section 2.6) by impeding dislocation motion (step 3 in Figure 2.3). The possibility to strengthen the material by precipitation during an age-hardening

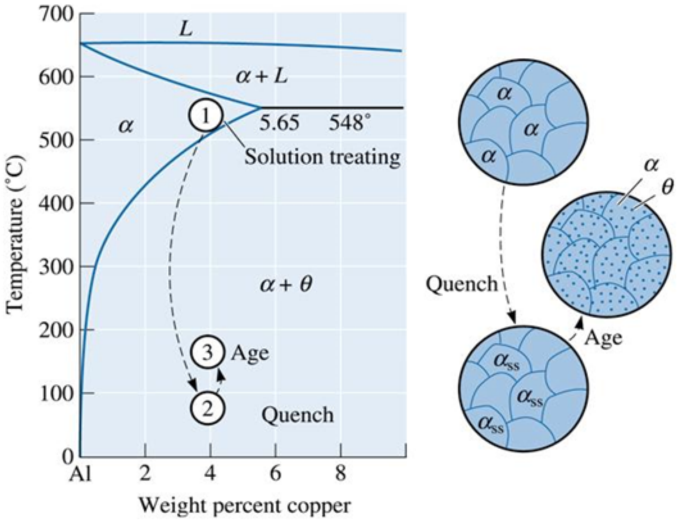

Figure 2.3: Schematic of the age hardening treatment consiting of (1) solutionizing heat treatment, (2) quench and (3) age hardening heat treatment, exemplarily for the Al-Cu system (pictures are taken from [31]).

treatment is the most important metallurgical feature of heat treatable Aluminium alloys and gives rise to their excellent mechanical properties. The precipitation of secondary phases from the supersaturated solid solution usually follows a complex sequence, which involves a number of metastable transition phases before the equilibrium phase is obtained. The precipitation sequence in AA7xxx alloys will be discussed in more detail in the next section.

2.3 Precipitation in 7xxx Aluminium alloys

Precipitation sequence

Due to the increasing technological importance as medium and high strength materials, precipitation in the Al-Zn-Mg (-Cu) alloys has been widely studied since the 1970's [3, 16, 17]. Reviews on the decomposition in the Al-Zn-Mg alloys were given by Löffler et al. and Lendvai [32, 33]. They argued that the precipitation sequence depends on the Mg/Zn ratio and that two sequences are possible ($SS \rightarrow GP - zones \rightarrow \eta' \rightarrow \eta$ and $SS \rightarrow T' \rightarrow T$), which lead to the equilibrium η phase (Mg(Al,Cu,Zn)$_2$) and T phase ((Al,Zn)$_{49}$Mg$_{32}$). In alloys of practical interest however, the T phase is only forming after long time above 200°C and is usually negligible. Mondal and Mukhopadhyay pointed out that in the 7xxx alloys containing copper in addition to the η and T phases the S phase (Al_2CuMg) and θ phase (Al_2Cu) can also appear, depending on the alloying elements [34]. However, the sequence that leads to the η phase is the most relevant one.

For the precipitation sequence leading to the equilibrium η phase, two routes have been proposed [35, 36]:

$$SS \rightarrow \text{GP(I) zones} \rightarrow \eta' \rightarrow \eta$$

$$SS \rightarrow \text{VRC} \rightarrow \text{GP(II) zones} \rightarrow \eta' \rightarrow \eta$$

GP(I) zones form during natural aging or at low aging temperatures. The GP(II) zones develop from or nucleate on solute aggregates that contain vacancies (called vacancy rich cluster (VRC)), which form during quench or within short aging time after the quench. GP(I) and GP(II) zones precede the semi-coherent η' phase [35, 36, 37]. Further growth of the η' precipitates will lead to the incoherent equilibrium η phase. In the following, the characteristics of different transition phases, such as the structure, composition and temperature range, will be discussed in more detail.

Vacancy-rich clusters

In literature it is reported that in addition to the GP(I) zones, which are forming during natural aging or aging at low temperatures, VRC appear during and/or shortly after quenching from the solutionizing temperature [38, 39, 40, 32, 41, 42]. Positron annihilation spectroscopy (PAS) supported the existence of clusters rich in vacancies [43]. Positrons are trapped by complexes with vacancies surrounded by Zn. The number of VRC depends sensitively on quench parameters, such as

quench temperature and rate [33]. Lacom et al. concluded that VRC are smaller than 1 nm and stable up to 200-250°C [44]. Therefore, VRC can act as nucleation site at higher temperatures compared to GP(I) zones. Katz and Ryum stated that the number of VRC decreases during natural aging as they anneal out. In contrast, the GP(I) zones volume fraction increases during natural aging [39].
As the VRC anneal out with time after the quench the chemical composition is not easy to estimate. Juhasz et al. proposed that VRC form with an Zn/Mg ratio of 4:1, which was supported by Jiang et al. who argued that VRC are zinc-rich cluster [45, 36]. Also PAS measurements indicated a Zn concentration of 72 ± 5 at% within the zones [43]. Yet, direct information on size, structure and composition of VRC have not been reported [32]. Recent 3D atom probe tomography (APT) studies evidenced solute clusters in Al-Zn-Mg-Cu alloys. Sha and Cerezo reported on clusters with 10-30 atoms in size and a Zn/Mg ratio of 0.85 in the as-quenched (AQ) and natural aged state (1.5h) for an AA7050 alloy [42]. Liddicoat et al. also observed clusters in an AA7075 alloy after natural aging. They were smaller in size (4-7 atoms) with a Zn/Mg ratio of 1 and an Al content of 36 at.% [46]. Since both, GP(I) zones and VRC can be present at room temperature, it is not clear if the solute clusters refer to VRC or GP(I) zones.

Guinier Preston zones

Two types of Guinier Preston zones have been reported for the Al-Zn-Mg-Cu alloys. Differential scanning calorimetry (DSC) and small angle X-ray scattering (SAXS) experiments evidenced their presence between 60 and 100°C [47, 32, 48].
The spherical GP(I) zones form at room temperatures and up to 120-150°C, depending on the Zn content. The GP(I) zones are fully coherent with the matrix and consist of layers parallel to {100} matrix planes and give rise to diffuse diffraction spots near $\{100\}_{Al}$ and $\{110\}_{Al}$ in the $\langle 100\rangle_{Al}$ projections [49, 32, 35]. It is reported that the GP(I) zone formation is not dependant on the the amount of quench-induced vacancies and is not influenced by VRC [50, 32, 51]. The coherent GP(II) zones form at aging temperatures above 70°C after quenching from above 450°C [47, 51]. They are described as Zn-rich clusters, which are parallel to {111} matrix planes with a thickness of 1-2 atom layers and a width of 3-6 nm [48].
The chemical composition of the GP(I) zones has been investigated in several studies by means of 3D-APT, SAXS and also first principle calculations. An overview of the results is given in Table A.1 in Appendix A. GP(I) zones contain Zn and Mg with a ratio between 1 - 1.3 depending on alloy composition, aging temperature and time. Cu can also be present in GP(I) zones. Controversy exists about the Al content in the GP(I) zones, which was reported in the range of 30 to

85 at.%. The radius of the zones is typically up to 1 nm.

The kinetics of GP zone formation has been found to be controlled by movement of the Mg atoms owing to the high binding energy of Mg atoms with vacancies. This is supported by the activation energy of GP(I) zone formation, which is close to Mg migration energy in Aluminium, around 0.6 ev [45, 52, 53]. In contrast, the activation energy for the growth of GP(I) zones and the transformation to η' is close to that of Zn migration [53, 54]. GP(I) zones and GP(II) zones have been reported to be precursors of the η' precipitates [36, 48, 42]. This also explains the industrial practice of a two-step aging. The critical size for GP zones is much smaller and therefore the density much higher compared to the η' precipitates. This results in a higher strength compared to a one step aging.

η' phase

The semi-coherent and metastable η' phase is generally seen as the main hardening phase in the Al-Zn-Mg-Cu alloys [18]. The η' phase is characterised by a hexagonal crystal structure with a = 0.496 nm and c = 1.40 nm [55, 48, 56]. The precipitates have a platelet like shape and are aligned with the Al matrix as follows: $(0001)_{\eta'} \parallel (111)_\alpha$ or $(12\bar{1}0)_{\eta'} \parallel (110)_\alpha$ [57]. The η' precipitates can either form on existing GP(I) or GP(II) zones or nucleate directly at higher temperatures [36, 48, 42]. The phase appears in the range of 120 to 180°C and has a solvus between 250-300°C depending on the alloy composition.

The chemical composition of the η' precipitates is known to change as a function of time and temperature [42, 58]. An overview of the chemical composition of η' is given in Table A.2 in Appendix A. The Zn/Mg ratio is reported to take values of 1 to 2.2. Sha and Cerezo evidenced an increasing Zn/Mg ratio from 1.1 - 1.3 during isothermal holding at 121°C [42]. Marlaud et al. observed an increasing Cu content in η' precipitates during isothermal holding at 160°C. Generally, the composition of η' is different from the equilibrium $MgZn_2$, but rather close to the GP zones. This supports the direct nucleation of η' on existing GP zones [59].

η phase

The incoherent equilibrium η phase has like η' a hexagonal structure but with a = 0.5221 nm and c = 0.8567 nm [48]. The homogeneous η phase can be found either forming above 180°C or during longer holding times at lower temperatures transforming from η' precipitates. The η precipitates are typically found in the overaged T7 state [57, 60, 18]. The η phase can have up to 11 types depending on their orientation and origin (nucleation on metastable phases, dislocations or in the bulk) [61].

Experimental results about the chemical composition of η are summarized in Table A.3 in Appendix A. The composition is typically far from the $MgZn_2$ but rather $Mg(Zn,Cu,Al)_2$. The Zn/Mg ratio is higher compared to GP(I) zones and η' and in the range of 1.4-2.1. The Aluminium content is generally smaller than in GP zones and η' precipitates.

The chemical composition of heterogeneous η phase, which forms heterogeneously at higher temperatures is given in Table A.4 in Appendix A.

Effects of excess vacancies on precipitation

Excess vacancies are point defects that can be present in the material after quench from high temperature or due to plastic deformation [62, 63]. It is generally accepted that vacancies increase the rate of solute diffusion and therefore the kinetics of phase transformations [64, 44, 7, 31, 42, 65]. Excess vacancies are responsible for the rapid formation of GP(I) zones at room temperature after quench. Moreover, it was pointed out that vacancies are also important in the nucleation of precipitates [64, 44]. One explanation is that the vacancies reduce the misfit strain energy of the nucleus. This will lead to a smaller critical size of the nucleus as illustrated in Figure 2.4. Excess vacancies can form clusters with solute atoms, which serve as nucleation sites for the GP zones or η' precipitates. A high vacancy density is necessary for the nucleation of a high number density of precipitates and a fine precipitate dispersion [64, 41, 66]. Slower quench rate will lead to a loss of excess vacancies and therefore, to a coarser distribution of clusters and a lower number density of hardening precipitates [64, 67].

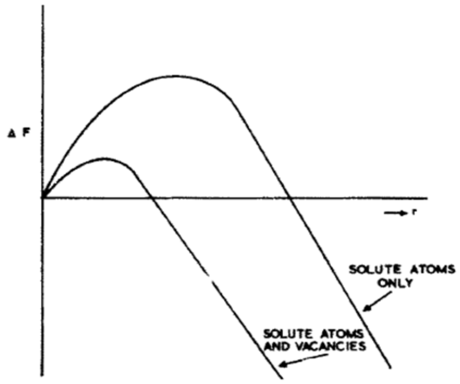

Figure 2.4: Schematic of the free energy change ΔF as a function of the critical nucleus radius r due to the presence of vacancies in solute clusters [64].

2.4 Precipitation during quench in 7xxx alloys

In general fast quenching is applied after solutionizing to obtain a supersaturated solid solution at room temperature by preventing any atom diffusion. However, the quenching of thick industrial components feature inhomogeneous cooling conditions between the surface and core. The high thermal gradients lead on the one hand to residual stresses due to non-homogeneous plastic strain near the surface [6] and on the other hand to variations of the microstructure (i.e. precipitation) owing to slower cooling rates towards the center of the component. Alloys with high solute contents are more sensitive (e.q. called quench sensitivity) to slower cooling conditions and have a higher tendency to form quench-induced precipitates. A general review on the metallurgical changes during quenching of heat treatable Aluminium alloys was given by Shuey and Tiryakioglu [67].

Heterogeneous quench induced precipitation

Quench-induced precipitation is generally referred to the formation of the coarse equilibrium η phase. The coarse η phase nucleates heterogeneously on lattice defects such as grain and subgrain boundaries, dispersoids and dislocations. These sites are thermodynamically and kinetically favoured since part of the free energy associated with the defect is released (Section 2.5) and diffusion is enhanced in the vicinity of these defects [9, 65, 68]. After a slow air quench, Deschamps and Brechet evidenced heterogeneous precipitation of the η phase mostly on Al_3Zr dispersoids, which were distributed in bands. The strong solute depletion inhibited the formation of hardening precipitates during aging. The lower amount of available solute not only decreases the driving force for η' precipitates, but also limits the GP zone formation, which act as nucleation sites for the η' phase [69, 9]. Zhang et al. showed that the nucleation on Al_3Zr dispersoids is more effective in recrystallized grains. During recrystallization the subgrain boundaries pass through the Al_3Zr dispersoids and change their interphase character from coherent to incoherent [29]. Godard et al. investigated the precipitation sequence during quenching using interrupted quenching in the AA7010 alloy. The η phase forms not only within the grains on coherent and semi-coherent dispersoids Al_3Zr, but also intergranular on grain- and subgrain boundaries. Precipitates (η-phase) were also found on dislocations at lower temperatures (250-150°C). The S' and T phase were also observed between 300 and 200°C after long holding times due to Mg and Zn depletion. Godard et al. summarized their microstrucural studies in a nucleation diagram and emphasized the temperature domains, where the different nucleation sites and phases are active [10].

Archambault and Godard used in situ electrical resistivity measurements to characterize the η precipitation kinetics at high temperatures above 200°C in the AA7010 alloy. They described the precipitation kinetics as a single process, which follows Mathiessen's rule. The mechanical softening was expressed with the power-law (n=2/3) relation [70]. Deschamps et al. showed that the size and volume fraction of the precipitates is quench rate dependant. In contrast the nature of the present quench induced precipitates was found to be the same, mainly consisting of coarse precipitates on dispersoids but also smaller intergranular precipitates. The precipitate free zone (PFZ) that formed around the quench-induced precipitates after aging depends only moderately on quench rate [71] (Figure 2.5a). Zhang et al. developed continuous cooling precipitation (CCP) diagrams for the AA7150 and AA7020 alloys by using DSC with different cooling rates (0.005-3 K/s). In the AA7150 three reactions were observed during the cooling's (Figure 2.5b). They ascribed the two high temperature reactions to η and also S phase precipitation. The chemical composition of the heterogeneous η formed during isothermal holding at 350°C was estimated to be 14.6Al-38.3Zn-33.3Mg-13.8Cu (in at.%) [58].

Heterogeneous precipitation at higher temperatures is thus undesirable since it lowers the mechanical properties such as yield strength, toughness, and fatigue in the resulting material [10, 11]. The loss of solute and vacancies leads to the formation of a PFZ around the heterogeneous η precipitates [71] (Figure 2.5a). The decreased fracture toughness was related to the PFZ, where crack initiation starts [12]. The heterogeneous η precipitates lowers the strength of the grain boundaries and decrease the intrinsic strength of the grain interior due to the absence of hardening precipitates. Reich and Kessler performed compression tests

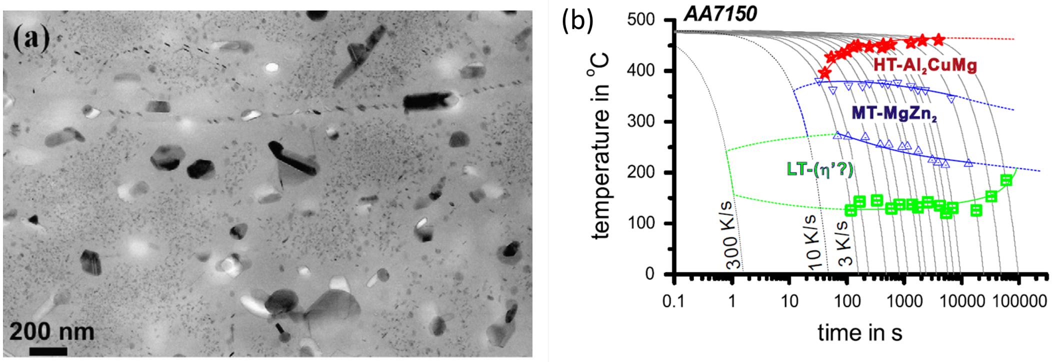

Figure 2.5: (a) Quench-induced η precipitates sourrounded by the characteristic precipitate free zone (PFZ) in a T6 sample [71] and (b) CCP diagram of the AA7150 alloy obtained by DSC experiments [15].

after cooling with different constant cooling rates with an AA7020 alloy. They evidenced an decreasing yield strength when the cooling rate is decreased, which was associated with solute loss due to high temperature precipitation [13].

A method to predict the effect of heterogeneous η during continuous cooling on the T6 yield strength was developed by Evancho and Staley, namely the quench factor analysis (QFA) method [72]. The hardness data obtained from isothermal or continuous cooling experiments is fitted numerically by multiple regression analysis based on classical nucleation theory. This method was theoretically proven by Staley [73]. It was applied to numerous Aluminium alloys in order to predict properties such as yield strength, corrosion resistance and toughness, to optimise quench residual stresses and to predict cast of aluminium alloys [74, 75, 76]. The numerical descriptions can be implemented into finite element (FE) simulations using internal variables [77, 78]. Some of the practical and theoretical limitations of this method were improved by several authors [79, 80, 81]. However the QFA still only describes the solute loss due to heterogeneous precipitates and therefore the reduced hardening potential after aging. The effects of homogeneous precipitation during quench are not taken into account.

Homogeneous precipitation

The quench-induced homogeneous precipitation has been studied much less. Investigations after quench are usually not effective since the decomposition after quench is rapid and natural aging occurs instantly at room temperature in most 7xxx alloys [18]. Studing the quench induced homogeneous precipitation directly during cooling is difficult due to the rapid time and temperature changes. Direct observations were made by Zhang et al. by using a DSC with cooling rates up to 3K/s. Figure 2.5b shows in addition to the high temperature precipitation, also a low temperature reaction between 250-150°C. Zhang et al. ascribed the low temperature peak to the formation of η' phase. However, the cooling rates are still much lower than the ones found in industrial practise. Indirect evidence of quench-induced homogeneous precipitation was given by residual stress measurements in 7xxx thick plates and forgings [8, 82]. The measured as-quenched residual stresses of up to 300 MPa are much higher than the as-quenched yield strength of the material. Further, several authors argued that vacancy rich clusters are appearing during quenching from the solutionizing temperature [38, 39, 40, 32, 41, 42]. Yet, no direct observations have been reported.

2.5 Thermodynamics of precipitation

Precipitation is generally defined by three stages; nucleation, growth and coarsening. In the following, the three steps and the basic thermodynamic concepts will be described shortly. The presented thermodynamic framework is taken from Reference [31], which provides also a more detailed description.

Nucleation of secondary phases

The free energy change ΔG related to the nucleation of a spherical secondary phase of radius r is shown in Figure 2.6a. The nucleation of the secondary phase of volume V decreases the free energy by $V\Delta G_v$, where ΔG_v is the volume free energy (chemical driving force). The creation of the interfacial area A between the matrix and the precipitate with an isotropic interfacial energy γ will increase the free energy by $A\gamma$. In addition, the misfit strain between the precipitate of volume V and the matrix will increase the free energy by $V\Delta G_s$, where ΔG_s is the misfit strain energy. The total free energy change ΔG due to nucleation of a spherical precipitate is summarized as:

$$\Delta G = -V\Delta G_v + A\gamma + V\Delta G_s = -\frac{4}{3}\pi r^3(\Delta G_v - \Delta G_s) + 4\pi r^2\gamma \tag{2.1}$$

The critical radius r^* and energy barrier ΔG^* to form a stable nuclei can be obtained by differentiation of the above equation:

$$r^* = \frac{2\gamma}{3(\Delta G_v - \Delta G_s)^2} \tag{2.2}$$

$$\Delta G^* = \frac{16\pi\gamma^3}{(\Delta G_v - \Delta G_s)} \tag{2.3}$$

In addition to homogeneous nucleation, secondary phases can also nucleate heterogeneously on defects such as grain boundaries, dislocations and dispersoids. These defects increase the free energy of the material. The activation energy barrier of the formation of a nucleus on a defect is reduced since part of the free energy is released. The heterogeneous nucleation on grain boundaries and dislocation will reduce the grain boundary energy and strain energy, respectively. A shape factor SF, which is related to the wetting angle θ_w, is commonly used to describe the reduction of the activation energy barrier due to heterogeneous nucleation:

$$SF(\theta_w) = \frac{\Delta G^*_{het}}{\Delta G^*_{hom}} \tag{2.4}$$

The homogeneous and heterogeneous nucleation rate N will depend on the migration of atoms $\omega \exp(-\Delta G_m/kT)$, the activation energy barrier of nucleation $\exp(-\Delta G^*/kT)$ and the number of (homogeneous or heterogeneous) nucleation sites N_{max}. The nucleation rate is then expressed as:

$$N = N_{max}\omega \exp\frac{-\Delta G_m}{kT} \exp\frac{-\Delta G^*}{kT} \tag{2.5}$$

where ω accounts for the vibration frequency of atoms and the area of the critical nucleus, ΔG_m is the activation energy for atomic migration, T is the temperature and k is the Boltzmann constant.

Growth of secondary phases

Once a stable nuclei is created the β precipitate can grow when the interface migrates. The concentration of solute in the precipitate C_β is higher than the one of the α matrix C_0 (Figure 2.6b). This leads to a solute depleted zone around the precipitate. Local equilibrium can be assumed on the precipitate/matrix interface. The growth rate v depends on the supersaturation ΔC_0, which is defined as the difference between the initial solute content C_0 and the equilibrium content C_e in the matrix. In order to migrate the interface of the precipitate, a certain flux of solute has to diffuse from the matrix to the precipitate. The flux of solute depends

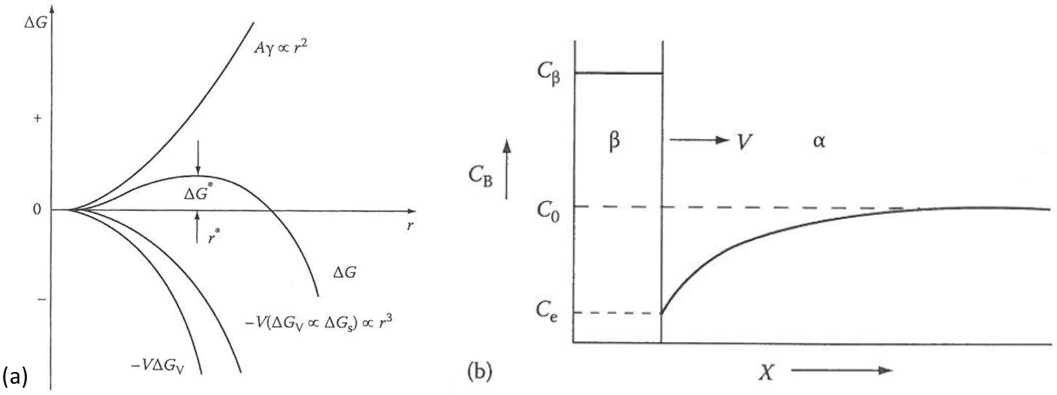

Figure 2.6: (a) Free energy change ΔG associated with the nucleation of a homogeneous spherical nucleus as a function of radius r (b) Concentration profile at the interface of the precipitate and matrix [31].

on the concentration gradient. Zener proposed a linearized approximation of the concentration gradient and showed that the growth rate can be calculated as:

$$v = \frac{\Delta C_0}{2(C_\beta - C_e)}\sqrt{\frac{D}{t}} \tag{2.6}$$

where t is the time and D the diffusion coefficient.

Coarsening

The concentration gradient will decrease with time as the matrix depletes of solute. This leads to an overlap of the diffusion fields around the precipitates (indirect impingement). When the matrix solute depletion reaches C_e, the diffusion controlled growth stage ends and the interface controlled coarsening stage starts. The curvature effect (Gibbs-Thomson effect) is the driving force for coarsening of the precipitates (even when all the available precipitate volume fraction has precipitated) [83]. This is due to the higher solubility of smaller particles, which become unstable and dissolve in favour of larger precipitates that grow.

Modeling the evolution of precipitates in heat treatable Aluminium alloys

Based on the classical nucleation and growth theory, three different approaches have been proposed to model precipitation in metallic alloys namely the mean radius approach, the Euler-like multi-class approach and the Lagrange-like multi-class approach [84]. The mean radius approach restricts the particle size distribution (PSD) to its mean radius and density in contrast to the two multi-class approaches, where the PSD is discretized in a large number of classes. The Euler-like multi-class approach is characterised by predefined size classes, where the fluxes between neighbouring classes are followed with time (left Figure 2.7). The Lagrange-like multi-class approach also discretizes the PSD into classes, but the radius evolution of each class with a fixed number of precipitates is calculated (right Figure 2.7). The three ways treat nucleation, growth and coarsening as concomitant processes.

Several models were proposed in the last years based on the three approaches to model the precipitate evolution during various isothermal and non-isothermal heat treatments in heat treatable Aluminium alloys. The evolution of the precipitate microstructure was modelled during isothermal heat treatments such as aging in 7xxx [85, 51, 86] and 6xxx [87] alloys and also homogenisation [88]. Several models were also proposed to simulate the precipitation state during non-isothermal heat treatments e.g. friction stir welding (FSW) of 7xxx [89, 90, 91] and 6xxx [92, 93] alloys, linear heating in 7xxx [94] and 6xxx [87] alloys. Further, reversion heat treatments and welding in 7xxx [95, 96] have also been modelled. Finally, the development of PFZ's after imperfect quenching [89] and during homogenisation was simulated [97].

Modelling of the precipitation in 7xxx alloys was often restricted to the equilibrium η phase and the chemical composition was assumed to be the stoichiometric equilibrium composition of $MgZn_2$. Sigli [86] proposed an aging model of the η phase, which allows for variation of the precipitate composition ($MgZn_{2(1-z)}Cu_zAl_z$) in order to maximise the nucleation rate. Few studies concerned the evolution of metastable phases in 7xxx. Kamp et al. simulated the evolution of heterogeneous precipitation during FSW and considered metastable η' and the equilibrium η phases and the transition between them. Lang et al. [94] modelled the evolution of GP zones, η' and η precipitates upon heating and they compared their results with DSC measurements.

Only few studies concerned the precipitation modelling during quench in 7xxx alloys. Yanjun et al. only considered the formation of the heterogeneous η phase with a MgZn2 stochiometry [14]. Further, they found that the η volume fraction decreased with increasing of cooling rate and they associated the increased hardness after quench to the hardening due to heterogeneous η precipitates. Godard simulated the heterogeneous η phase and a homogeneous hardening phase at lower temperatures during quench of 400 mm AA7010 thick plates [98]. He showed that both precipitation types form during the quench and influence the residual stresses

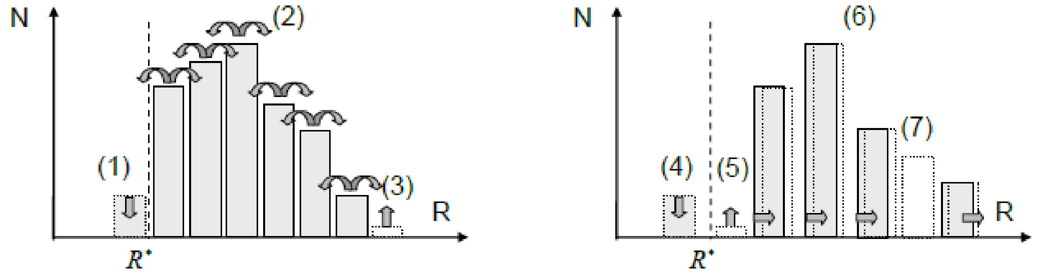

Figure 2.7: Schematic of an Euler-like (left) and Lagrange-like multi-class model. Step 1 and 4: disappearance of a class below the critical radius of nucleation. Step 2: flux of precipitates between neighbouring classes. Step 3 and 5: Creation of new classes. Step 6: Growth of present classes. Step 7: Reduction of interclass distance by introducing a new class. (taken from [18]).

by changing the yield stress of the material. Yet, he could not directly compare the modelling results against experimental data. Further, he pointed out that influence of excess vacancies on the kinetics need to be considered.

The outcome of precipitation modelling can be used in many ways. Deschamps and Perez emphasized that precipitation modelling is a useful tool for extracting physical parameters of phase transformations in metallic alloys [99]. Further, the output of the physical precipitation models such as the volume fraction, PSD, average radius and number density of precipitates can be directly compared with the results from SAXS experiments. In addition, the output can be used in FE simulations through physical based strengthening models as proposed by Kocks-Mecking or Deschamps [100, 101].

2.6 Strengthening mechanism

Plastic deformation at low homogeneous temperatures occurs in conventional metals mainly by the glide of dislocations. The required shear stress necessary to initiate slip in a slip system of a single crystal is defined as the critical resolved shear stress τ_c (CRSS). The tensile yield stress is related to the CRSS by the Schmid factor (cosϕ cosφ) [102]:

$$\tau_c = (cos\phi cos\varphi)\sigma_{ys} \tag{2.7}$$

where ϕ is the angle between the normal of the slip plane and the direction of the applied stress and φ is the angle between the slip plane direction and the direction of the applied stress. The macroscopic yield strength of the polycrystalline material with grains of random orientation is linked to the CRSS by the Taylor factor M, which depends on the crystal structure and on the activated slip systems. The macroscopic yield strength is then defined as [102]:

$$\sigma_{ys} = M\tau_c \tag{2.8}$$

The Taylor factor was calculated to 2.6 for fcc polycrystals using elasto-plastic self-consistent modelling (EPSC) [103]. For rolled 7xxx material a Taylor factor of 2.7 was reported for the rolling direction [57].

A material can be strengthened by impeding dislocation motion. Different obstacles to dislocation motion can be present in a material. A short overview of different strengthening mechanism is given in the following. More detailed information can be found in the References [104, 102].

Lattice friction

To move a dislocation in the periodic structure of the crystal lattice, a friction stress (called Peierls-Nabarro stress) has to be overcome [102]. The internal friction is generally very low in fcc materials and in the order of 10^{-6} to $10^{-5}\mu$ (shear modulus). In Aluminium alloys the lattice friction only accounts for a small stress contribution to the yield stress of about 1MPa.

Dislocation strengthening

The shear stress in a material increases when the dislocation density is increased.

This is usually expressed by the Taylor hardening law:

$$\tau_\rho = \alpha \mu b \sqrt{\rho_D} \tag{2.9}$$

where α is a constant, μ is the shear modulus, b represents the Burgers vector and ρ_D is the dislocation density.

Grain boundary strengthening

Grain boundaries are strong obstacles for dislocation motion. The Hall-Petch relationship relates the grain size d with grain boundary strengthening.

$$\sigma_{GB} = \sigma_0 + k_{GB} d^{-n} \tag{2.10}$$

where σ_0 is a constant stress of uncertain origin, n is an exponent in the order of 0.5 and k_{GB} is a materials constant [102].

Solid solution strengthening

Point defects such as substitutional impurities can also interact with dislocations. The elastic distortion around the point defect due to the size misfit can oppose the stress field of the dislocation and make the dislocation motion more difficult [102]. A review of solid-solution hardening of crystalline materials is given in Reference [105]. The strengthening effect due to a solute of concentration C can be expressed as [106]:

$$\tau_{SS} = \tau_{pure} + K\, C^n \tag{2.11}$$

where τ_{pure} is the flow stress of the pure metal, K is a strengthening coefficient and C is the alloy concentration. The exponent n is typically 1/2, 2/3 or 1. . For ternary or quaternary alloys the following relationship was proposed [107]:

$$\tau_{SS} = \tau_{pure} + \sum_i (K_i C_i)^n \tag{2.12}$$

where K_i describes the strengthening per at. % of a solute element i and C_i is the concentration. This equation is commonly used for Aluminium alloys [24, 108]. Some authors use a global average parameter K_{SS} instead of considering each solute element [101, 18].

Precipitation strengthening

The main strength contribution in high strength Aluminium alloys such as 7xxx alloys originates from precipitation hardening. Precipitates increase substantially the yield strength of a material. Strengthening of the precipitates can be due to modulus strengthening, order strengthening, chemical effect, coherency strengthening and stacking fault strengthening [109]. In addition, the strengthening effect depends also on the size, shape and distribution of the precipitates [104]. Homogeneously distributed precipitates will randomly intersect slip planes and interact with gliding dislocations. Dislocation can either cut through (shear mechanism) or bow around the obstacle (Orowan or by-passing mechanism) depending on the lowest resistance (Figure 2.8). In addition, the obstacles can be overcome by cross-slip at elevated temperatures [102]. The transition from shearing to Orowan mechanism defines in most cases the peak aged T6 state of a material. More in depth information about strengthening due to precipitation can be found in References [110, 104, 109, 102].

The strengthening due to statistically distributed shearable precipitates of radius R can be expressed as [109]:

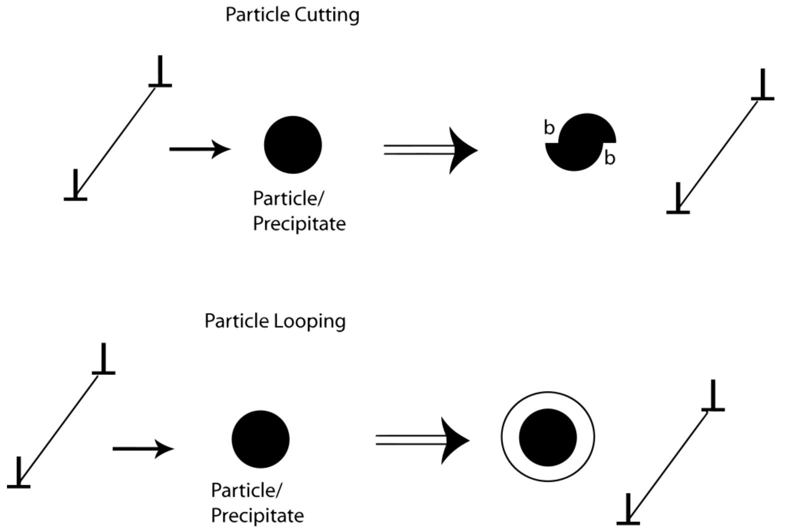

Figure 2.8: Illustration of the two dislocation precipitate interaction mechanisms: precipitate shearing and precipitate bypassing (Orowan). [111].

$$\tau_{shear} = 0.7\alpha^{3/2}\mu\sqrt{\frac{Rf_v}{b}} \tag{2.13}$$

where α is a constant related to the obstacle strength and f_v the precipitate volume fraction. When the precipitates are bypassed the strength contribution can be calculated as:

$$\tau_{Orowan} = \mu b \frac{\sqrt{\pi}}{2} \frac{\sqrt{f_v}}{R} \tag{2.14}$$

The precipitates are often characterised by a particle size distribution. Several author proposed to take this into account for the strength calculation [86, 112].

2.7 Internal stresses

Residual stresses refer to stresses that remain in a material when all external forces are removed. They are present in every engineering material due to thermal and mechanical processing [113].

Residual stresses introduced during processing usually emerge over macroscopic distances and are defined as macrostresses or type-I stresses (Figure 2.9). In addition, internal stresses are generated during plastic deformation due to heterogeneous plastic flow on the microscopic length scale (microstresses or type-II stresses)[114]. In single phase polycrystalline materials type-II stresses arise because of strain incompatibilities between neighbouring grains with different orientations due to elastic and plastic anisotropy (intergranular microstresses). Type-II stresses evolve also in multiphase materials or when phase transformations take place. The interphase microstresses develop because of large property mismatches between the phases and can become more significant than the intergranular stresses [115]. Furthermore, microstresses can be also inside single grains and are called third order internal stresses. Stresses caused by dislocations, second phase particles or misfit stresses inside a single grain are called intragranular microstresses or type-III stresses and are highly localized. These short range type-II and type-III stresses add to the macrostresses. A review on the origin and nature of residual stresses can be found in Reference [116].

Residual stresses are self-equilibrating, therefore the residual stress over the whole body is zero. This means that the residual stresses must vary spatially within the body to hold the stress balance condition ($\int_A \sigma_{ij} dV = 0$) unless it is zero everywhere [114].

2.7.1 Macroscopic residual stresses in large AA7xxx components

Heat treatable 7xxx alloys undergo a complex thermo-mechanical treatment. In particular the quenching step of the age hardening treatment generates macroscopic residual stresses in large industrial components. High thermal gradients between during quenching lead to thermal strain and inhomogeneous plastic strain, especially close to the surface [6]. This results in residual stresses, which are observed typically after quench in plates and forging made of AA7xxx alloys [117, 82, 8]. Macroscopic residual stresses can be determined by different techniques such as diffraction or material removal methods [118]. The residual stress profile of thick plates features generally compressive stresses in the surface and compensating tensile stresses in the center, the so called skin-core effect (Figure 2.10). The residual stresses can be up to 300 MPa at the plate surface, which is much higher than the as-quenched strength of the material [8, 18]. Stretching is applied to reduce the RS, typically by a factor of 10 [3]. Still, part distortions during machining are not uncommon and require expensive corrections [1, 2].

Influence of quench-induced precipitation on macroscopic residual stresses

Tanner and Robinson argued that heterogeneous and homogeneous precipitates increase the as quenched strength, since large forgings show higher surface hardness than smaller ones after quench. Such pieces preserve for a longer time intermediate temperatures around 100°C at the surface by conserving larger temperatures in the center. During quench, precipitates can interact with dislocations and thereby alter the yield stress and work hardening [120]. Robinson et al. found that less quench sensitive alloys show much higher stresses in forgings. The alloys with higher quench sensitivity will experience higher solute loss during quenching, which lowers the yield stress and therefore the residual stresses [82].
The residual stress formation can be modelled by using finite element (FE) computational techniques [5, 117, 6]. To predict the RS a good knowledge about the heat transfer coefficient as a function of temperature is required in order to

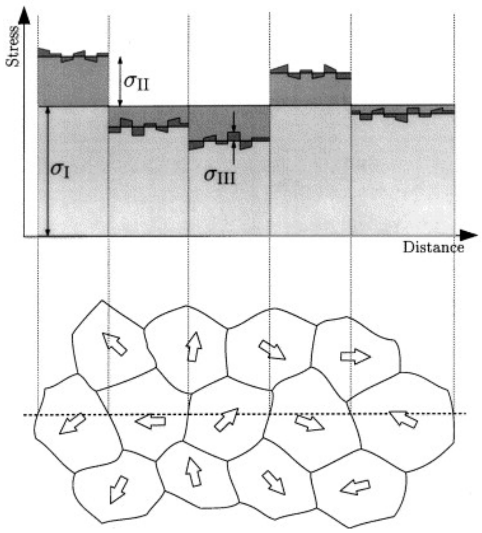

Figure 2.9: Illustration of macrostresses (σ_I), intergranular microstresses (σ_{II}) and intragranular microstresses (σ_{III}) in a randomly orientated polycrystalline material [113].

calculate the cooling condition in the component. In addition, an appropriate thermo-mechanical model is needed to describe the elasto-viscoplastic properties of the material. However, in the case of quench sensitive alloys precipitation has to be considered to account for changes of the yield strength during quench [7, 8]. Godard showed that precipitation has to be taken into account for residual stress simulations of AA7010 thick plates (400 mm) [7]. He pointed out that two types of precipitation phenomena occur during imperfect quenching. Heterogeneous η precipitates form at high temperatures and decrease the yield strength due to solute loss. This promotes an increasing plastification and therefore a lower residual stress level. In contrast, homogeneous precipitation occurs at lower temperatures, which is responsible for the hardening during cooling and therefore higher residual stresses. Further, he argued that residual stresses are mainly affected by the mechanical properties at lower temperatures, e.g. the strain hardening rather than the rate dependency. He proposed to couple macroscopic residual stress simulation with a precipitation model to better simulate residual stresses.

A simple model to take into account the effects of precipitation was proposed by Chobaut et al. [121]. They used a Gleeble machine to reproduce the cooling conditions on the plate surface and measured the yield strength at room temperature. By knowing the yield strength at the end of the quench, they could reproduce the measured residual stresses in several 7xxx plates.

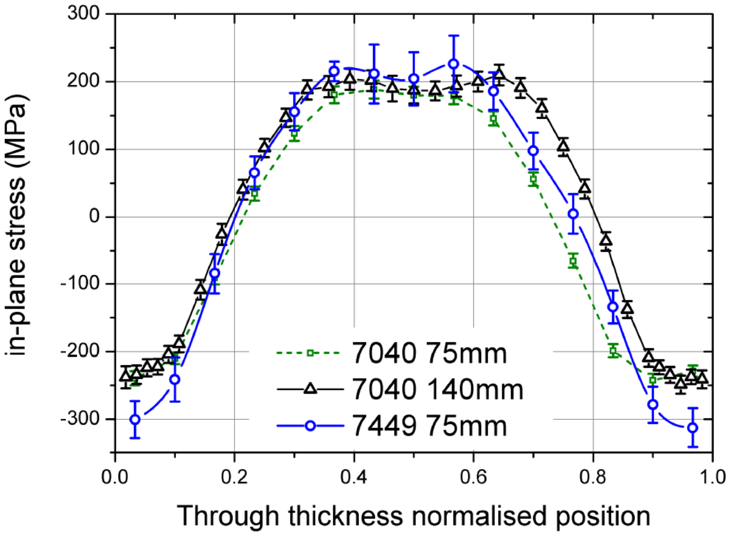

Figure 2.10: Residual stress in several AA7xxx thick plates measured by neutron diffraction [119].

2.7.2 Intergranular and interphase microstresses

Powerful tools to evaluate type-II stresses in single and multiphase materials are in-situ testing techniques such as neutron (ND) and synchrotron X-ray diffraction (XRD) [122]. Diffraction measurements are sensitive to individual phases and also to grain families. The diffraction peaks allow determining the relative change in interplanar spacing and therefore the lattice strain in each phase and for each particular orientation.

Intergranular microstresses

In polycrystalline single phase materials intergranular stresses are generally observed because of the different mechanical response of differently oriented crystallites (grain families). Figure 2.11a shows schematically the lattice strain response upon loading of three grain families ({111}, {002} and {220}) with lattice planes perpendicular to the loading direction (axial direction) in a single phase polycrystal. As the material is elastically anisotropic and the three grain families have different diffraction elastic constants, the lattice strain evolution in the elastic regime is different [118]. When the material plastifies deviations from linearity are observed. Once slip is initiated in certain grain families part of the elastic load they carry is transferred to grains in other orientations ({111} and {220}). The plastically deformed grains show a roughly constant lattice strain while the grains that have not yet plastified show large increases in lattice strain ({002}). When the material is unloaded residual tensile or compressive microstrains $\Delta\epsilon_{hkl}$ remain in the specific grain families [113].

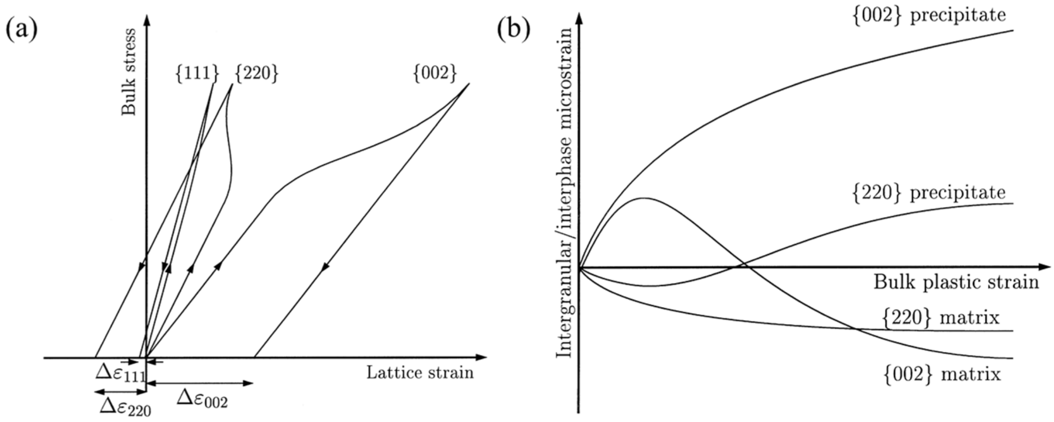

Figure 2.11: Schematic illustration of (a) intergranular microstrain evolution in a single crystalline polycrystal and (b) intergranular and interphase microstrain in a two-phase material [taken from [113]]

The intergranular microstrain formation during deformation was investigated for several fcc polycrystals [123, 124, 125, 126]. Clausen and Lorentzen measured the intergranular strain evolution in a commercial purity Aluminium polycrystal (AL2S). They found that the 111 grain families carry the highest elastic strains (hard direction) and the 220 grain families the smallest elastic strains (soft direction). The 200 reflection were found in between these two [123]. Clausen et al. used an EPSC model to simulate the development of elastic strains in an Aluminium polycrystal during uniaxial deformation [103]. They evidenced a low elastic anisotropy. The deviations from linearity in the plastic regime for the axial (grain families with lattice planes perpendicular to the loading direction) and transverse direction (grain families with lattice planes parallel to the loading direction) are shown in Figure 2.12. In both directions the largest differences are seen between the stiffest 111 and most compliant 200 reflections. The 220 reflection shows also a stiff behavior whereas the 311 reflection is only little affected. Similar trends were observed in the plastic regime for an Al-2Mg alloy and an AA7050 alloy that was artificially aged to the T7451 Temper [127, 128]. The elastic properties were found to change with alloying. Further, Pang et al. pointed out that intergranular stresses can have a large impact on macroscopic residual stresses and that intergranular stresses introduced by rolling are much more complicated than by uniaxial tension [128].

Interphase microstresses

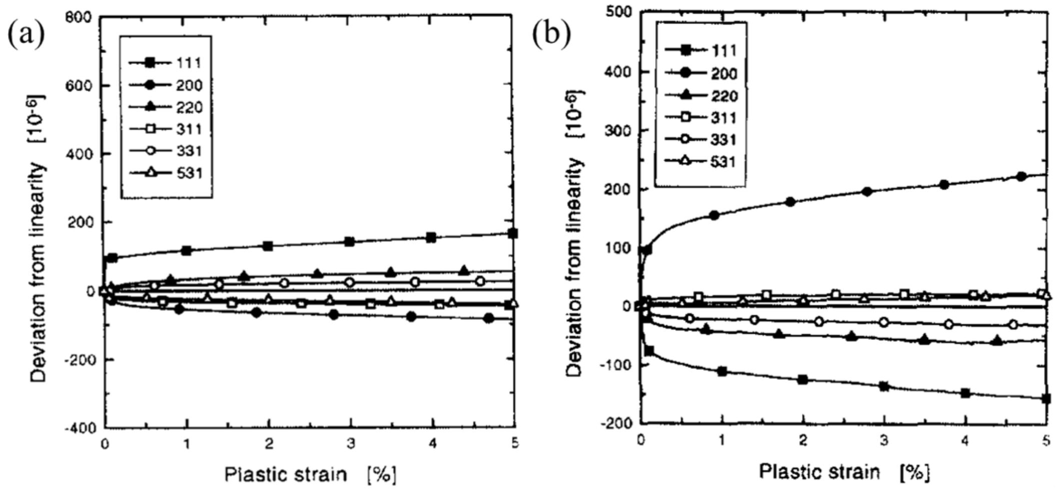

Figure 2.12: Deviations from linearity during plastic deformation of a Aluminium polycrystal in the (a) axial and (b) transverse direction [taken from [103]]

In multi-phase materials interphase stresses are generated due to different elastic and plastic properties of the phases, which will superpose the intergranular stresses in each phase [113]. Internal stresses build-up due to different elastic properties of the phases, which leads to a load transfer between them. Further, the local differences in yield stress and hardening behavior during plastic flow results in local reaction stresses and redistribution of the macroscopic applied load [118]. Figure 2.11b illustrates schematically the evolution intergranular and interphase microstrains in a matrix containing precipitates as a function of plastic deformation. After the yielding of the {220} matrix grains the load transfers to the {002} matrix grains, which have not yet yielded. When all matrix grains have yielded the load is partitioned to the precipitate phase [113].

An increasing amount of in situ diffraction studies have been accomplished during the last two decades in order to study different phenomena in multi-phase materials. Phase transformations have been studied in TiAl based alloys [129, 130, 131] and Aluminium alloys [132]. Further, the kinetics of the martensitic phase transformation were studied in metastable austenitic steels and its influence of the deformation behavior discussed [133, 134, 135, 136, 137, 114].

Several studies concerned also the internal stress generation in ferritic, bainitic and dual-phase steels [138, 139, 140, 141]. The main focus was on the interplay between the ferrite phase and reinforcing phases such as cementite and their influence on internal stresses [140, 142, 143, 144, 145]. Yet, the influence of precipitates on internal stress formation during deformation has not been studied in Aluminium alloys.

The understanding of the formation of type-II microstresses is important. On the one hand, they can have a marked influence on macroscopic RS measurement because diffraction measures the superposition of type-I and II stresses [128, 118]. On the other hand, type-II microstresses can have an influence the materials properties, e.g. by crack initiation or cause void formation [146]. Finally, the information obtained from the in situ diffraction experiments are useful to validate and improve micromechanical models of materials deformation [147, 118, 128].

3 Experimental and numerical methods

In this section the experimental and numerical applied in this thesis are presented and explained. Section 3.1 concerns the investiagted alloys and the different performed heat treatments. Details about the used microscopy techniques and thermal analysis methods are given in Sections 3.2 and 3.3. Section 3.4 provides an overview about small angle scattering experiments applied in the study and Section 3.5 introduces the solubility product, the applied precipitation model and the phenomenological framework to estimate the influence of vacancies on the diffusion. The used yield strength model is outlined in Section 3.6 and details about the in situ mechanical testing using diffraction are given in Section 3.7.

3.1 Materials and heat treatments

Two commercial heat treatable Aluminium alloys from the Al-Zn-Mg-Cu (AA7449 and AA7040) system were investigated in this study. Both alloys were provided by Constellium CRV as as-quenched (and natural aged) plates with a thickness of 75 mm and 142 mm for the AA7449 and AA7040, respectively. The nominal chemical compositions of both alloys are displayed in Table 3.1.

The two alloys were used in different tempers during the study. Table 3.2 gives an overview of the different tempers and the corresponding heat treatment parameters. To homogenize the material a solution heat treatment was applied before natural and artificial aging. The T4 state describes a material that has been quenched from the solutionizing temperature and kept at room temperature for at least 3 days (and up to more than 1 year) to ensure a substantially stable condition. The T6x state refers to a slightly overaged state, which is close to the peak aged T6 state. The T7x state describes an overaged state for the AA7449, obtained by performing the T6x heat treatment and in addition, 24 h at 210°C.

Table 3.1: Nominal composition (in wt.%) of the AA7449 and AA7040

Alloy	Zn	Mg	Cu	Al	trace elements
7449	7.5-8.7	1.8-2.7	1.5-2.3	balance	Si, Fe, Mn, Zr
7040	5.7-6.7	1.7-2.4	1.4-2.1	balance	Si, Fe, Mn, Zr, Ti, Cr

The heat treatments at low temperatures, such as aging, were performed in a low temperature furnace or in an oil bath. The SHT and high temperature isothermal holdings were conducted in a salt bath or in a vacuum furnace. The samples for the experiments were taken from the quarter thickness of the plate (if not stated otherwise) to ensure a homogeneous chemical composition.

Table 3.2: Laboratory heat treatment performed for this study

Heat treatment	Alloy	Procedure
SHT	7449	1h at 474°C
SHT	7040	ramp to, 1h at 483°C
T4	7449 & 7040	water quenched after the SHT and naturally aged for at least 3 days
T6x	7449	SHT, 4 days at 20°C, 30K/h to 120°C, 6h at 120°C, 15 K/h to 160°C, 9h at160°C
T7x	7449	T6x + 24h at 210°C

3.2 Electron microscopy

Different electron microscopy techniques were applied to characterise the microstructure on different length scales.

Scanning electron microscopy (SEM)

A FEI-XLF30-FEG scanning electron microscope was applied in secondary-electron (SE) or backscattered electron (BE) mode to study the intermetallic phases. Energy dispersive X-ray spectroscopy (EDX) was conducted to characterise the chemical composition of the intermetallic phases and matrix material with an EDAX Si(Li) EDX detector. In general, an acceleration voltage of 20 kV was used.

The grain and subgrain structure and also local texture was investigated by electron back scattered diffraction (EBSD). The investigations were conducted with a FEI-XLF30-EBSP microscope, which is equipped with an Oxford Instruments INCASynergy 350 and a NordlysS II EBSD detector. An acceleration voltage of 20 kV, a tile angle of 70° and a working distance of 12 mm were typically applied.

High resolution scanning electron microscopy (HRSEM) was performed with a Zeiss Merlin microscope to study the heterogeneous precipitation. The in-lens SE or energy selective backscattered electron (EsB) detector was used with an acceleration voltage in the range of 2 to 5 kV.

The samples investigated by SEM were compression hot mounted with KonductoMet and ground with silicon carbide paper (finish with Buehler P4000). The subsequent polishing was performed with diamond solution (0.25 μm). In addition, the samples used for EBSD and HRSEM were finished by 2 h polishing with a vibrating polisher (Buehler Virbromet).

Transmission electron microscopy (TEM)

Transmission electron microscopy was applied to study the nature and size of the heterogeneous and homogeneous precipitates. The bright and dark field TEM images and also the selected area diffraction patterns (SAED) were obtained either with a Philips/FEI CM12 or FEI Tecnai Osiris using an acceleration voltage of 120 kV and 200kV, respectively. The TEM EDX measurements were conducted at the FEI Tecnai Osiris, which is equipped with four Super-X SDD EDX detectors. The TEM samples were prepared from 3 mm discs, which were extracted from the thick plates by electrical discharge machining. The samples were ground down to 100 μm and then electro polished with Struers Tenupol-5 twin-jet. A solution of HNO_3 and methanol (1:3 in volume) was used at -20°C with a voltage of 18V.

3.3 Differential scanning calorimetry

Differential scanning calorimetry (DSC) experiments were performed on a Perkin Elmer power compensation DSC8000 machine. Typical sample size was 4 mm in diameter and 1 mm in thickness with a weight around 33 mg. Cooling and heating experiments were performed with varying rates between 2 and 80 K/min (0.033 - 1.33 K/s). The sample was always measured together with a pure Aluminium sample (Al4N) as a reference. Before or after each sample measurement one baseline measurement was performed using two pure Aluminium samples in order to account for baseline drift and variability [148, 149].

Typically, the baseline measurement was subtracted from the sample data. The heat flow was then normalised for the sample weight and the applied heating/cooling rate. The normalized data was then analysed using the peak analyser option of the Origin software. A spline background was fitted to the DSC curves using temperatures, where the heat flow should be zero (usually: -20, 5 and 476°C). A review concerning the use of DSC to study precipitation phenomena in Aluminium alloys can be found in Reference [149].

Peak temperature analysis

When solid state transformations occur during DSC analysis, the change in thermal properties and heat content is characterised by a peak or deflection from the baseline. The peak temperature can be associated with the temperature of maximum reaction rate. If the reaction is thermally activated the position of the peak and the peak temperature will change as the heating rate changes. Therefore, the activation energy of the reaction can be estimated from this change of the peak temperature by applying the a peak temperature analysis [150, 151, 152, 153]:

$$ln\frac{h}{T_p^2} = -\frac{\Delta E}{\bar{R}T_p} + C_1 \tag{3.1}$$

where h is the heating rate, T_p is the peak temperature, ΔE is the activation energy for dissolution/formation, $\bar{R}$ is the gas constant and C_1 is a constant. When h/T_p^2 is plotted against 1/RT$_p$ the slope of the linear fit yields the activation energy of the reaction.

DSC heating experiments were performed on samples that were as-quenched and natural aged for more than one year with heating rates of 2, 5, 10 and 20 K/min. Further, DSC heating experiments were also performed on samples directly after quench with heating rates of 10, 20 and 40 K/min.

3.4 Small angle scattering

Small angle scattering using X-rays (SAXS) or neutrons (SANS) has proven to be a useful tool for the investigation of precipitation phenomena as for example in heat treatable 2xxx, 6xxx and 7xxx Aluminium alloys [11, 154, 155, 156, 157, 158, 159, 58, 160, 161, 62, 162].

Small angle scattering (SAS) is a well-established technique for investigating inhomogeneities with sizes in the range of 0.4 nm to 400 nm that have a high contrast with respect to the matrix. SAXS is sensitive to the electron density and therefore to fluctuations of the atomic number (chemical composition). Due to the high flux of modern synchrotron sources, SAXS experiments can be performed time resolved and in situ during specific heat treatments. The contrast in SANS experiments originates from the atom nuclei and their magnetic moment. SANS is typically used when the precipitates have a low contrast in atomic number and/or a low volume fraction because of the high penetration depth of the neutrons and therefore a large illuminated sample volume (increased statistics) [163].

Both techniques has been used extensively to study precipitation phenomena in Al alloys ex situ and also in situ during aging [51, 164, 161] or non-isothermal heat treatments [96, 18]. Providing information on the size and volume fraction of the precipitates, SAS is very useful to validate thermodynamic-based precipitation model predictions [96, 84, 18, 99].

3.4.1 Scattering theory

Small angle scattering is based on the general theory of diffraction. The incoming wave k_0 (X-rays or neutrons) is diffracted or scattered wave k_1 under the scattering angle 2θ in the sample by objects such as electrons (for X-rays) and nuclei (for neutrons) as schematically shown in Figure 3.1. The difference between the incident wave and the scattered wave can also be expressed by the scattering vector q, which is defined as q = $4\pi/\lambda \ sin(2\theta/2)$, where λ is the wavelength. The amplitude of the scattered wave by a single scatterer positioned at $\vec{r}$ is defined by [163]:

$$I(q) = e^{i\vec{q}\vec{r}} \tag{3.2}$$

Small angle scattering probes fluctuations that are larger than the interatomic spacing. Therefore, the contribution of all scatterers per unit volume Vhas to be considered. This is defined by the scattering factor density (scattering length

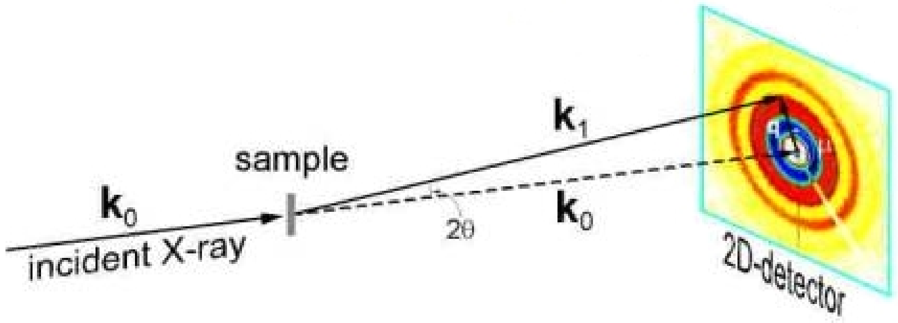

Figure 3.1: Schematic illustration of a SAXS [taken from [165]]

density (SLD) for neutrons) $\rho(\vec{r})$. The scattered intensity is then calculated as [163]:

$$I(\vec{q}) = |A(\vec{q})|^2 \tag{3.3}$$

where A is the scattered amplitude

$$|A(\vec{q})| = \int\int_V\int \rho(\vec{r})\, \exp(-i\vec{q}\vec{r})\, dV \tag{3.4}$$

In the case of an isotropically scattering sample (isotropic inhomogeneities or a textureless polycrystal with small grain size compared to the beam size), the vectors can be replaced by their amplitude [163]:

$$I(q) = \left|\int\int_V\int \rho(r)\, \exp(-iqr)\, dV\right|^2 \tag{3.5}$$

With the assumption of a dilute solution of identical particles of scattering factor density ρ_p dispersed in a matrix of scattering factor density ρ_m, this term can be simplified by averaging over all orientations ($\exp(-iqr)dV = \frac{sin(qr)}{qr}$ - Debye formula) [18]:

$$I(q) = 4\pi^2(\rho_p - \rho_m)^2 \int_V \frac{sin(qr)}{qr} r^2 dr \tag{3.6}$$

For a single spherical precipitate of radius R and volume $V_p = 4/3\pi R^3$ the scattered intensity is then written as:

$$I(q,R) = 4\pi^2(\rho_p - \rho_m)^2 V_p^2 (3\frac{sin(qR) - qR\,cos(qR)}{qR}^3)^2 \tag{3.7}$$

In real metallic systems, precipitates typically feature a size distribution $N(R)$ and they are not always spherical, which has to be considered using different form factors $F(q, R)$. Further, in some cases (e.g. GP(I) zones) the interparticle distance of the precipitates is similar to the precipitate size, which can result in interference effects when the volume fraction f_v is high. The interference effects can be considered for the scattered intensity by a structure factor $S(q, R, f_v)$. The difference in scattering factor density of the precipitates ρ_p and the matrix ρ_m is defined as $\Delta\rho$. The scattered intensity at scattering vector q is then expressed in the general form [63]:

$$I(q) = (\Delta\rho)^2 \int_0^\infty F(q, R)^2 \, S(q, R, f_v) \, N(R) \, dR \tag{3.8}$$

For metallic alloys the lognormal size distribution is often used to describe the precipitate size distribution [63]:

$$N(R) = n_0 \, f(R) = n_0 \frac{1}{\sqrt{2}Rs} \exp \frac{-(ln(R/\mu_0))^2}{2s^2} \tag{3.9}$$

where n_0 is the number density of precipitates, $f(R)$ is the normalized lognormal distribution of the precipitates radii, s is the dispersion parameter and μ_0 is the location parameter.

3.4.2 SAS experiments

In the scope of this thesis, different SAXS and SANS experiments were performed at different facilities. The heterogeneous η precipitates were examined by SANS measurements at the SANS-I beamline of the Swiss Spallation Neutron Source (SINQ) at the Paul Scherrer Institut (PSI) [166]. Time-resolved in situ SAXS experiments during fast heating and cooling were realised at the cSAXS beamline of the Swiss Light Source (SLS) at PSI. The laboratory SAXS source of the Science et Ingénierie des Matériaux et Procédés (SIMAP) Laboratory at the Institut national polytechnique de Grenoble (Grenoble INP) was used for isothermal holdings and slow heating experiments. The experimental details are explained for each beamline in the following.

SANS at the SANS-I beamline (PSI)

SANS measurements were performed to study the quench-induced heterogeneous η precipitates in the 75 mm AA7449 and the 142 mm AA7040 thick plates, which were in the as-quenched (and natural aged $>$ 1 year) state. The samples were taken out parallel to the rolling direction between the surface and the center of the plates. The samples featured a thickness of 2 mm and a diameter of 26 mm. The samples were labelled by distance between the middle of the sample and the surface of the plate. A wavelength λ of 0.6 nm and an aperture with a diameter of 19 mm were used in the experiments. The measurements were performed at three different detector to sample distances (18 m, 6m and 1.5 m) allowing to measure the scattering vector q in the range of $0.001\,\text{Å}^{-1} \leq \text{q} \leq 0.21\,\text{Å}^{-1}$.

SAXS at the cSAXS beamline (PSI)

Time-resolved in situ SAXS experiments were performed at the cSAXS beamline, owing to the high photon flux provided by the synchrotron source at the SLS (PSI). The specimens were taken from the quarter thickness of a 75 mm AA7449 plate (T4 state) exhibiting a size of 3 × 25 × 0.5 mm (width x length x thickness). The samples were solutionized for 1h at 474°C and quenched in water to dissolve residual precipitation before the SAXS experiment.

A laser-based heating system [167], which was originally designed for the TOMCAT beamline of the SLS, was used to apply different heat treatments to the sample. The samples were positioned upright and the laser system was installed around the sample position (Figure 3.2). The sample was heated by the laser from both sides at the same height to ensure a homogeneous radial heat distribution. This setup allows heating up the sample to the solutionizing temperature and subsequent fast cooling of the sample by carefully controlling the power of the lasers. The temperature profiles were PID controlled by manipulating the output power of the lasers based on the temperature readings from a K-type thermocouple. The thermocouple was attached to the sample by spot welding and reinforced by a two-component glue. The laser spots were positioned at the height of the X-ray beam, which was around 2 mm above the thermocouple. The temperature gradient between the heating position and the thermocouple position was measured for different temperatures and accounted for in the applied temperature profile and during further data analysis.

Before the rapid cooling, the samples were heated to solutionizing temperature and held for 7 min to homogenise the microstructure. The cooling was performed either by 3 linear temperature ramps or by switching off the lasers to get the fastest possible cooling. The obtained cooling rate between the solutionizing temperature and 200°C were in the range of -80 to -5 K/s. Below 200°C the cooling rates slowed down and followed a Newtonian cooling to near room temperature. The heating to the solutionizing temperature and the isothermal holdings were controlled manually.

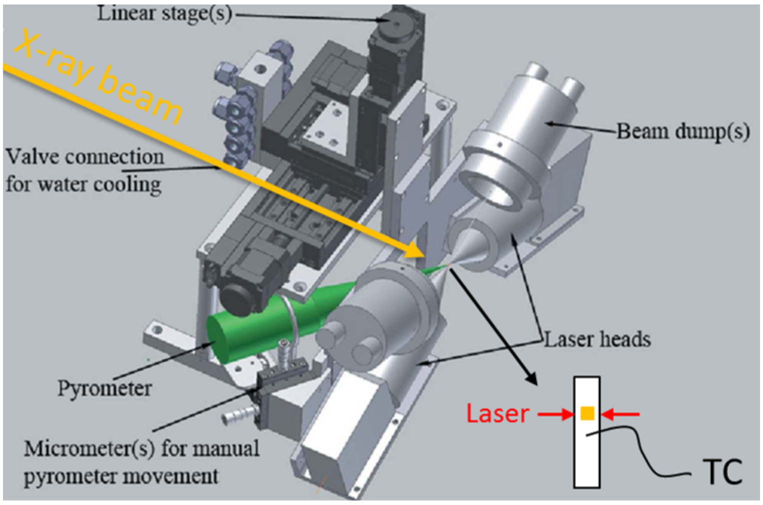

Figure 3.2: Schematic of the set-up used to perform the in situ SAXS experiments at the cSAXS beamline (adapted from [167])

In order to observe the dynamic processes during quenching, scattering patterns were recorded every 0.5 seconds.

The small angle X-ray scattering experiments were performed at a wavelength of 0.774 Å (16 keV). The distance between the sample and the Pilatus 2M pixel detector was either 7 m or 2.1 m giving an accessible scattering vector range of $0.0023\,\text{Å}^{-1} \leq q \leq 0.3\,\text{Å}^{-1}$ and $0.007\,\text{Å}^{-1} \leq q \leq 1\,\text{Å}^{-1}$, respectively. The beam diaphragm was completely opened ($\sim 200 \times 200\,\mu\text{m}^2$) to ensure good grain statistics.

SAXS at the SIMAP laboratory

The SAXS experiments of long duration have been performed on the laboratory rotating anode at the SIMAP laboratory in Grenoble. A Cu K_α source was used giving an energy of 8 keV and a wavelength λ of 1.54 nm. The samples featured typically a thickness of 80-120 μm. The size of the X-ray beam was 1 x 1 mm^2 giving an illuminated volume of roughly 1x1x0.1 mm3. In situ heating experiments or isothermal holdings were carried out using a dedicated furnace [96]. The signal was recorded with a CCD camera. The detector to sample distance was adjusted for each experiment in order to better observe the scattering due to GP(I) zones or η'/η hardening precipitates. The accessible scattering vector range was limited to $q_{min} \geq 0.01\,\text{Å}^{-1}$ and $q_{max} \leq 0.7\,\text{Å}^{-1}$.

Three different types of experiments have been performed on the laboratory source. SAXS mappings were performed through the half thickness of a 75 mm AA7449 plate. To this aim thin slices were machined out from the surface to 45 mm below the surface (center = 37.5 mm) by electrical discharge machining (EDM)

and subsequently polished down to 100 micron. Three different microstructural states were investigated. The samples were in the T4 (sample as received from the as-quenched and natural aged thick plate), T6 (sample as received from T4 thick plate and artificial aged to T6) and perfect T6 state (sample solution treated, quenched as thin sample and artificially aged to T6). For the T4 sample only 1 scan was performed from the surface to 44 mm below the surface, whereas for the T6 and perfect T6 samples 3 scans have been investigated. The distance between measurement points was 1 mm in the scan direction, 1.5 mm between each scan. The measurement time for one image was 500s.
Isothermal holdings were performed at temperatures of 75 and 105°C. The small samples were heat treated and quenched before the SAXS experiment. The time at room temperature between the quench and the start of the experiment was between 5 to 10 min. The samples were heated at approx. 5 K/s to the holding temperature. An image was averaged over a measurement time of 500s for 75°C and 150s for 105°C.
Reversion heat treatments were applied to samples that were taken from the surface, quarter and center position of a 75 mm thick plate. The samples were in the T4 state and were heated to approx. 300°C with two different heating rates of 1 and 5 K/min. The measurement times for one image were 150s and 30s for 1 and 5 K/min, respectively.

3.4.3 Data treatment

In general, the recorded scattering pattern has to be corrected for any data distortions introduced by the x-ray or neutron detection system and normalised for measurements and sample parameter in order to obtain the intensity in absolute units [168]. The most important raw data correction steps and their appropriate order are outlined in Figure 3.3. The raw data is usually recorded as a 2D image, which has to be read-in (DS) and corrected for detector defaults if necessary (e.g. for CCD cameras). In addition, a mask needs to be created, which allows covering e.g. incorrect pixels and the beamstop (MK). The measured intensity has to be normalized by sample measurement time (TI) before it can be radially or azimuthally averaged to obtain 1D data. The corrected intensity I_{corr} will then be normalized by the sample transmission (TR) and thickness (TH). Further, the background noise I_{bg} has to be subtracted from the raw data. The background should be measured for the same amount of time as the sample. As a last step, the corrected data needs to be scaled to absolute intensity. Typically a secondary

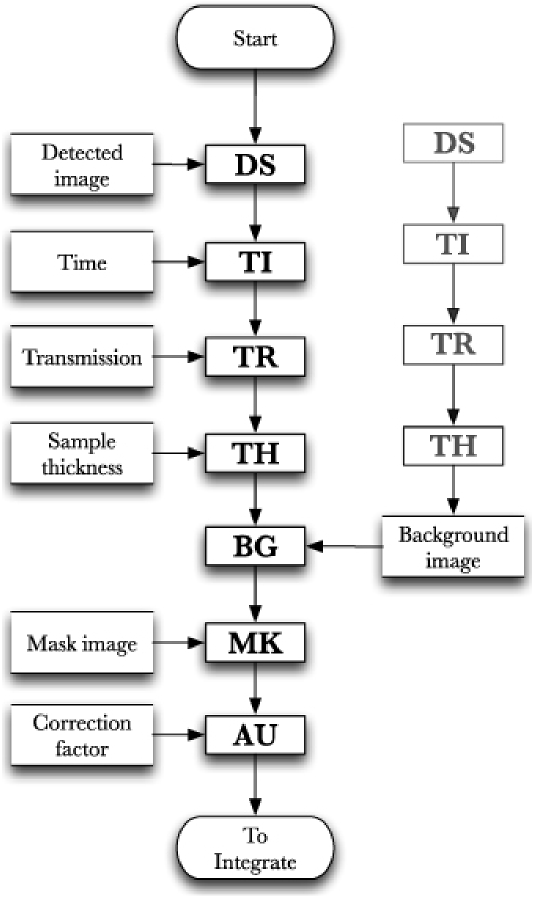
Start
Detected image
DS
Time
TI
Transmission
TR
Sample thickness
TH
BG
Mask image
MK
Correction factor
AU
To Integrate
DS
TI
TR
TH
Background image

Figure 3.3: Necessary amount of corrections for SAXS raw data when the samples are without a strongly absorbing container, the X-ray beam is stable, a good detector is used and low dark current and/or natural background is present [168]

standard such as glassy carbon is used to determine a calibration factor F, which is calculated by comparing the intensity of the calibrated data file with the locally collected intensity [169]. The data normalisation after the radial averaging can be summarized as:

$$I_{abs} = F(\frac{I_{corr}}{TR \cdot TH} - \frac{I_{bg}}{TR_{bg} \cdot TH_{bg}}) \tag{3.10}$$

The scattering vector q is commonly calibrated by using Silver Behenate as standard. Details on the data treatment for each beamline are presented in the following.

SANS at the SANS-I beamline

The Grasp software was used to apply the corrections and normalisations and to perform the radial averaging [170]. The 2D SANS images were corrected for empty cell contribution, background noise (Cd spectrum) and detector efficiency. The measured intensity was further normalised by the sample transmission, sample thickness and the measurement time. The absolute intensity was calibrated using water as secondary standard.

SAXS at the cSAXS beamline

The radial averaging of the 2D images was done with a Matlab routine that was provided by the cSAXS beamline. An additional Matlab routine was written to perform the data treatment and normalisation. In order to increase the measurement statistics, the 1D intensity data files taken during the rapid cooling from solutionizing to room temperature were averaged over 100 equidistant temperature segments (Δ T $\approx$ 4.5K). In addition, the data was subjected to a median filter treatment and was then normalised by the sample thickness and sample transmission (direct flux measurement). The scattering spectrum at the solutionizing temperature was used for background subtraction. The absolute intensity was calibrated using glassy carbon as a secondary standard [169].

SAXS at the SIMAP laboratory

The data treatment of the SAXS data was performed with programs provided by the SIMAP laboratory. The 2D-SAXS images were corrected for read-out noise, distortion, dark field (correction of detector noise) and flat field (different efficiencies of each pixel). The images were then integrated over 360 degrees and the background noise was subtracted. The intensity data was normalised by the sample thickness and sample transmission before a median filter treatment was applied.

Another correction has to be applied to the SAXS data. The normalised intensity has to be corrected for the scattering of the disordered solid solution and the fuorescence of secondary elements, the so called Laue correction. This correction was done during the data analysis procedure as explained in the next section.

3.4.4 Data analysis

Model independent analysis has been applied in this study to extract structural parameters such as average radius and volume fraction from the scattering experiments. A Matlab routine was written that allows to fit the Guinier radius R_g of the scatterers and the scattering invariant Q. An additional Matlab routine was written that allows to calculate the volume fraction from the estimated scattering invariant by making assumptions on the chemical composition of the precipitates. The details of the analysis are presented in the following.

Size analysis

The size of scattering objects is estimated by using the Guinier approximation. At low q (q → 0), the equation 3.7 can be written as:

$$I(q) = (\Delta\rho)^2\, V_p^2\, exp(-\frac{q^2 R_g^2}{3}) \tag{3.11}$$

where R_g is the radius of gyration (Guinier radius) of the precipitate. The Guinier radius is measured by a linear fit in the Guinier plot ($log(I)\ vs\ q^2$). The Guinier radius is then calculated from the initial slope m as [171]:

$$R_g = \sqrt{-3}m \tag{3.12}$$

For monodispersed precipitates the radius can be estimated from the Guinier radius as $R_g = \sqrt{3/5}R$. However, precipitates in metallic systems are typically characterised by a size distribution. It was shown that when the dispersion of the PSD is 0.2 the average precipitate radius of the PSD is equal to the Guinier radius as shown in Figure 3.4 [171]. Further, it can be seen that for a constant average radius R_m of the PSD, an increasing dispersion of the PSD will lead to a higher Guinier radius. This originates from the higher sensitivity of the Guinier radius to the large precipitates ($I \propto R_g^2$).

For practical reasons, throughout the thesis the PSD dispersion is considered to be around 0.2, if not stated otherwise. This allows using the Guinier radius as average precipitate radius.

The size of the scatterers can also be estimated from the position in the maximum intensity of the Kratky plot ($Iq^2\ vs\ q$) [163]. The position of the maximum q_{max} can be interpreted as the q-value, which has the largest contribution to the integrated intensity. The so-called pseudo Guinier radius R_{max} can be calculated as:

$$R_{max} = \frac{\sqrt{3}}{q_{max}} \tag{3.13}$$

The pseudo Guinier radius can be used as a first estimate for the boundaries ($a/R_{max} < q < b/R_{max}$ for typical values of a =1 and b = 2) of the linear Guinier fit. This allows to measure the Guinier radius R_g in a self-consistent way [171].

The number of atoms N_{atoms} with the atomic radius R_a in a cluster or precipitate

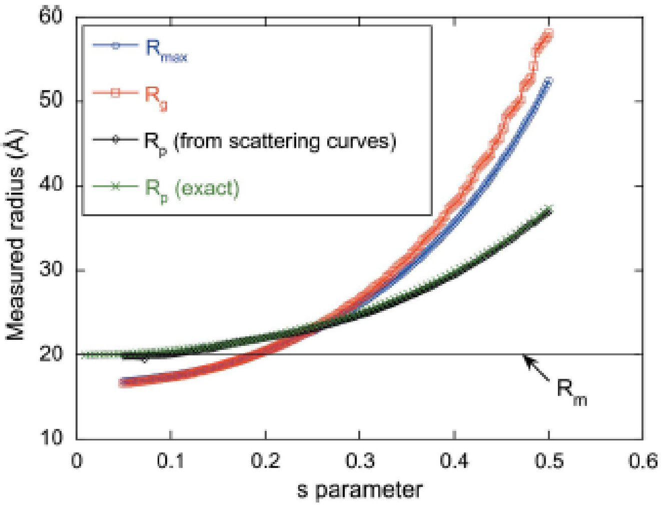

Figure 3.4: The influence of the dispersion s of the particle size distribution on the measured Guinier and pseudo Guinier radius (taken from [171]).

with the radius R_g can be calculated as:

$$N_{atoms} = \frac{V_{cluster}}{V_{atom}} \frac{\pi\sqrt{2}}{3} = \frac{R_g^3}{R_a^3} \frac{\pi\sqrt{2}}{3} \tag{3.14}$$

Volume fraction analysis

The volume fraction of the scattering precipitates is proportional to the invariant or integrated intensity Q, which is proportional to the area under the scattering curve in the Kratky plot. Assuming a two phase model, separated by a sharp interface, the volume fraction can be calculated as [162]:

$$Q_0 = \int_0^\infty I(q)q^2 = 2\pi^2(\Delta\rho)^2 f_v(1 - f_v) \tag{3.15}$$

Measuring the whole scattering curve from 0 to infinity is not possible due to a limited q-range in the experimental measurements. Therefore, extrapolations for the low-q and high-q regions are necessary.

In the low-q region, a linear extrapolation from the first measured point q_0 to 0 can be performed, which is exemplarily shown in Figure 3.5a. This is only valid if there is no strong parasitic scattering, e.g. double Bragg scattering or scattering from large particles. In the high q-region, the integral can be extended to infinity

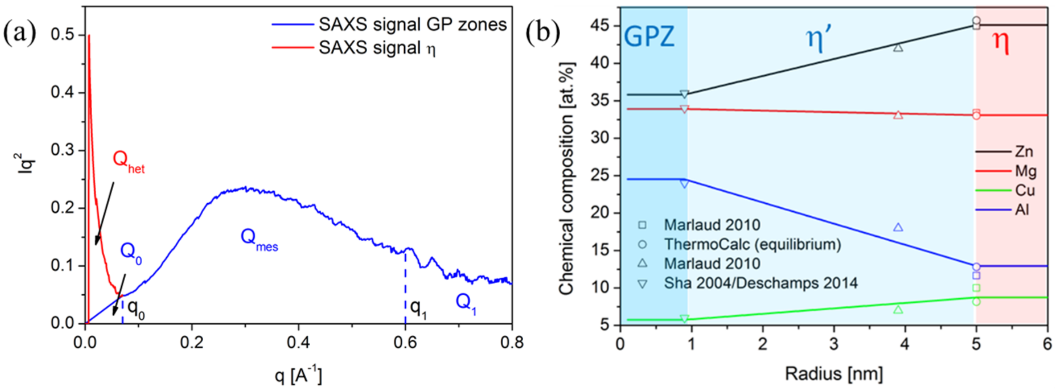

Figure 3.5: (a) SAXS signal in Kratky representation and (b) Evolution of the chemical composition is shown as a function of the precipitate size.

by fitting the scattered intensity with the Porod law:

$$I_{q\to\infty} = \frac{K_p}{q^4} + I_{Laue} \tag{3.16}$$

with K_p being the Porod constant and I_{Laue} the background noise, which originates from Laue scattering of the disordered solid solution, but also from fluorescence of secondary elements. The I_{Laue} is usually subtracted from the scattering curves and K_p can be used to extend the integral from the last measurement point q_1 to infinity. Finally, the scattering invariant Q can be estimated as [163]:

$$Q = \int_0^{q_0} I(q)q^2dq + \int_{q_0}^{q_1} I(q)q^2dq + \int_{q_1}^{\infty} I(q)q^2dq \tag{3.17}$$

and

$$Q \approx \frac{I(q_0)q_0^3}{2} + \int_{q_0}^{q_1} I(q)q^2dq + \frac{K_p}{q_1} \tag{3.18}$$

When the integrated intensity and the Porod constant are known, it can be useful to calculate the Porod radius R_p. The Porod radius represents the radius of a sphere, which has a surface to volume ratio that is equal to that of the precipitate size distribution. It is therefore equal to the ratio of the total volume V_t and total surface S_t of the precipitate population and is given by:

$$R_p = \frac{3Q}{\pi K_p} = \frac{3V_t}{S_t} \tag{3.19}$$

In certain cases the scattering contribution of more than one phase can be present in the scattering signal. Figure 3.5a shows exemplarily the scattering signal that arises from the presence heterogeneous η phase and homogeneous GP(I) zones. The two scattering contributions were deconvoluted as follows: the scattering invariant of the homogeneous phase (blue curve) was estimated as described before and subsequently subtracted from the whole scattered intensity (red + blue curve). This approach is of course only a simple estimate and inherits an uncertainty.

For selected SAXS spectra model dependant analysis was applied using the SASfit software [172]. The form factor of a sphere was used and a lognormal distribution was assumed to simulate the scattering signal of GP(I) zones at the end of rapid cooling's.

Assumptions on the chemical composition of the second phase precipitates

In order to convert the integrated intensity or scattering invariant into volume fraction the scattering factor density (or SLD for neutrons) contrast between the matrix and precipitates has to be calculated. The scattering length density used to analyse the SANS measurements was estimated using the SLD calculator of the SASfit software. For the SAXS measurements, the scattering factor density in each phase was calculated by [162]:

$$\rho = \frac{\sum_i f_i X_i}{\Omega} \tag{3.20}$$

where Ω is the average atomic volume, X_i is the atomic fraction of the element i and f_i is the scattering factor of each element. The scattering factor f_i is given by:

$$f_i = Z_i + f_i^{'} + i f_i^{''} \tag{3.21}$$

where Z_i is the atomic number and $f_i^{'}$ and $f_i^{''}$ are the real (coherent) and imaginary (absorption) contributions to the resonant corrections, respectively.
A good knowledge of the precipitate chemistry is crucial to calculate the scattering factors and therefore an appropriate scattering contrast $\Delta\rho$. The chemical composition of the GP(I) zones changes when they grow and transform in η' and η precipitates (Section 2.3 and Appendix A). In order to have more accurate predictions, a size dependant chemical composition was assumed to calculate the scattering contrast as shown in Figure 3.5b. The size dependant chemical composi-

tion is based on recent publications [42, 58, 173, 63], but also follows the general observed trends of increasing Zn and Cu content and decreasing Al content with increasing precipitate size. The volume fraction of η was calculated using the chemical composition presented in Section 2.3 and reported in [58].
A matlab program was written that calculates in dependence of the size the scattering factor density of the precipitates and of the matrix (from the solute balance). The volume fraction was calculated in an iterative way until the initial guess of the volume fraction and the calculated volume fraction match.

Number density of precipitates
When the size and volume fraction of the precipitates are known, the number density of spherical precipitates is calculated as:

$$N_{prec} = f_v/(4/3\pi\, R_g^3) \tag{3.22}$$

Note on the influence of the scattering vector range
Most cSAXS experiments were performed with a detector to sample distance of 2m in order to focus on the evolution of the fine homogeneous precipitates. At this distance, scattering of the heterogeneous η precipitates was also observed at low q. However, it has to be mentioned that, due to the measurable momentum transfer was limited to q ≥ 0.007 Å^{-1}, the Guinier radius could not be reliably measured for the η phase. In addition, the scattering invariant cannot be reliably measured since part of the scattering contribution is cut off. This is shown exemplarily in Figure 3.6. The scattering due to large η precipitates ($R_g \approx 60$ nm) is shown that was measured at a detector distance of 7 m. It is obvious that this contribution cannot be measured well at a detector distance of 2m as indicated by the vertical black line. Therefore, volume fraction of η (measured at a 2m distance) will be smaller than the actual volume fraction of η. Yet, the underestimated volume fraction still provides a good estimate of the temperature range of the η formation and gives qualitative information.

Note on the reproducibility of the cSAXS experiments:
Figure 3.7 shows experimental results obtained from in situ SAXS from two similar cooling conditions. The applied cooling rates and the volume fraction evolution are very similar in both cases. Small differences can be seen for the Guinier radius (and therefore also for the calculated density) in the temperature range of 150-100°C. This can be related to a small scattered intensity and broad scattering signal, which

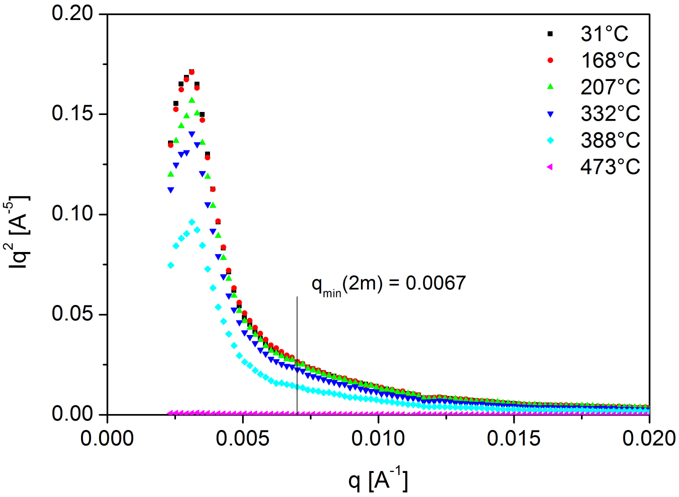

Figure 3.6: Influence of the sample-to-detector distance (7m and 2m) for the scattering due to large η precipitates ($R_g \approx 60$ nm) at a distance of 7m. The lowest q-value for the 2 m distance is indicated by the vertical line.

make the estimation of the Guinier radius difficult. However, it can be seen that the experimental setup allows reproducing similar cooling conditions, which also give very similar results.

3.4.5 Considerations about the accuracy of SAS analysis

Guinier radius

The uncertainties of the Guinier radius that are presented throughout the thesis were calculated from the error associated with the slope of the linear Guinier fit. The error associated with the influence of the PSD on the average radius is not considered.

Scattered intensity

Figure 3.8a and b show typical scattering curves obtained from SANS and SAXS experiments and the associated error of the scattered intensity. The standard error I_{err} shown for each point was calculated from the radial averaging as [174]:

$$I_{err} = \frac{I_{std}}{\sqrt{N}} \tag{3.23}$$

where I_{std} is the standard deviation of the intensity and N is the number of pixels averaged. It can be seen that the errors of the scattered intensities of the SANS

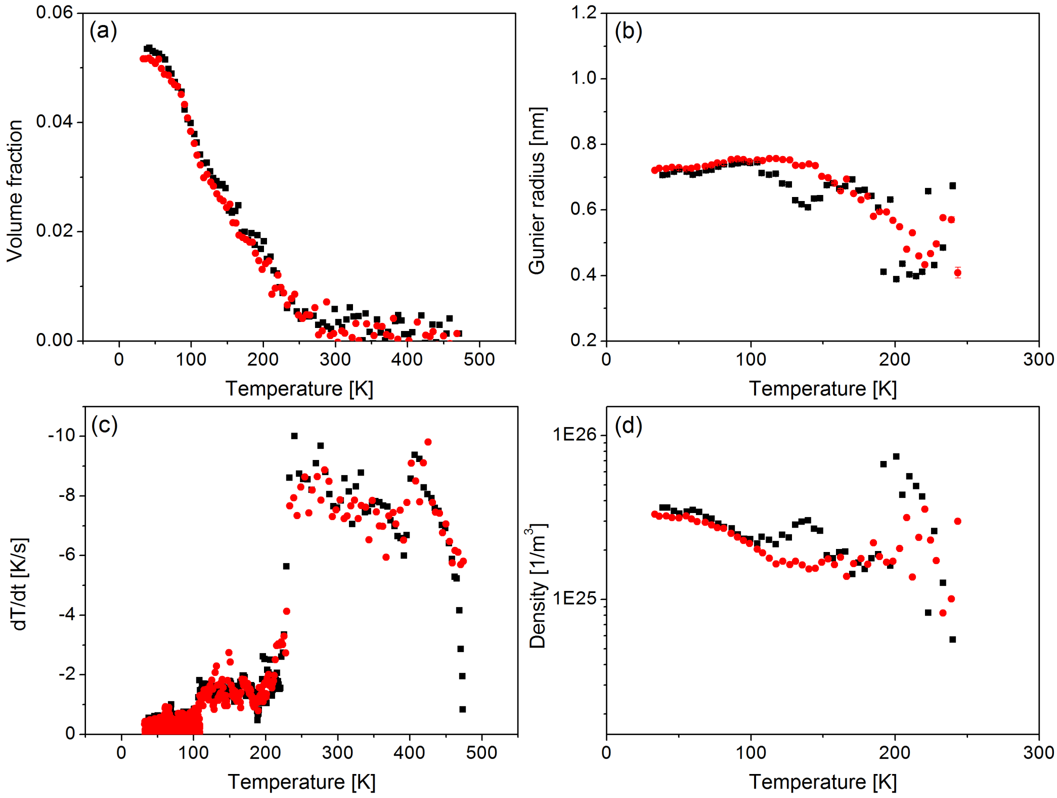

Figure 3.7: (a) Volume fraction, (b) Guinier radius, (c) cooling rates and (d) calculated density as function of temperature for two similar cooling conditions performed at the cSAXS beamline.

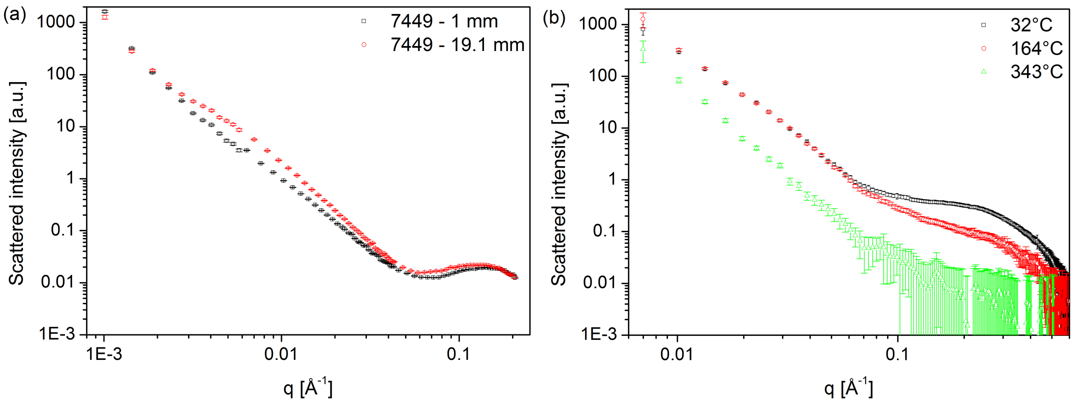

Figure 3.8: Scattering curves and the corresponding error for (a) two SANS experiments with a 75 mm AA7449 plate on samples with 1 mm and 19.1 mm distance to the surface and (b) SAXS during cooling performed at the cSAXS beamline for scattering spectras taken at 343, 162 and 32°C.

experiments are typically very small. For the SAXS measurements the errors are smaller when the intensity is higher. Low (background) scattering in the high-q region leads to a high error (green line). In addition, the measurement point close to the beamstop features also a higher error. The uncertainty of the intensity is not shown in the figures of the thesis for better clarity. If the transmission is not measured for each sample, small thickness variations due to machining introduce an additional source of error. The extrapolations of the scattering signal from q_0 to 0 and more importantly from q_1 to infinity are other sources of uncertainty. Especially the latter, inherits a large uncertainty if the scattering signal is not measured to sufficiently high q values.

Volume fraction

Sources of errors when estimating the volume fraction originates from the uncertainty due to the absolute intensity calibration with a secondary standard, the assumptions of the chemical composition of the precipitates and the accuracy of the scattered intensity calculation.

The uncertainty resulting from the absolute intensity calibration was reported to be in the range of 5-10% [169, 162]. The error associated with assumptions of the chemical composition is not easy to estimate. Generally, the error will be higher for phases, where the exact composition is not well known or changes quickly as a function of time and temperature (e.g. VRC and GP(I) zones). For the equilibrium η phase the composition is relatively well known and the error is considerably smaller.

3.5 Precipitation modelling

3.5.1 Calculation of the cooling conditions in the plates

The cooling conditions during quenching of the 75 mm AA7449 and 142 mm AA7040 thick plates were calculated by using the COMSOL software. The heat transfer coefficients (HTC) were taken from Reference [175].

3.5.2 Thermodynamic description of phases

Reliable phase diagram data are crucial for the modelling of precipitation. The stability of precipitates is described by its solubility curve. The thermodynamic description of equilibrium phases, such as η, are available from commercial CALPHAD (Calculation of Phase Diagrams) databases e.g. the Al-Data database from ThermCalc [176, 173]. Gibbs free energy minimization methods are used to establish the phase diagram of the specific system [177]. The equilibrium phase is typically described by their chemical composition and solubility curve as function of temperature.

The chemical composition of the metastable phases, such as GP(I) zones and η' is generally not provided by commercial databases. The chemical composition of the metastable phases can vary substantially from the one of the equilibrium phase and can also change as a function of temperature and aging time (Section 2.3 and Appendix A).

The solubility curve of a phase can also be calculated using the solubility product when the chemical composition is known from experiments or by making assumptions as presented in References [95, 108]. The regular solution model is only valid when the alloy is sufficiently dilute, which is the case for most commercial AA7xxx alloys.

The relationship between the standard free energy of a chemical reaction and the solubility product K is given by:

$$\Delta G^0 = \Delta H^0 - T\Delta S^0 = -\overline{R}T\ln K \tag{3.24}$$

where ΔH^0 is the standard enthalpy of reaction, T is the temperature and ΔS^0 is the standard entropy of reaction. At a given temperature, a precipitation or dissolution reaction is presented by:

$$mM + xA + yB \Leftrightarrow M_mA_xB_y \tag{3.25}$$

where $M_mA_xB_y$ is the precipitate phase and M is main constituent of the alloy, A and B are the alloying elements. The equilibrium constant K is defined as:

$$\mathrm{K} = (a^A)^x(a^B)^y \tag{3.26}$$

with a^A and a^B being the activities of elements A and B. For dilute regular solid solutions, the activities are equal to the solubility limits c_e^A and c_e^B in the solid solution. Pure solids (compounds) and the matrix are not considered in the solubility product equation since their activities or concentrations are equal to one. The relationship of the standard free energy can be rewritten as:

$$\ln(a^A)^x(a^B)^y = \ln(c_e^A)^x(c_e^B)^y = \frac{-\Delta H^0}{\overline{R}T} + \frac{\Delta S^0}{\overline{R}} \tag{3.27}$$

The above equation can be rearranged so that the solvus of the $M_mA_xB_y$ precipitate can be calculated:

$$(c_e^A)^x(c_e^B)^y = \exp(\frac{-\Delta H^0}{\overline{R}T} + \frac{\Delta S^0}{\overline{R}}) \tag{3.28}$$

The expressions are only valid for precipitates of an infinite size. For precipitates of radius R, the influence of the curvature on the solubility has to be considered. The solvus of a precipitate of radius R is then calculated by the Gibbs-Thompsons equation that is generalised to the solubility product:

$$K(r) = K_\infty \exp(\frac{2\gamma V_m}{RT}) \tag{3.29}$$

where K_∞ is the equilibrium value, γ is the interfacial energy and V_m is the molar volume of the precipitate. The solvus temperature of the phase is calculated using the nominal composition C_A and C_B of the alloying elements as [95]:

$$T_{sol} = \frac{\Delta H^0}{\Delta S^0 - \overline{R}ln(C_AC_B)} \tag{3.30}$$

In this thesis, the solubility product has been used to establish a thermodynamic description of GP(I) zones. The solvus boundary of the GP(I) zones was estimated from the change in volume fraction during several dissolution heat treatments. The experimental volume fraction curves where normalized on the intial volume fraction to compare the solvus boundary of the different experiments. Subsequently, the thermodynamic description was obtained by adjusting the parameters ΔH^0 and ΔS^0 so that the normalized volume fraction of the thermodynamic description fits the experimental results. The volume fraction of the thermodynamic description was calculated by using the solute balance.

3.5.3 Precipitation model

The precipitation model used in this thesis was developed by Mickael Serriere in his PhD thesis [88, 178] and extended later by Gandin and Jacot to account for non-stoichiometric precipitates in multi-component alloys [97]. The particle size distribution method of Eulerian type is applied to describe the evolution of the precipitates [84]. The model is capable to treat nucleation, growth and coarsening of more than one phase simultaneously. The model was written such that it can be coupled with thermodynamic calculations (f.e. ThermoCalc and the Al-Data thermodynamic database) in order to compute the driving forces for nucleation and the local equilibrium concentrations.

Model assumptions [178]
The model assumptions can be described as follows:

- At a given temperature, the precipitates form with a uniform composition. The diffusion in the precipitates is considered infinitely high, thus the composition of the precipitates is the equilibrium one in the case of changing temperature.
- All particles are spherical and embedded in the matrix.
- The misfit strain energy ΔG_s is not considered.
- A steady state diffusion field is assumed around the particles by using the Laplace approximation.
- A local equilibrium is assumed at the interface between the matrix and precipitate

Model description [97]
The conservation equation for the density of v-phase precipitates, N^v, in the supersaturated matrix m is defined as:

$$\frac{\partial N^v}{\partial t} = -\nabla \cdot (N^v v^{v+} n^{v+}) + S^v, \qquad v \in [1, q] \tag{3.31}$$

where v^{v+} is the growth rate of the precipitates with radius r^v, n^{v+} is the normal vector to the v/fcc interface pointing towards the matrix, S^v is the source term for nucleation and q is the number of precipitation phases present in the matrix phase. The indexation "'+"' stands for values taken at the v/fcc interface. The growth rate for the v-phase precipitates, v^v of radius R^v, is expressed as:

$$v^v = \frac{D_i^m}{R^v} \frac{x_i^m - x_i^{m+}}{x_i^{v+} - x_i^{m+}}, \qquad v \in [1, q], i \in [1, n] \tag{3.32}$$

where x_i^m is the average composition of element i in the matrix. The diffusion coefficient of solute i in the Al matrix phase, D_i^m is defined using an Arrhenius law. The source term for the v-phase precipitates, S^v, is calculated by a heterogeneous nucleation law given by:

$$S^v = (N_{max}^v - N_{tot}^v) Z \beta \exp\left[\frac{\Delta G_{hom}^{v*} f(\theta)^v}{k_B T}\right], \qquad v \in [1, q] \tag{3.33}$$

where N_{max}^v is the nucleation sites density of the v-phase precipitates and N_{tot}^v is the total density of v precipitates already present in the matrix phase. The term β accounts for the attachment rate of solute atoms from the matrix to the nucleus. For binary alloy, it can be calculated by:

$$\beta = 4\pi (R^{v*})^2 \frac{D_i^m x_i^m}{(\lambda^m)^4} \tag{3.34}$$

where λ^m is the diffusion distance in the matrix phase. In multi-component alloys the element with a slow diffusion rate in the matrix and a low composition is the limiting factor for the growth of the nucleus. The energy barrier to form new v-phase precipitates of critical radius $R^{v*}$is given by:

$$\Delta G_{hom}^{v*} = 4/3\pi \gamma^{v/m} (R^{v*})^2 \tag{3.35}$$

where $\gamma^{v/m}$ is the interfacial energy of the v/m interface. The critical radius of a new v-phase nucleus is calculated as:

$$R^{v*} = \frac{\gamma^{v/m} V^v}{\Delta G_n^v} \tag{3.36}$$

where V^v is the molar volume of the v-phase precipitate and ΔG_n^v is the driving force for nucleation of the v-phase precipitate in the matrix. Z denotes the Zeldovitch's factor, which accounts for nucleus size fluctuations due to solute emission from the nucleus back into the matrix. It is estimated from the following relationship:

$$Z = \frac{\Delta (G_n^v)^2}{8\pi V^v (\gamma^{v/m})^{3/2} N_{Av} \sqrt{k_B T f(\theta_v)}} \tag{3.37}$$

where k_B is the Boltzmann's constant and N_{Av} Avogadro's number. The conservation equation of solute element i is expressed as:

$$\sum_v \sum_r \frac{4}{3}\pi (R^v)^3 N^v (x_i^v - x_i^m) = x_i - x_i^m, \qquad v \in [1,q], i \in [1,n] \tag{3.38}$$

where x_i is the average composition of element i in the matrix and x_i^v the precipitate composition. It is given by the interface composition x_i^{v+} and can vary with temperature since the precipitates are not stoichiometric. An ideal solution approximation is used to calculate the driving force for nucleation of the v-phase precipitates:

$$\Delta G_n^v = \overline{R}T \sum_{i=1}^{n} x_i^{v\infty} ln \frac{x_i^m}{x_i^{m\infty}}, \qquad v \in [1,q] \tag{3.39}$$

The equilibrium compositions of element i at the (v/m) interface in the Al matrix ($x_i^{m\infty}$) and in the v-precipitate ($x_i^{v\infty}$) are given by equilibrium calculations at temperature, T, and average composition of elements i, x_i.

The Gibbs-Thompson effect is accounted for based on a modification of the solubility product, K^v, with respect to its equilibrium value, $K^{v\infty}$, which is computed from the equilibrium compositions:

$$K^v = K^{v\infty} \exp(\frac{2}{R^v} \frac{\gamma^{v/m} V^v}{\overline{R}T}) \tag{3.40}$$

with

$$K^v = \prod_{i=1}^{n} [x_i^{m+}]^{x_i^{v+}} \qquad \text{and} \qquad K^{v\infty} = \prod_{i=1}^{n} [x_i^{m\infty}]^{x_i^{v\infty}}, \qquad v \in [1, q]$$

where x_i^{m+} and x_i^{v+} are the compositions of elements i at the (v/m)-interface in the Al matrix and in the v-precipitate, respectively.

In this thesis, a thermodynamic description was derived for the GP(I) zones using the solubility product. The description was used to the calculate the equilibrium compositions $x_i^{m\infty}$ and $x_i^{v\infty}$.

3.5.4 The influence of excess vacancies on diffusion

Equilibrium vacancy concentration

The site fraction of vacancies increases as a function of temperature. The equilibrium site fraction of vacancies $y_{0,eq}$ depends on the temperature T and can be calculated as [65]:

$$y_{0,eg} = \exp(-\frac{H_0}{\overline{R}T}) \tag{3.41}$$

where H_0 is the vacancy formation energy. If one considers the equilibrium vacancy concentration in a solid solution, the interactions between solute element and vacancies have also to be taken into account. The solute element can stabilise vacancy concentration and therefore increase the equilibrium concentration [7]. Fabian and Wolter [179] applied the Lomer equation to account for the interactions between solute elements and vacancies in the Al-Zn-Mg system:

$$y_{0,eg} = A\exp(-\frac{H_0}{\overline{R}T})(1-13(c_{Zn}+c_{Mg})+12\cdot c_{Zn}\exp(\frac{E_{Zn-vac}}{\overline{R}T})+12\cdot c_{Mg}\exp(\frac{E_{Mg-vac}}{\overline{R}T})) \tag{3.42}$$

where E_{Zn-vac} and E_{Mg-vac} are the bindings energies between Zn and Mg with the vacancies, respectively. A simplified equation was proposed by Godard [7] by using a unified interaction energy $E_{Sol-vac}$ between all solute elements and the vacancies:

$$y_{0,eg} = A\exp(-\frac{H_0}{\overline{R}T})(1+0,1\exp(\frac{E_{Sol-vac}}{\overline{R}T})) \tag{3.43}$$

Annihilation of excess vacancies

Rapid temperature changes, e.g. quenching, annealing but also plastic deformation can lead to states that are far from equilibrium with a marked supersaturation of vacancies y_{vac} [98, 62, 63, 65]. In order to lower the free energy of the system, the excess vacancies will annihilate on sinks, such as grain boundaries, incoherent interfaces (e.g. dispersoids) and jogs at dislocations [49]. Additionally, vacancies may lead to the nucleation and growth of Frank loops, which can also act as sinks. The condensation of the excess vacancies is controlled by the vacancy diffusion D_{vac}, which is expressed for mono vacancies as:

$$D_{vac} = C_{Ei} a^2 \exp(-\frac{H_m}{RT}) \tag{3.44}$$

where C_{Ei} is the Einstein constant, a is the lattice parameter and H_m the migration energy of the vacancies. The annihilation rate $\dot{y}$ depends on the vacancy supersaturation, but also on the density of sinks. A simplified equation based on Fick's law was proposed by Godard [7], which only takes into account grain boundaries as sinks for vacancies:

$$\frac{\partial y_{vac}}{\partial t} = -\frac{y_{vac} - y_{0,eq}}{\tau} \tag{3.45}$$

where τ is the characteristic time ($\tau = (l/2\pi)^2/D_{vac}$) and l is the distance between the vacancy sinks.

Influence of vacancies on the diffusion of solute elements

It is well known that vacancies are responsible for the transport of solute elements in the bulk material. Therefore, a supersaturation of vacancies elevates the solute diffusion compared to the case of an equilibrium vacancy concentration. A phenomenological approach was proposed by Godard [7] to take into account the effect of excess vacancies on the diffusion of solute. The supersaturation S of vacancies for a specific temperature is given by:

$$S = \frac{y_{vac}}{y_{0,eq}} \tag{3.46}$$

The supersaturation of vacancies increases the diffusion so that the effective diffusion D^i_{eff} of an element i is calculated as:

$$D^i_{eff} = S\, D^i_0 \exp(-\frac{Q^i}{RT}) \tag{3.47}$$

where D_0^i is the diffusion constant and Q^i the activation energy of the element i in the matrix.

A Matlab routine was written to compute an input file for the precipitation model, which contains the tabulation of the thermodynamic equilibrium description of the GP(I) zones and the solubility of the solute element in the Al matrix for a specific thermal path. In addition, the effective diffusion of Mg (slowest diffusion element present in GP(I) zones) was calculated and the effective diffusion parameter Q_{eff} and $D_{0,eff}$ were fitted in the lower temperature regime (40-220°C) and used as input for the precipitation modelling. The equilibrium vacancy concentration was calculated using equation 3.42 with H_0, E_{Zn-vac} and E_{Mg-vac} being 68000, 12520 and 24080 J/mol, respectively [98]. The condensation rate of the excess vacancies was calculated using $H_m = 68700$ J/mol and $l = 0.25e^{-6}$m.

3.6 Yield strength model

The changes of the yield strength due to solute depletion in the matrix and the presence of shearable precipitates was estimated by using the additive yield strength model as proposed by Fribourg [18]:

$$\sigma_{YS} = 10\,MPa + \sigma_{ss} + \sigma_{prec} = 10\,MPa + K_{ss}\,C^{\frac{2}{3}} + p\,M\,\mu\sqrt{f_v R/b} \qquad (3.48)$$

The strengthening contribution originating from the lattice friction, the dislocations and the grain boundaries are considered to be a constant value of 10 MPa. The parameters K_{ss} of the solid solution contribution and p of the precipitate shearing contribution were calibrated against results obtained by Gleeble measurements performed by Nicolas Chobaut [119, 121]. He performed one test for each cooling condition and reported an uncertainty of ± 5 MPa.

The global parameter K_{ss} [101, 18] was calibrated from the as-quenched yield strength of the AA7449 and AA7040 alloy (Figure 3.9). Tensile tests were performed directly after rapid cooling ($\sim$ 50-80 K/s) from the solutionizing temperature to room temperature in a Gleeble machine [119]. The global solid solution strengthening coefficient was found to be 800 MPa per atomic fraction of solute.

The parameter p of the precipitate shearing law was calibrated by performing the same cooling conditions with the Gleeble as done for the in situ SAXS experiments (cooling's Q1 and Q3 for the AA7449 and cooling Q16 for the AA7040). The cooling was interrupted at different temperatures (e.g. 200, 150, 100 and 50°C) and the yield strength was measured as shown in Figure 3.9. The microstructural information, such as precipitate size and volume fraction, estimated from SAXS measurements were linked with the mechanical properties obtained by the Gleeble tests. The parameter p for the shearing of the cluster was found to give the best agreement as a function of temperature. For the three experimental findings, p calculated as $p = 0.00665 +$ (-0.82e^{-5} • T [°C]) gives the best compromise for all three datasets.

This equation does not account for visco-plastic deformation behaviour and is therefore only valid at temperatures that are smaller than 200°C.

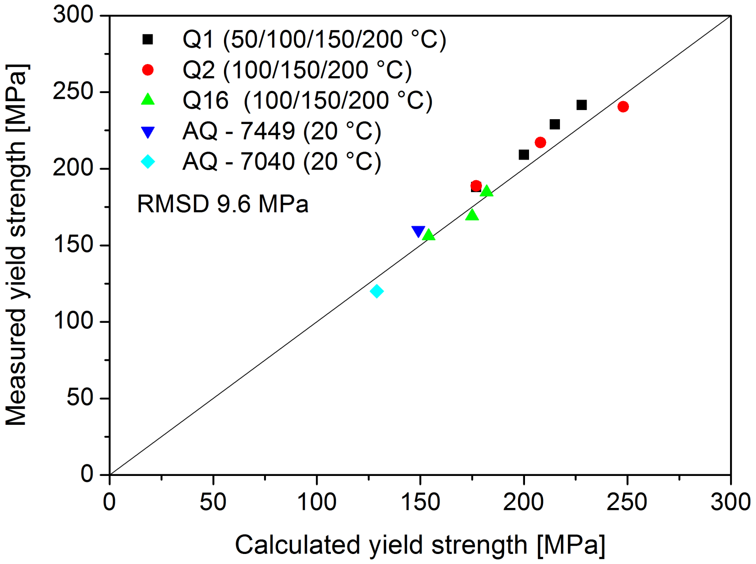

Figure 3.9: Calculated yield strength for the AA7449 and AA7040 is compared to the measured yield strength in the Gleeble machine [121] for different cooling conditions. The root mean square deviation (RMSD) is 9.6 MPa.

3.7 In-situ mechanical testing using diffraction

3.7.1 Diffraction

Neutrons and X-rays may be used for elastic lattice strain determination. X-rays interact primarily with the “electron cloud” surrounding each atom. Neutrons, on the other hand, interact primarily with the nucleus. Both, neutrons and X-rays penetrate deep into the material and provide information about the bulk structure since their wavelength is comparable to the size of atoms. This is achieved by constructive interference of the incoming wave, usually in the form of a monochromatic X-ray beam or thermal neutrons, with a set of planes of same Miller indices hkl (Figure 3.10). The diffraction of an incident beam of wavelength λ only occurs from a particular set of planes (hkl) at a particular diffraction angle θ. This relation is known as Bragg’s law, which is expressed as: [180].

$$n\lambda = 2d_{hkl}\,sin\,(\theta) \tag{3.49}$$

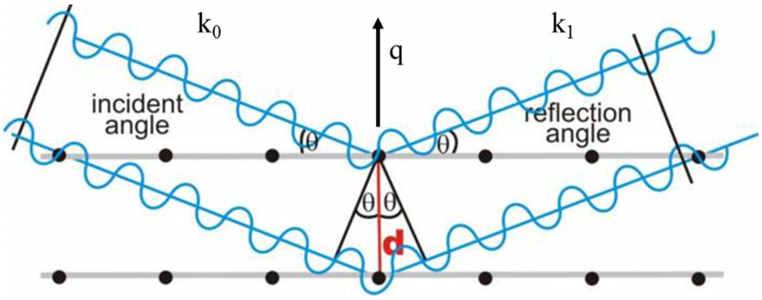

Figure 3.10: Schematic illustration of Bragg's law: constructive interference of incoming waves k_0 after diffraction at a particular set of lattice planes (hkl) under a diffraction angle θ fulfilling Bragg's law. The scattering vector q is defined as k_0-k_1. (Image adapted from [181])

Here, n is the reflection order, λ the X-ray wavelength, d_{hkl} the lattice spacing and θ the diffraction angle. The wavelength of X-ray beam is calculated as:

$$\lambda = \frac{c\,h}{E_{beam}} \tag{3.50}$$

where c is the velocity of light, h is Planck's constant and E_{beam} is the energy of the X-ray beam. The distance between two parallel planes of atoms can be calculated from the lattice cell constant a and the Miller indices (hkl) of the diffracting planes as illustrated for cubic structures.

$$d_{hkl} = \frac{a}{\sqrt{h^2+k^2+l^2}} \tag{3.51}$$

When a load is applied to a material the interplanar spacing d_{hkl} changes, which will lead to a shift of the diffraction peak. The change of the interplanar spacing between particular planes of atoms with respect to the initial state $d_{0,hkl}$ (stress free reference) allows calculating the lattice strain generated in a family of planes (hkl) during the deformation in the elastic and plastic regime:

$$\epsilon_{hkl} = \frac{d_{hkl} - d_{0,hkl}}{d_{0,hkl}} \tag{3.52}$$

From the measured lattice strain ϵ_{hkl} the stress tensor σ_{ij} can then be calculated by using Hooke's law as:

$$\sigma_{ij} = \frac{E_{hkl}}{1+\nu^{hkl}}\left[\epsilon_{ij}^{hkl} + \frac{\nu^{hkl}}{1-2\nu^{hkl}}\left(\epsilon_{11}^{hkl}+\epsilon_{22}^{hkl}+\epsilon_{33}^{hkl}\right)\right] \tag{3.53}$$

In situ mechanical testing allows measuring only two strain components, the axial and one transverse component, of the stress tensor σ_{ij}. To calculate correctly the type-II stresses a third strain components should be measured. Yet, in order to estimate the type-II stresses, the transverse strain component (ϵ_{22} and ϵ_{33}) is considered to be isotropic and equal for all direction perpendicular to the principle tensile axis (ϵ_{11}).

3.7.2 Diffraction experiments

In situ mechanical test were performed using neutrons and also synchrotron X-ray diffraction in order to investigate the lattice strain evolution in the AA7449 alloy exhibiting different precipitation microstrutures. The experimental details are given in the following.

Neutron diffraction

In situ neutron diffraction experiments were performed at the pulsed overlap time-of-flight (ToF) strain scanner (POLDI) at the Swiss Spallation Neutron Source (SINQ) at PSI. More details of the strain scanner and the concept are presented in the References [182, 183]. The wavelength of the incident neutron beam was 1.1-5 Å. The strain scanner is equipped with one detector bank, which is positioned horizontally at a 90° scattering angle. Therefore, the loading rig (25kN) had to be mounted either horizontally or vertically to investigate the materials response in the axial (grain families with diffraction planes perpendicular to the tensile axis) and transverse (grain families with diffraction planes parallel to the tensile axis) direction. Figure 3.11a shows the round tensile samples with a M12 thread and a diameter of 6 mm that were used. The samples were taken out from the quarter thickness of a 75 mm AA7449 plate so that the tensile axis is aligned with the rolling direction. The sample elongation was measured with a clip-on axial extensometer. The illuminated gauge volume was 3.8 x 3.8 x 3.8 mm and 3.8 x 3.8 x 10 for the axial and transverse direction, respectively. The measurement time for one diffraction pattern was 120 min for the axial direction and 60 min for the transverse direction.

Synchrotron X-ray diffraction

The in situ synchrotron X-ray diffraction experiments were performed at the ID15B beamline at the European Synchrotron Radiation Facility (ESRF) in Grenoble, France. The beam energy was 89.4 keV. The beamline is equipped with a Pixium area detector, which features a pixel array of 1910 × 2480 pixels and a pixel size of 154 μm × 154 μm. The loading rig (an Instron electro-thermo mechanical testing (ETMT)) was limited to a maximum force of 3 kN. Therefore, small flat tensile samples were used as illustrated in Figure 3.11b. The samples were also taken out from the quarter thickness of a 75 mm plate AA7449 so that the tensile axis is aligned with the rolling direction. The illuminated gauge volume was 0.3 x 0.3 (beam size) x 2 (samples thickness) mm. An extensometer could not be used for this sample geometry. Therefore, the motor encoder position of the loading rig was used as displacement to calculate the strain. Diffraction patterns were taken every 1.6 seconds during continuous loading. In the unloaded state, the diffraction pattern was acquired for 16 seconds.

3.7.3 Data treatment and analysis

Neutron diffraction

The tensile test was performed stepwise with a long holding period for the neutron diffraction measurement after each step in order to have adequate counting statistics. The stress-strain curve for a T4 sample is shown exemplarily in Figure 3.12. Typically, the sample was deformed up to a specific load (elastic regime) or displacement (plastic regime) and held constant during the measurement. The diffraction measurement points are visible in the stress-strain curve due to the stress relaxation during the long holding time. The inset of Figure 3.12 illustrates the stress relaxation during the holding time. Within the first 5-10 minutes the stress drops quickly, but stays relatively constant for the remaining holding time (120 min). Therefore, the neutron diffraction pattern was acquired after a 10 min

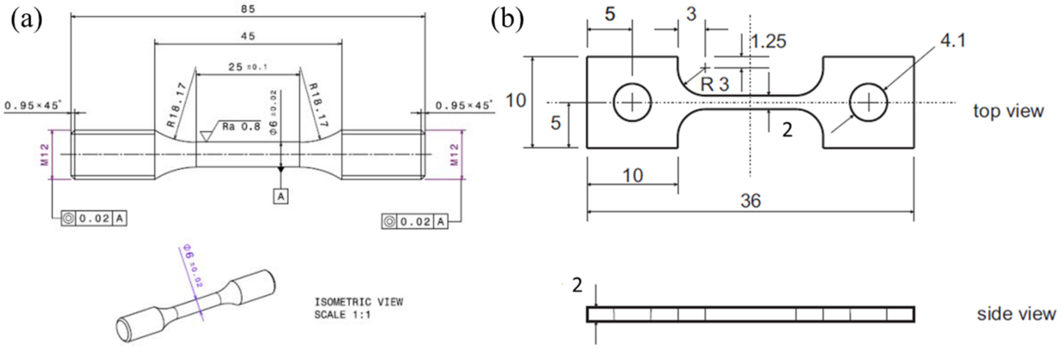

Figure 3.11: Illustration of the tensile samples used for the (a) neutron diffraction and (b) X-ray diffraction experiments.

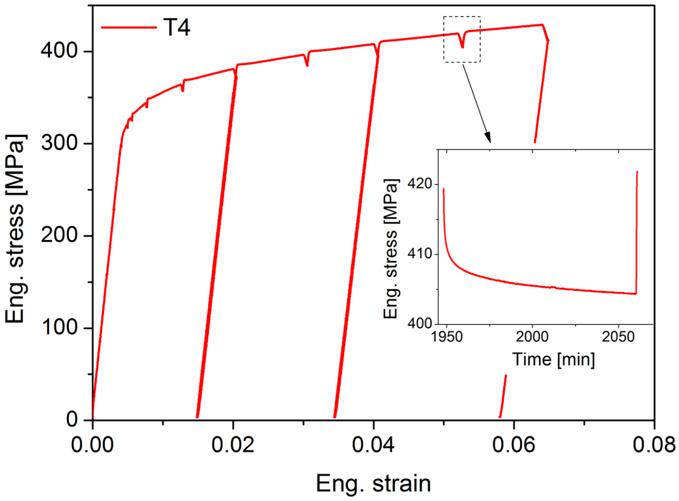

Figure 3.12: (a) Stress-strain curve of a T4 sample investigated at the POLDI beamline. The inset shows the stress relaxation during holding time for the diffraction measurement.

waiting period.

The diffraction data obtained from the experiments performed at POLDI were processed by using the software programs available at the beamline. Single peak fitting was performed using the Gaussian function, which allowed to determine the peak position, the full width half maximum (FWHM) and the peak intensity of the (111), (200), (220) and (311) diffraction peaks of Aluminium.

Synchrotron X-ray diffraction

In contrast to the neutron diffraction experiment, the tensile test and the X-ray diffraction was performed continuously. Before the in situ experiment, the beam center and the wavelength of the beam were determined using a standard CeO_2 sample since its lattice constant is precisely known. The beam center was estimated from the CeO_2 diffraction rings by using the Fit2D software program [184]. Further, the wavelength of the X-ray beam was estimated by taking diffraction pattern of CeO_2 at two different sample-to-detector distances. The beam energy was found to be 89.4 keV, which corresponds to a wavelength of 0.1389 Å.

The Fit2D program was used to integrate the 2D-diffraction over an azimuthal range of ±15° for the axial and also for the transverse direction. This was done by using a python script for batch processing that was provided by M. Weisser [185]. The azimuthal range was chosen so that the results can be compared to the findings of the neutron experiments at POLDI, which features also an azimuthal range of 30°.

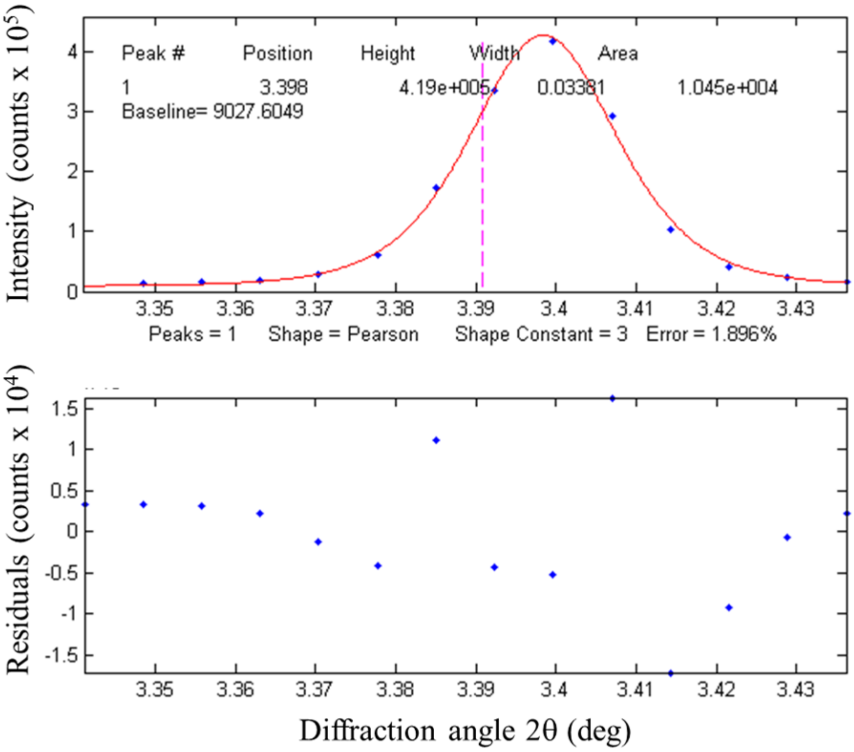

Figure 3.13: The (111) diffraction peak (blue points) measured at the ID15B beamline is shown together with the peak fit (red line) and the fitted results in the upper part. The lower part shows the residuals of the fit.

Single peak fitting was performed on the 1D-data. The peakfit.m function [186] was implemented in a Matlab routine. This allowed fitting the peak using the Pearson VII function as shown in Figure 3.13. The fit error was typically in the range of 0.5 to 2 %. The error can be associated to the low number of points (7 to 9 points per peak) that define a peak. Subsequently the lattice strain was calculated for each specific orientation. In addition, the diffraction elastic constants were fitted in the elastic regime in order to obtain the deviation from linearity. Single peak fitting was performed for the (111), (200), (220) and (311) diffraction peak of the Aluminium matrix and also (100), (002) and (101) diffraction peaks of the η precipitates.

4 As-quenched microstructure and precipitation during quench

This Chapter focusses on the characterization of the quench-induced precipitation in industrial thick plates. The precipitation microstructure in the industrial plates was investigated after the quench (Section 4.1) and in situ during rapid coolings (Sections 4.2 and 4.3). The precipitation during rapid coolings and the quench sensitivity of the AA7449 is compared to the AA7040 alloy in Section 4.4 and a CCP diagram is proposed for the AA7449 alloy in Section 4.5. Section 4.6 highligths the influence of the quench-induced precipitation on the macroscopic residual stresses.

4.1 Characterisation of the plate microstructure after quench

The as-quenched microstructure of the 75 mm AA7449 plate was investigated at the surface, quarter and center region. Figure 4.1a shows a SEM-EBSD image, which illustrates exemplarily the inhomogeneous grain structure present in the material. Large elongated grains are aligned in the rolling direction L and feature a length up to 1000 μm and a thickness in the range of 100-200 μm. The grains comprise subgrains with a diameter in the range of 1-10 μm and an average size of 2 μm as estimated from EBSD analysis. This is similar to the 1.5 μm found in literature [57]. The subgrain size is an important quantity to estimate the diffusion path length for vacancies to annihilate on the subgrain boundaries. Further, it also gives an idea about the nucleation site density for heterogeneous nucleation on grain boundaries [187]. In addition, some recrystallized grains with a grain size of 150-200 μm and without subgrain structure can be observed.

The SEM image in Figure 4.1b shows the elongated grains and further evidences the presence of two coarse intermetallic phases, which give white and black phase contrasts. The two phases were characterised as Al_7Cu_2Fe and Mg_2Si by EDX measurements. The Al_7Cu_2Fe (white) phase is elongated and oriented along the

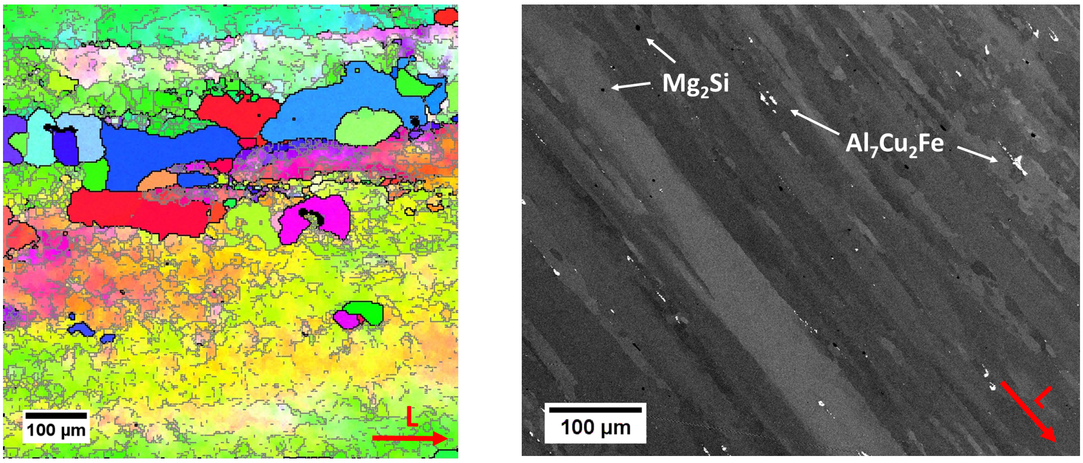

(a) (b)

Figure 4.1: (a) EBSD image showing the heterogeneous grain microstructure with unrecrystallized and recrystallized grains (black lines = large angle boundaries), which show no subgrains (grey lines= low angle boundaries) structure. (b) HR-SEM image in EsB mode illustrating the presence of intermetallic Al_7Cu_2Fe, (white) and Mg_2Si (black) phases in the AA7449 alloy. Both samples were taken from the quarter thickness of the plate and L defines the rolling direction.

rolling direction in contrast to Mg_2Si, which is rather spherical. The two phases are found throughout the plate thickness in rather low quantities. Image analysis showed surface area fractions of $0.4\,\%$ and $\leq 0.1\,\%$ for the Al_7Cu_2Fe and Mg_2Si phase, respectively. This is in a similar range compared to the results reported in [25]. Overall, the amount of solute depletion due to the intermetallic phases is rather small. Therefore, the solute depletion will not be taken into account for the modelling of precipitation presented in Chapter .

In addition to the two intermetallic phases, a third phase is observed on the SEM image taken from the center of the 75 mm thick plate (Figure 4.2). This phase is much smaller in size and is situated mainly on the grain boundaries, but also inside the grains. The phase is inhomogeneously distributed, regions with a high density were observed as well as regions with no presence. These characteristics indicate the presence of the quench-induced η phase. Image analysis revealed an area fraction of $\sim 0.15\,\%$ but the error associated with the binarisation of the image is very high because of the small size of the precipitates compared to the scale of the image and the large interaction volume of the beam with the sample. TEM and SAS techniques were applied to overcome these limitations and study the material on the nanoscale. The results are presented in the following.

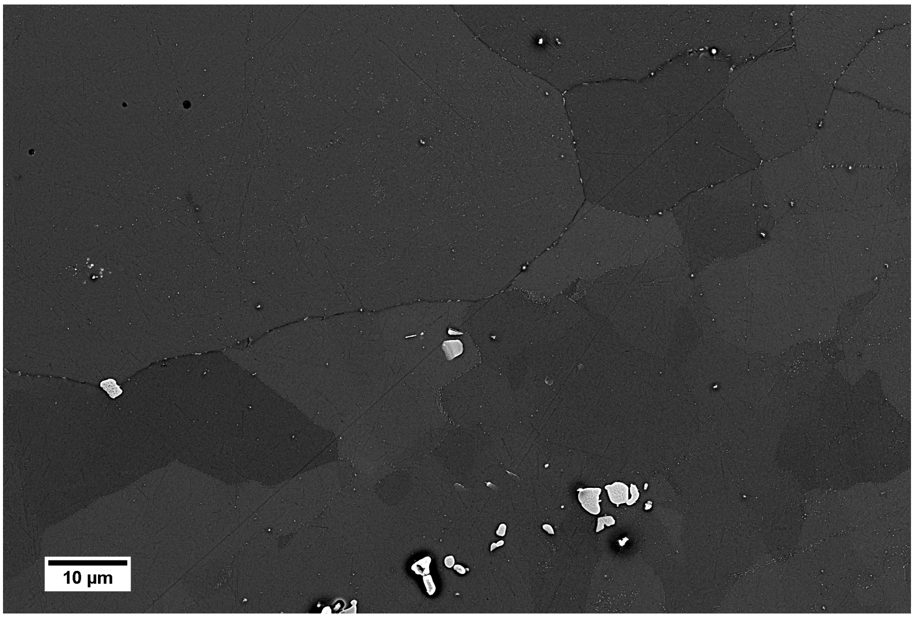

Figure 4.2: High resolution SEM image of the AA7449 material taken from the center of the 75mm plate evidences phase contrast at grain boundaries and inside the grains. The size of that phase is much smaller in comparison with the intermetallic phases.

4.1.1 Characterisation of the homogeneous precipitates after quench

Transmission electron microscopy

The as-quenched microstructure of the 75 mm thick plate was investigated by TEM in the surface, quarter and center region. Figure 4.3a shows a high angle annular dark field (HAADF) TEM image of a sample taken from the quarter thickness of the 75 mm plate, which was in the as-quenched and natural aged T4 state. It evidences the presence of homogeneously distributed precipitates (white contrast) with a radius in the range of 0.5 to 1 nm. The selected area diffraction pattern (SADP) reported in Figure 4.3b shows the $\langle 100\rangle$ projection with the main diffraction peaks coming from the Al matrix. Weak and diffuse diffraction spots can be seen at $\{1,(2n+1)/4,0\}$ positions that are characteristic for GP(I) zones [42]. GP(I) zones form in the AA7xxx alloys even at room temperature due to natural aging. Therefore, it cannot be clarified if these GP(I) zones are quench induced. In addition, diffraction spots, which are characteristic for the η' phase (at 1/3 and 2/3 of $\{220\}_{Al}$) and Al_3Zr dispersoids (at $\{100\}$ and $\{110\}$ positions) can be seen. The η' precipitates usually do not form at room temperature, which implies that they are quench induced. Objects with a size of 3-4 nm, which is a typical size of η' precipitates [18], are seen on dislocations. The TEM images that were taken on samples at the surface and center position of the plate showed qualitatively the same features as observed in the quarter position.

Small angle X-ray scattering

In order to characterise quantitatively the fine homogeneous precipitates in the T4 state, SAXS spectra were taken every 1 mm through the half thickness of the 75 mm plate. The measurements were performed at two different sample-to-detector distances. Shorter sample-to-detector distances allowed measuring reasonably well the scattering contribution of the GP(I) zones and it was used to estimate the size and volume fraction. The measurements at longer distance were performed to measure the contribution of larger objects such as quench-induced heterogeneous η precipitates, which scatter at smaller scattering vectors. Two representative Kratky plots for the two distances are shown in Figure 4.4a. The scattering contribution at large q with the peak at 0.2 Å^{-1} originates from the GP(I) zones. At small q values (below 0.05 Å^{-1}) one can observe a scattering contribution that is attributed to larger objects. The analysis of the large scatterers will be presented in the next Section 4.1.2.

The Guinier radius and volume fraction of the GP(I) zones are presented as function

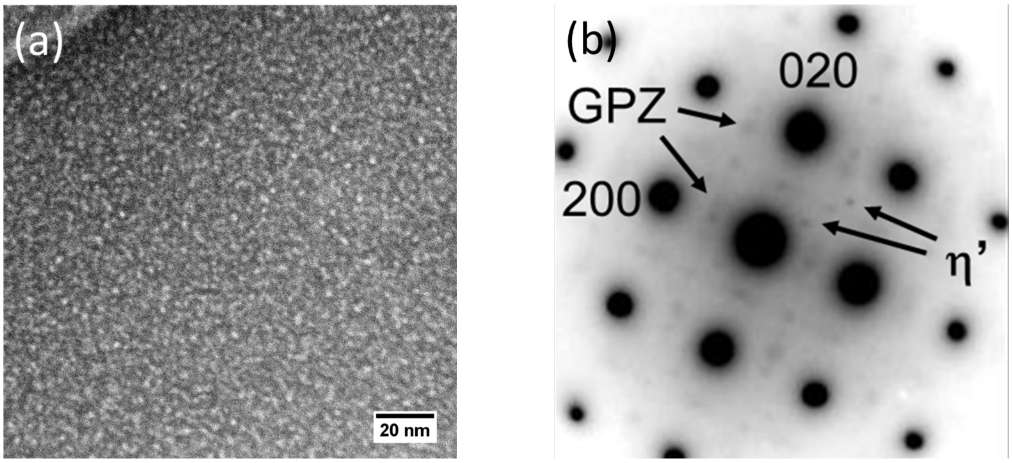

Figure 4.3: (a) HAADF-TEM image showing GP(I) zones (white contrast) and their characteristic diffuse spots in the (b) selected area diffraction pattern in Al ⟨100⟩ projection.

of the position in the plate in Figure 4.4b. The radius of the GP(I) zones is in the order of 0.94 nm, which confirms the first qualitative results from the TEM. Very small variations of the size can be seen through the plate thickness. The largest GP(I) zones (0.95 nm) are found in the quarter thickness of the plate. In the surface and center region, the GP(I) zone radii are slightly smaller (0.925 nm). The size of the GP(I) zones is in the range of what has been reported in literature after long natural aging at room temperature [18, 54].
The volume fraction oscillates between 10 and 10.5 % between the surface and the quarter thickness of the plate. From the quarter thickness to the plate center the volume fraction decreases down to 9 %. The dip observed for the size and volume fraction seems to be symmetrical around the plate center.

In the case of a homogeneous solute content throughout the plate one would expect hardly any variations of the volume fraction and precipitate size. Yet, the volume fraction variations indicate that the solute content changes through plate thickness due to macrosegregation and/or quench-induced heterogeneous precipitation. Further, the existence of quench induced homogeneous precipitates cannot be clarified due to the large amount of GP(I) zones that formed during the long natural aging time, which would overlap with the scattering of the quench-induced homogeneous precipitates.

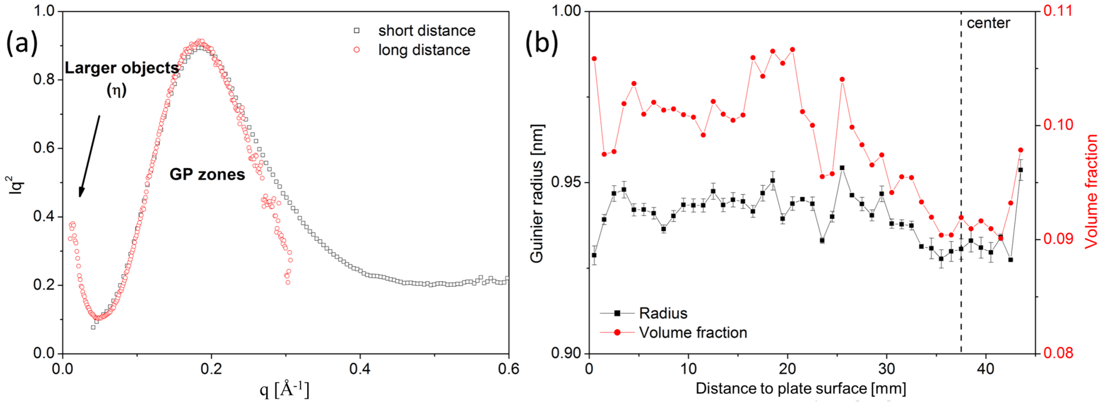

Figure 4.4: (a) Kratky plots of the T4 state for two sample-to-detector distances and (b) the Guinier radius and volume fraction measured in 1 mm steps through the half plate thickness of the 75 mm AA7449 plate.

4.1.2 Characterisation of the heterogeneous precipitates after quench

Transmission electron microscopy

In addition to the fine homogeneous precipitates, TEM revealed also the presence of larger precipitates, which showed the characteristic diffraction spots of the η phase in the SADP pattern. The η phase was observed on grain and subgrain boundaries. Their thickness is in the range of 2-8 nm and the radius ranges from 4-35 nm as it can be seen in Figure 4.5a.

The η phase is also observed inside the grains (Figure 4.5b) located on Al_3Zr or $Al_3(Cr,Ti)$ dispersoids. The radius is between 20-40 nm and the length in the range of 60-120 nm. The EDX map in Figure 4.5b indicates that the Cu-containing η precipitates (light blue) are more likely to nucleate on $Al_3(Cr,Ti)$ (red) than on Al_3Zr (dark blue) dispersoids. This might be due to a different coherency of the two dispersoids with the matrix.

Comparing TEM images from the surface, quarter and center position qualitatively, one can conclude that the surface region features the smallest amount and the smallest size of η precipitates whereas the quarter and center region showed similar precipitate distributions in size and overall appearance.

The influence of the heterogeneous η precipitation on the solute content in the Al matrix is illustrated qualitatively in Figure 4.6. A TEM-EDX map was recorded across a η precipitate, using a 40 nm x 400 nm area as shown in Figure 4.6a. The measurement was averaged in width in order to improve the signal-to-noise ratio. Figure 4.6b shows the averaged EDX linescans of the Zn, Mg and Cu solute contents, as well as the Al content. The concentrations were normalised by the compositions found in the matrix far away from the precipitates. Figure 4.6b shows that the solute content around the η precipitate is reduced locally in the matrix. The diffusion zone around the 70 nm thick precipitate extends to about 120 nm. This shows that the solute depletion is localised suggesting that the thermodynamic driving force for nucleation of hardening precipitates far away from the large precipitates is unaffected. The concentration profiles exhibit the typical shape, which corresponds to Zener's approximation (Section 2.5). In the η precipitate the amount of Zn, Mg and Cu is, as expected, much higher compared to the matrix and in return the Al content is much lower.

Small angle X-ray scattering

In addition to the SAXS map through the thickness of the plate in the T4 state, two more SAXS maps were performed on samples, which were in the T6 (sample as received from T4 thick plate and artificial aged to T6) and perfect T6 state (sample solution treated, quenched as thin sample and artificially aged to T6) as explained in Section 3.4.2. In the case of quench-induced precipitation in the 75 mm plate, differences should be visible between the T6 and perfect T6 sample since residual precipitation will be dissolved in the perfect T6 sample.

The measured volume fraction and Guinier radius are shown in Figure 4.7a for the T6 and perfect T6 sample. The volume fraction of η'/η precipitates is rather constant from the surface to 30 mm below the surface with values between 8 and

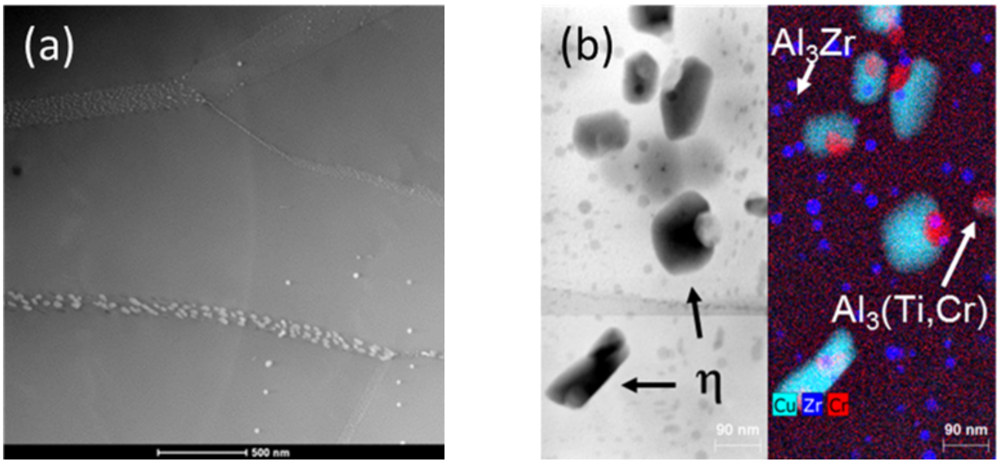

Figure 4.5: TEM images revealing η precipitation on (a) grain and subgrain boundaries and on (b) Al_3Zr or Al_3(Cr,Ti) dispersoids. The TEM-EDX reveals that the Al_3(Cr,Ti) dispersoids are more effective nucleation sites inside the grain.

8.5 % in both samples. Also, the strange oscillation at about 25 mm is found in both samples. Therefore, it seems to be related to local variations of composition rather than to a measurement artefact. Besides, there are also large variations between the measurement lines as it can be seen from the error bars. Overall, the volume fractions of the two samples are remarkably similar. This indicates that the heterogeneous η precipitates give a very small contribution to the total volume fraction. Furthermore, similarly to the measurement in the T4 state (Figure 4.4b) a symmetrical dip is also observed in the center region of the plate in both samples. This can be associated with macrosegregation, which is known to occur in thick plates [7].

The precipitate size is around 4 nm in both samples, which is similar to the findings of Fribourg [18] and to typical sizes for homogeneous η' and η hardening precipitates. The size of the hardening precipitates is larger in the T6 sample compared to the perfect T6 sample, although the difference is only in the range of 0.1 to 0.2 nm. Since the T6 treatment of both samples was performed together, the major difference is the natural aging time. The size of the GP(I) zones in the T6 sample was about 0.95 nm after more than 1 year of natural aging. The perfect T6 sample was only four days at room temperature, which results in GP(I) zones with a radius of 0.7 nm (Section 7.1). In addition, there are quench-induced artefacts such as plastic deformation and variations of vacancy concentrations. Any plastic deformation present in the T6 sample (due to quench induced internal stress

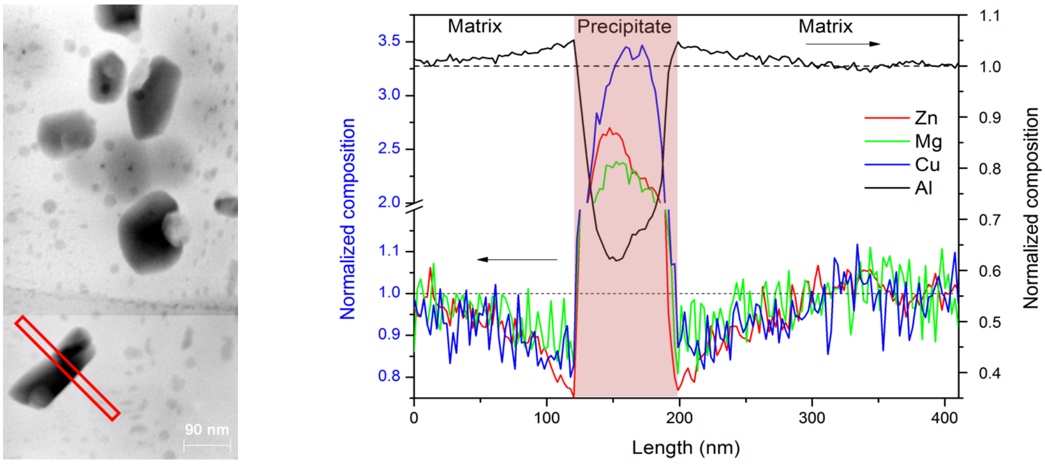

(a) (b)

Figure 4.6: (a) TEM images illustrating the position of the EDX map across a η precipitate. (b) The concentration profiles of Zn, Mg, Cu and Al evidence the different solute content in the matrix and the precipitate and the solute depletion around the precipitate.

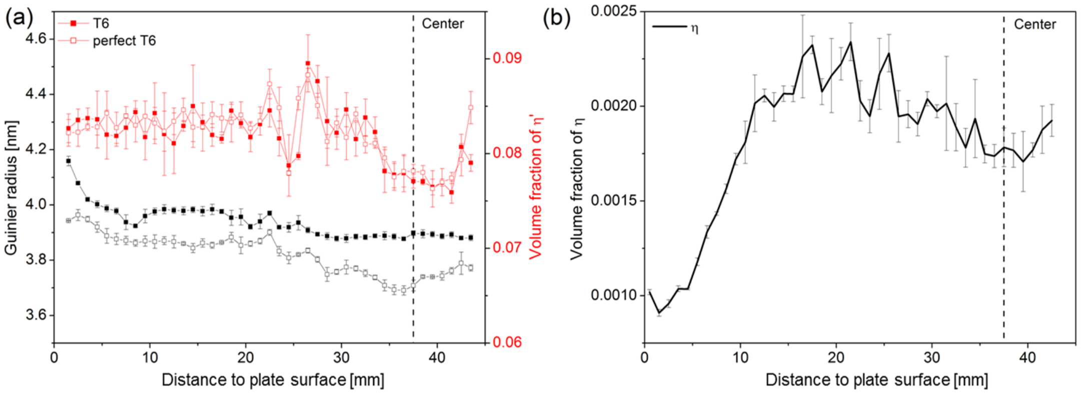

Figure 4.7: (a) Guinier radius and volume fraction of the precipitates in the T6 and perfect T6 state as a function of the distance to plate surface. (b) The volume fraction of heterogenous η precipitates through the plate thickness.

relaxation) will increase the precipitate size after ageing. This can explain the larger size when one gets closer to the plate surface where plastic deformation is largest [6]. The smaller size towards the center can be related to the macrosegregation such as for the volume fraction.

In the previous Section 4.1.1 the scattering due to large objects was visible in the Kratky plot on top of the scattering contribution of GP(I) zones (Figure 4.4a). The scattering contribution was analysed as explained in Section 3.4.4 and the volume fraction is shown as a function of the distance to plate surface in Figure 4.7b.
The volume fraction of the heterogeneous η precipitates increases from about 0.1 % in the surface region to a maximum of 0.25 % in the quarter thickness. Towards the center, the volume fraction decreases to 0.17 %. It appears that the heterogeneous η precipitation is influenced by the cooling conditions that differs through the thickness but also by the macrosegregation that is present in the plate.
This implies that macrosegregation, and therefore changes in the thermodynamic driving force, has to be taken into account when the heterogeneous precipitation of η is to be modelled in thick plates. Yet, one has to keep in mind that the scattering was measured close to the beamstop and that scattering vector was limited to 0.01 Å^{-1} (Sections 3.4.2 and 3.4.4).

Small angle neutron scattering

Figure 4.8a illustrates the low scattering vector part of the measured scattering curves in Kratky representation on samples taken out between the surface (0 mm) and up to 41.7 mm below the surface of the 75 mm plate. The scattered intensity, which is proportional to the volume fraction, increases from the surface to 23.6 mm. By going further to the plate center and beyond, the intensity is found to decrease, except for the position at 30.4 mm. No large variations of the scattering peak maxima are observed, which indicates a similar size of the precipitates. The scattering curves are very broad, which means that the size distribution of the scatterers is large. 2 types of heterogeneous precipitates with different sizes and morphologies form during quenching as shown in Figure 4.5 and reported in reference [10]. Therefore, the broad scattering signal is explained by the superposition of two scattering contributions.

The Guinier radius and volume fraction of η are shown in Figure 4.8b. In a similar way to the scattering signal, the volume fraction of η is increasing up to 23.6 mm below the surface and decreasing towards the plate center, except for 30.4 mm. The same trend is observed in Figure 4.7b. Overall, the volume fraction of the heterogeneous η is very small. The volume fraction of η is smallest in the surface region (0.04 %) and highest at 23.6 mm (0.08 %). The volume fractions obtained by SANS are by a factor of 2.5 smaller compared to the SAXS results shown in Figure 4.7b because the q-range was limited and the SAXS measurement and analysis were very close to the beamstop. The oscillation of the volume fraction around 25 mm seems strange but relates well with the volume fraction variations seen between 25 and 30 mm in Figures 4.4b and 4.7a. This does not seem to be a measurement artefact but rather due to local composition variations.

The Guinier radius of η is about 25 nm in the surface region and increases to roughly 35 nm at 23.6 mm. Towards the center, the Guinier radius decreases to

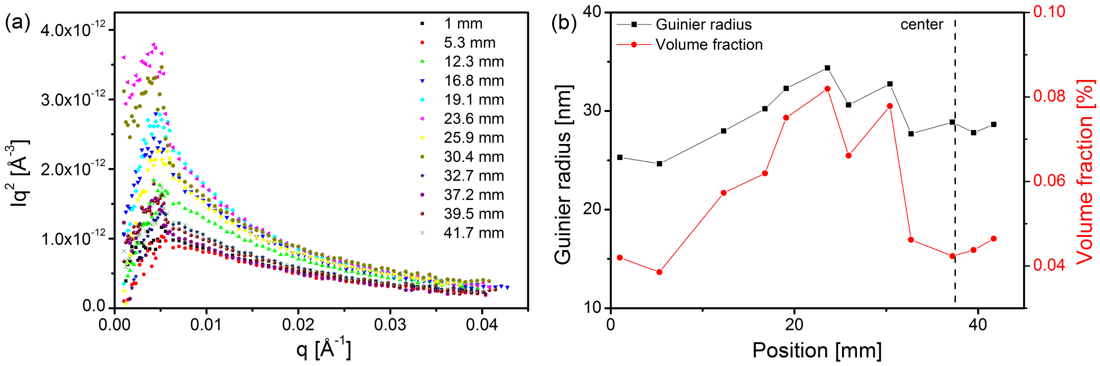

Figure 4.8: (a) SANS curves due to heterogeneous η precipitates is represented by Kratky plots for different positions in the plate, where 0 mm presents the plate surface and 37.5 mm the plate center. (b) Guinier radius and volume fraction of the heterogenous η precipitates as a function of the position in the 75 mm AA7449 plate.

about 30 nm. These sizes coincide with what has been observed in TEM images taken from the surface, quarter and center position.

Heterogeneous precipitation in a 142 mm AA7040 plate

In addition to the AA7449 plate, SANS measurements were also performed at selected positions of a 142 mm AA7040 thick plate in the T4 state. Figure 4.9a shows the measured SANS signals in Kratky representation for the different samples. The scattered intensity increases from the surface up to 47.5 mm and decreases again towards the plate center. The first three samples, which are closest to the surface show a very broad scattering signal with two peak maxima. This indicates the presence of scatterers with two different size distributions. The other samples do not exhibit large variations of the scattering peak maxima, suggesting a similar size of the precipitates.

The estimated Guinier radius and volume fraction of the η are presented in Figure 4.9b. Similarly to the observations obtained from the scattering curves, the η volume fraction is increasing from 0.02 % at 8 mm to 0.06 % at 47.5 mm. Towards the plate center, the volume fraction of η decreases to 0.03 %. Two Guinier radii of η could be estimated for the samples at 8, 12.5 and 17 mm below the surface. The larger precipitates show a constant size of about 22 nm. The smaller precipitates increase from 10 nm to 18 nm from 8 to 17 mm below the surface. The larger precipitates might refer to the η precipitates that nucleate on the dispersoids and the smaller ones the η precipitates on the grain boundaries. Between 20 mm and 56 mm below the surface, η size is roughly 35 nm and decreases slightly towards the plate center.

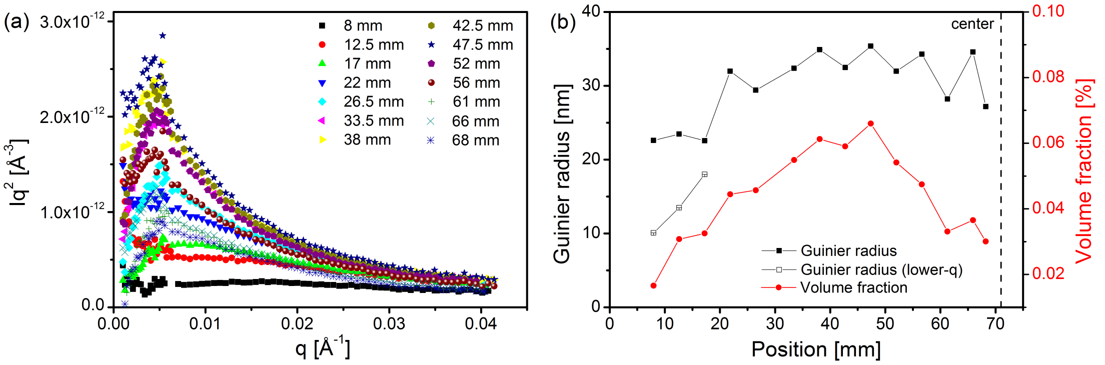

Figure 4.9: (a) The scattering curves are shown as a function of the different positions in the plate, where 71 mm represents the plate center. (b) The Guinier radius and volume fraction of the η precipitates is shown as function of the position in the 142 mm AA7040 plate.

4.2 Characterisation of homogeneous precipitation during rapid cooling

The characterisation of the precipitate microstructure after quench does not allow to estimate the amount of quench-induced homogeneous precipitates. Therefore, dedicated small angle X-ray scattering experiments were performed to investigate in situ the precipitation during rapid coolings as explained in details in Section 3.4.2.

Figure 4.10 presents the scattering during the fastest cooling using the Kratky representation (Iq^2 vs q), where the intensity scales in z-direction. Since the scattering curve at the solutionizing temperature was used for the background subtraction of the data, no scattering effects can be observed at the solutionizing temperature. During cooling, in most cases two scattering phenomena are observed. First, upon cooling, the intensity increases dramatically for small q values, which indicates large-scale scatterers. This phenomena will be discussed in Section 4.3. The second phenomena is observed during further cooling and leads to an increase in the scattering intensity around a q-value of 0.3 $Å^{-1}$. This indicates that the scatter is within a length scale of a nanometre, which corresponds to vacancy-rich or solute-rich clusters and/or GP zones. In the following the small scatterers will be addressed as clusters since the nature of this phase cannot be clarified from the scattering experiment.

AA7449

Figure 4.11a illustrates the five different coolings that were applied to AA7449 (solid lines) and also the cooling conditions found in the surface, quarter and center region (dashed lines) of the 75 mm plate. The cooling conditions found in the plate could be reproduced relatively well below 200°C. At high temperatures, the applied cooling rates are different from the cooling condition in the plate. Also, the high cooling rate at the plate surface could not be reproduced. The 5 coolings are labelled in correspondence to their cooling rate at high temperature where Q1 is the fastest and Q5 the slowest cooling.

The Guinier radius of the small scatterers is illustrated as function of temperature in Figure 4.11b together with the associated error. The Guinier radius decreases from 260°C to 220°C to a minimum value of about 0.4 nm. This size corresponds to about 17 atoms. The decreasing radius can be related to the decrease of the critical radius of nucleation as temperature decreases. Yet, the scattering signal at high-q values in this temperature region is low and the uncertainty of the Guinier radius is high. During further cooling to 120°C the Guinier radius of the clusterss increases for all five cooling conditions. It is evident that the clusters growth depends on the cooling conditions at lower temperature: the radius is largest (~ 0.75 nm) for the slowest quench condition and smallest (~ 0.59 nm) for the fastest quench. These sizes are in the range of those reported by Sha and Cerezo who evidenced GPI zones with 10-30 solute atoms by 3D-APT in as-quenched condition [42]. Further cooling to room temperature shows a decrease in the average radius of the clusterss for all coolings. This indicates that limited mobility inhibits further growth of the existing clusterss but that ongoing nucleation of new clusters with a smaller critical radius than the average size of the clusterss already present in the sample does occur.

Figure 4.11c shows the volume fraction of the small scatterers. For all five coolings the volume fraction starts to increase at around 300°C and increases as temperature decreases to room temperature. Surprisingly, the evolution is very similar for all cases and only small variations can be seen at temperatures lower than 200°C. At the end of cooling, Q4 features the lowest volume fraction of clusterss (4.7 %) compared to the Q2, Q3 and Q5, which exhibit the highest volume fractions of clusterss

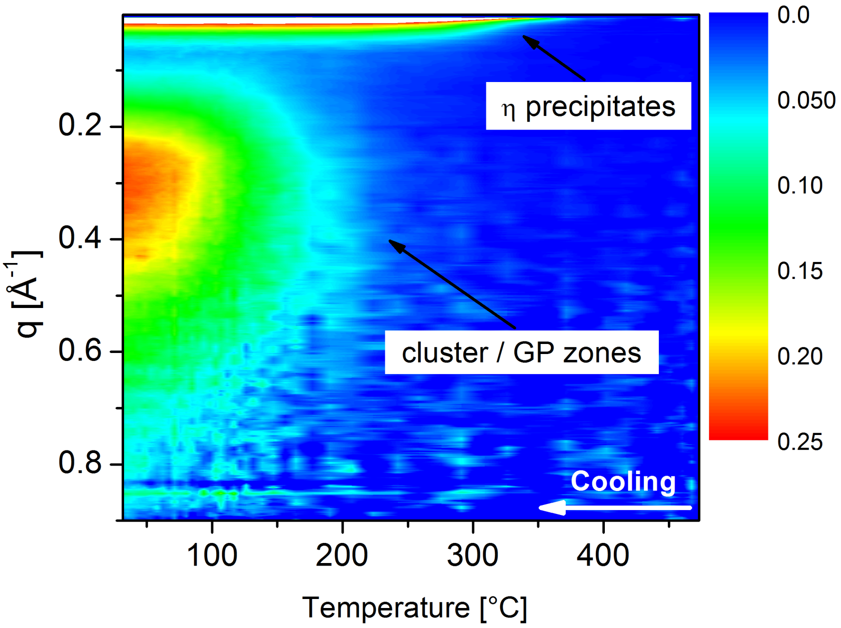

Figure 4.10: Kratky plot (Iq^2 vs. q) as a function of temperature for the fastest quench (FQ). The Iq^2 scale in the Kratky plot was set to a value of 0.25 in order to better observe the evolution at high-q.

around 5.2 %. The formation of clusters does not seem to be dependent on the cooling rate, at least for rates between -25 and -5 K/s at higher temperatures. This is unexpected since faster quenching should lead to less precipitation. Moreover, the clusters volume fractions seem to be high as compared to the maximum volume fraction of hardening η' precipitates in the T6 state, which is about 8 %. This might be due to wrong assumptions on the clusters composition, which is crucial in order to extract absolute volume fraction from the scattering invariant. It was assumed that the clusters have the same composition as GP(I) zones (cf. Section 3.4).

The clusters density was calculated from the volume fraction and the Guinier radius by using equation 3.23 and assuming spherical precipitates. This is a valid assumption since the 2D SAXS spectra showed isotropic scattering. In addition, Sha and Cerezo evidenced clusters with a blocky and therefore rather spherical structure in the as-quenched state using 3D-APT [42]. The density increases

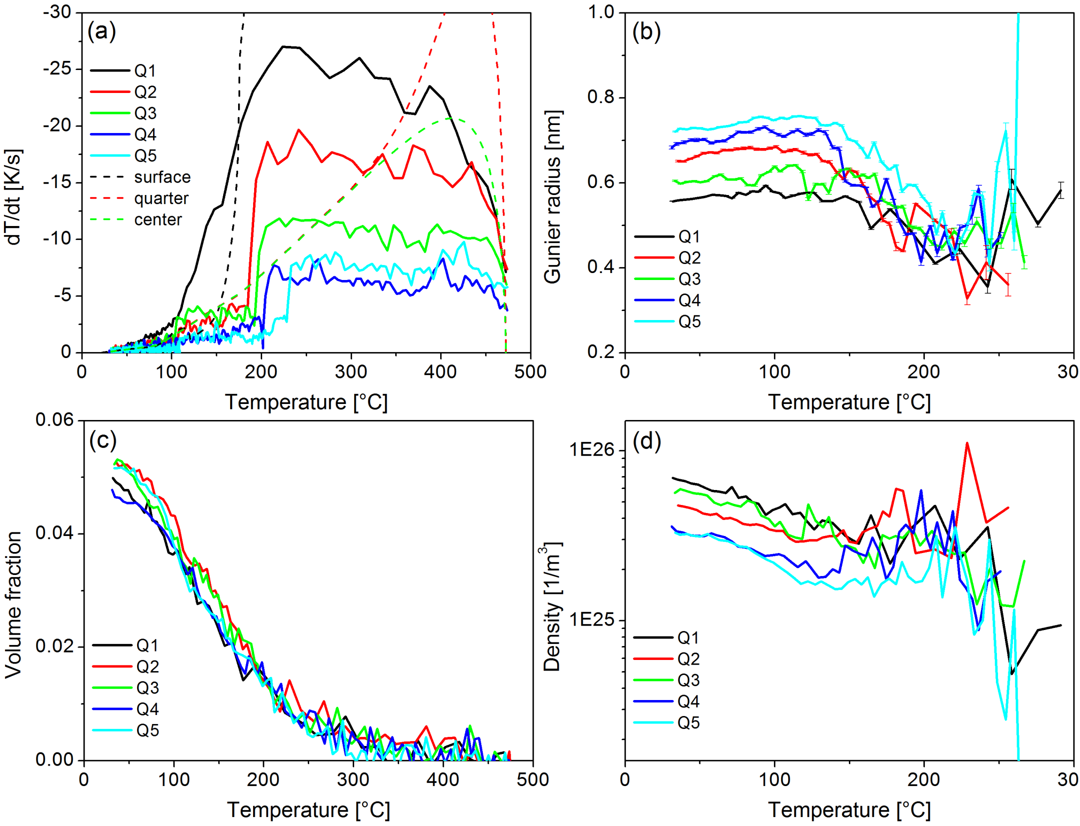

Figure 4.11: (a) The cooling rates of 5 different coolings (the fastest Q1 to the slowest Q5) for the AA7449 are illustrated along with the measured (b) Guinier radius and (c) volume fraction. (d) The calculated precipitate density during cooling is shown.

continuously in all five cases as temperature decreases although there are deviations between 220°C and 150°C (Figure 4.11d). In this temperature range the size estimation is difficult due to the low and broad scattering signal. The higher density in this range indicates an underestimated clusters size; this in turn leads to an overestimation of the clusters density. Below 150°C the trends of an increasing density becomes clear and justifies the statement of an increasing clusters density to room temperature. Overall, at room temperature the highest clusters density is observed after the fast cooling ($7 \bullet 10^{25}$ m^{-3}) and lowest in the slowest cooled sample ($3 \bullet 10^{25}$ m^{-3}).

Slower cooling rates at higher temperatures lead to lower densities of excess vacancies at lower temperatures due to annihilation on defects [65]. This can explain the lower number density of clusters for lower cooling rates since early clustersing is strongly influenced by the number of excess vacancies, as suggested by [33]. This is however not experimentally observed. It might also explain the similar volume fraction evolution for the five cooling rates. The longer time for precipitation during slower quench is balanced by a smaller amount of excess vacancies due to their annihilation on defects. In addition to the vacancies that influence clustersing, the solute loss associated with the η precipitation also influences the clusters formation by decreasing the available solute content and thermodynamic driving force for precipitation. The η formation during the rapid coolings is presented in the next section.

AA7040

In addition to the AA7449 alloy, in situ SAXS during cooling has also been performed on AA7040 samples with the same setup and specifications. Figure 4.12a shows the six applied cooling rates (solid lines), which are labelled from Q11 for the fastest to Q16 for the slowest cooling. Additionally, typical cooling conditions found in the 75 mm and 140 mm plate are displayed as dashed lines. For the AA7040 maximum cooling rates up to -90 K/s were obtained for Q11 and Q12 at around 350 °C.

The Guinier radii for each cooling are presented as function of temperature in Figure 4.12b. For coolings Q13 to Q16 the Guinier radius is around 0.4 nm at 200°C and increases slightly to about 0.45 nm at room temperature. Similar to the other coolings, the two fastest cooling rates Q11 and Q12 show a Guinier radius of about 0.4 nm around 200°C. But further cooling from 150°C leads to an increase to roughly 0.55 nm at the conclusion of the quench. Again, the uncertainty of the Guinier radius is high at high temperatures where the scattered intensity is low. The clusters size after the quench is largest (~ 0.55 nm) for the fastest cooling at high temperature Q11 and Q12 and smallest (~ 0.45 nm) for the coolings Q13-Q15 with highest cooling rates at low temperatures. The clusters size after the quench is higher when cooling rates are high at high temperatures and low at low temperatures.

The volume fraction of the clusters is shown in Figure 4.12c. Scattering of the data is evident but one can observe that the volume fraction starts to evolve in the temperature range between 250°C and 300°C for the 6 cases and increases as temperature decreases to room temperature. Down to 125°C the kinetics are very similar for all 6 cooling rates. Further cooling yields a higher volume fraction around 3.5 % for Q11 and Q12 compared to roughly 2.6 % for the other four coolings. Similarly to the clusters size, the volume fraction of the clusters is not dependent on the cooling rates at high temperatures. This is unexpected since faster quenching

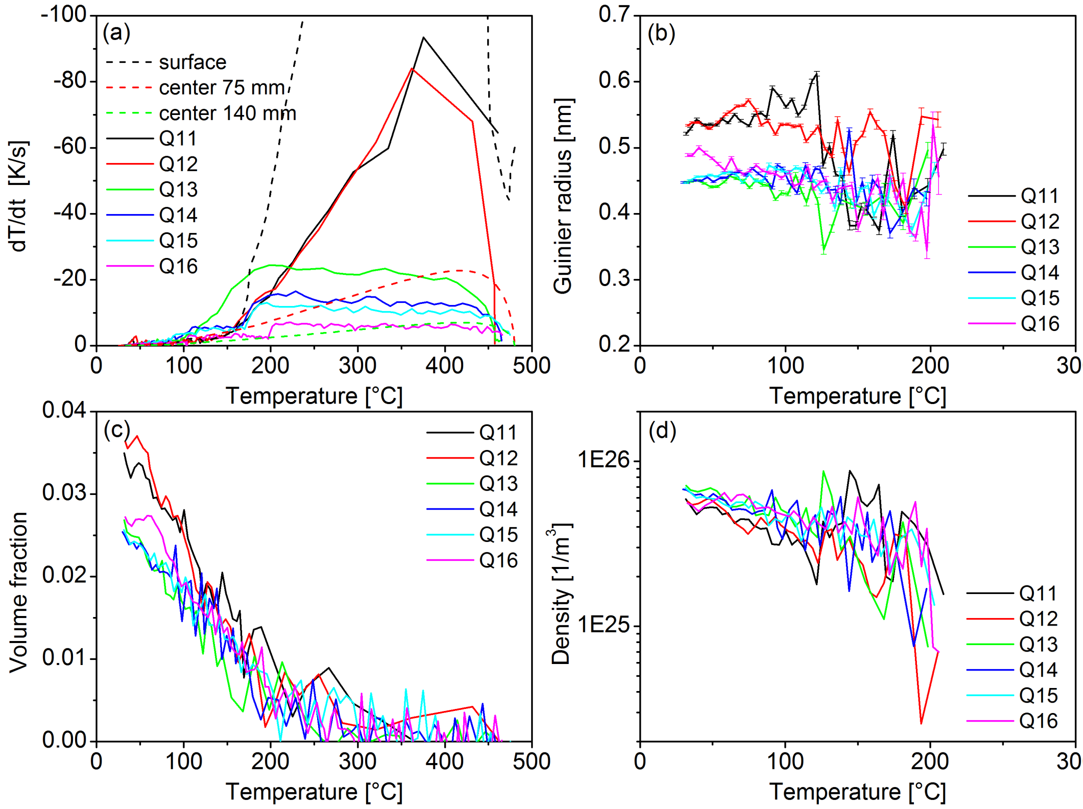

Figure 4.12: (a) The cooling rates of 6 different coolings (the fastest Q11 to the slowest Q16) for the AA7040 (b) Guinier radius, (c) volume fraction and (d) precipitate density.

should lead to less precipitation and smaller clusters size.

Figure 4.12d presents the calculated clusters density. Despite the scattering of the data a continuous increase of the clusters density is observed for all six coolings. The evolution of the clusters density is very similar for all cases. At room temperature, the density of Q11 and Q12 is around $6 \bullet 10^{25}$ m^{-3} whereas Q13 to Q16 yield a slightly higher density of $7 \bullet 10^{25}$ m^{-3}. Therefore, the higher volume fraction of Q11 and Q12 is due to the larger clusters size suggesting a higher vacancy density.

At the surface of the AA7040 plate, the cooling rates are similar to Q11 and Q12 below 170°C, but much higher at high temperatures. This indicates that the homogeneous precipitation is in terms of size and volume fraction in a similar range or even higher.

Evolution of the precipitate microstructure directly after rapid cooling in the AA7040

After the fast quench Q12 and the slower quench Q14, the evolution of the quench-induced precipitates was followed during a short period of time, e.g. during natural aging. The temperature evolution is presented as a function of time in Figure 4.13a. room temperature (below 35°C) was reached after 65s and 148s for the fast and slow quench, respectively. The vertical dashed lines indicate the start of the natural aging and serve as guide to the eyes. The holding time below 35°C was approximately 880s ($\sim$ 15 min) for Q12 and 360s ($\sim$ 6 min) for Q14.

Figure 4.13b shows the Guinier radius evolution as a function of time. As it was described in the previous paragraph, during cooling the Guinier radius is larger for the fast cooling. Moreover, in both cases the radius first increases as temperature decreases but decreases again before reaching room temperature. During the short natural aging, the Guinier radius stays roughly constant and yields 0.465 nm for Q12 and 0.44 nm for Q14.

In contrast to the radius, the volume fraction and the density increase during the natural aging (Figure 4.13c and d). This indicates continuous nucleation of clusters. The nucleation kinetics do not seem to depend on the applied cooling speed. The increase of the volume fraction and density with time is very similar for both cases. This implies that there is either no big difference in the vacancy concentration or that the influence of the vacancies on the precipitation at room temperature is not so high. Yet, the time at room temperature after the slow quench might not be long enough to see the impact of a higher vacancy concentration. The clusters density is almost identical but the volume fraction is higher in Q12 due to more precipitation during cooling. In general, the increase in volume fraction during cooling is much higher than during short natural aging. This might also explain the similar precipitate evolution after the cooling.

Overall, the findings are similar to the results reported by Kenesei et al. who evidenced a nucleation regime for up to 50 min after quench for a Cu containing 7xxx alloy close to the AA7040 after a very fast quench. They reported a size of 0.3 nm which is slightly smaller than the ones measured here, but they performed water quench [54].

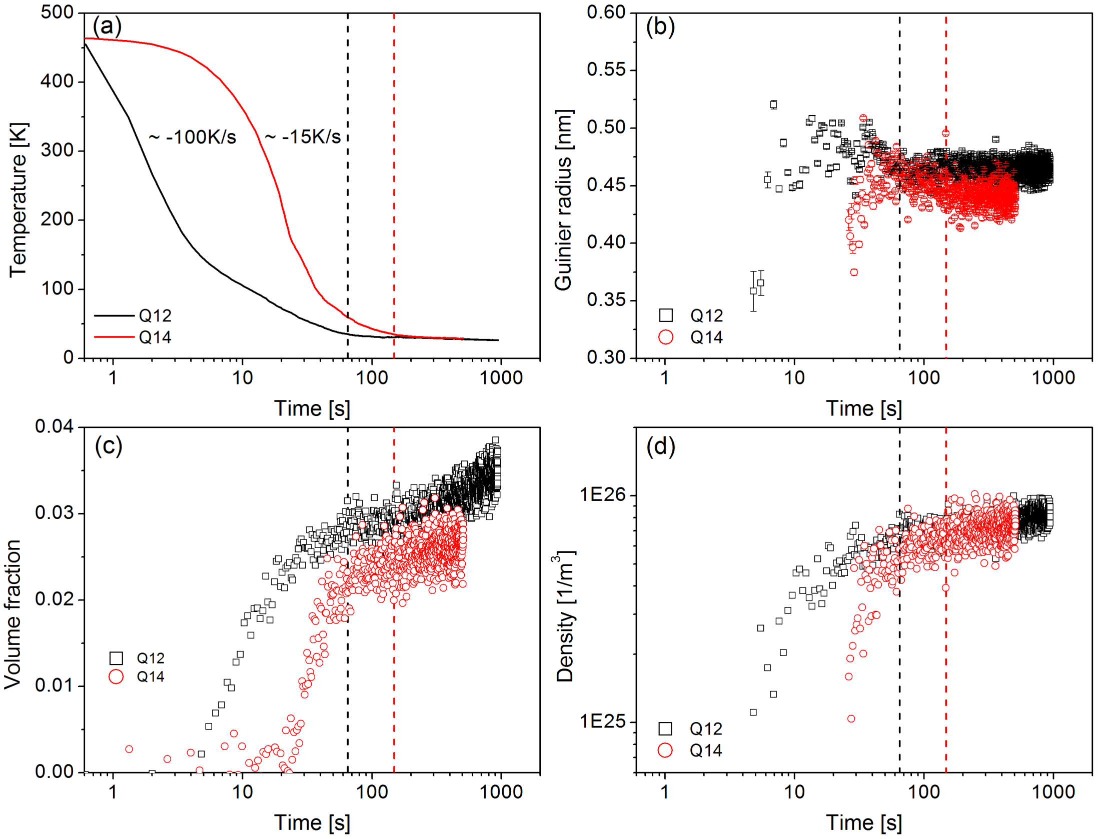

Figure 4.13: (a) Cooling curves of Q12 and Q14 for the AA7040 with the corresponding (b) Guinier radius, (c) volume fraction and the (d) calulated precipitate density during cooling and natural aging. The vertical dashed lines show the beginning of the natural aging.

4.3 Characterisation of heterogeneous precipitation during cooling

In situ small angle X-ray scattering

During cooling from the solutionizing temperature, scattering was evidenced at high temperature and at low q values as shown in Figure 4.10. These scattering objects refer to the equilibrium η phase, which is known to precipitate heterogeneously on dispersoids and grain boundaries. The volume fraction and size, typically ranging from 10 - 100 nanometres, is known to depend strongly on the cooling rate (Section 2.4). As pointed out in Section 3.4.4 the limited measurable q-range does not permit quantitative analysis of the η phase. But it still provides valuable information such as the temperature range where the heterogeneous η forms as presented in the following.

Figure 4.14a and b illustrate again the different cooling conditions that have been performed for the AA7449 and AA7040 alloy, respectively. In the AA7449 material, η starts to form around 400°C and saturates around 200°C regardless of the applied cooling rate as evidenced in Figure 4.14c. The precipitation kinetics are fastest between 380 and 280°C. The volume fraction of η is 0.18 % for the fastest cooling and 0.45 % for the slowest cooling. Clearly, the formation of η increases with decreasing cooling rate, which is expected due to longer time at high temperatures.

Figure 4.14d shows the volume fraction evolution of η in the AA7040 samples for the coolings Q11 to Q16. The η phase starts to form around 350°C and finishes at roughly 200°C for all applied cooling conditions. Precipitation exhibits the fastest kinetics between 350 and 250°C. The same trend has been observed in the AA7449 alloy. The volume fraction of η increases when slower cooling rates are applied. The largest fraction of η is obtained during cooling Q16 (0.08 %) and the lowest during the coolings Q11, Q12 and Q13 (0.02 %).

DSC during cooling - AA7449

In addition to the SAXS measurements during cooling, DSC (cf. Section 3.3) was applied to study the precipitation behavior of the AA7449 upon cooling. The range of applicable cooling rates was in the range of 2 to 80 K/min, which is much slower compared to the typical cooling conditions found in AA7xxx thick plates.

Figure 4.15a shows the specific heat curves during cooling at different rates. For the cooling rates of 40 and 80 K/min a second experiment was performed (dashed

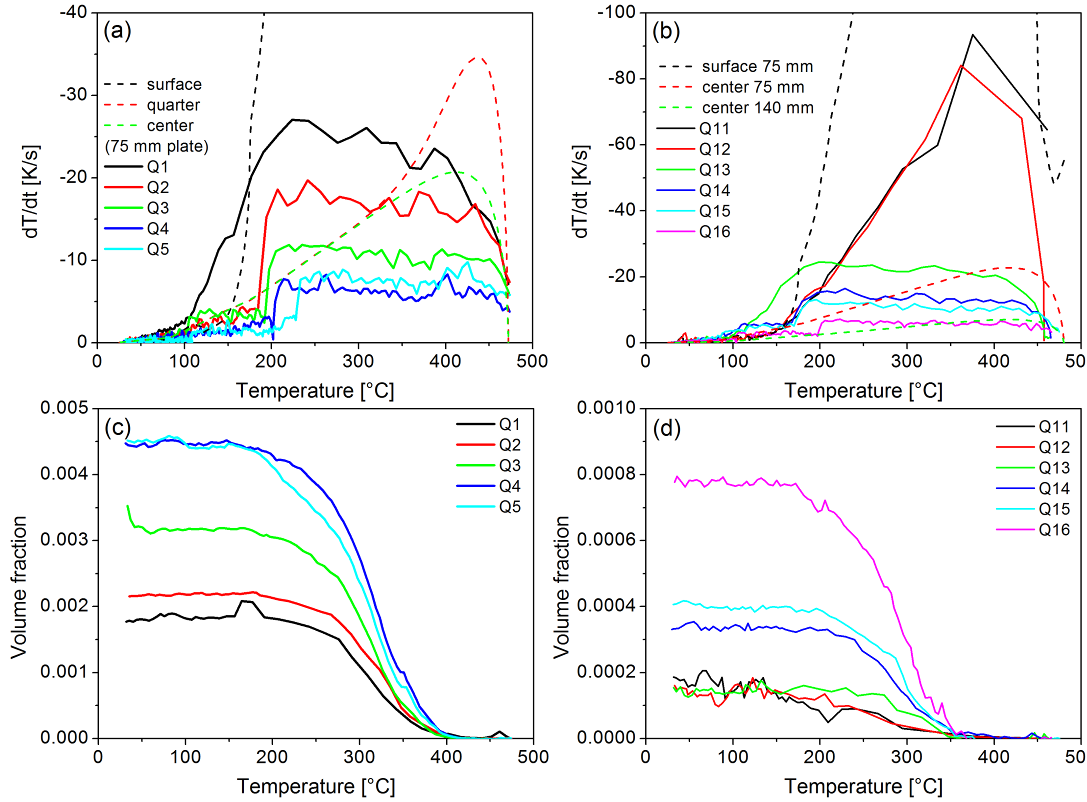

Figure 4.14: Cooling curves and corresponding evolution of the η volume fraction for the AA7449(a,c) and AA7040 (b,d).

lines) to evidence the reproducibility of the DSC measurements. Two exothermal precipitation reactions are observed regardless of the applied cooling rate.

The high temperature reaction, which can be ascribed to the formation of η, starts around 450°C for the slowest cooling rate of 2 K/min and shifts to 430°C as the cooling rate increases to 80 K/min. The shape of the high temperature heat effect shows two maxima. This might be related to the precipitation at different heterogeneous nucleation sites. Godard et al. showed that η forms during cooling first on dispersoids and with further cooling also on grain boundaries [7]. The peak size and therefore the amount of η that is formed, increases as the cooling rate decreases. This can be also seen in Figure 4.15b which shows the precipitation heat as a function of the cooling rate. The high temperature reaction slows down markedly below 300°C where it overlaps with the low temperature reaction, except for the cooling at 2 K/min for which the two reactions cannot be separated.

The second exothermal reaction is observed between 260°C and 130°C with a maximum around 200°C. This temperature range is usually associated with the formation of η' as discussed in Section 2.4. Below 130°C no heat effect is observed. The precipitation heat for the low temperature reaction is much lower and does not change much with the applied cooling rates in comparison with the high temperature precipitation (Figure 4.15b). Higher cooling rates should be applied to study the kinetics of the low temperature reaction as presented in [188, 15]. This would avoid the formation of η precipitates, which deplete solute and reduces the driving force for homogeneous precipitation at lower temperatures.

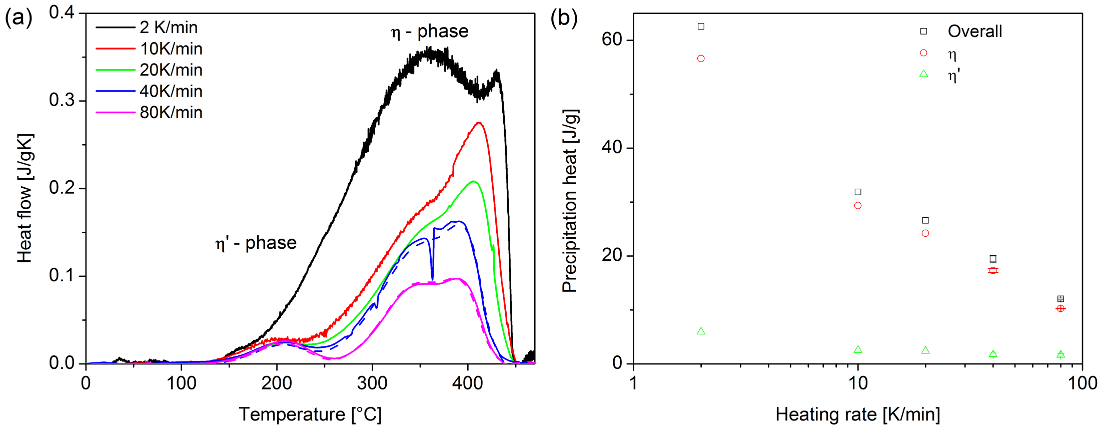

Figure 4.15: (a) DSC heat flow curves with varying cooling rates from 2 to 80 K/min for the 7449 alloy. (b) Precipitation heat for the two precipitation reactions as a function of the the cooling rate.

4.4 Comparison of AA7449 and AA7040

Homogeneous precipitation

The evolution of the precipitate microstructures in the AA7449 and AA7040 alloy during cooling are compared for three cooling conditions that have been performed for each alloy (Q1-Q13, Q3-Q15, Q4-Q16).

Figure 4.16a shows the cooling rates as a function of temperature for the 6 coolings and evidences comparable cooling rates in both alloys. The corresponding Guinier radius evolution is illustrated in Figure 4.16b. Around 200°C the Guinier radius is similar for both alloys and in the range of 0.4 - 0.45 nm. But at the end of the quench, large differences in the clusters size appear. Slower cooling rates at lower temperatures yield an increasing Guinier radius of the clusters in the AA7449 alloy with a clusters radius of up to 0.75 nm for the slowest quench. In contrast, the Guinier radius of the clusters forming in the AA7040 is unaffected by the different cooling rates. They show a constant radius around 0.45 nm.

Differences between the two alloys are also observed in the evolution of the clusters volume fraction during quench (Figure 4.16c). Clusters (and/or η') start to form around 300°C in the AA7449 compared to 250°C in the AA7040 alloy. They evolve in both alloys continuously during cooling to room temperature and the amount of volume fraction formed is found not to dependent on the applied cooling rates. This is unexpected since faster quenching should lead to less precipitation. Only when the cooling rates are very high, at high temperature as in the case of Q11 and Q12 for AA7040 (Section 4.2) the volume fraction varies significantly and is even higher. This indicates that a higher number of excess vacancies favour cluster formation. The total volume fraction is about twice as high in the AA7449 compared to the AA7040 alloy.

The clusters density evolution during quench is very similar in both alloys (cf. Figure 4.16d). The density increases continuously during cooling and is in the range of $6 \bullet 10^{25}$ m^{-3} to $7 \bullet 10^{25}$ m^{-3} at the conclusion of the coolings in both alloys except for the slow cooling in the AA7449 alloy. The clusters density for Q4 is lower and in the order of $3 \bullet 10^{25}$ m^{-3}. This can be associated with the heterogeneous precipitation at high temperature and therefore the solute depletion, which is highest for the Q4 as it is shown in Figure 4.17b. Overall, the clusters density has the same order of magnitude as the density of GP(I) zones after natural aging (Section 7.1).

During the quenching of AA7xxx thick plates, the evolution of homogeneous hardening precipitates can be expected to be similar in terms of size and volume fraction since the cooling rates are comparable to the ones applied here. In the surface region, where the cooling rates are even higher, the size and volume fraction can be expected to be even higher based on the trend observed for the AAA7040 alloy (Q11 and Q12).

Heterogeneous precipitation

The evolution of the heterogeneous precipitation during quench for the three cooling conditions of the AA7449 and AA7040 alloy is compared in Figure 4.17. The onset of η precipitation is shifted from around 400°C in the A7449 material to 350°C in the AA7040 alloy. In both alloys, the η volume fraction increases as the cooling rate decreases. The total amount of η formed is roughly one order of magnitude

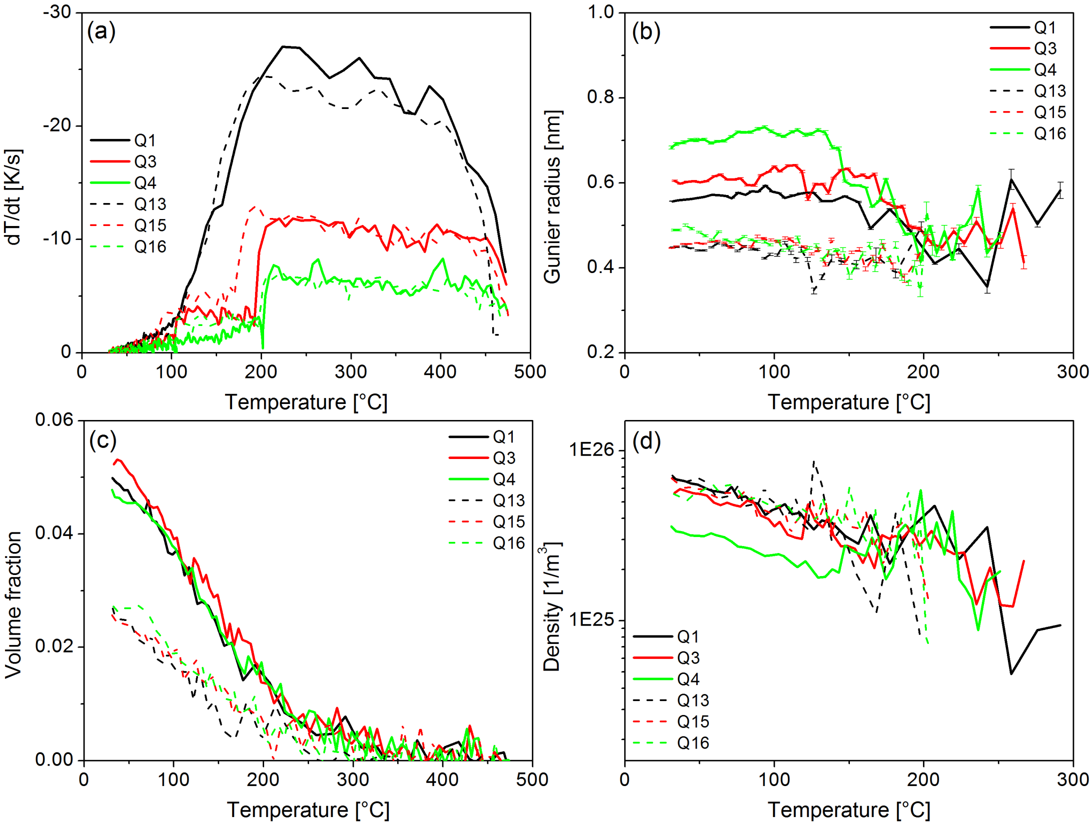

Figure 4.16: (a) cooling rates, (b) volume fraction, (c) Guinier radius and (d) precipitate density as a function temperature for selected AA7449 and AA7040 coolings.

higher in the AA7449 compared to the AA7040 alloy.

The SANS measurements showed a similar trend, but the AA7449 alloy exhibited only a two times higher volume fraction of η for the cooling at 20 mm distance to the surface compared to the AA7040. The absolute values measured with SANS and SAXS after quench compare well for the AA7040 alloy. For similar cooling conditions and chemical composition (Q13 and Q14 compared to the cooling in quarter thickness of the 142 mm plate), a volume fraction of 0.04 % and 0.03 % was obtained by SAXS and SANS, respectively.

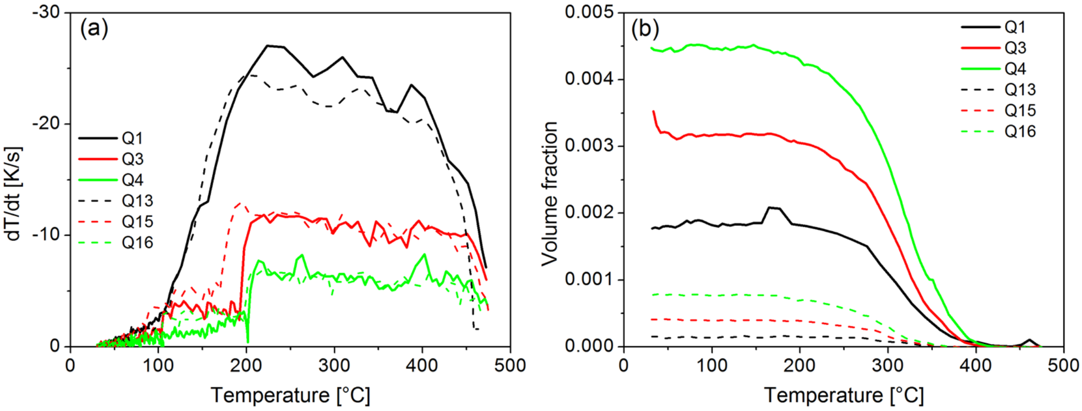

Figure 4.17: Comparison of the (a) cooling curves and the (b) evolution of volume fraction of η during cooling for the AA7449 (solid lines) and AA7040 (dashed lines).

In contrast, the results of the AA7449 alloy are rather different. The coolings Q1 and Q2, which are similar to the cooling in the quarter position of the 75 mm plate, revealed a volume fraction around 0.2 % compared to the 0.07 % measured with SAXS. The differences might be related to uncertainties due to the intensity calibration and/or a higher scattering intensity owing to measurements close to the beamstop (SAXS experiments). Nevertheless, the volume fraction of the heterogeneous η is very small compared to the maximum amount that can form ($\sim$ 7 % and 5 % for the AA7449 and AA7040).

In summary, the amount and size of homogeneous and heterogeneous precipitates that form during rapid coolings is higher in the AA7449 compared to the AA7040 alloy. The higher solute content increases the thermodynamic driving force for precipitation and leads therefore, as expected, to a higher quench sensitivity of the AA7449 alloy.

4.5 Continuous cooling precipitation diagram - AA7449

Figure 4.18 shows the CCP diagram, which has been derived from the precipitation start and end temperatures observed in the DSC curves. Due to the overlapping of the high and low temperature reaction in the DSC curves and for simplicity, the minimum between the two reactions was defined as the start temperature for the η' phase and as end temperature for the η phase [148]. In reality the reactions do overlap but fitting the two peaks by using the Multiple Peak Fitting option of the Origin program was not possible due to the unusual peak shape of the high temperature η reaction (cf. Figure 4.15).

In addition to the information obtained from DSC measurements, the findings of the SAXS experiments were also plotted in the CCP diagram, although the cooling rates are not constant below 200°C. The start and end temperatures of the volume fraction evolution are used. Similar to the DSC results, the SAXS signal also features the problem of overlapping contributions. The precipitates with large differences of the scattering length scale such as clusters and η phase can be relatively well separated. However, the formation of the η' affects the scattering contribution of both other phases. Nevertheless, from the Kratky plots the beginning of the clusters formation was roughly estimated.

The start temperature of η is decreasing to low temperatures as the cooling rates increase. In return, the end temperatures are seen to decrease with decreasing cooling rate except for the points obtained from SAXS. The longer time to form η balances the decreased mobility at lower temperatures. The lower end temperatures of η obtained by the SAXS measurements could be explained by an overlap with the formation of η'. The end temperatures of η obtained from SAXS seem to match the end temperatures for the η' precipitates if one extrapolates the points from DSC. In the SAXS analysis only two peaks were separated. Yet, the formation of homogeneous η' can lead to an increase of the analysed η contribution. Overall, at high temperature the η phase is clearly defined by the typical C-curve. At low temperature, the fast cooling and SAXS revealed the formation of clusters, which start between 200 and 250°C and form continuously down to room temperature. This reaction was not observed in DSC, maybe owing to solute and vacancy loss at higher temperatures.

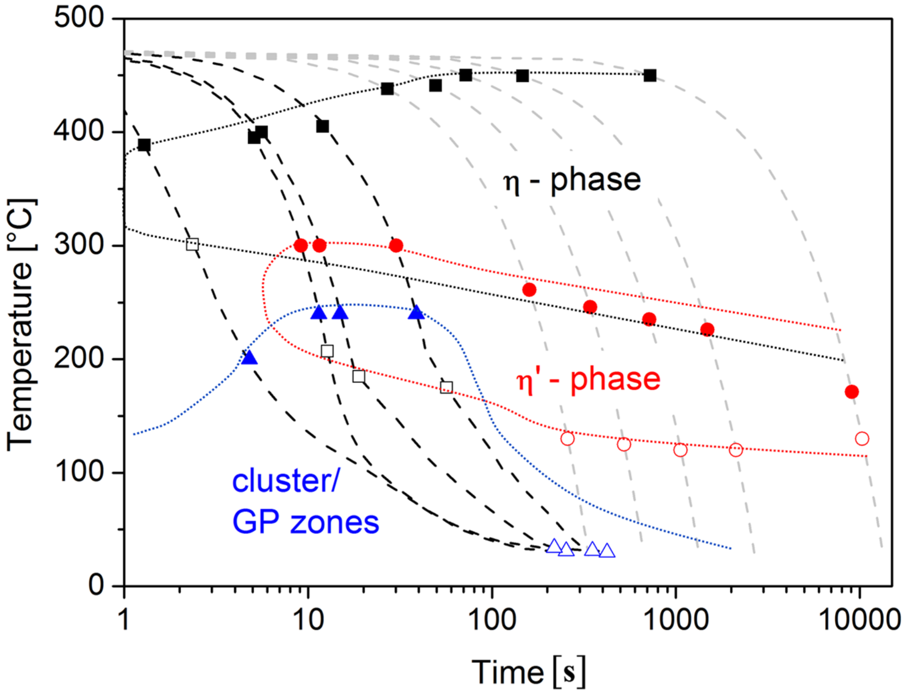

Figure 4.18: Continuous cooling precipitation diagram using cooling rates in the DSC (dashed grey lines) and SAXS (dashed black lines). The start and end temperature of η are indicated by full and open black squares. The η' phase is described by full and open red circles and the clusters by blue triangles that are full and open. The full black, red and blue lines serve as guide to the eyes for the temperature regime, where the η, η' and clusters are forming.

4.6 Implications for macroscopic residual streses

The results presented in the 4.2 and 4.3 evidence the formation of homogeneous solute clusters at low temperatures and heterogeneous η precipitates at high temperatures during coolings that are similar to the ones found during the quenching of industrial thick plates. The appearance of both phases alters the mechanical properties of the material during quench through changes of solid solution strengthening and precipitation hardening. The effect of the quench-induced precipitation on the yield strength is estimated by using equation 3.48 (cf. Section 3.6.

The calculated yield strength for coolings Q1 to Q5 and the yield strength measured with Gleeble tests (crossed open points) are shown in Figure 4.19a as a function of temperature. Besides, a black dashed line is shown, which serves as a guide for the eyes in the temperature region where the yield strength cannot be estimated correctly (precipitate strengthening contribution). At high temperature a small decrease (up to 15 MPa) of the yield strength can be seen due to the formation of η. Around 250°C when the clusters size and volume fraction can be estimated the yield strength is about 170 MPa for all coolings. Further cooling leads to an increasing yield strength down to room temperature. The slowest coolings Q5 results in the highest yield strength of 258 MPa and after the fastest cooling the lowest strength of 245 MPa is observed. The measured and calculated yield strengths agree reasonably well for Q1 and Q3 between 200 and 150°C. At lower temperatures, the agreement is less good. In the case of Q1 the yield strength is overestimated by about 15 MPa and for Q3 the yield strength is underestimated by roughly 10 MPa. These differences can result from cooling conditions, which were not exactly the same for the SAXS and Gleeble experiment, from limitations of the SAXS analysis and/or the influence of the PSD on the yield strength.

Figure 4.19b presents the evolution of the yield strength for the coolings Q11 to Q16 performed with the AA7040 alloy. To guide the eyes, a dashed line is drawn for the yield strength between 200 and 250°C. The solute depletion due to the η phase at high temperature is very low in the AA7040. At 200°C the strength already increase up to $\sim$ 155MPa. With further decrease in temperature, the yield strength continues to increase. The slower coolings Q13 to Q16 show a similar yield strength of about 200 MPa at the conclusion of the quench. The measured and the calulcated yield strengths compare well for Q16. Similar to the evolution of the Guinier radius and volume fraction, the yield strength is higher for the two

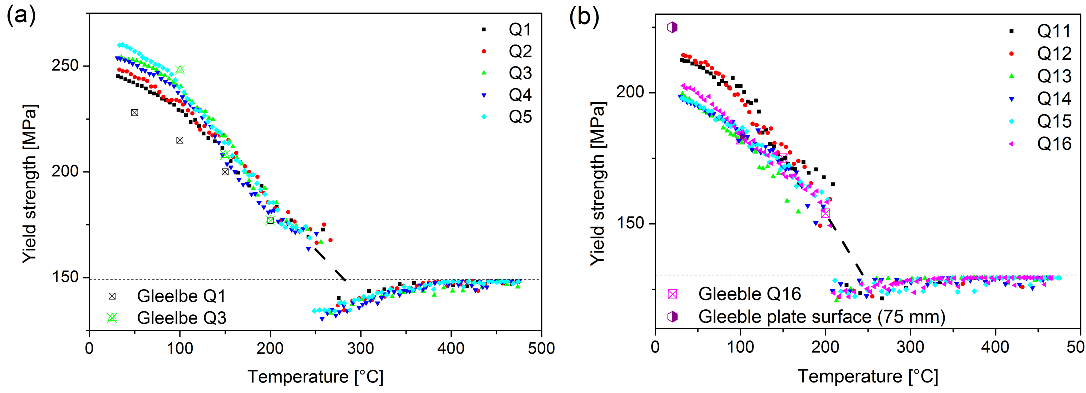

Figure 4.19: (a) Calculated yield strength of the AA7449 for the coolings Q1 to Q5 together with the yield strength measured with the Gleeble machine (crossed points) using the cooling paths Q1 and Q3. (b) Calculated yield strength of the AA7040 for the coolings Q11 to Q16 together with the measured yield strength using the cooling paths Q16 and at the surface of a 75 mm AA7040 plate(crossed points).

fast coolings Q11 and Q12. The yield strength starts to deviate around 130°C and yields 214 MPa at room temperature. This is close to the yield strength of the plate surface (75 mm), which was measured to be 225 MPa after performing the surface cooling in the Gleeble. In comparison with the AA7449, the yield strength of AA7040 is about 50-60 MPa lower after similar cooling conditions owing to the smaller amount and size of clusters.

The formation of the homogeneous precipitates at low temperatures during cooling has a marked effect on the yield strength, which increases due to clusters strengthening. The yield strength at the conclusion of the performed coolings is about 260 and 210 MPa in the AA7449 and the AA7040 alloy, respectively. The yield strength increase due to the clusters formation explains the unexpected high residual stresses of about 300 MPa and 250 MPa that have been measured in the AA7449 and the AA7040 75 mm thick plates [119] (cf. Section 2.7). Robinson et. al. [82] argued that a higher quench sensitivity results in a softening due to η precipitation and therefore lower residual stresses. The obtained results show that the higher quench sensitivity of the AA7449 can also lead to higher residual stresses in the case of thick plates owing to a higher volume fraction of clusters and only a small amount of η.

4.7 Summary

In this Chapter, the microstructural changes during rapid coolings of the AA7449 alloy, and to some extent in the AA7040 alloy, have been investigated after and during different coolings. The combination of time resolved SAXS measurements and a laser based heating system allowed us to observe directly the microstructural changes during rapid coolings.
At least two different phases are evidenced during coolings, which were close to industrial practice. At high temperatures the heterogeneous η phase forms. At temperatures below 300°C the formation of homogeneous hardening precipitates are evidenced. Their sizes refer to solute clusters, vacancy rich clusters and Guinier Preston zones. In addition, there are indications that the η' phase also forms during quench, even though only in small quantity.
From the technological point of view, the experiments reported in this chapter clearly show that quench-induced precipitation cannot be avoided in thick plates made of these two alloys.

In more detail, the formation of heterogeneous η during cooling is strongly linked to the cooling rate. The start temperature, but also the volume fraction and size increase with decreasing cooling rate, in contrast to the end temperature that decreases. Cooling rates of up to 100 K/s at high temperature are not sufficient to completely suppress the heterogeneous precipitation in both alloys. The kinetics of the heterogeneous η formation is most pronounced between 380 and 280°C and 350 to 250°C for AA7449 and AA7040, respectively. In addition, the quench induced heterogeneous precipitation is also strongly influenced by macrosegregation present in the thick plates. Therefore, macrosegregation needs to be taken into account when the formation of quench-induced η is to be modelled in thick plates.
However, the amount of heterogeneous η that forms during quenching of the investigated thick plates is very low. The amount of quench-induced η could be further decreased by increasing the cooling rates in the temperature range where the kinetics is maximum.

Homogeneous hardening precipitates form below 300°C and 250°C in AA7449 and the AA7040, respectively. Scattering of clusters was only observed below 250°C, which indicates that η' precipitates might also form. Higher cooling rates yield the same or an even higher volume fraction of clusters in comparison with smaller cooling rates. This is unexpected and was associated with the presence of a larger number density of excess vacancies that are present after fast coolings. The average radius of the clusters is smaller than 1 nm. The size depends on the cooling rate and increases when the cooling rates are high at high temperature and low at low temperatures. The observations on the size and volume fraction indicate that the excess vacancies play a vital role in the formation of the homogeneous clusters. The density of clusters increases as the temperature decreases and is very similar way for the applied cooling rates. Only the slowest cooling yields a considerably smaller density of clusters in the AA7449. This is explained by the solute loss and not by a vacancy loss at high temperature since similar coolings with the AA7040 did not show this effect.

It is apparent that the AA7449 is more quench sensitive compared to the AA7040 due to a higher solute content. For similar cooling conditions the size of η is larger and the volume fraction is at least double in the AA7449 compared to the AA7040. Further, the amount of homogeneous precipitation is two times higher in the AA7449 then in the AA7040 alloy. The same trend is also observed for the clusters size, which is generally higher. Only the clusters number density was similar in both alloys.

It is shown that the observed precipitation during rapid coolings change the mechanical properties of the alloys. The low amount of η, which forms at high temperature decreases only slightly the solid solution strength. With the appearance of the homogeneous phase, the yield strength of both alloys increase markedly due to clusters strengthening. The estimated yield strengths after the applied coolings are in the range of 245-260 MPa and 200-215 MPa, for the AA7449 and AA7040, respectively. The cooling conditions on the surface of thick plates are much faster than the ones applied in the in situ SAXS experiments. From the observed trend a higher amount of clusters can be expected, which would results in higher yield strength. The increased yield strength due to the clusters formation explains the unexpected high residual stresses of 300 MPa and 250 MPa measured on the surface of the 75 mm AA7449 and AA7040 plate.

Main findings:

1. At least two phases, subnanometre clusters and η precipitates, form during quenching of industrial thick plates
2. The very low amount of η precipitates form heterogeneously at high temperatures

3. The high amount of subnanometre clusters that form at low temperatures is influenced by excess vacancies
4. Macrosegregation is important and influences the formation of the η phase and the clusters in the plates
5. The clusters increase the yield strength during quench and therefore the macroscopic residual stresses

5 Reversion heat treatments

In the previous Chapter the quench-induced precipitation in the AA7449 (and to some extent also in the AA7040) alloy has been characterized after and during quench. It was shown that at least two different precipitation reactions take place when cooling conditions similar to those during industrial quenching of thick plates are applied. Further, it was evidenced that only homogeneous clusters have a marked effect on the yield strength and therefore on the residual stress level. In contrast, the η phase was found to have minor influence.

This chapter reports on reversion (also called dissolution) heat treatments that have been performed to characterise the nature (Section 5.1) and thermodynamic properties of the quenched-induced homogeneous clusters in order to establish a thermodynamic description (Section 5.2). In addition, the activation energy of GP(I) zones dissolution after natural aging is compared to the activation energy of GP(I) zones formation directly after quench to investigate the influence of excess vacancies on the precipitation kinetics (Section 5.3).

5.1 Nature of the quench-induced homogeneous phase

AA7449

In comparison to the high temperature phase that forms during quench, the nature of the subnanometre homogeneous precipitates is not known. TEM investigations used for the heterogeneous η phase are not useful since the homogeneous precipitates evolve with time at room temperature as reported in References [18, 54]. In the previous chapter this phase was referred to as clusters. To get a better idea about the nature of the homogeneous phase, dissolution upon heating of the as-quenched (AQ) clusters was compared to the one of GP(I) zones.

Figure 5.1a illustrates the heat treatment, which was performed on a AA7449 sample. The sample was in the T4 state ($\approx$ 4 days) and contained only GP(I) zones. The sample was heated up with $\approx$ 7K/s to the solutionizing temperature and hold for 7 min before it was cooled down rapidly. The precipitation during quench refers to Q1, which has been reported in Section 4.2. After the quench the sample was heated up again with $\approx$ 5K/s to the solutionizing temperature.

The corresponding scattering data for the dissolution of the GP(I) zones and of the AQ clusters is shown in Figure 5.1b and c, respectively. The scattering curves are shown in Kratky representation as a function of the temperature. The intensity is illustrated by the colour of the 2D image. Low scattering is in blue and high scattering in red or white when the intensity is higher than 0.25. The maximum of 0.25 was chosen to better observe the scattering peak resulting from the AQ clusters in Figure 5.1c.

A broad scattering peak due to GP(I) zones is visible at a q-value of 0.3 before the heat up in Figure 5.1b . The absence of scattering at low q values shows that no heterogeneous η was formed during the quench of the sample. Upon heating the GP(I) zones scattering peak is stable until 100°C. With further heating the intensity of the GP(I) zones peak at high-q values starts to decrease. This is due to the dissolution of smaller particles, which become unstable (curvature effect) and the particle distribution becomes therefore narrower. Around 150°C the GP(I) zones scattering peak has decreased drastically. With further increasing temperature around 170°C the scattering peak splits into two parts, which indicates two different phenomena.

The smaller GP(I) zones dissolve completely between 200-250°C. The larger GP(I) zones seem to remain stable and transform into η' precipitates as indicated by the connected scattering peaks. Alternatively, they also dissolve and η' forms from the solid solution. Yet, this point cannot be clarified only from the scattering data. The η' precipitates grow with further heating and transforms into η, which is evidenced by a shift of the scattering peak to lower q values. Around 300°C, η start to dissolve but continues to grow until 440°C when the scattering signal disappears from the measured q-range.

The dissolution of the AQ clusters shows very similar features compared to the case of GP(I) zones (Figure 5.1c). Before the heat up a scattering peak due to the quench-induced clusters is seen, yet with a smaller intensity compared to the GP(I) zones. In addition, at lower q values scattering is observed that originates from the quench induced η precipitates. Increasing the temperature leads to dissolution of the clusters. As in the case of GP(I) zones, at 200°C the scattering peak of the clusters splits up into two parts.

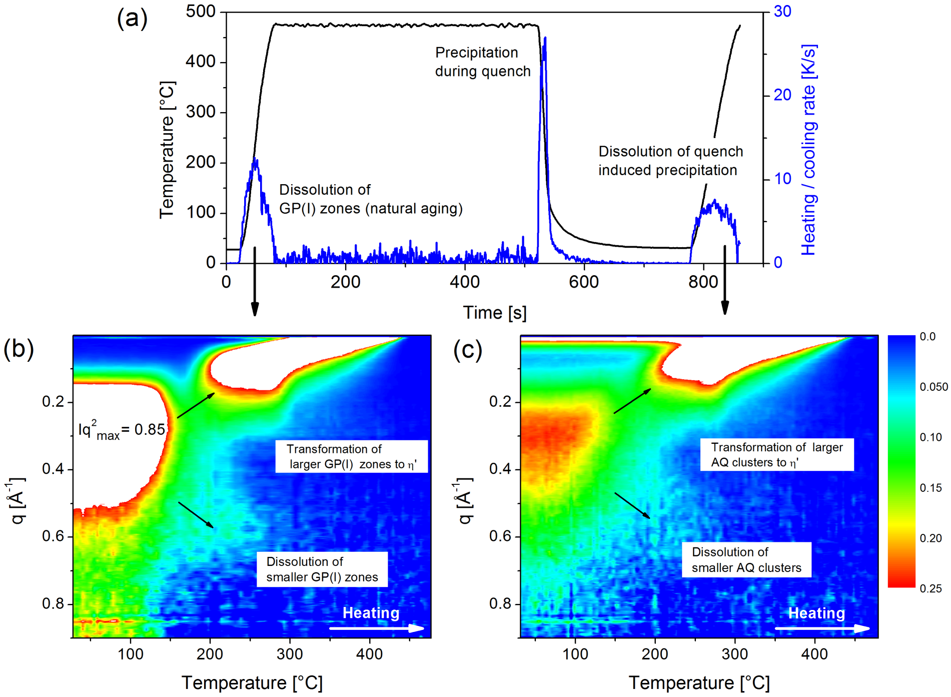

Figure 5.1: (a) Heat treatment details with corresponding heating and cooling rates applied to the AA7449 sample. Evolution of the scattering signal upon heating after (b) natural aging and (c) directly after the cooling Q1. Kratky plots are shown as function of temperature, where the intensity (scale bar) scales in z-direction. The intensity was scaled to a value of 0.25, which presents the intensity maximum of the high-q peak in (c).

The smaller particles continue to dissolve until 250°C. In contrast, the shift of the scattered intensity to lower q-values starts slightly earlier compared to the GP(I) zones. This small difference can be related to either the smaller heating rate (5K/s vs 7K/s) and/or a higher amount of excess vacancies directly after quench compared to natural aging of 4 days. Further heating shows a similar behavior of the η' and η phase as observed for the dissolution of the GP(I) zones. But the scattering peak is slightly shifted to lower q-values, thereby indicating a larger size.

Figure 5.2 shows quantitatively the evolution of the GP(I) zones and AQ clusters in terms of Guinier radius and volume fraction upon heating. The trends observed in the scattering plots are supported by the quantitative analysis.

The volume fraction and radius of the GP(I) zones (10 % and 0.6 nm) is higher compared to the AQ clusters (5 % and 0.5 nm). Between 80 and 150°C the volume fraction decreases and the average radius increases in both cases. The average radius increases due to the dissolution of smaller particles. The splitting of the precipitate size distribution takes place earlier for the AQ clusters (100°C) compared to the GP(I) zones (150°C), which can be linked to the smaller size and volume fraction. The increasing radius between 150 and 200°C relates to the appearance of η', which also stabilises the volume fraction. η' is seen to form earlier in the case

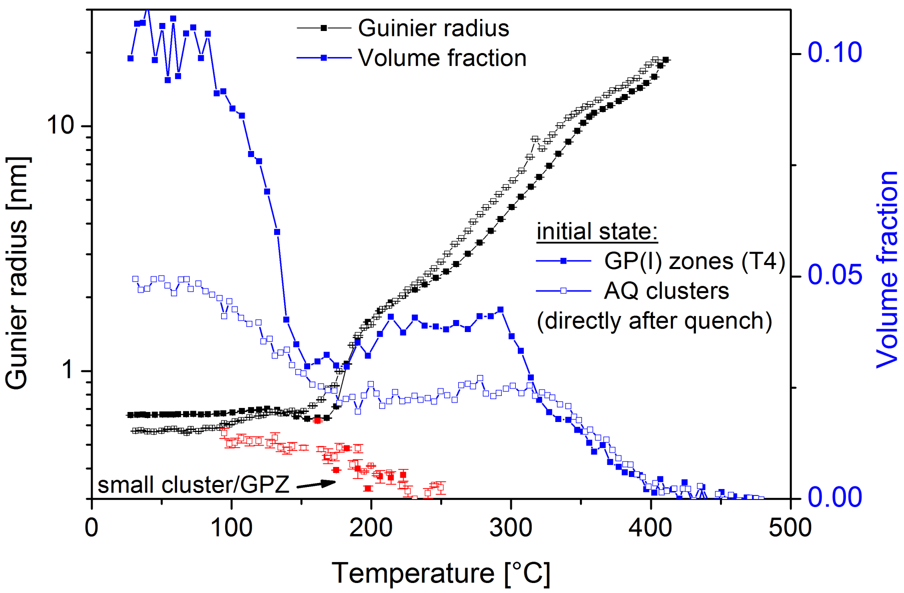

Figure 5.2: Evolution of the Guinier radius (black) and volume fraction (blue) upon heating is shown for the T4 state (full symbols) and the as-quenched Q1 state (open symbols). The size of the smaller precipitates is also shown as red symbols without line.

of the AQ clusters. As mentioned before, this can be due to the slower heating rate and/or a higher concentration of non-equilibrium vacancies. Further heating shows an increasing radius of η' and η and decreasing volume fraction from around 300°C until 470°C.

AA7040

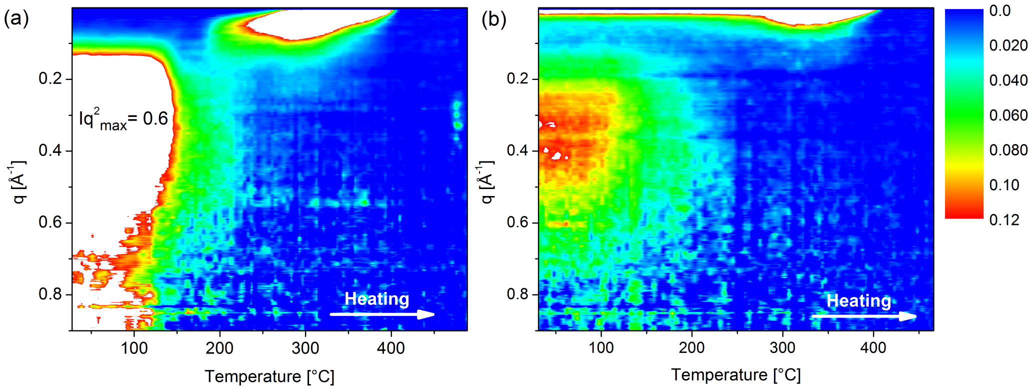

Figure 5.3: Evolution of the scattering signal upon heating is shown starting with an initial microstructure of (a) GP(I) zones that formed during 4 days of natural aging and (b) AQ clusters that formed during cooling. The intensity is scaled to a value of 0.12 in order to observe better the scattering peak in (b).

The reversion heat treatment with an initial state of T4 and AQ is also performed with the AA7040 alloy. The heating rate is around 8 K/s for both cases. The corresponding scattering curves for T4 and AQ state are illustrated in Figure 5.3. The intensity is scaled to the maximum of the scattering peak (0.12) in Figure 5.3b.

Similarly to AA7449, the GP(I) zones in the AA7040 remain stable until 100°C (Figure 5.3a). Further heating leads to the dissolution of the GP(I) zones until 200°C. Around 180°C a second scattering peak due to η' precipitates appears at lower q-values. The two scattering contribution are much less connected compared to AA7449. At high temperatures the η' precipitates grow until 300°C before they start to dissolve and disappear from the measured q-range at around 410°C.

Figure 5.3b shows the reversion heat treatment of the AQ state, which features a scattering peak from the AQ clusters and also a scattering contribution from heterogeneous η at lower q values. When the samples is heated up, the AQ clusters start to dissolve around 100°C. With increasing temperature the cluster size

distribution gets smaller until 240°C, where the scattering signal disappears. In comparison to what has been observed in the case of GP(I) zones in both alloys and the AQ clusters for AA7449, the second scattering peak due to η' does not appear. In contrast the scattering contribution at low q starts to broaden between 200°C and 300°C, before it starts to decrease again.
The absence of η' indicates that a stable amount of clusters is needed to serve as starting point of η'. Therefore, the GP(I) zones (can) serve as nucleation site for the η'. An alternative explanation is that the critical time to form η' from the solid solution at the intermediate temperature is not reached in comparison with AA7449. Moreover, the splitting of the high q scattering peak is also not observed.

Figure 5.4 shows the evolution of the Guinier radius and volume fraction during

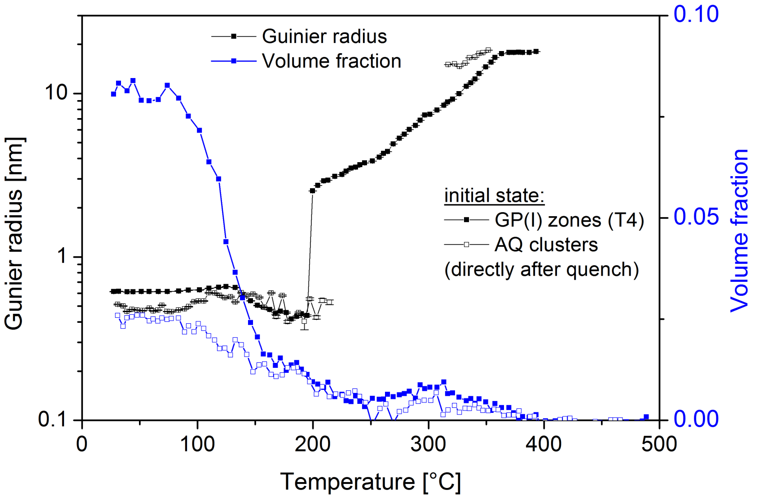

Figure 5.4: The changes of the Guinier radius (black) and volume fraction (blue) during heating to the solutionizing temperature are presented for the T4 state (full symbols) and the as-quenched Q13 state (open symbols).

the reversion heat treatment of the GP(I) zones and AQ clusters. The volume fraction and size is again larger for the GP(I) zones (8 % and 0.65 nm) compared the AQ clusters (2.5 % and 0.45 nm). A sharp decrease of the GP(I) zones volume fraction form 8 to 2 % is evidenced between 80 and 150°C. The radius stays rather constant until 140°C and then decrease to 0.45 nm before it disappears at 200°C. The volume fraction continues to decrease up to 250°C but less pronounced due to the η' formation as evidenced by the jump of the precipitate radius to around 3 nm at 200°C. With further heating η' precipitates grow until 300°C, where it starts to disappear.

The AQ clusters also decrease from 80°C in terms of volume fraction until 250°C where it tends to zero. The average cluster radius increases between 80 and 150°C from 0.45 nm to 0.6 nm but decreases again to 0.45 nm until 200°C. At 200°C the Guinier radius cannot be estimated anymore due to the small intensity and broad scattering of the AQ clusters and the absence of η'. The volume fraction evolution from 150°C to 400°C is very similar for both cases although no η' forms when the AQ clusters are dissolved.

From the dissolution behavior observed in the AA7449 and AA7040 one can state that the AQ clusters behave thermodynamically in the same way as GP(I) zones that formed during natural aging for 4 days. The onset of dissolution, the size and volume fraction evolution is almost identical for the AQ clusters and the GP(I) zones. Yet, the AQ clusters seem to be stable up to slightly higher temperature. The small differences can be explained by the difference of the initial state (small difference in size and volume fraction), the heating rate and the number of excess vacancies.
Therefore, in the following the AQ clusters will be considered as GP(I) zones and a thermodynamic description will be derived using the solubility product.

The dissolution of AQ clusters in the AA7040 alloy did not result in the formation of η' formation, as it was the case for the AA7449 and the GP(I) zones in the AA7040. Lendvai argued that in more concentrated alloys (such as the A7449) GP(I) zones reach faster a critical radius that make them suitable for η' precipitation [41]. Therefore, the observed difference can be due to a too small volume fraction and size of the AQ clusters in the temperature range where η' forms in AA7040. Also, the critical time for precipitation is higher in AA7040 compared to AA7449.

5.2 Thermodynamic description of GP(I) zones

In Sections 4.2 and 4.6 it was shown that subnanometre clusters form during rapid coolings and that they are responsible for high residual stresses due to cluster strengthening. Further, it was pointed out in Section 5.1 that the quench-induced clusters behave thermodynamically in the same way as GP(I) zones, which form during natural aging. In order to model the GP(I) zones formation during quenching a thermodynamic description is needed. In the following a thermodynamic description for the GP(I) zones will be established from dissolution (reversion) experiments by using the solubility product.

In addition to the fast reversion treatments performed at the cSAXS beamline, reversion heat treatments have also been performed at laboratory SAXS source using slower heating rates of 1K/s and 5K/s (Section 3.4.2). The samples were taken from the surface, quarter and center position of the 75 mm plate, which was in the T4 state.

The Kratky plot in Figure 5.5a shows the changes of the scattering signal during heating with 5 K/min. The position of the scattering maxima at 0.2 Å^{-1} stays constant during heating up to 125°C. This indicates a constant precipitate size. In contrast, the intensity of the peak is decreasing, which relates to a decrease in volume fraction. With further heating, the peak is observed to shift towards lower q-values, which corresponds to an increasing precipitate size. Above 225°C the scattering signal shifts to low q-values, which could not be measured with the setup.

The estimated Guinier radius and volume fraction during heating with the two rates is shown in Figure 5.5b for a sample taken from the quarter thickness. Due to long natural aging time of more than 1 year, the precipitation microstructure consists of GP(I) zones with a volume fraction of 16 % and a size of about 0.9 nm. The volume fraction of GP(I) zones starts to decrease around 90 and 70°C for a heating rate of 5 and 1 K/min, respectively. In contrast, the Guinier radius increases only slightly up to 140 and 126°C in the case of 5 and 1 K/min. This behavior is typical for reversion heat treatments. The smaller precipitates of the size distribution dissolve whereas the larger ones remain stable as it was also observed in Figure 5.5a. With the increase of the Guinier radius the decrease of the volume fraction stops at 8.5 % and 7.5 % for 5 and 1 K/min, respectively. This is due to the formation of η'. It is obvious that the reversion is not complete and only the GP(I) zones are only partially dissolved before η forms. The size of η' increases as the temperature increases in contrast to the volume fraction, which stabilises first before decreasing. At 225 and 200°C (5 and 1 K/min) the scattering signal starts to shift out of the measurable q-range.

Comparison of GP(I) zone dissolution for different plate positions

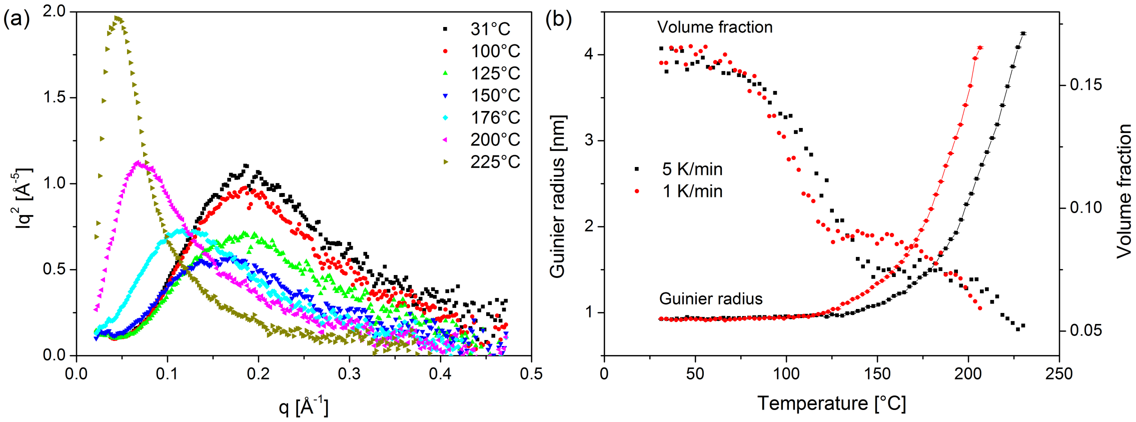

Figure 5.5: (a) Kratky plot at selected temperatures during heating of the surface sample at 5 K/min. (b) Evolution of the Guinier radius and volume fraction during heating with 1K/min (red) and 5K/min (black) of a quarter thickness sample in the T4 state.

The same heat treatments reported in Figure 5.5 for the quarter position have also been performed with samples taken from the surface and center position. The initial microstructure consists in all three cases of GP(I) zones with a Guinier radius of about 0.9 nm. The volume fraction was found to be slightly lower in the surface (15 %) and center position (13.5 %) compared to the quarter position (16 %). This can be associated with the macrosegregation that is present in the plate (see Section 4.1.2). In order to compare the dissolution kinetics of the three positions the volume fraction was normalized by its initial value.

Figure 5.6a illustrates the changes of the GP(I) zones in terms of Guinier radius and volume fraction upon heating with 5 K/min. Within the scatter of the data, the behavior of the three positions is remarkably similar. The partial reversion finishes when almost half of the GP(I) zones is dissolved at 142°C. Also the formation of the η' precipitates is very similar for the three cases.

With a heating rate of 1 K/min, the evolution of GP(I) zones is again very similar for the three positions (Figure 5.6b). The dissolution of the GP(I) zones starts around 70°C and stops with the appearance of η' at 126°C after about half of the GP(I) zones have dissolved. The dissolution of the GP(I) zones starts earlier and the temperature of η' formation is lower compared to the heating with 5 K/min. This is a classic influence of heating rate. Further, after partial reversion the volume fraction stabilises at a higher value. The evolution of the η' precipitates is again similar for all three cases when the temperature increases further.

The comparison of the GP zone dissolution kinetics did not show large differences for the three positions. This implies that there are no large differences in the vacancy concentration and also in the dislocation densities between the three positions.

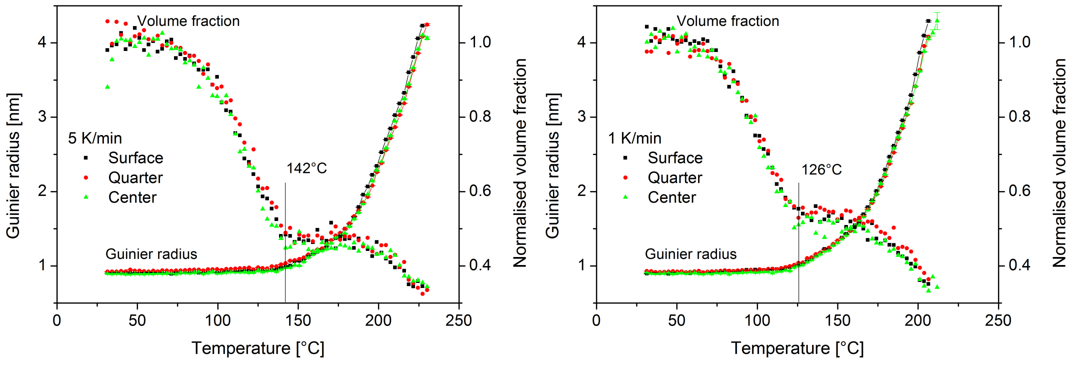

(a) (b)

Figure 5.6: The evolution of the Guinier radius and the volume fraction during heating with (a) 5 K/min and (b) 1 K/min is compared for the surface (black), quarter (red) and center (green) position.

Comparison of experimental results and the thermodynamic description

Figure 5.7a shows the volume fraction evolution of the different reversion heat treatments that have been performed on the AA7449 alloy. The volume fraction was normalised to its initial value in order to better compare the dissolution kinetics. Only the reversion of the AQ clusters (light blue) was normalised on the value found after 4 days of natural aging (the green and dark blue points).
The dissolution of the GP(I) zones starts for all heating rates at a similar temperature. The decrease in volume fraction is very similar for all heating rates, except for the case of 1 K/min, which drops faster. The end temperature of the partial reversion shifts to higher values as the heating rate increases. In addition, the amount of volume fraction present in the sample when η' appears decreases with increasing heating rates.

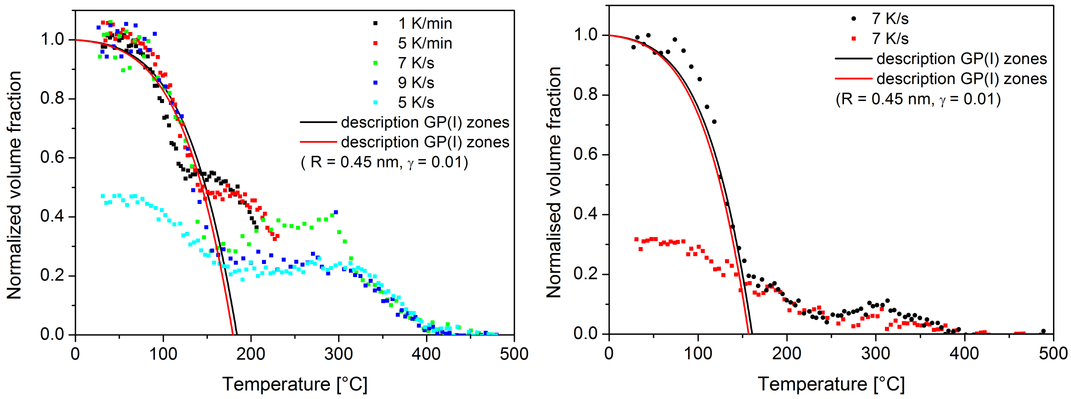

(a) (b)

Figure 5.7: Normalised volume fraction evolution during several reversion heat treatments for the (a) AA7449 and (b) 7040 alloy. The normalized equilibrium volume fraction calculated with the solubility product is also shown (black line) and the influence of the curvature effect of the solvus boundary is emphasized (red line).

Based on the reversion heat treatments and the dissolution behavior of the GP(I) zones a thermodynamic description has been established using the solubility product (Section 3.5.2). It is assumed that the composition of the GP(I) zones have an AlZnMg (at.) stoichiometry. This assumption agrees reasonably well with results reported in literature [42, 46, 63] as described in Section 2.3 and Appendix A. Copper was excluded from the description since it is the slowest diffusing element. Also it was shown that the activation energy of GP(I) zone nucleation and growth is close to the Mg activation energy (0.6 eV $\approx$ 58 kJ/mol) in Aluminium [32, 52]. Therefore, the GP(I) zone formation is controlled by the motion of Mg atoms [34] and not Cu. In addition, the Cu content in GP(I) zones is typically small [42] and increases with time in the precipitates [58]. The formalism described in Section 3.5.2 was used and adjusted to match the dissolution behavior observed in the reversion experiments.

Good agreement was found for values of 31 kJ/mol and 11 J/mol K for the energy and entropy of formation, respectively. These values are in a similar range of what has been reported for Mg-Cu co-clusters in AA2xxx alloys ($\Delta H^0 = 38$ kJ/mol [108]) and for GP(I) zones in an Al-Zn-Mg alloy ($\Delta H^0 = 48$ kJ/mol, $\Delta S^0 = 10$ J/mol K [95]). The solvus temperature of the GP(I) zones in the AA7449 is then 184°C (equation 3.30). This solvus temperature agrees reasonably well with results reported in literature [32].

The normalised equilibrium volume fraction obtained (black curve) with the thermodynamic description is also shown in Figure 5.7a. In addition, the influence of the curvature effect on the equilibrium volume fraction is emphasized (red curve) using the measured radius at the end of the reversion heat treatment (0.45 nm) and a typical value for the interfacial energy (0.01 J/m^2) of coherent precipitates. The thermodynamic description of the GP(I) zones is found to compare well the dissolution behavior observed for the GP(I) zones in the experiments until the η' phase appears.

The same values for the formation enthalpy and entropy were also applied to the AA7040. The resulting thermodynamic description is shown in comparison with the experimental results from the reversion heat treatments (Figure 5.7b). For the AA7040 only one reversion from the natural aged state (black points) and one reversion directly after quench (red points, normalised on the value found after 4 days of natural aging) were performed. The thermodynamic description compares also well with the experimental results. The solvus temperature of the GP(I) zones in the AA7040 amounts to 161°C.

With the present thermodynamic description, the modelling approach is limited to the solvus boundary of the GP(I) zones. A second description for the η' phase and a conversion criteria to pass from one phase to the other would be needed to describe the complete reversion heat treatments. However, during rapid coolings predominantly GP(I) zones were found to form and increase the yield strength. Therefore, focus will only lie on the GP(I) zones in the scope of this study.

5.3 Activation energy of GP(I) zone formation and dissolution

The influence of quench-induced excess vacancies on the GP(I) zone formation was studied by DSC on samples taken from the quarter thickness of the plate. The peak temperature analysis was applied to estimate the activation energies associated with the formation and dissolution of the GP(I) zones as described in Section 3.3.

DSC heating experiments were performed on samples in the T4 state. The vacancy concentration can be expected to be in equilibrium due to the long-time of natural aging, more than 1 year. The endothermic GP zone dissolution peak was observed to shift to higher temperatures with increasing heating rate. This is expected since precipitation is thermally activated process. The result of the peak temperature analysis is shown in Figure 5.8a in a $\ln(\mathrm{h}/\mathrm{T}_p^2)$ vs $-1/\overline{R}\mathrm{T}_p$ plot together with a linear fit. The estimated activation energy for the GP zone dissolution is 114 kJ/mol. This value is close to the activation energy for self-diffusion of Zn in Al-Zn-Mg and Mg in Aluminium [151].

DSC heating experiments were also performed on samples directly after quench to evaluate the activation energy of GP zone formation in the vicinity of excess vacancies. Similarly to the GP(I) zones dissolution, the exothermic GP zone formation peak shifts to higher temperatures as the heating rate increases. The result of the peak temperature analysis is shown in Figure 5.8b. The activation energy of GP(I) zone formation during heating and directly after quench is found to be 65.6 kJ/mol (0.68 eV). In literature activation energies of 0.68 eV and 0.69 eV were reported for the initial GP(I) zone formation after quench in Al-Zn-Mg and Al-Zn-Mg-Cu, respectively [45],[52]. The value is also close to the migration energy of Mg in Aluminium, which is 0.6 eV or 57.9 kJ/mol [32].

The activation energy of GP(I) zone formation is much lower than the activation energy of GP zone dissolution. This clearly shows that the excess vacancies play an important role in the GP(I) zone formation and need to be considered in the modelling of precipitation during queching.

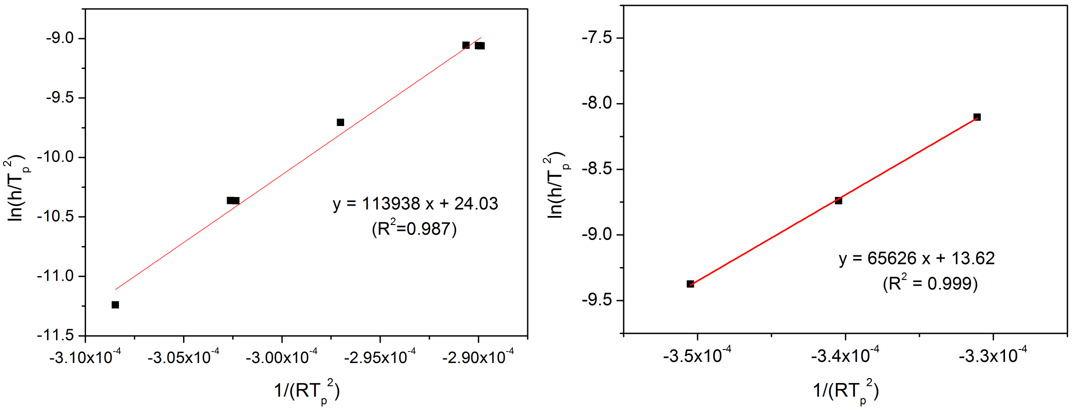

(a) (b)

Figure 5.8: Peak temperature analysis applied to GP(I) zones (a) dissolution after natural aging and (b) formation directly after quenching

5.4 Summary

In this Chapter it is shown that the dissolution behavior of the quench-induced homogeneous clusters is thermodynamically very similar to the one of GP(I) zones. Therefore, it is assumed that the quench-induced homogeneous phase are GP(I) zones. In addition, the absence of the η' formation during heating from the AQ state with the AA7040 alloy indicates that stable amount of GP(I) zones is needed to serve as nucleation site for the η' formation.

From the dissolution behavior of GP(I) zones a thermodynamic description is derived by using the solubility product and assuming a chemcial composition of AlZnMg (at.). The obtained parameter for the entropy and enthalpy of formation allow reproducing well the dissolution behaviour of GP(I) zones in the AA7449 and AA7040 alloy.

Further, the peak temperature analysis evidences that excess vacancies decrease the activation energy for GP(I) zone formation. Therefore, excess vacancies need to be taken into account for the modelling of GP(I) zones.

Main findings:

1. The AQ clusters behave thermodynamically like GP(I) zones
2. A thermodynamic description using the solubility product allows reproducing the observed dissolution behavior of GP(I) zones

3. Excess vacancies decrease the activation energy of GP(I) zone formation

6 Precipitation modeling during rapid cooling

In Chapter 4.1 it was shown that homogeneous clusters form during industrial quenching of thick plates and have a marked effect on the yield strength and therefore on residual stress level. Further, it was evidenced that the η phase also forms during quench but has a negligible influence on the residual stresses. In Chapter 5 the quench-induced clusters were characterized as GP(I) zones and a thermodynamic description was established.

This chapter reports on an approach to model the GP(I) zone formation during rapid cooling. The model parameters were calibrated against the experimental in situ SAXS of the AA7449 alloy (Section 6.1) presented in the Chapter 4.1. Further, the calibrated model is applied to rapid coolings of AA7040 alloy (Section 6.2), to the quenching of an industrial 75 mm AA7449 thick plate (Section 6.3) and to the surface cooling of different AA7xxx thick plates (Section 6.4).

6.1 GP(I) zones formation during rapid cooling of AA7449

The formation of GP(I) zones during the coolings Q1, Q3 and Q4 presented in Section 4.2 will be modelled since they present the fastest, the intermediate and the slowest cooling condition measured with the AA7449 alloy. This allows finding appropriate values for the different parameters by directly comparing the experimental and simulation results. The formation of the heterogeneous η phase is neglected.

The model parameters used to simulate the GP(I) zone formation upon rapid coolings are presented in Table 6.1. The nucleation parameters of the model were adjusted in order to have an average size of GP(I) zones that is close to the experimentally measured size. An interfacial energy of 0.01 J/m^2 and a nucleation site density of 1 • 10 ^{28} m^{-3} (if every atom is a nucleation site the density would be 6.02 • 10 ^{28} m^{-3}) were found to give results in a similar range. The values are representative of the homogeneous nucleation of coherent precipitates.

The parameter used to estimate the excess vacancies, e.g. H_0, H_m and l, were adjusted in an iterative way so that the modelling results for Q1, Q3 and Q4 match the experimental results. The outcome of the modelling depends sensitively on these three parameters and therefore, on the effective diffusion parameter.
The 68 kJ/mol found for H_0 is in between the values proposed in literature (67 and 72.24 kJ/mol) [189, 7]. The migration energy (H_m = 68.7 kJ/mol) is higher

Table 6.1: Model parameters

Parameter	Value
Interfacial energy γ	0.01 J/m^2
Nucleation site density ρ_{NS}	1 • 10 ^{28} 1/m^3
Molar volume V_m	0.7 • 10 $^{-5}$ m^3/mol
Formation energy of vacancies H_f	68000 J/mol
Migration energy of vacancies H_m	68700 J/mol
Distance between vacancy sinks l	0.25 • 10 $^{-6}$m
Number of classes for the particle size distribution	1000
Maximum radius for the particle size distribution	2 • 10 $^{-8}$ m
Time step	2 • 10 $^{-2}$ s

compared to 55.86 and 61 kJ/mol reported in the References [189, 7] but at the upper limit of the migration energy of vacancies in Al-Cu alloys (41–66.9 kJ/-mol) [190]. The characteristic diffusion length for vacancy annihilation, $l = 0.25 \bullet 10^{-6} m$, is slightly smaller than when annihilation is considered on subgrain size (1-2 μm) $l_{SG} = 0.5\text{-}1 \bullet 10^{-6} m$ or on Al$_3$Zr dispersoids $l_D = 0.45 \bullet 10^{-6}$ m (assuming spherical dispersoids, 15 nm in radius with a density of $4 \bullet 10^{19}$ m^{-3} [26]).

Effective diffusion coefficients

It was shown in the previous Section that excess vacancies have a marked influence on the activation energy of GP zone formation. Therefore, the influence of excess vacancies on kinetics is taken into account in the modelling of precipitation during cooling by using adapted diffusion coefficients. The details of the phenomenological approach were presented in Section 3.5.4.

Figure 6.1a shows the calculated supersaturation (enhancement factor S) of vacancies together with the cooling rates of Q1, Q3 and Q4. In all three cases, the vacancy concentration is in equilibrium until 250°C. Further cooling to room temperature shows an increasing supersaturation. At the conclusion of the quench, the highest supersaturation of vacancies is observed for the fastest cooling Q1. It is ten times higher than the supersaturation associated with the slowest cooling Q4.

In the following only the Mg diffusion will be considered since it is the slowest diffuser present in the AlZnMg GP(I) zones and therefore the limiting factor for the GP(I) zone formation. Similarly to the supersaturation of vacancies, the calculated

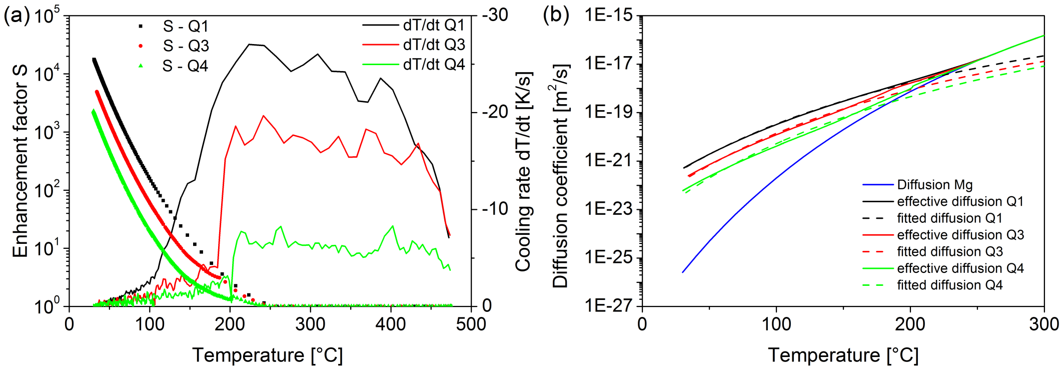

Figure 6.1: (a) Calculated supersaturation of vacancies S (solid points) together with the specific cooling rates (solid lines) of Q1, Q3 and Q4. (b) Fitted diffusion coefficients (dashed lines), calculated effective diffusion coefficients (solid lines) and the diffusion of Mg (blue line) for the three coolings Q1, Q3 and Q4.

Table 6.2: Fitted effective Mg diffusion parameters of Mg for the coolings Q1, Q3 and Q4

Cooling	$D_{0,eff}$ [m^2/s]	Q_{eff} [kJ/mol]
Q1	$4.04 \bullet 10^{-12}$	57.7
Q2	$4.58 \bullet 10^{-12}$	60.8
Q3	$7.68 \bullet 10^{-12}$	64.4

effective diffusion is highest for Q1, intermediate for Q3 and slowest for Q4 as shown in Figure 6.1b. The effective diffusion of the three coolings deviate at 250°C from the self-diffusion of Mg and is three to four orders of magnitude higher at room temperature. The fitted effective diffusion coefficients are also presented (dashed lines) for the three coolings. They represent relatively well the effective diffusion coefficients at lower temperatures (20-200°C). Yet, the quality of the fits decreases from Q1 to Q4. In the case of Q4, the diffusion is overestimated between 100 and 150°C and underestimated below 50°C. At higher temperatures the fitted diffusion deviates for the three cases markedly from the effective diffusion.

The fitted $D_{0,eff}$ and Q_{eff} for the three coolings are shown in Table 6.2. For Q1, the effective activation energy for Mg (57.7 kJ/mol) is in a realistic range and almost identical to the migration energy of Mg in Aluminium (57.9 kJ/mol) [32].

Modelling the GP(I) zone formation during rapid cooling

The volume fraction evolution of GP(I) zones during cooling Q1, Q3 and Q4 obtained from in situ SAXS results is shown in Figure 6.2a together with the modelling results. In addition, the equilibrium volume fraction of GP(I) zones is presented, which is calculated with the established thermodynamic description. In contrast to the experimental results, no GP(I) zone formation can be seen for the modelling above 184°C since this is the solvus boundary of the GP(I) zones. The precipitation observed experimentally at higher temperatures might be due to the formation of η' or the influence of vacancies on the nucleation of GP(I) zones.

The GP(I) zones form rapidly below their solvus temperature and feature a volume fraction close to the experimental values around 150°C. The volume fraction evolution modelled for Q1 compares very well against the experimental results during further cooling from 150°C to room temperature. At room temperature the volume fraction is slightly overestimated, which indicate too high diffusion parameters. For the coolings Q3 and Q4, the evolution of the volume fraction is very similar to the experimental evolution between 150 and 80°C. But further cooling leads to deviations and lower volume fraction for the modelling results. It seems that the

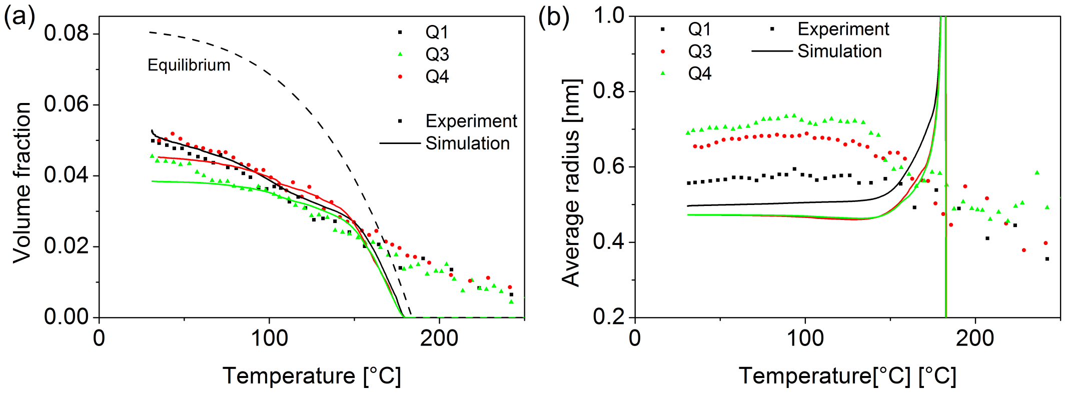

Figure 6.2: Comparison of the (a) volume fraction and (b) average radius evolution during the rapid coolings Q1, Q3 and Q4 obtained from in situ SAXS experiment (points) and precipitation modelling (solid lines). In addition, the equilibrium volume fraction of the GP(I) zones is shown as dashed black line in (a).

diffusion is too low. This discrepancy can originate from the underestimation of the diffusion observed in Figure 6.1b.

The evolution of the simulated average radius is presented in Figure 6.2b together with the measured Guinier radius. For all three coolings the simulated initial radius of the GP(I) zones is high due to the small undercooling but decreases rapidly due to a decreasing critical radius. At 150°C the average radius is higher for Q1 than for Q3 and Q4, both of them showing the same evolution. During further cooling to room temperature the average radius decreases slightly for Q1 to 0.5 nm. In contrast the average radius increases slightly for Q3 and Q4 and reaches 0.47 nm at the end of the cooling.

In general, the modelled average radius is lower compared to the experimental results. On the one hand, the experiments showed that slower cooling results in a higher radius. This is not supported by the simulations, which give the highest radius for the highest cooling rate. Further, the measured increase in average radius between 200°C and 150°C cannot be reproduced. One reason is the thermodynamic description of the GP(I) zones with the lower solvus boundary.

Measured and modelled PSD's after cooling

To allow for a more accurate comparison of the modelled and measured radii, the simulated PSD is compared with the PSD obtained from the scattering signal. The scattering signal at the end of the cooling was fitted in the q-range from 0.12 to 0.7 $\mathring{A}^{-1}$ using a lognormal size distribution and the form factor of a sphere (Section 3.4.1). The fitted PSD parameters are shown in Table 6.3 and the fitted

Table 6.3: Fitted PSD parameter for Q1,Q3 and Q4 (lognormal distribution with constant shape parameter p=1)

Cooling	number density n_0	location parameter μ	dispersion parameter s	fit quality R
Q1	$3.084 \bullet 10^{26}$	4.02	0.305	0.0341
Q3	$4.458 \bullet 10^{26}$	3.30	0.42	0.0211
Q4	$3.079 \bullet 10^{26}$	3.50	0.43	0.0327

and measured scattering signals are presented together in Figure 6.3a.
The number density of precipitates is similar for all three cases but slightly higher for Q3. The dispersion is around 0.42 for Q3 and Q4 and thereby larger compared to Q1, which shows a dispersion of 0.3. This can be associated with longer time at higher temperatures, which results in larger precipitates compared to precipitates that form at lower temperatures. In general, the dispersion of the PSD is much larger than 0.2. This indicates that the Guinier radius estimated from the SAXS signal is larger than the average radius of the PSD (Section 3.4.4).

The fitted scattering curves allow reproducing relatively well the scattering contribution due to the GP(I) zones (Figure 6.3a). The increasing intensity around $q = 0.07$ Å^{-1} of the Q3 and Q4 indicates also the presence of η' precipitates.
Figures 6.3b-d show the simulated and fitted PSD for Q1, Q3 and Q4 at the conclusion of the cooling. The PSD's are normalised to the maximum number density so that the shape of the size distributions can be compared. Overall, the agreement between the simulations and the experiments is good at small radii for the three cases. For Q1 the simulated PSD is shifted slightly to lower radii compared to the experiment results.
For larger precipitate radii, differences can be observed. The PSD's obtained from SAXS extend to larger radii compared to the simulated PSD's. This can be due to homogeneous precipitates that form between 300 and 180°C (Section 4.2). In this temperature range the formation of precipitates cannot be modelled due to the limitations of the thermodynamic description to the GP(I) zones.

Overall the agreement between the simulated and measured PSD is much better compared to the measured Guinier radius and the simulated average radius. The Guinier radius is sensitive to larger radii of the PSD ($I \propto R_g^2$) and therefore overestimates the average radius of a PSD with a large dispersion. In the case of quench induced GP(I) zones it is more favourable to compare directly the PSD's.

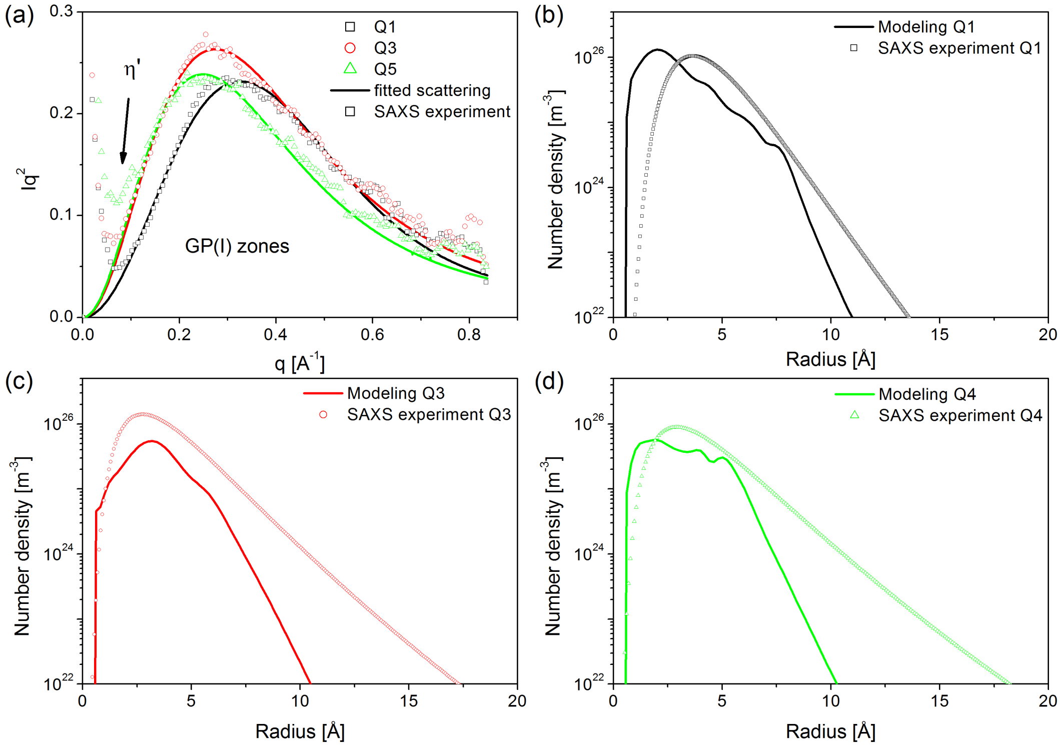

Figure 6.3: Comparison of the (a) the measured and fitted scattering signal for Q1, Q3 and Q4 at the end of the cooling. The simulated and fitted PSD's for (b) Q1, (c) Q3 and (d) Q4.

Modelling of the dissolution of GP(I) zones after cooling Q1

The dissolution of GP(I) was modelled during the heat up after the cooling Q1. The temperature vs time is shown in Figure 6.4a together with the calculated supersaturation S of vacancies. During cooling, the supersaturation of vacancies increases until room temperature. The following heat up increases the vacancy mobility and leads to a rapid decrease of the supersaturation due to annihilation on defects. At 80°C the vacancy concentration is almost at equilibrium.

Figure 6.4b shows the volume fraction evolution during the entire heat treatment. The simulation match well the experimental results during cooling, although the volume fraction evolution at near room temperature is slightly higher compared to the measured values. This was associated with a slightly overestimated diffusion at near room temperature. During the subsequent heating, the simulation shows an accelerated nucleation of GP(I) zones up to 116°C. This is in contrast to the experimental results, which evidence the dissolution of the GP(I) zones between 80

and 150°C before η' forms.
As discussed in the previous paragraph, the broad PSD leads to an overestimated measured radius compared to the simulated average radius (Figure 6.4c). During heating, the simulated radius stays constant until 116°C. When the GP(I) zones start to dissolve, the average radius increases with increasing temperatures.
The simulated increase of the average radius is similar to the measured one, except that the increase of the simulated average radius starts at higher temperatures in the simulations compared to the experiments

Figure 6.4d shows the number density of precipitates during the heat treatment. The number density was normalised to the maximum density in order to better compare its evolution in the experiments and simulations (the overestimated radius from SAXS leads to an underestimated density). The simulated and measured (calculated) number density is seen to increase during the cooling. During heating the simulated density continues to increase up to 116°C and then decreases because of the dissolution of the GP(I) zones. The measured density stays roughly constant up to 80°C and then decreases until the precipitates dissolve.

The differences between the simulations and the experiments during the heat up are explained by an overestimated effective diffusion. The high supersaturation of vacancies present after the rapid cooling decreases fast when the sample is heated up as shown in Figure 6.4a. The decrease of the effective diffusion cannot be taken into account since the effective diffusion is accounted for by adapted diffusion parameters, which are set for the cooling Q1. This is a limitation of the present model.
The phenomenological approach to calculate the vacancy concentration should be included in the model to account for the changes of the effective diffusion during different heat treatments. This would also avoid an under- or overestimated diffusion due to imperfect fitting as shown in for Figure 6.1.

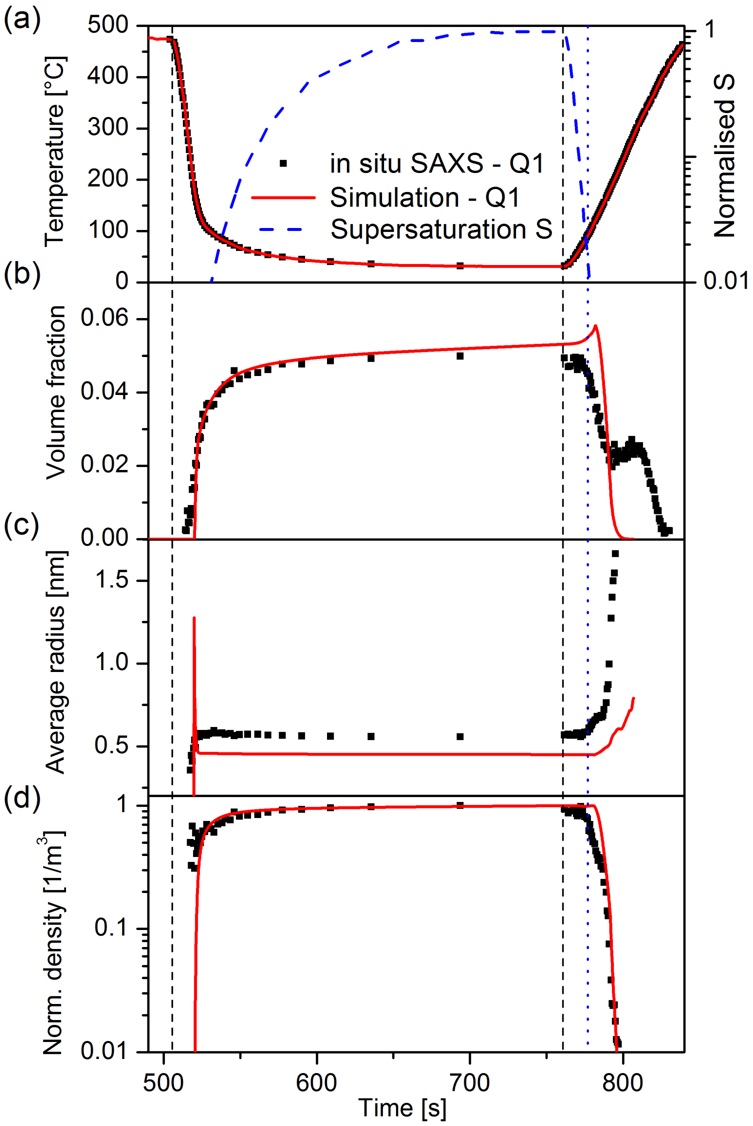

Figure 6.4: (a) Temperature vs time for the Q1 cooling and the subsequent heat up of the sample. In addition the vacancy supersaturation S is shown on the right. Evolution of (b) volume fraction, (c) average radius and (d) density of GP(I) zones during the cooling Q1 and the following heat up. The dashed black lines serve as guide to the eyes for the beginning and end of the cooling.

6.2 GP(I) zone formation during rapid cooling of AA7040

In order to test the range of application of the modelling approach and the calibrated model parameters, the cSAXS experiments performed with the AA7040 are simulated. The formation of the heterogeneous η phase is neglected and only the formation of GP(I) zones is simulated for the coolings Q11, Q13, Q15 and Q16.

Effective diffusion coefficients and modelling results
The fitted effective diffusion parameters used to simulate the GP(I) zone formation during the four cooling conditions performed during SAXS are shown in Table 6.4.

Figure 6.5a shows the simulated volume fraction evolution together with the measured results. The precipitates observed at temperatures higher than 161°C (solvus boundary) cannot be simulated due to the present thermodynamic description.
The simulated volume fraction for Q11 is overestimated to a large extent. At the end of the cooling the simulation shows roughly 6% of GP(I) zones compared to 3.5% measured with SAXS. For the other three coolings the agreement between simulations and experiments is reasonably good. At the conclusion of the coolings, the simulations show volume fractions around 2.5%, which is very close to the measured values except for Q16, which is slightly underestimated.

Table 6.4: Fitted effective diffusion parameter for the coolings Q11, Q13, Q15 and Q16

Cooling	$D_{0,eff}$ [m^2/s]	Q_{eff} [kJ/mol]
Q11	$5.46 \bullet 10^{-12}$	60.0
Q13	$3.46 \bullet 10^{-12}$	57.3
Q15	$3.49 \bullet 10^{-12}$	59.1
Q16	$4.95 \bullet 10^{-12}$	62.7

The evolution of the average radius is shown in Figure 6.5b. Generally, the simulated average size match well the measured Guinier radius for the four cooling conditions. The evolution of the radius for Q11 agrees well until 100°C. Further cooling leads to a slightly overestimated simulated radius (0.59 vs 0.54 nm). In contrast, the simulated radius of Q13 underestimates the Guinier radius below 120°C. For the two coolings Q15 and Q16 the simulated radius matches very well the measured one.

The model parameters that were calibrated for specific cooling conditions performed with the AA7449 alloy allow reproducing the experimental results obtained with the AA7040 when similar cooling conditions are applied.
Yet for faster cooling rates at higher temperatures, the simulation overestimates the volume fraction and to some extent also the precipitate size. This indicates that the chosen parameters to calculate the vacancy supersaturation and therefore the effective diffusion are not suitable for very fast cooling conditions. The set of parameters needs to be adapted to increase the range of applicability to higher cooling rates.
However, the parameters used work fairly well for intermediate cooling rates at high temperatures (5-30 K/s) for both alloys.

Measured and modelled PSD's after cooling

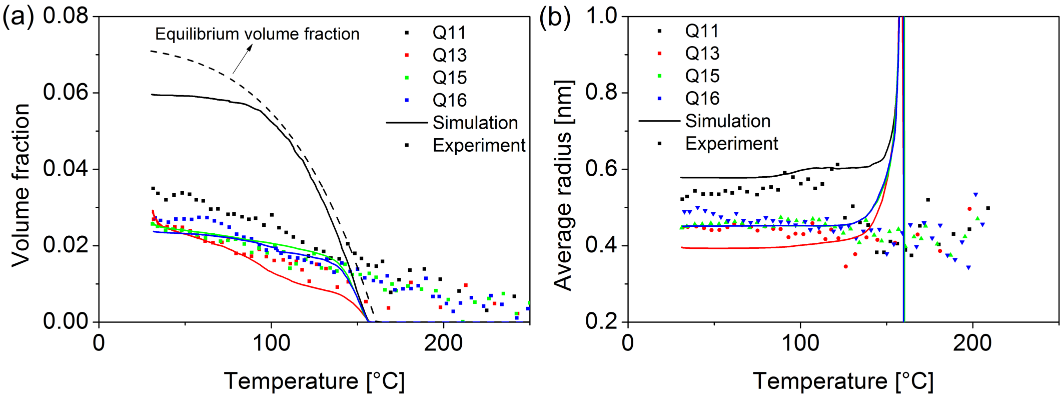

Figure 6.5: Comparison of the (a) volume fraction and (b) average radius evolution during the rapid coolings Q11, Q13, Q15 and Q16 obtained from in situ SAXS experiment (points) and precipitation modelling (solid lines). In addition, the equilibrium volume fraction of the GP(I) zones is shown as dashed black line in (a).

Similarly to the AA7449 alloy, the scattering signals at the end of the four coolings were fitted using a lognormal size distribution and the form factor of a sphere (Section 3.4.1). The obtained PSD parameters, which were fitted in the range of $0.08\ \text{Å}^{-1} \leq q \leq 0.61\ \text{Å}^{-1}$, are presented in Table 6.5.

The fitted number densities and the location parameters are close for all four coolings and only small differences can be seen. The dispersion parameter shows the largest differences. Q11 exhibits the highest dispersion of 0.341 and Q13 the lowest of 0.272.

The values obtained for the AA7040 are close to the ones fitted for the AA7449. The largest difference is seen for the dispersion. Q3 and Q4 show much larger dispersions around 0.42 compared to ≈ 0.3 for AA7040. Further, the fit quality is less good for the AA7040, which can be associated with a smaller scattered intensity.

Figures 6.6a-d show the simulated and experimental PSD's for Q11, Q13, Q15 and Q16. Generally, the agreement is good for all four cooling conditions. This is not surprising since the Guinier radius and the simulated average radius were already very close.

A good agreement is found for Q13, Q15 and Q16. In the case of Q11 the agreement is less good. The PSD obtained from the SAXS measurements extends to larger radii that are not reproduced by the simulations. Also the shape of the PSD exhibits large differences between 0.2 and 0.7 nm.

The differences in the simulated PSD's for larger radii are much smaller compared to the AA7449. In the AA7040 alloy, the homogeneous precipitation starts at lower temperatures compared to the AA7449. This can explain the narrower distribution and therefore, a better match of the simulated and fitted PSD's.

Table 6.5: Fitted PSD parameter for Q11, Q13, Q15 and Q16 (lognormal distribution with constant shape parameter p=1)

Cooling	number density n_0	location parameter μ_0	dispersion parameter s	fit quality R
Q11	$2.873 \bullet 10^{26}$	3.55	0.341	0.0532
Q13	$2.850 \bullet 10^{26}$	3.49	0.272	0.1083
Q15	$2.974 \bullet 10^{26}$	3.32	0.305	0.0529
Q16	$2.350 \bullet 10^{26}$	3.55	0.325	0.0443

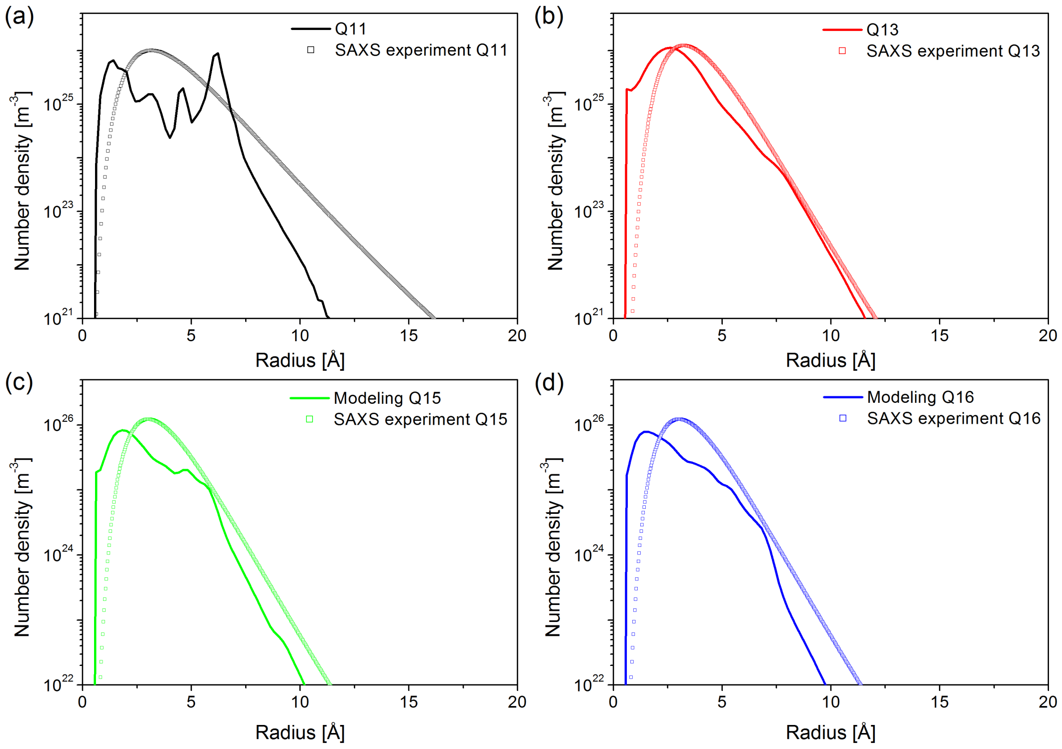

Figure 6.6: Simulated and fitted PSD's for (a) Q11 (b) Q13, (c) Q15 and (d) Q16 cooling conditions.

6.3 Application to quenching of a 75 mm AA7449 thick plate

The calibrated precipitation model is applied to the quenching of an industrial 75 mm AA7449 thick plate. The formation of GP(I) zones is simulated for selected positions in the plate and their effect on the yield stress is shown. The formation of the heterogeneous η phase is not considered because (i) the amount of η in the plate is negligible and (ii) the solute depletion is only localised and does not affect the thermodynamic driving force away from the coarse precipitates as shown in Section 4.1.2.

Effective diffusion coefficients

The fitted effective diffusion parameter obtained for the cooling conditions found in the surface, quarter and center of the 75 mm plate are presented in Table 6.6. The effective activation energies are similar with values around 60 kJ/mol for the three cases. The quarter and center position feature almost the same effective diffusion since the cooling rates are very similar as illustrated in Figure 4.11a. The effective diffusion at the surface position is roughly 4 times higher due to the fast cooling at high temperature.

Modelling results

Figure 6.7a and b show the simulated evolution of the volume fraction and the average radius during cooling at the three positions. The solid lines consider the chemical composition of the quarter position for the three positions, whereas the dashed lines show the simulation results considering the macrosegregation in the plate.

At the surface the kinetics is high. This leads to a fast decomposition of 7.9% volume fraction at room temperature, which corresponds almost the equilibrium

Table 6.6: Fitted effective diffusion parameter of Mg for the cooling conditions at the surface, quarter and center position of a 75 mm AA7449 plate

Cooling	$D_{0,eff}$ [m^2/s]	Q_{eff} [kJ/mol]
Surface	$1.40 \bullet 10^{-11}$	58.2
Quarter	$3.99 \bullet 10^{-12}$	60.2
Center	$4.00 \bullet 10^{-12}$	60.3

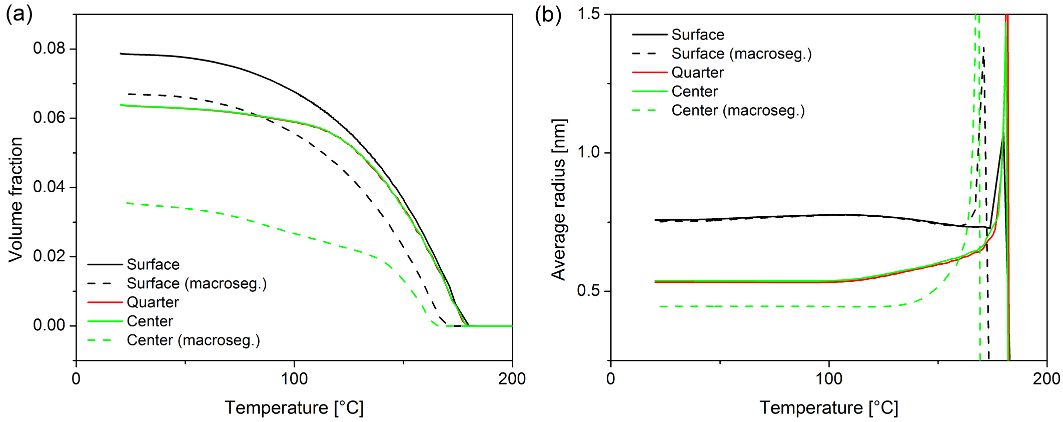

Figure 6.7: Evolution of (a) GP(I) zones volume fraction and (b) average radius as function of temperature for the surface, quarter and center position of a 75 mm thick plate of AA7449. The influence of macrosegregation is shown with dashed lines.

volume fraction. The quarter and center position show 6.4% at the conclusion of the quench. This is in a similar range compared to Q2 and Q3, which feature close cooling rates.
When the macrosegregation is considered differences can be distinguished for the surface and center position. The chemical composition is only decreased in the surface compared to the quarter position, which is evidenced by a smaller volume fraction (6.7%) and a smaller solvus boundary of GP(I) zones. The center features a considerably smaller solute content and shows the largest effect of macrosegregation. The solvus boundary is shifted to a lower temperature and the volume fraction is decreased to only 3.6% at the end of the cooling.

The evolution of the average radius is shown in Figure 6.7b. The radius is highest in the surface region with 0.76 nm compared to 0.54 nm for the quarter and center position. The macrosegregation has only little influence on the size in the surface but leads to a decreased radius of 0.44 nm at the center position.

The fact that the highest radius and volume fraction are found at the surface where the cooling rate is highest seems strange at first but agrees with the trend observed for the AA7040 alloy (Section 4.2).

The changes of the yield strength due to the GP(I) zone formation are presented in Figure 6.8. With the appearance of the precipitates, the yield strength increases rapidly for all positions. At the end of the quench, the yield strength

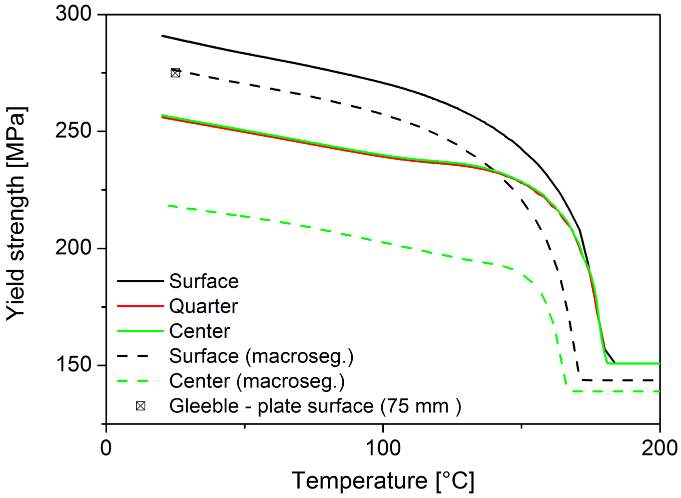

Figure 6.8: The calculated yield strength for the surface, quarter and center position during quench in the 75 mm AA7449 thick plate. The solid lines present the prediction for a constant chemical composition, whereas the dashed lines take into account the macrosegregation in the plate.

is highest at the surface position and reaches about 291 MPa. The quarter and center positions show similar yield strength of 257 MPa. When macrosegregation is considered, the yield strength is 277 MPa at the surface and 218 MPa at the center.

The residual stresses at the surface of the 75 mm AA7449 thick plate are in the range of 300-310 MPa [8, 121]. Therefore, the simulated surface yield stress of 277 MPa seems to be a good estimate keeping in mind that plastic deformation and strain hardening does occurs in the surface region. The yield strength measured with a Gleeble machine for the cooling conditions of the surface gave 275 MPa and thus is in very good agreement with the value predicted here [119].
It seems that the values used for H_0, H_m and l are also suitable for the high cooling rates in the surface region of the AA7449 plate when the correct chemical composition is used.

Figure 6.9 shows the simulated precipitation characteristics and yield strength at the end of the quench as function of the distance to the plate surface in the 75 mm AA7449 thick plate. The macrosegregation in the plate was taken into account.
Figure 6.9a presents the GP(I) zones volume fraction through the half-thickness of the plate. The highest volume fraction ($\sim 7.8\,\%$) is found at 1.5 mm below the surface and the lowest at the center ($\sim 4\,\%$). In general, the volume fraction is decreasing from the surface to the center, except for the surface position and at 20

mm below the surface. At the surface, a reduced solute content leads to a lower volume fraction. In contrast, at 20 mm below surface the increased solute content results in an increased volume fraction.
The average radius at the end of the quench is shown in Figure 6.9b as function of the distance to the surface. The average radius shows 0.75 nm at the surface and decreases towards the center, where the average radius yields 0.44 nm. Similar to the volume fraction, a slightly increased average radius is found at 20 mm below the plate surface.
The density of GP(I) zones is shown in Figure 6.9c, which shows the opposite trend compared to the average radius. The density of GP(I) zones is lowest at the surface and increases towards the plate center. Deviations are again seen for the position at 20 mm below the surface.
The yield strength is calculated from the simulation results as presented in Figure 6.9d. The highest yield strength of 288 MPa is found at 1.5 mm below the surface and the center yields the lowest yield strength of 218 MPa. The calculated yield strength in the plate at the end of the quench seems to be reasonable. textrm-Chobaut et al. reported compressive residual stresses of -300 MPa in the surface and balancing tensile residual stresses of 200 MPa in the center (cf. Subsection 2.7.1) [8]. Further, the calculated yield strength of 277 MPa at the surface compares well with the value of 275 MPa measured in the Gleeble machine [121]. In the center, the residual stress level yields 200 MPa and plastic deformation is not reported for the plate center. Therefore, the calculated yield strength of 218 MPa seems reasonable.

Unfortunately, there are no direct measurements of the precipitation characteristics in the plate after quench. But the simulated values for the radius and volume fraction are in a similar range to what have been observed with the in situ SAXS experiments with the AA7449 alloy (c.f. Section 4.2). The trend of an increased volume fraction and average radius in the surface region, where the cooling rates are highest, was also observed for the AA7040 alloy.

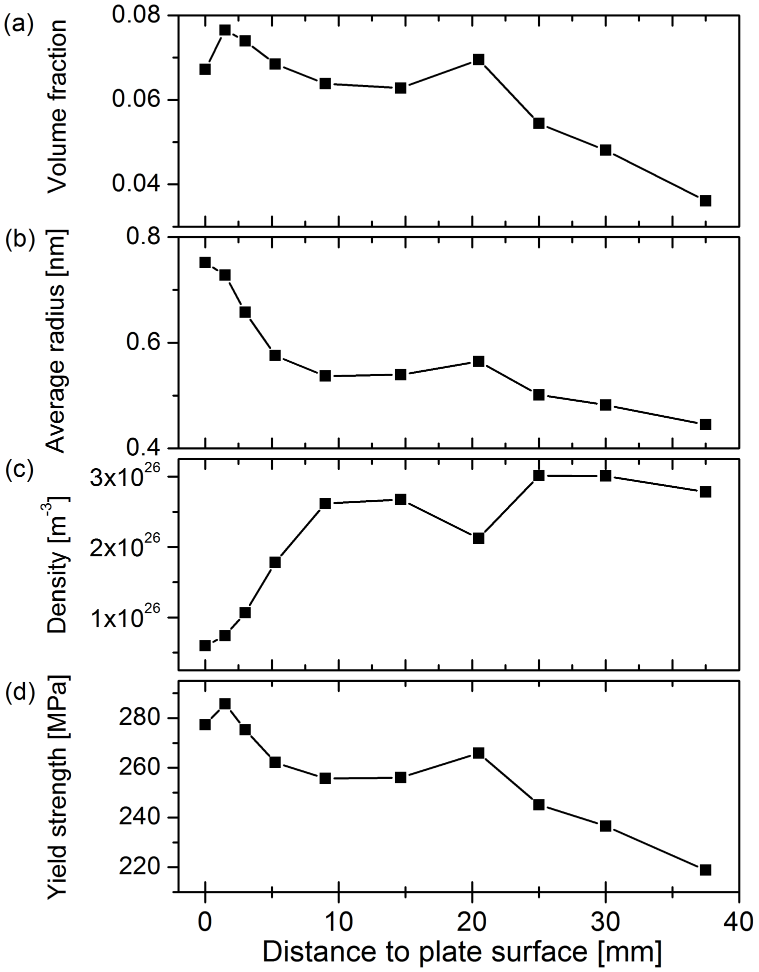

Figure 6.9: Simulated (a) volume fraction, (b) average radius and density of GP(I) zones as function the distance the plate surface at the end of the quench by taking into account macrosegregation. (d) Calculated yield strength through half-thickness of the 75mm AA7449 plate.

6.4 Application to the surface cooling of different thick plates

Chobaut et al. [121] showed that the knowledge of the yield strength at the surface of a thick plate after the quench is sufficient to simulate well the residual stress profile in a thick plate. They performed several Gleeble tests to measure the yield strength at the surface after quench in 20 mm and 75 mm AA7449 thick plates and 75 mm and 140 mm AA7040 thick plates.
Figure 6.10a shows the cooling condition at the surface of the four plates. The increasing plate thickness does not affect the cooling rates at high temperatures but leads to slower cooling rates at low temperatures below 150°C. The formation of the GP(I) zones is simulated for the four surface coolings and the yield strength is calculated. The simulated and measured yield strength are presented in Figure 6.10b. Overall, the trend of higher surface stresses for thicker plates ([120, 121]) is well reproduced by the simulations for both alloys. Very good agreement is found for the two AA7449 thick plates. In contrast, the agreement between the simulated and measured yield strength is less good for the two AA7040 thick plates. The simulations overestimate the yield strength in both cases by roughly 20 MPa.

The origin of the differences for the AA7040 alloy is not so clear since the in situ SAXS results could be reproduced reasonably well for the AA7449 alloy but also for the AA7040 alloy. One reason can be the uncertainty of the exact

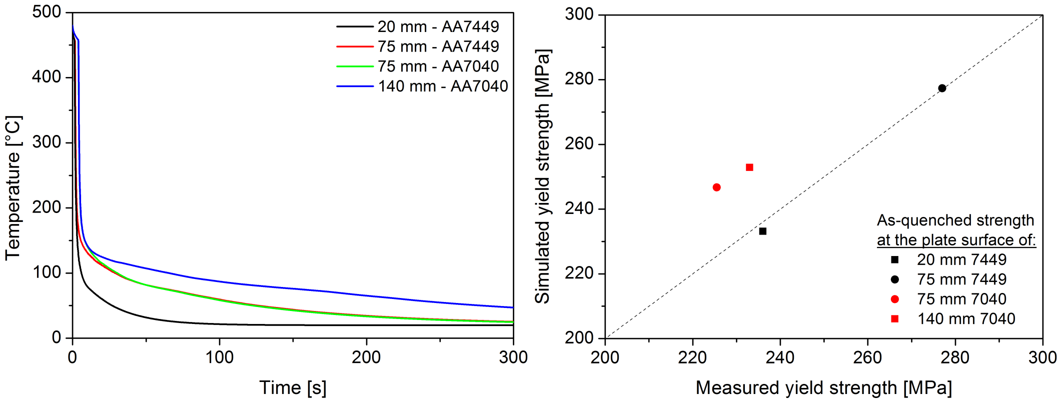

(a) (b)

Figure 6.10: The simulated and measured yield strength at the surface of two AA7449 plates with 20 and 75 mm thickness and two AA7040 plates with with 75 and 140 mm thickness.

composition of the AA7040 through the plate thickness. For the 75 mm AA7449 thick plate, the chemical composition through the half-thickness was provided by Constellium CRV, which was measured by electron micro probe analysis (EMPA). For the AA7040 the measurements have not been performed.

In addition to the calibrated model parameters, the simulations are also very sensitive to the Mg but also Zn content since it changes the solvus boundary of the GP(I) zones as it was also emphasized in the previous section. An overestimated Mg and/or Zn content of the AA7040 alloy results in a higher solvus temperature of the GP(I) zones and therefore leads to an overestimated yield strength due to a higher radius and volume fraction.

6.5 Summary

In this Chapter it was shown that the formation of GP(I) zones during rapid cooling of the AA7449 and AA7040 alloy can be simulated by using the derived thermodynamic description and by taking into account the influence of excess vacancies on the diffusion kinetics. The experimental findings of Section 4.2 are reproduced reasonably well in the temperature range where the residual stresses form during quench.

For intermediate quench rates at high temperatures (5-30 K/s) the agreement between the experimental and simulation results is good for the AA7449 and AA7040 alloy with the present set of parameters. When the cooling rates are higher at high temperature, the simulations seem to overestimated the size and volume fraction of the GP(I) zones. The parameters to calculate the evolution of the vacancy supersaturation should be adjusted in order to extent the applicability to higher cooling rates.

The agreement between the Guinier radius and the simulated average radius (and also the PSD's) is better for the AA7040 than for the AA7449 alloy. On the one hand, the homogeneous precipitation starts at 300°C in the AA7449 compared to 250°C in the AA7040 alloy. This leads to precipitates with larger radii and to a broader PSD. Subsequently, the high dispersion of the PSD leads also to a Guinier radius, which overestimates the average radius of the PSD. Therefore, model dependant analysis should be applied to estimate more accurately the size of the precipitates.

On the other hand, the thermodynamic description used here does not allow homogeneous precipitation above the solvus boundary of the GP(I) zones. Yet, in the experiments precipitation was observed above the solvus boundary. This can be due to the formation of η' precipitates or the influence of vacancies, which allow the nucleation of GP(I) zones at higher temperatures. To avoid this problem, a description for the η' phase should be used and a conversion criteria should be implemented that allows to pass from one phase to the other. This would allow predicting more accurately the formation of the quench induced precipitates and also their dissolution during heat treatments.

A thermodynamic description of the η' phase was proposed by ThermoCalc in July this year, which was too late to be considered in this study. Further, since the phenomenological approach to estimate the effective diffusion is not included in the model, the diffusion above 200°C it wrong (c.f. Figure 6.1). Therefore, the simulation of the η' is not practical.

The evolution of the volume fraction of GP(I) zones is simulated reasonably well for intermediate cooling conditions. Yet, in certain temperature regimes the volume fraction is under- or overestimated by the model. This is associated with an inaccurate effective diffusion due to the fitting of the diffusion parameters. The formalism to calculate the effective diffusion from the supersaturation of vacancies should be implemented in the model. This would enable a better accuracy of the effective diffusion and a description of the vacancy annihilation during subsequent treatments such as reversion or aging heat treatments.

The calibrated precipitation model is finally applied to predict the evolution of GP(I) zones during quench of an industrial 75 mm AA7449 thick plate. The simulated volume fraction and average radius are in a similar range to what have been observed in the cSAXS experiments during cooling. However, for high cooling rates at high temperature the predictions of the simulations seem to be overestimated in terms of size and volume fraction as it was also observed for the AA7040 alloy. Yet, the calculated yield strength at the end of the quench is very close to what one measured experimentally. Further, it is shown that macrosegregation also influences the GP(I) zone formation and has to be taken into account.

Overall, the yield strength after quench is well simulated for a 20 mm and 75 mm AA7449 thick plate but is overestimated for a 75 mm and 140 mm AA7040 thick plate. One reason for this discrepancy is that the chemical composition is not exactly known for the AA7040.

Main findings:

1. A simplified approach of only considering GP(I) zones was proposed to simulate the quench-induced precipitation in AA7xxx thick plates
2. The GP(I) zone formation is well reproduced for intermediate quench rates and in the temperature range where the residual stresses form
3. The simulated AQ surface yield strength compares well for two 7449 thick plates but is slightly overestimated for two AA7040 thick plates

Main limitations of the modelling approach:

1. The simplified approach is not suitable for cooling conditions that lead to substantial η formation
2. The formalism of the generation and annihilation of excess vacancies should be included in the model in order to (i) avoid fitting problems and (ii) simulate more complex heat treatments where excess vacancies annihilate
3. A thermodynamic description for η' precipitates is needed and conversion criteria for the transition of GP(I) zones to η' and η' to η are required
4. The influence of excess vacancies on the nucleation is not considered

7 Influence of precipitation on internal stresses formation

This Chapter concerns the question how the type-II strain formation in the aluminium matrix is influenced by different precipitation types. The microstructure dependant lattice strain formation in the aluminium matrix during tensile loading and the residual lattice strain build-up after deformation was investigated by performing in situ mechanical load-unload tests using neutron and X-ray diffraction. For this purpose, the AA7449 alloy was studied exhibiting three different microstructures. The precipitate characteristics of the three microstructures are presented in Section 7.1. The orientation specific lattice strain evolution measured in the aluminium matrix by neutron diffraction is shown in Section 7.2. Section 7.3 compares the residual lattice strain in the aluminium matrix measured by ND and XRD measurements and provides the residual lattice strain evolution for the η precipitates. Section 7.4 outlines the differences of the lattice strain formation in the aluminium matrix for the three precipitation states and discusses the impact of the type-II stresses on macroscopic residual stress measurements using the (311) reflection.

7.1 Microstructures

The internal strain formation was investigated for three different precipitation microstructures of the AA7449 alloy. The microstructural details are summarized in Table 7.1. The T4 state is characterised by GP(I) zones with a Guinier radius of 0.7 nm and a volume fraction of 7.7 %. The T6x defines a slightly overaged state that contains η' and η precipitates with a Guinier radius of 4 nm and a volume fraction of 8 %. The T7x microstructure is characterises a long-time overaged aged state, which contains only η precipitates with a Guinier radius of 15.5 nm and a volume fraction of 7.3 %. The heat treatment details were shown in Table 3.2.

Figure 7.1a illustrates XRD pattern of the three microstructures that were obtained at the ID15B beamline (ESRF). The high intensity peaks refer to the Aluminium reflections. The (111), (200), (220) and (311) peaks were used for single peak fitting as described in Section 3.7.3. In addition, several low intensity peaks can be seen. In the case of the T7x sample, the secondary peaks were identified as η peaks using the FullProf program [191]. The first three η reflections ((100), (002) and (101)) were subjected to single peak fitting. The T6x sample does not show clear secondary peaks but rather smeared or overlapping peaks. Therefore, the secondary peaks could not be identified using FullProf. One reason is the presence of η' and η precipitates, which have a slightly different crystallographic structure. Additional secondary peaks can be seen for the T4 and T6x sample. These peaks could also not be identified, but may originates from the coarse intermetallic phases reported in Section 4.1.

Table 7.1: Precipitate characteristics for the T4, T6x and T7x microstructure

State	Guinier radius [nm]	Volume fraction	Density [m^{-3}]	Yield strength [MPa]
T4	0.69	0.076	$5.41 \bullet 10^{25}$	320
T6x	4.03	0.08	$2.18 \bullet 10^{23}$	560
T7x	15.54	0.073	$4.61 \bullet 10^{21}$	250

Figure 7.1b shows typical stress strain curves for samples containing the three microstructures. The near peak aged T6x state shows the highest yield strength of about 560 MPa but only small strain hardening. The underaged T4 state and the overaged T7x state have a yield strength of about 320 and 250 MPa respectively and exhibit a higher strain hardening compared to the T6x state. Typically, load-unload mechanical test were performed to investigate also the formation of

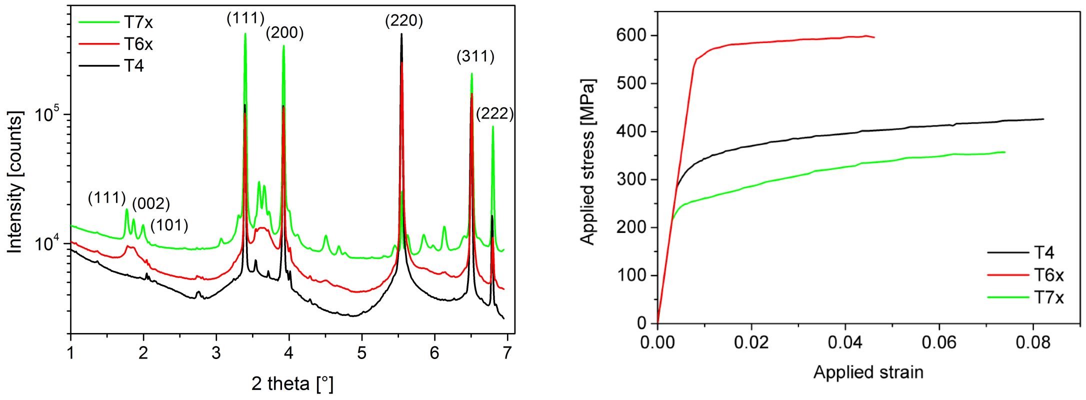

(a)

(b)

Figure 7.1: (a) X-ray diffraction pattern of the T4, T6x and T7x microstructure with the high intensity (111), (200), (220) and (311) aluminium peaks. The intensity is in log-scale to emphasize to low intensity peaks of the secondary phases such as the (111), (002) and (101) η peaks. (b) Typical stress-strain curves for the T4, T6x and T7x samples.

residual lattice strain.

7.2 Neutron diffraction

T4 microstructure

Figure 7.2 illustrates the lattice strain evolution with applied stress in the axial and transverse direction of the four investigated Aluminium reflections. When stress is applied the four directions show a linear response up to the yield strength of the material of around 320 MPa. Little differences are evidenced between the four reflections, which indicate a low elastic anisotropy. This is supported by the estimated diffraction elastic constants that are shown in Table B.1 in Appendix B. With the onset of plasticity deviations from the linear elastic behavior are observed for both directions.

In the axial direction, the (111) and (200) reflections deviate towards higher lattice strain and therefore, take more load. This is supported by residual tensile strain when the sample is unloaded. The (220) and (311) grain families show only slight deviations from the linear response and only little residual tensile strain after unloading. In the transverse direction, the (111) and (220) shift to higher compressive lattice strain in contrast to the (200) and (311), which tend into the opposite direction.

Figure 7.3 shows the lattice strain evolution as function of plastic strain. The elastic part of the macroscopic and microscopic strain response were subtracted

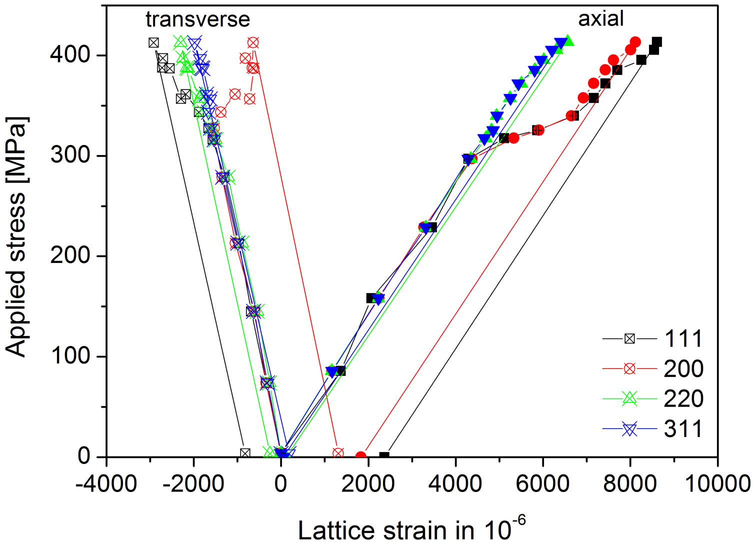

Figure 7.2: Lattice strain evolution as a function of applied stress of the (111), (200), (220) and (311) reflections of the T4 sample.

from the data, which allows observing better the deviations from linearity.

In the axial direction, the (111) and (200) reflections develop large tensile lattice strain within the first 0.5 % plastic deformation but increase only slightly with further deformation (Figure 7.3a). The (220) and (311) grain families are only little affected and show small tensile lattice strain. In the unloaded state both directions show almost no residual lattice strain.
In the transverse direction, the lattice strain increase or decrease for all four directions until 2.5 % and stays roughly constant with further deformation (Figure 7.3b). The (111) and (220) reflections show compressive lattice strain in contrast to (200) and (311) reflections that show tensile strain. In the unloaded state, the (311) reflections shows again the smallest residual lattice strain.

In the transverse direction, the observed lattice strain evolution does compare qualitatively well to the EPSC modelling results for commercially pure aluminium reported in Reference [103] and shown in Section 2.7.2. The agreement is less good in the axial direction. The EPSC model predicted compressive lattice strain for the (200) and (220) grain families in contrast to the ND results, which yield tensile lattice strains for both grain families. The observed differences can originate from differences in crystallographic texture. EPSC model considers random polycrystal, whereas the samples taken from the quarter thickness of the thick plate feature moderate texture (shear component) from the rolling process [19, 20, 21]. The texture can influences the intergranular strains and explain the observed differences. Another explanation is that the GP(I) zones influence the intergranular strains in the aluminium, which consist of layers parallel to (100) matrix planes.

T6x microstructure

The lattice strain evolution as a function of applied plastic deformation is illustrated in Figure 7.4 for the T6x sample. In addition, the residual lattice strains for different level of plastic deformation are shown in the unloaded state.

In the axial direction, all four reflections show tensile lattice strain during deformation. The (111) and (200) grain families develop high tensile strain during the initial 0.1 % plastic deformation but decrease slightly when further plastic deformation is applied. The (220) and (311) reflections show only small tensile lattice strain that increases slightly with increasing plastic deformation. In the unloaded state, the (111) and (200) directions show high residual tensile strain after small plastic deformation, which decrease substantially with further applied

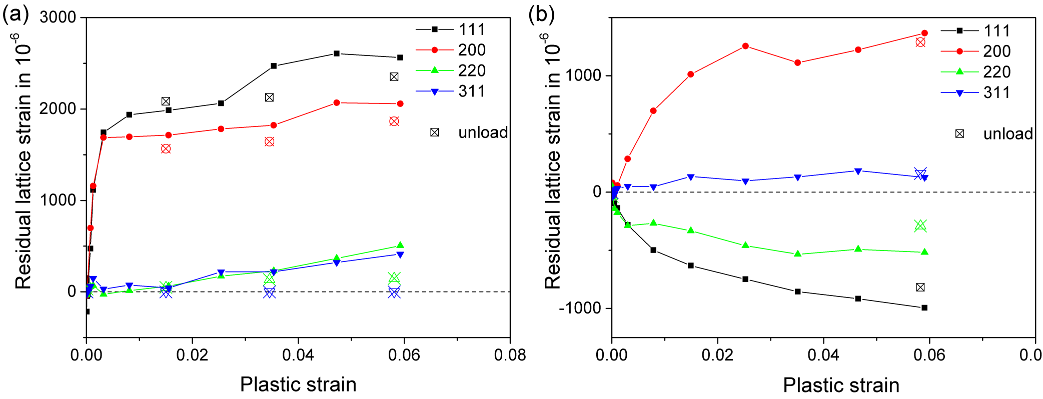

Figure 7.3: Lattice strain evolution as function of plastic deformation of the (111), (200), (220) and (311) reflections for the (a) axial and (b) transverse directions of the T4 sample. The open crossed points represent the residual lattice strain after unloading.

stress. In contrast, the (220) and (311) reflections show no residual lattice strain after small plastic deformation but increasing compressive residual strain with further plastic deformation.
In the transverse direction, the (111) reflection generates compressive lattice strain in contrast to the (200) reflections, which shows tensile lattice strain. The (220) and (311) reflection show only small compressive and tensile deviations, respectively. Similar trends are observed when the sample was unloaded and less variation are observed compared to the axial direction. The (111) and (220) reflections develop compressive residual strain and the (200) and (311) residual tensile strain.

The lattice strain evolution of the four investigated reflections of the T4 and T6x sample show qualitatively the same behaviour during deformation. But the amount of lattice strain is smaller in the T6x compared to the T4 sample, especially for the (111) and (200) direction. Further, the difference in terms of lattice strain in the loaded and unloaded state is higher in the T6x than in the T4 state. This leads to compressive residual lattice strain for the (220) and (311) directions in the T6x sample. This indicates that the precipitates have a marked influence on the lattice strain formation in the matrix.
Further, it can be stated that the (311) reflection (commonly used for macroscopic residual stress measurements) is well suited to determine the residual stresses when small shearable precipitates are present in the plate. In the unloaded state only very small residual strains were observed in the axial and transverse direction for the T4 sample. However, in the case of larger precipitates (e.g. T6x sample)

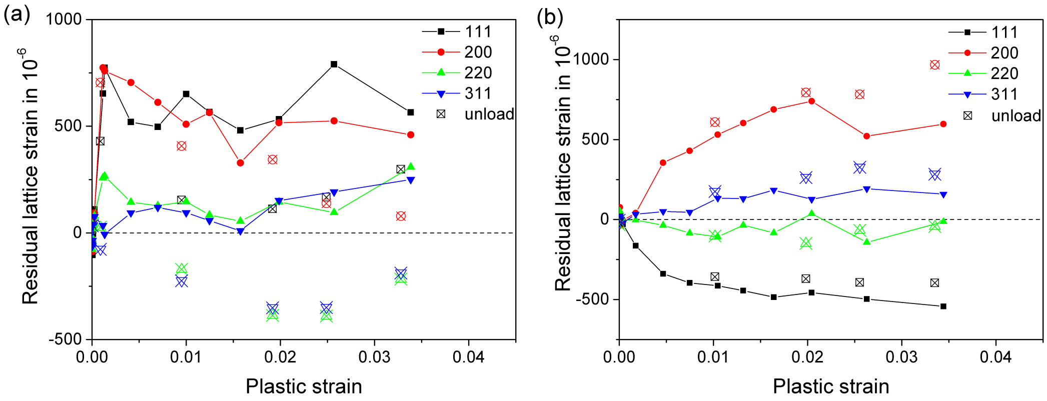

Figure 7.4: Lattice strain evolution as function of plastic deformation of the (111), (200), (220) and (311) reflections for the (a) axial and (b) transverse reflections of the T6x sample. The open points refer to the residual lattice strain after unloading.

the situation is more complex and the use of the (311) reflections may not be appropriate.

For the T7x microstructure in situ neutron diffraction measurements could not be performed since the approved beamtime at the POLDI beamline was cancelled. But in situ XRD diffraction experiments were performed as presented in the next Section.

7.3 X-ray diffraction

For the X-ray diffraction results, only the residual lattice strain evolution is shown as function of plastic deformation since the evolution during deformation is similar to the strains after unloading and only some relaxation occurs during unloading. The lattice strain evolution upon loading for the three microstructures are presented in Appendix C.

T4 microstructure

The residual lattice strains of the aluminium matrix as function of plastic deformation obtained by in situ XRD (line and solid points) and also ND (open points) are shown in Figure 7.5.

In the axial direction, the XRD measurements show qualitatively the same lattice strain response as evidenced by in situ ND (Figure 7.5a) except for the (220) reflection. After 0.5 % plastic deformation and a strong initial response, the residual lattice strain stays roughly constant when the sample is deformed further up to 6%. The (111) and (200) reflections develop tensile residual lattice strains, which are quantitatively lower than the strains measured by in situ ND. The (311) reflection shows almost the same amount of residual tensile strain. The (220) reflections exhibits residual compressive strain, which is not observed in the ND results.

In the transverse direction, similar trends can be observed for the XRD compared to ND measurements as shown in Figure 7.5b. The (111) and (200) grain families show qualitatively the same behavior but are quantitatively lower. The (311)

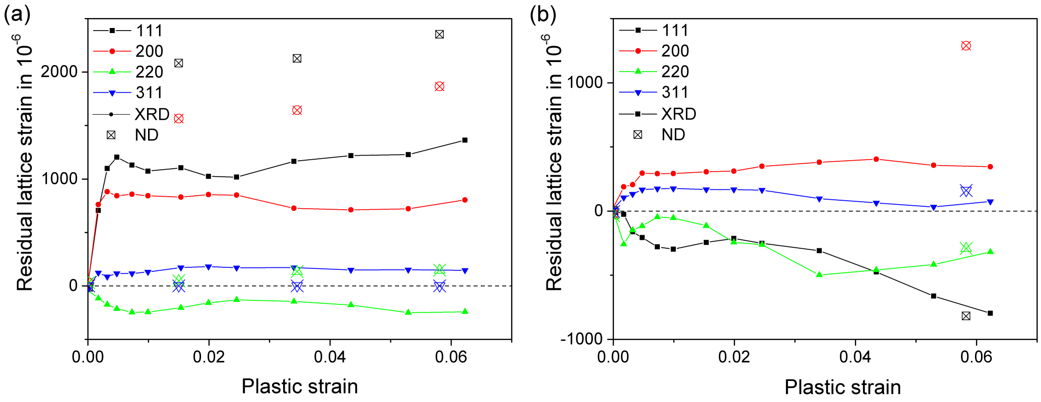

Figure 7.5: Residual lattice strain evolution as function of plastic deformation of the (111), (200), (220) and (311) reflections for the (a) axial and (b) transverse direction of the T4 sample. The X-ray diffraction (solid lines and points) and neutron diffraction (open points) results are shown.

reflection show the same behavior for in situ XRD and ND.

T6x microstructure

Figure 7.6 shows the residual lattice strain of the T6 sample in the axial and transverse direction (line and points) for different level of plastic deformation. In addition, the ND results are shown as single points.

In the same way as the T4 sample, in the axial direction the residual lattice strain evolution obtained from XRD is qualitatively similar to the ND results for up to 2 % plastic deformation. The (111) and (200) reflections show residual tensile strain, which decrease with increasing deformation. The (220) and (311) reflections show residual compressive lattice strain that increase with increasing plastic deformation. When more than 2 % plastic deformation are applied, small differences are seen for the XRD and ND results. In the ND experiments, the residual tensile lattice strain increases again for the (111) and (200) reflections and the residual compressive lattice strain decreases for the (220) and (311) reflections. This is not observed for the XRD results.

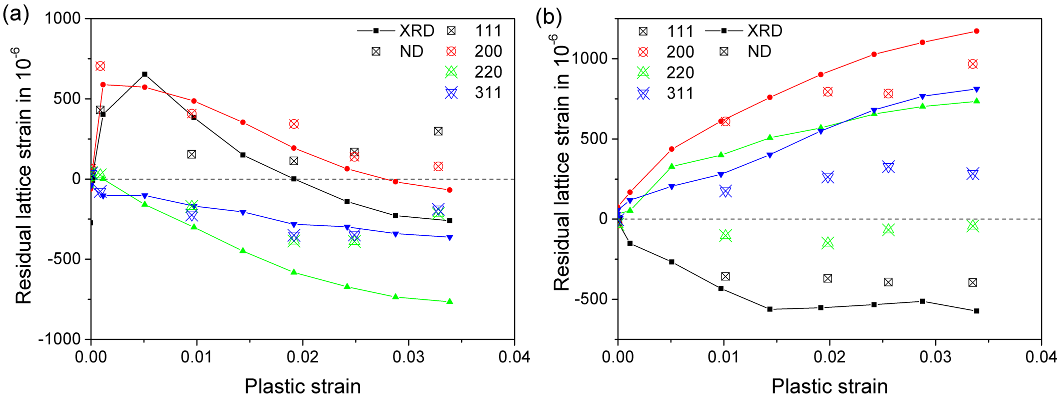

Figure 7.6: Residual lattice strain evolution as function of plastic deformation of the (111), (200), (220) and (311) reflections for the (a) axial and (b) transverse direction of the T6x sample. The X-ray diffraction (solid lines and points) and neutron diffraction (open points) results are shown.

In the transverse direction, the residual lattice strains of the (111) and (200) grain families obtained from XRD and ND are very similar. The (311) reflection the residual lattice strain deviates to larger residual tensile strain compared to the ND measurements. The XRD measurements of the (220) reflection show tensile residual strain in contrast to the ND measurements, which yield residual compressive strain.

T7x microstructure

For the T7x sample in addition to the aluminium peaks the first three reflections of the secondary η phase are fitted. Figure 7.7 shows the lattice strain of the (111), (200), (220) and (311) aluminium reflections and the (100), (002) and (101) reflections of the η precipitates during tensile testing at room temperature.

In the elastic regime, differences can be seen for the matrix and precipitate reflections. The measured elastic constants are shown in the Table B.2 in Appendix B. The aluminium shows only little elastic anisotropy, which is expected and was also observed in the neutron diffraction experiment. The three investigated η reflections show 20-40 % higher elastic constants compared to the aluminium matrix and they are also different for the three investigated directions. This implies that the η phase features an anisotropic elastic behavior.

When the yield strength is reached opposite behaviour is observed for the matrix and precipitate reflections. The (200), (220) and (311) aluminium reflections show decreasing lattice strains while the (111) continues with a linear elastic lattice strain increase. Around 300 MPa, the (111) shows deviation from the linear elastic behaviour and decreasing lattice strain while the (220) shows increasing lattice strain again. Overall, the (111) reflection shows the smallest and the (220) reflection the highest decrease in lattice strain. In contrast, with the onset of plasticity the lattice strains increase to a notably large extent for the three η reflections and

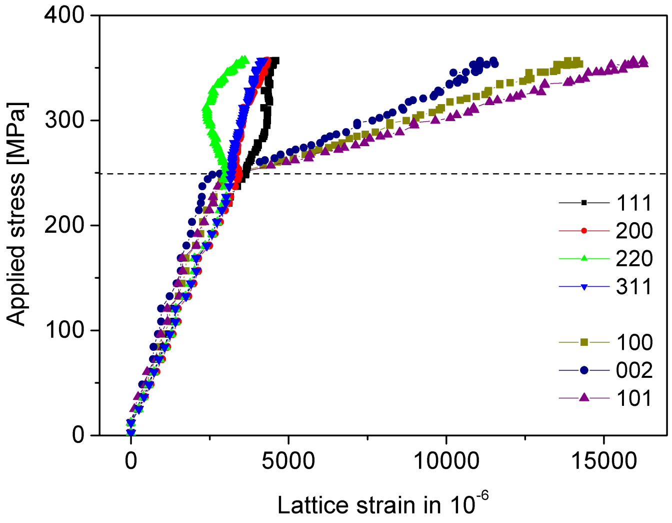

Figure 7.7: Applied stress as a function of the lattice strain of the (111), (200), (220) and (311) aluminium reflections for the axial direction of the T7x sample. In addition, the (100), (002) and (101) reflections of the η precipitates are shown.

increase further when the applied stress is increased. The (002) reflection, which is elastically the stiffest, shows the smallest increase in lattice strain. The elastically softest reflection ((101)) shows the largest increase in lattice strain. This indicates that the η phase behaves not only anisotropic in the elastic but also plastic regime.

Figure 7.9 illustrates the residual lattice strain as function of plastic deformation for the four aluminium and three η reflections in the axial and transverse direction.

In the axial direction, all four aluminium reflections show residual compressive lattice strains, which are increasing with increasing plastic deformation, except for the (220) reflection as seen in Figure 7.9a. The (111) and the (220) reflection show the smallest and the highest residual compressive lattice strain, respectively. In contrast, the three η reflections yield high residual tensile lattice strains that also increase with increasing plastic deformation. The (101) reflection yields the highest and the (200) reflection features the lowest residual tensile strain. The magnitude of the residual lattice strain of the η reflections is 5 to 11 times higher compared to the aluminium reflections.

In the transverse direction the opposite behaviour is observed. All aluminium reflections yield residual tensile lattice strain in contrast to the η reflections, which show compressive residual lattice strain.

The observed behaviour of lattice strain of opposite sign for the aluminium matrix and the η precipitates is similar to the case of high carbon and bainitic steels, which contain reinforcing cementite particles in the ferrite matrix [140, 142, 145]. It was argued that when the yield point is reached, load is transferred from the plastifying

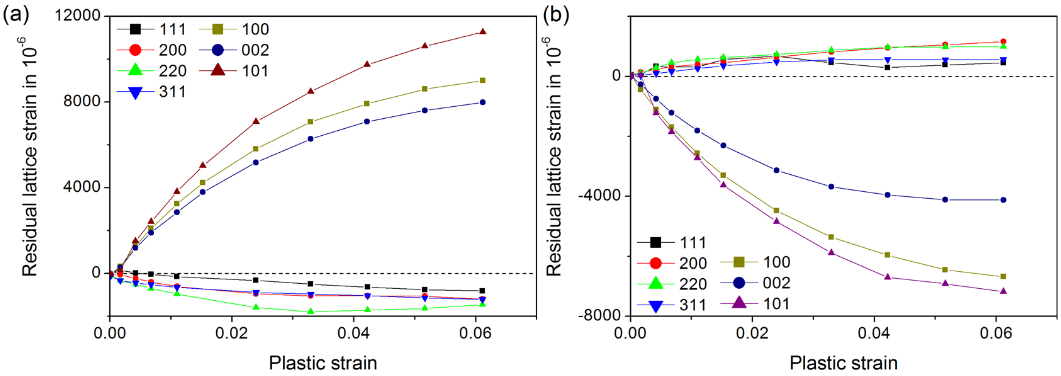

Figure 7.8: Residual lattice strain evolution as function of plastic deformation of the (111), (200), (220) and (311) aluminium and (100), (002) and (101) η reflections for the axial (a) and transverse (b) direction of the T7x sample.

ferrite matrix to the reinforcing secondary cementite phase. Although the size of the cementite particles is larger compared to the η precipitates, a reinforcing effect and a load transfer from the aluminium matrix to the η precipitates can explain the observed behaviour.

The neutron and X-ray diffraction results of the T4 and T6x samples compare overall qualitatively good but quantitative differences are often observed. Weisser et al. showed that neutron diffraction allows bulk representative and reproducible measurements due to the large illuminated gauge volume [145]. In contrast, X-ray diffraction often suffers from sample-to-sample variations, especially in the case of a large grain size with respect to the illuminated gauge volume or a heterogeneous grain microstructure [185]. The investigated aluminium samples feature a heterogeneous grain microstructure (c.f. Figure 4.1a), which can explain the quantitative differences.

7.4 Comparison of aluminium lattice strain evolution for the three microstructures

Figure 7.9a shows the residual lattice strain for the four aluminium grain families as a function of plastic deformation for the T4, T6x and T7x states, which were measured by XRD. The transverse direction is omitted because the trends are clearer in the axial direction. This is due to the fact that the transverse intergranular strains are strongly influenced by texture and the transverse grain families comprise a wide range of axial orientations.

When the residual lattice evolution is compared for the aluminium matrix with the three different precipitation types, a clear change of the residual lattice strain built-up is evidenced. On the one side, the grain families of the T4 sample show an initial increase of residual lattice in the early plastic regime and a rather constant and tensile residual lattice strain with further plastic deformation, except for the (220) reflection that shows small compressive residual lattice strain. On the other side, the grain families of the T7x sample shows a compressive residual lattice strain, which increases with increasing plastic deformation. The grain families of the T6 samples show a behavior that is in between the other two samples. The (111) and (200) reflections generate tensile residual lattice strain in the early elastic regime but show decreasing lattice strain with further plastic deformation, which leads finally to compressive residual lattice strain. Similar to the T7x sample, the (220) and (311) reflections show an increasing compressive lattice strain with applied plastic deformation, but they yield quantitatively lower values.

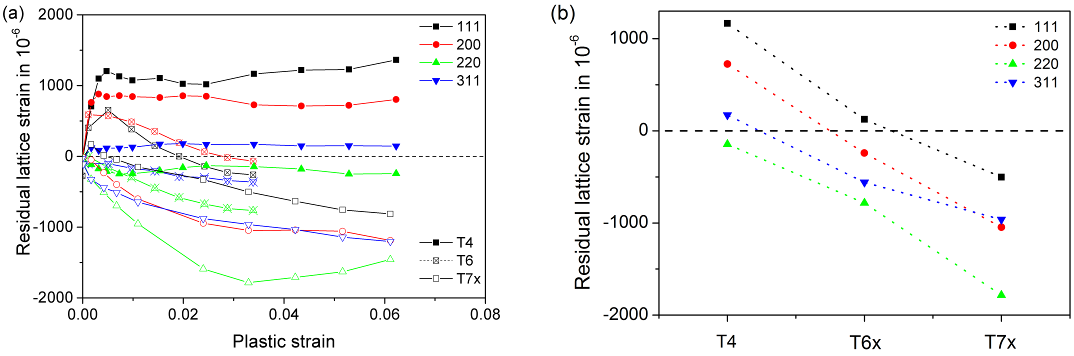

Figure 7.9: (a) Residual lattice strain as function of applied strain of the (111), (200), (220) and (311) aluminium reflection in the T4, T6x and T7x samples measured by XRD. (b) Residual lattice strains versus the precipitation state after 3.3 % plastic deformation.

The described trends are more easily observed in Figure 7.9b, which shows the residual lattice strain as function of the precipitation state for the four aluminium matrix reflections after 3.3 % plastic deformation. When the precipitation state changes from small coherent shearable GP(I) zones to intermediate semi-coherent η' precipitates to large incoherent non-shearable η precipitates, the residual lattice strain in aluminium matrix changes from tensile to compressive. This indicates that in the T4 sample the type-II strain formation is dominated by intergranular strains due to the plastic anisotropy of the aluminium matrix. In contrast, the type-II strain formation in the T7x sample is influenced by interphase strains due to the significant load transfer to the reinforcing effect of the η phase. In the T6x sample, the formation of type-II strains seems to be a mixture of intergranular and interphase strains.

In addition, the type-II strains are increasing with plastic deformation in the T6x and T7x samples in opposition to the T4 sample, where the type-II strains stay rather constant after an initial response in the early plastic regime.

Influence of type-II strains on macroscopic residual stresses

The influence of the residual lattice strain in the aluminium matrix for the three precipitation states on macroscopic residual stress measurements is emphasized in Table 7.2. The calculated type-II residual stresses are shown for the axial and transverse direction after 3.3 % plastic deformation. The (311) reflection was used for this purpose since this reflection is commonly used for macroscopic residual stress measurements [6]. The residual stress was estimated using equation 3.53 and a Young's modulus of 71 GPa and a Poisson's ratio of 0.3. The transverse strain (component ϵ_{22} and ϵ_{33}) is considered to be isotropic and equal for all direction perpendicular to the principle tensile axis (component ϵ_{11}). This allows estimating the residual stress components in the axial and transverse direction assuming no large texture variation in the directions perpendicular to the principle tensile axis (Yet, it has to be kept in mind that there is shear texture in the investigated samples).The residual stresses were calculated from the XRD measurements and also from the ND measurements using the residual lattice strains presented in Table C.1 in Appendix C.

Similarly to the residual strains, the type-II residual stresses increase for the T6x and T7x samples with higher plastic deformation. For the T4 sample, the residual stresses decrease slightly with increasing plastic deformation. The residual type-II stresses calculated from the XRD experiments are generally higher than the ones calculated from the ND measurements. This verifies that ND measurements are better suited for macroscopic residual stress measurements because of better grain statistics. The Overall, the residual stresses that originate from the type-II strains are relatively high compare to residual stresses measured after quench (up to -300 MPa in the surface) [8] or after FSW (up to 210 MPa) [192] for the AA7449 alloy. This shows that the type-II stresses can have a significant influence on macroscopic residual stress measurements, especially in the case of a high amount of larger precipitates and a considerable amount of plastic deformation.

The impact of type-II stresses on the as-quenched residual stress measurements in thick plates using neutron diffraction that have been performed in the project is negligible [8, 121]. The plastic deformation in the plate is relatively small ($<$ 1 %) and only occurs in the surface region. Further, the GP(I) zones that form during quench in the plate are similar to the T4 state. They are featuring a similar quantity but they are lower in radius. The in-situ mechanical tests using ND with the T4 sample show that the residual stress from the type-II strain amount only for 10-22 MPa. When XRD is used to estimate the macroscopic residual stresses the type-II effects (20-45 MPa) might not be negligible.

In the case of FSW, type-II strains can have a large influence on the macroscopic residual stress measurements. On the one hand, the initial precipitation microstructure before FSW can be the T6 or T7 state [89]. In the case of an initial T4 state, GP(I) zones are often dissolved and coarse homogeneous precipitates can form due a considerable long time above 200°C in the thermal cycle. One the other hand, the rotating tool introduces a high amount of plastic deformation. As it was pointed out before, in the case of T6 and T7 microstructures the residual stresses due to type-II strains are relatively high and increase with increasing plastic deformation. Therefore, the type-II stress impact on the residual stress imposed by FSW can be considered to be high and may not be neglegible, especially when

Table 7.2: Calculated stress using equation 3.53 and a Young's modulus of 71 GPa and a Poisson's ratio of 0.3 in the axial and transverse direction for an applied plastic strain ϵ_{pl} of 3.3% from the XRD and ND experiments.

Condition	Stress axial-XRD [MPa]	Stress trans-XRD [MPa]	Stress axial-ND [MPa]	Stress trans-ND [MPa]
T4	24	20	10	21
T6x	32	96	5	31
T7x	-46	36		

XRD is used (31-96 MPa) as for examples in Reference [192].

7.5 Summary

In this the Chapter the aluminium lattice strain formation during tensile testing was investigated by in situ mechanical testing using X-ray and neutron diffraction. Three different precipitation states were chosen to study to influence of different precipitation types on the lattice strain evolution in the aluminium matrix. In addition, the behaviour of the η phase was also investigated.
From the obtained results the impact of the precipitation state on the type-II strains was outlined. Further, the impact of the formation of type-II strains due to different precipitate types on macroscopic residual stress measurements was discussed.

On the microstructural length scale:
The change of the precipitation state from small coherent and shearable GP(I) zones to larger incoherent and unshearable η precipitates leads changes in the type-II strain formation in the aluminium matrix. The type-II strain formation in the aluminium matrix comprising GP(I) zones is dominated by intergranular strains due to the plastic anisotropy of the aluminium matrix. In contrast, the type-II strain formation in the aluminium matrix comprising η precipitates is clearly dominated by interphase strains due to different elastic (and plastic) properties of the two phases. The η phase has a reinforcing effect and load is transferred from the plastifying aluminium matrix to the secondary η phase. The observed behaviour is similar to the widely studied effect of the reinforcing cementite phase in the ferrite matrix.
In addition, an elastic and plastic anisotropy is observed for the η phase and their elastic constants are 20-40 % higher compared to the aluminium matrix.

The agreement between the ND and XRD measurements was qualitatively good, but quantitatively differences are often observed. The differences are associated with the heterogeneous grain microstructure of the AA7449 alloy. Similar to what was observed by Weisser et al. [145], the large illuminated gauge volume obtained by neutron diffraction gives a better grain statistics and allows observing a bulk representative behaviour. In contrast, X-ray diffraction feature less good grain statistics due to a small illuminated gauge volume, but allows measuring the behaviour of the η phase due to the high photon flux.

On the macroscopic length scale:
It is shown that type-II stresses can have a significant impact of macroscopic residual stress measurements when the commonly used (311) reflections is employed. It is evident that ND is better suited for macroscopic residual stress measurement than XRD for the rolled plates investigated here due to the larger illuminated gauge volume.
The (311) reflection is well suited to measure macroscopic RS in as-quenched plates by ND. The type-II residual stress formation is very low in the case of small shearable such as GP(I) zones, which form during quench. In the case of larger precipitates such as η and higher degrees of plastic deformation the type-II residual stress for the (311) reflection can be much higher and need to be considered. These characteristics are typical for the FSW process. Therefore, the type-II stresses are expected to have a large impact on macroscopic residual stress formation during FSW.

Main findings:

1. During tensile deformation intergranular stresses are dominant when the aluminium matrix contains small GP(I) zones, whereas interphase stresses are governing in the presence of large η precipitates
2. The η phase shows anisotropic behaviour during deformation in the elastic and plastic regime
3. The influence of type-II residual stresses on macroscopic residual stresses is increasing when (i) the size of the precipitates is increasing (such as η'/η precipitates) and (ii) the plastic deformation is increasing

8 Conclusions and outlook

8.1 Conclusions

In this thesis the influence of precipitation in the AA7449 alloy on the internal stresses at different length scales has been investigated.
On the one hand, the impact of quench-induced precipitation in thick AA7xxx plates was studied and their influence on residual stresses on the macroscopic length scale is discussed. Further, a simplified modelling approach is proposed to take into account precipitation effects on macroscopic residual stresses that occur during quench.
On the other hand, the impact of different precipitation types on the internal strain formation in the aluminium matrix on the microstructural length scale is investigated and their effect on macroscopic residual stresses emphasized.

The quench-induced precipitation in thick plates during quenching is investigated after and during quench. It is shown that quench-induced precipitation cannot be avoided in the investigated plates and alloys.
Post-mortem studies reveal the presence of heterogeneous η precipitates on grain boundaries and dispersoids. Both, the size and the volume fraction of the η phase varies through the plate thickness and are influenced by the cooling rate but also macrosegregation that is present in the plate. Overall, the volume fraction of the η precipitates is very low through the plate thickness. In addition, GP(I) zones are found in the as-quenched plates, but they form also during natural aging. The size of the GP(I) zones do not vary much through the plate thickness in contrast to the volume fraction, which is influenced by macrosegregation.
Time-resolved in situ SAXS measurements allow investigating the quench-induced

precipitation during coolings close to industrial practice. Two main precipitation reactions are observed:

1. The heterogeneous η phase forms at high temperatures. The formation of heterogeneous η during cooling is strongly linked to the cooling rate, which is evidenced by increasing size and volume fraction with decreasing cooling rate.
2. Below 300°C the formation of homogeneous hardening precipitates is evidenced. Reversion heat treatments show that the homogeneous quench-induced phase refers to GP(I) zones.

Excess vacancies are found to play a vital role in the GP(I) formation during quench. Higher cooling rates yield the same or an even higher volume fraction of GP(I) zones in comparison with slower cooling rates. These observations are associated with the presence of a larger number density of excess vacancies after fast coolings. The average radius of the clusters is typically smaller than 0.8 nm. The higher quench sensitivity of the AA7449 compared to the AA7040, which has a lower solute content, is clearly evidenced.
Both, the heterogeneous η and the GP(I) zones that form during similar cooling conditions show a smaller size and volume fraction in the AA7040 compared to the AA7449.
Further, it is shown that the two precipitation reactions alter the yield strength during quench. Whereas the low amount of η only decreases slightly the solid solution strength, the appearance of the GP(I) zones increase significantly the yield strength by precipitation strengthening. This high yield strength explains the unexpected high residual stresses in the as-quenched thick plates before the stress is relieved by stretching.

In order to simulate correctly the residual stress formation in thick plates, precipitation effects during quench need to be simulated as well. Based on the assumption that the η volume fraction is negligible, a simplified modelling approach is proposed to account only for the GP(I) zone formation during quenching of thick plates.
An Eulerian multi-class model is applied by using a thermodynamic description for GP(I) zones that is derived from several dissolution heat treatments. Further, the influence of vacancies on the diffusion kinetics is taken into account by adapted diffusion coefficients because peak temperature analysis showed a decreased activation energy of formation for GP(I) zones in the presence of excess vacancies.

The model parameters are calibrated with the in situ SAXS experiments. The derived set of parameters allowed reproducing reasonably well the experimental results in terms of volume fraction and size for the AA7449 and AA7040 alloy in a temperature range where residual stresses form during quench. But, in the experiments precipitation is also observed above the estimated solvus boundary of GP(I) zones, which cannot be simulated with the current approach. This precipitation is associated with either the formation of η' precipitates or the influence of vacancies, which allow the nucleation of GP(I) zones at higher temperatures. The implementation of a thermodynamic description for the η' phase and a conversion criteria to pass from one phase to the other would avoid this problem. Further, it is shown that it is better to compare the precipitate size in terms of the precipitate size distribution rather than the average radius. During quench, GP(I) zones form with a high dispersion of the PSD. This leads to a Guinier radius, which overestimates the average radius of the PSD. Therefore, model dependant analysis should be applied to estimate more accurately the size of the precipitates.
This calibrated model is finally applied to simulate the evolution of GP(I) zones during quench of thick plates by taking into account the macrosegregation in the plates. In the case of the AA7449 alloys the yield strength calculated at the plate surface after quench is well predicted for a 20 mm and 75 mm thick plate. In contrast, the yield strength at the plate surface is overestimated by around 20 MPa for 75 mm and 140 mm AA7040 thick plates. This discrepancy can be explained by the unknown chemical composition of the AA7040 alloy.

In situ mechanical testing using X-ray and neutron diffraction evidence that the precipitation state influences the type-II strain formation in the aluminium matrix. When small shearable GP(I) zones are present in the aluminium matrix, their type-II strain formation is dominated by intergranular strains due to the plastic anisotropy of the aluminium. In contrast, when the aluminium matrix contains large and non-shearable η precipitates the type-II strain formation in the aluminium matrix is triggered by interphase strains due to different elastic (and plastic) properties of the two phases. The η phase shows a reinforcing effect by taking load from the plastifying aluminium matrix similarly to the widely studied case of reinforcing cementite in a ferrite matrix. Further, the η phase exhibits an anisotropic behaviour in the elastic and plastic regimes during deformation and elastic constants are 20-40 % higher compared to the aluminium matrix.
Quantitative differences are observed between the ND and XRD measurements, which are associated with the heterogeneous grain microstructure of the AA7449 alloy. The large illuminated gauge volume obtained by neutron diffraction gives

a better grain statistics and allows observing a bulk representative behaviour, in contrast to X-ray diffraction, which features less good grain statistics but allows measuring the behaviour of the η phase.

The differences in the type-II strain formation can have a significant impact on macroscopic residual stress measurements. It is shown for the commonly used (311) reflection that for larger precipitates such as η and higher degrees of plastic deformation, the type-II residual stresses for the (311) reflection are significantly high and need to be considered as in the case of friction stir welding.

8.2 Outlook

Experimental characterisation

In this study, the SAXS technique is extensively used, especially to study in a time resolved manner the precipitation during rapid coolings. Several aspects of these experiments could be improved.

From the experimental side, higher cooling rates could be reached by using a cooling media such as compressed air to cool the sample instead of only using the thermal gradient that is present in the sample due to the localised heating.

The analysis of the SAXS data can also be improved. In this thesis model independent analysis is performed to a large extent. But, it is shown that the high dispersion of the quench-induced GP(I) zones PSD leads to an overestimated Guinier radius compared to the average radius of the PSD. Therefore, model dependant analysis should be applied to estimate more accurately the size of the precipitates but also their size distribution. Further, the high amount of quench-induced GP(I) zones may also permit to estimate their Zn and Cu content by analysing interference effect as proposed in Reference [63]. The knowledge of the precipitate composition during cooling is especially important for precipitation modelling, to derive thermodynamic description of metastable phases and also to estimate correctly the scattering contrast for volume fraction analysis in SAXS. This information is not accessible by 3D-APT due to the complicated and long sample preparation.

Modelling of precipitation

The simplified modelling approach proposed in this thesis is limited to cases where (i) a negligible amount of η forms and (ii) the fitted effective diffusion does not change as a function of time e.g. due to vacancy annihilation on defects.

The applicability of the model could be easily extended if the phenomenological approach to estimate the effective diffusion is included in the model:

1. On the one side, this would allow to include the heterogeneous η but also the homogeneous η' and η phases in the simulation. At the present, the diffusion coefficients are adjusted to describe the effective diffusion below 200°C (c.f. Figure 6.1b). This leads to too high diffusion at temperatures above 200°C, which also change for each cooling condition. This requires finding appropriate nucleation parameters for each cooling for each phase that is present above 200°C.

2. One the other side, the model would be able to treat more complicated heat treatments, such as (multi-step) aging and reversion heat treatments, where excess vacancies anneal out with time. This methodology is for example implemented in the MatCalc software [193, 194, 65].

Further, the option to set an initial microstructure in the model would be of advantage as it would allow simulating for example reversion heat treatment starting with GP(I) zones in order to extract physical parameter [99].

A Chemical composition of GP zones, η' and η

Table A.1: Chemical composition of Guinier Preston zones

Alloy [at.%]	Techniques & heat treatment	Composition [at.%]	Zn(+Cu) /Mg	Radius [nm]	Ref.
Al-2.3Zn-1.4Mg	TEM, APT, 1.5h@100°C	84.5Al-9Zn-7.5Mg (matrix: 0.5Zn, 0.5Mg)	1.2 (-)	2.5	[35]
Al-2.1Zn-1.7Mg	TEM, APT, 168h@60°C	85Al-8.7Zn-6.3Mg	1.4 (-)	1	[59]
Al-2.73Zn-2.59Mg-1.03Cu	TEM, APT, 0.5-24h@121°C	42-46Zn-48-45Mg-12-6Cu	1 (1.2)	0.3-1.4	[42]
Al-2.55Zn-2.89Mg-0.61Cu	APT, natural aged	35.98Al-28.56Zn-28.85Mg-5.75Cu	1 (1.2)	0.3	[46]
Al-2.42Zn-2.96Mg-0.74Cu	SAXS, natural aged	36(Zn+Cu)	- (-)	0.9	[63]
Al-Zn-Mg	First principles (VASP)	50Al-25Zn-25Mg	1 (-)	–	[56]

Table A.2: Chemical composition of η' phase

Alloy [at.%]	Techniques & heat treatment	Composition [at.%]	Zn(+Cu) /Mg	Radius [nm]	Ref.
Al-2.6Zn-1.2Mg	TEM	10.5Al-68.4Zn-25Mg	1 (-)	–	[195]
Al-2Zn-2Mg-0.2/0.5Cu	TEM, APT, 48h@120°C	52-62Al-20-25Zn-15-20Mg	1.3 (-)	9/15	[196]
Al-2.3Zn-1.4Mg	TEM, APT, 5h@100°C + 6h@120°C	55-65Al	1 (-)	6	[35]
Al-2.1Zn-1.7Mg	TEM, APT, 168h@90°C	85Al-13Zn-12Mg	1.2 (-)	2	[59]
Al-2.7Zn-2.6Mg	TEM, APT, SAXS	54.2Al-28.7Zn-17.1Mg	1.68 (-)	2.5-4.5	[197]
Al-2.3Zn-1.38Mg	TEM, APT, 5h@100°C + 6h@150°C	55-70Al-15-23Zn-15-23Mg	1 (-)	2.5-5	[198]
Al-2.35Zn-0.92Mg	TEM, APT, 6h@100°C + 15h@140°C	25Al-50Zn-25Mg	2 (-)		[96]
Al-2.73Zn-2.59Mg-1.03Cu	TEM, APT, 0.5-24h@121°C	46-53Zn-45-41Mg-11-5Cu	1.2 (1.3)	0.9-5.3	[199]
Al-2.35Zn-0.92Mg	TEM, APT, 15h@140°C	55Zn-25Mg-20Al	2.2 (-)		[164]
Al-3.6Zn-2.6Mg-0.8Cu	TEM, APT, ASAXS, T6	18Al-42Zn-33Mg-7Cu	1.3 (1.5)	3.9	[58]
Al-Zn-Mg	First principles (VASP)	6.25Al-68.75Zn-21Mg	3.27 (-)	–	[56]

Table A.3: Chemical composition of η phase

Alloy [at.%]	Techniques & heat treatment	Composition [at.%]	Zn(+Cu) /Mg	Radius [nm]	Ref.
Al-2.3Zn-1.4Mg	TEM, APT, 5h@100°C + 6h@120°C	Cigars:35-65Al	1-1.6 (-)	6	[35]
Al-2.7Zn-2.6Mg	TEM, APT, SAXS	30.4Al-44.5Zn-25.1Mg	1.77 (-)	4-11	[197]
Al-3.6Zn-2.6Mg-0.8Cu	TEM, APT, ASAXS, T6	12Al-45Zn-33Mg-10Cu	1.4 (1.7)	5	[58]
Al-3.6Zn-2.6Mg-0.8Cu	CALPHAD	12.81Al-45.74Zn-33.31Mg-8.15Cu	1.4 (1.6)	∞	[173]

Table A.4: Chemical composition of heterogeneous η phase

Alloy [at.%]	Techniques & heat treatment	Composition [at.%]	Zn(+Cu) /Mg	Radius [nm]	Ref.
Al-3.6Zn-2.6Mg-0.8Cu	TEM, APT, ASAXS, 10h@350°C	14.6Al-38.3Zn-33.3Mg-13.8Cu	1.15 (1.6)	20000	[58]
Al-3.6Zn-2.6Mg-0.8Cu	CALPHAD	Al-40.18Zn-33.36Mg-Cu	1.2 (-)	∞	[173]

B Diffraction elastic constants

Table B.1: Axial and transverse diffraction elastic constants for the T4 and T6x state from neutron diffraction

Reflection	axial T4	transverse T4	axial T6x	transverse T6x
111	67.8 ± 3.4	213.4 ± 3.0	69.7 ± 1.1	220.2 ± 3.5
200	67.2 ± 0.8	201.8 ± 9.6	67.5 ± 0.9	219.7 ± 5.2
220	76.2 ± 0.6	225.2 ± 8.9	68.8 ± 0.7	218.5 ± 4.3
311	68.1 ± 0.5	205.7 ± 5.9	68.2 ± 0.7	214.0 ± 2.5

Table B.2: Axial diffraction elastic constants

Reflection	T4	T6x	T7x	η
111	73.8 ± 1.7	67.8 ± 2.6	69.8 ± 1.3	
200	67.0 ± 3.2	69.3 ± 2.4	70.5 ± 1.2	
220	72.5 ± 4.2	74.4 ± 3.6	73.3 ± 1.4	
311	69.7 ± 3.1	70.7 ± 3.4	71.9 ± 1.2	
100				84.9 ± 1.5
002				96.5 ± 2.4
101				82.7 ± 2.6

C Lattice strain evolution during loading and residual lattice strain

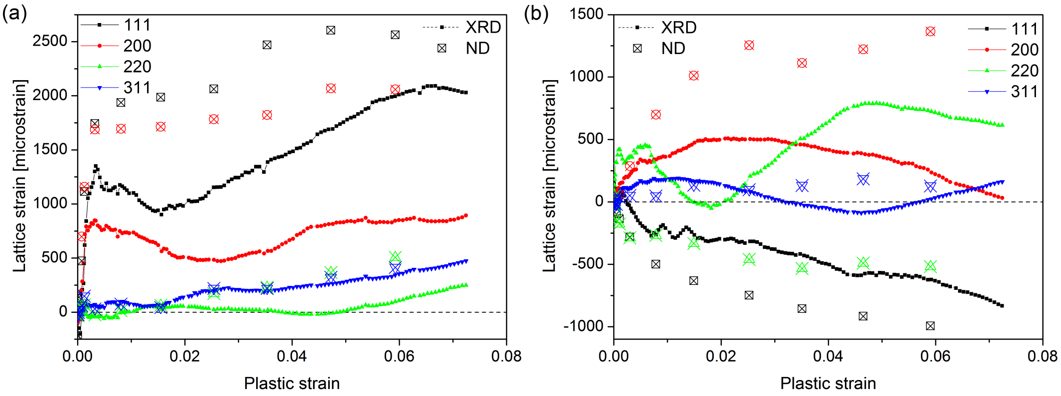

Figure C.1: Lattice strain evolution as function of plastic deformation of the (111), (200), (220) and (311) reflections for the (a) axial and (b) transverse direction of the T4 sample. The X-ray diffraction (solid lines and points) and neutron diffraction (open points) results are shown.

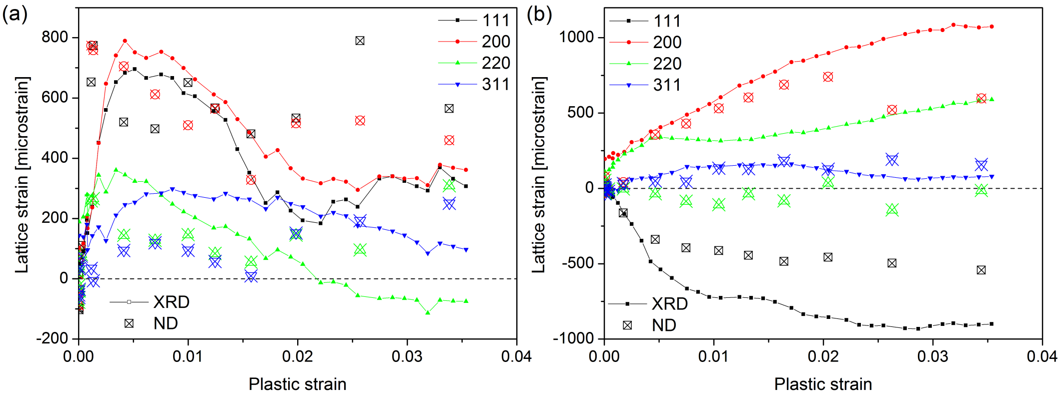

Figure C.2: Lattice strain evolution as function of plastic deformation of the (111), (200), (220) and (311) reflections for the (a) axial and (b) transverse direction of the T6x sample. The X-ray diffraction (solid lines and points) and neutron diffraction (open points) results are shown.

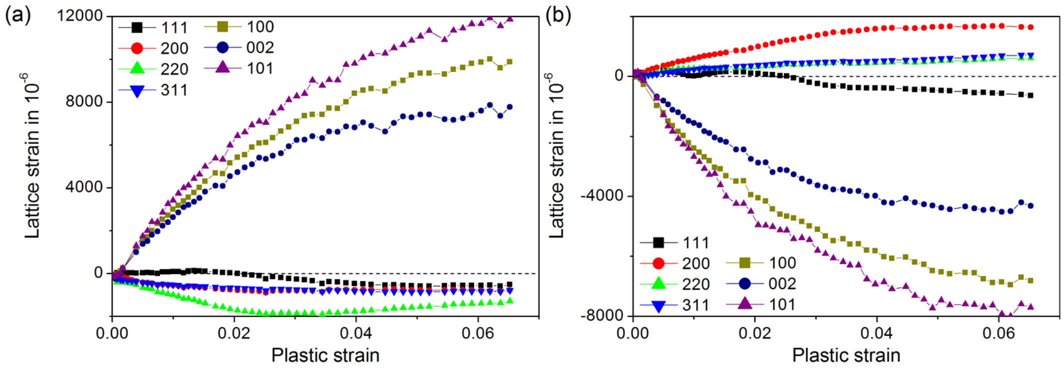

Figure C.3: Lattice strain evolution as function of plastic deformation of the (111), (200), (220) and (311) aluminium and (100), (002) and (101) η reflections for the (a) axial and (b) transverse direction of the T7x sample.

Table C.1: Residual lattice strain (in 10^{-6}) after $\approx$ 3.4% plastic deformation for the T4, T6x and T7x microstructure

Peak	T4 (ND)	T4 (XRD)	T6x (ND)	T6x (XRD)	T7x (XRD)	T7x (eta)
111 ax	2126	1166	298	-260	-502	7077
200 ax	1643	727	79	-68	-1046	6279
220 ax	134	-145	-216	-766	-1784	8486
311 ax	-29	171	-188	-363	-963	
111 tr	-818	-309	-396	-573	454	-5363
200 tr	1288	381	967	1171	819	-3677
220 tr	-291	-499	-43	734.7	870	-5882
311 tr	160	98	284	811.7	552	

Bibliography

[1] Prime, M. B. and Hill, M. R. *Scripta Materialia* **46**(1), 77–82 January (2002).

[2] Lequeu, P., Lassince, P., Warner, T., and Raynaud, G. *Aircraft Engineering and Aerospace Technology* **73**(2), 147–159 (2001).

[3] Heymes, F., Commet, B., Du Bost, B., Lassince, P., Lequeu, P., and Raynaud, G.-M. *ASM International(USA),* , 249–255 (1997).

[4] Vorster, W. and Korsunsky, A. *The Journal of Strain Analysis for Engineering Design* **44**(1), 71–91 (2009).

[5] Drezet, J.-M. and Phillion, A. B. *Metallurgical and Materials Transactions A* **41**(13), 3396–3404 October (2010).

[6] Robinson, J., Tanner, D., and Truman, C. *Strain* **50**(3), 185–207 (2014).

[7] Godard, D. *Influences de la précipitation sur le comportement thermomécanique lors de la trempe d'un alliage Al-Zn-Mg-Cu.* PhD thesis, Institut National Polytechnique de Lorraine Nancy, (1999).

[8] Chobaut, N., Repper, J., Pirling, T., Carron, D., and Drezet, J.-M. In *Proceedings of the 13th International Conference on Aluminum Alloys (ICAA13)*, number EPFL-CONF-186767, 285–291. Hasso Weiland, Anthony D. Rollett, William A. Cassada, (2012).

[9] Deschamps, A., Livet, F., and Brechet, Y. *Acta Materialia* **47**(1), 281–292 (1998).

[10] Godard, D., Archambault, P., Aeby-Gautier, E., and Lapasset, G. *Acta Materialia* **50**(9), 2319–2329 (2002).

[11] Dumont, D., Deschamps, A., Brechet, Y., Sigli, C., and Ehrström, J. *Materials Science and Technology* **20**(5), 567–576 (2004).

[12] Morgeneyer, T., Starink, M., Wang, S., and Sinclair, I. *Acta Materialia* **56**(12), 2872–2884 July (2008).

[13] Reich, M. and Kessler, O. *Materials Science and Technology* **28**(7), 769–772 (2012).

[14] Xie, Y., Zhou, T., Liu, P., and Ma, C. In *Proceedings of the 12th International Conference on Aluminium Alloys*, 2010, (2010).

[15] Zhang, Y., Milkereit, B., Kessler, O., Schick, C., and Rometsch, P. *Journal of Alloys and Compounds* **584**(0), 581 – 589 (2014).

[16] Warner, T. and Shahani, R. *ASM International(USA),* , 77–88 (1997).

[17] Warner, T. *Materials Science Forum* **519-521**, 1271–1278 (2006).

[18] Fribourg, G. *Couplages entre précipitation et plasticité dans un alliage d'aluminium 7xxx: application à des traitements thermomécaniques de réduction des distorsions.* PhD thesis, L'Institut Polytechnique de Grenoble, (2009).

[19] Engler, O., Sachot, E., Ehrström, J., Reeves, A., and Shahani, R. *Materials science and technology* **12**(9), 717–729 (1996).

[20] Becerra, G., Ramos-Grez, J., and Montecinos, J. *Journal of Materials Engineering and Performance* **18**(8), 1144–1150 February (2009).

[21] Contrepois, Q., Maurice, C., and Driver, J. *Materials Science and Engineering: A* **527**(27-28), 7305–7312 October (2010).

[22] Kamp, N., Sinclair, I., and Starink, M. *Metallurgical and Materials Transactions A* **33**(4), 1125–1136 (2002).

[23] Dumont, D., Deschamps, A., and Brechet, Y. *Materials Science and Engineering: A* **356**(1), 326–336 (2003).

[24] Starink, M., Gao, N., Davin, L., Yan, J., and Cerezo, A. *Philosophical Magazine* **85**(13), 1395–1417 (2005).

[25] Cvijović, Z., Rakin, M., Vratnica, M., and Cvijović, I. *Engineering Fracture Mechanics* **75**(8), 2115–2129 May (2008).

[26] Robson, J. and Prangnell, P. *Acta Materialia* **49**(4), 599 – 613 (2001).

[27] Robson, J., Jones, M., and Prangnell, P. *Acta Materialia* **51**(5), 1453–1468 March (2003).

[28] Mukhopadhyay, A., Shiflet, G., and Starke Jr, E. *Scripta Metallurgica et Materialia* **24**(2), 307–312 (1990).

[29] Zhang, X., Liu, W., Liu, S., and Zhou, M. *Materials Science and Engineering: A* **528**(3), 795–802 January (2011).

[30] Morere, B., Shahani, R., Maurice, C., and Driver, J. *Metallurgical and Materials Transactions A* **32**(3), 625–632 (2001).

[31] Porter, D. and Easterling, K. *Phase Transformations in Metals and Alloys.* Cheltenham, (2001).

[32] Löffler, H., Kovacs, I., and Lendvai, J. *Journal of Materials Science* **18**(8), 2215–2240 (1983).

[33] Lendvai, J. In *Materials Science Forum*, volume 217, 43–56. Trans Tech Publ, (1996).

[34] Mondal, C. and Mukhopadhyay, A. *Materials Science and Engineering: A* **391**(1), 367–376 (2005).

[35] Stiller, K., Warren, P., Hansen, V., Angenete, J., and Gjø nnes, J. *Materials Science and Engineering: A* **270**(1), 55–63 September (1999).

[36] Jiang, X., Tafto, J., Noble, B., Holme, B., and Waterloo, G. *Metallurgical and Materials Transactions A* **31**(2), 339–348 (2000).

[37] Ringer, S. and Hono, K. *Materials Characterization* **44**(1), 101–131 (2000).

[38] Ryum, N. *Zeitschrift fur Metallkunde* **66**(6), 344–346 (1975).

[39] Katz, Z. and Ryum, N. *Scripta Metallurgica* **15**(3), 265–268 (1981).

[40] Kovacs-Csetenyi, E. and Ryum, N. *Scripta Metallurgica* **15**(7), 705–707 (1981).

[41] Lendvai, J. *Crystal Research and Technology* **19**(10), 1341–1346 (1984).

[42] Sha, G. and Cerezo, A. *Acta Materialia* **52**(15), 4503–4516 (2004).

[43] Dlubek, G., Kabisch, O., Brümmer, O., and Löffler, H. *Physica status solidi (a)* **55**(2), 509–518 (1979).

[44] Lacom, W., Degischer, H., Zahra, A., and Zahra, C. *Z. Metallkd.* **73**(12), 781–785 (1982).

[45] Juhász, A., Kovács, I., Lendvai, J., and Tasnádi, P. *Journal of materials science* **20**(2), 624–629 (1985).

[46] Liddicoat, P. V., Liao, X.-Z., Zhao, Y., Zhu, Y., Murashkin, M. Y., Lavernia, E. J., Valiev, R. Z., and Ringer, S. P. *Nature communications* **1**, 63 (2010).

[47] Ungár, T., Lendvai, J., Kovacs, I., Groma, G., and Kovács-Csetényi, E. *Journal of Materials Science* **14**(3), 671–679 (1979).

[48] Berg, L., Gjø nnes, J., Hansen, V., Li, X., Knutson-Wedel, M., Waterloo, G., Schryvers, D., and Wallenberg, L. *Acta Materialia* **49**(17), 3443–3451 October (2001).

[49] Mukhopadhyay, A., Yang, Q., and Singh, S. *Acta metallurgica et materialia* **42**(9), 3083–3091 (1994).

[50] Ryum, N. *Acta Metallurgica* **16**(3), 327–332 (1968).

[51] Werenskiold, J., Deschamps, A., and Brechet, Y. *Materials Science and Engineering: A* **293**(1), 267–274 (2000).

[52] Ferragut, R., Somoza, A., and Torriani, I. *Materials Science and Engineering: A* **334**(1-2), 1–5 September (2002).

[53] Dlubek, G., Krause, R., Brümmer, O., and Plazaola, F. *Journal of materials science* **21**(3), 853–858 (1986).

[54] Kenesei, P., Horváth, G., Bernstorff, S., Ungár, T., and Lendvai, J. *Zeitschrift für Metallkunde* **97**(3), 315–320 (2006).

[55] Li, X., Hansen, V., Gjønnes, J., and Wallenberg, L. *Acta materialia* **47**(9), 2651–2659 (1999).

[56] Wolverton, C. *Acta Materialia* **49**(16), 3129–3142 September (2001).

[57] Starink, M. and Wang, S. *Acta Materialia* **51**(17), 5131–5150 (2003).

[58] Marlaud, T., Deschamps, A., Bley, F., Lefebvre, W., and Baroux, B. *Acta Materialia* **58**(1), 248–260 (2010).

[59] Maloney, S. K., Hono, K., Polmear, I. J., and Ringer, S. P. **41**(10), 1031–1038 (1999).

[60] Hansen, V., Karlsen, O. B., Langsrud, Y., and Gjø nnes, J. *Materials Science and Technology* **20**(2), 185–193 February (2004).

[61] Degischer, H., Lacom, W., Zahra, A., and Zahra, C. *Zeitschrift fur Metallkunde* **71**(4), 231–238 (1980).

[62] Deschamps, a., Fribourg, G., Bre, Ychet, Y., Chemin, J., and Hutchinson, C. *Acta Materialia* **60**(5), 1905–1916 March (2012).

[63] Deschamps, A., De Geuser, F., Horita, Z., Lee, S., and Renou, G. *Acta Materialia* **66**, 105–117 (2014).

[64] Embury, J. and Nicholson, R. *Acta Metallurgica* **13**(4), 403 – 417 (1965).

[65] Fischer, F., Svoboda, J., Appel, F., and Kozeschnik, E. *Acta Materialia* **59**(9), 3463–3472 (2011).

[66] Ber, L. *Materials Science and Engineering: A* **280**(1), 91–96 (2000).

[67] Shuey, R. T. and Tiryakioğlu, M. *Quenching Theory and Technology* (1966), 43–83 (2010).

[68] Falahati, A., Lang, P., and Kozeschnik, E. *Materials Science Forum* **706-709**, 317–322 January (2012).

[69] Deschamps, A. and Brechet, Y. *Sripta Materialia* **39**(11), 1517–1522 (1998).

[70] Archambault, P. and Godard, D. *Scripta materialia* **42**(7), 675–680 (2000).

[71] Deschamps, A., Texier, G., Ringeval, S., and Delfaut-Durut, L. *Materials Science and Engineering: A* **501**(1), 133–139 (2009).

[72] Evancho, J. and Staley, J. *Metallurgical Transactions* **5**(1), 43–47 (1974).

[73] Staley, J. T. *Materials Science and Technology* **3**(11), 923–935 November (1987).

[74] Dolan, G. and Robinson, J. *Journal of Materials Processing Technology* **153-154**, 346–351 November (2004).

[75] Flynn, R. J. and Robinson, J. *Journal of Materials Processing Technology* **153-154**, 674–680 November (2004).

[76] Ma, S., Maniruzzaman, M., MacKenzie, D., and Sisson, R. *Metallurgical and Materials Transactions B* **38**(4), 583–589 September (2007).

[77] Barlas, B. *Etude du comportement et de l'endommagement en fatigue d'alliages d'aluminium de fonderie.* PhD thesis, ole Nationale Supeure des Mines de Paris, (2004).

[78] Güzel, A., Jäger, A., Ben Khalifa, N., and Tekkaya, A. E. *Key Engineering Materials* **424**, 51–56 (2010).

[79] Rometsch, P., Starink, M., and Gregson, P. *Materials Science and Engineering: A* **339**(1-2), 255–264 January (2003).

[80] Dolan, G., Flynn, R., Tanner, D., and Robinson, J. *Materials science and technology* **21**(6), 687–692 (2005).

[81] Tiryakioğlu, M. and Shuey, R. T. *Metallurgical and Materials Transactions A* **41**(11), 2984–2991 July (2010).

[82] Robinson, J. S., Tanner, D. A., van Petegem, S., and Evans, A. *Materials Science and Technology* **28**(4), 420–430 April (2012).

[83] Perez, M. *Scripta materialia* **52**(8), 709–712 (2005).

[84] Perez, M., Dumont, M., and Acevedo-Reyes, D. *Acta materialia* **56**(9), 2119–2132 (2008).

[85] Deschamps, A. and Brechet, Y. *Materials Science and Engineering: A* **251**(1), 200–207 (1998).

[86] Sigli, C. In *Materials science forum*, volume 519, 321–326. Trans Tech Publ, (2006).

[87] Myhr, O. and Grong, O. *Acta Materialia* **48**(7), 1605–1615 April (2000).

[88] Serriere, M., Gandin, C.-A., Gautier, E., Archambault, P., and Dehmas, M. In *Materials Science Forum*, volume 396, 747–752. Trans Tech Publ, (2002).

[89] Kamp, N., Sullivan, A., Tomasi, R., and Robson, J. *Acta materialia* **54**(8), 2003–2014 (2006).

[90] Kamp, N., Sullivan, a., and Robson, J. *Materials Science and Engineering: A* **466**(1-2), 246–255 September (2007).

[91] Robson, J., Kamp, N., and Sullivan, A. *Materials and manufacturing processes* **22**(4), 450–456 (2007).

[92] Gallais, C., Denquin, A., Bréchet, Y., and Lapasset, G. *Materials Science and Engineering: A* **496**(1), 77–89 (2008).

[93] Carron, D., Bastid, P., Yin, Y., and Faulkner, R. *Technische Mechanik* **30**, 29–44 (2010).

[94] Lang, P., Wojcik, T., Povoden-Karadeniz, E., Falahati, A., and Kozeschnik, E. *Journal of Alloys and Compounds* **609**, 129–136 (2014).

[95] Nicolas, M. *Evolution de l'état de précipitation dans un alliage Al-Zn-Mg lors de traitements thermiques anisothermes et dans la zone affectée thermiquement de joints soudés.* PhD thesis, INP Grenoble, (2002).

[96] Nicolas, M. and Deschamps, A. *Acta Materialia* **51**(20), 6077–6094 (2003).

[97] Gandin, C.-A. and Jacot, A. *Acta Materialia* **55**(7), 2539–2553 April (2007).

[98] Godard, D., Archambault, P., Houin, J., Gautier, E., and Heymes, F. In *Proc. ICAA*, volume 6, 1033–38, (1998).

[99] Deschamps, A. and Perez, M. *Comptes Rendus Physique* **11**(3-4), 236–244 April (2010).

[100] Mecking, H. and Kocks, U. *Acta Metallurgica* **29**(11), 1865–1875 (1981).

[101] Deschamps, A. and Brechet, Y. *Acta Materialia* **47**(1), 293–305 (1998).

[102] Hull, D. and Bacon, D. J. *Introduction to dislocations.* Butterworth-Heinemann, (2001).

[103] Clausen, B., Lorentzen, T., and Leffers, T. *Acta Materialia* **46**(9), 3087–3098 May (1998).

[104] Haasen, P. In *Physical Metallurgy (Fourth Edition),* Haasen, R. W. C., editor, 2009 – 2073. North-Holland, Oxfordfourth edition edition (1996).

[105] Butt, M. and Feltham, P. *Journal of materials science* **28**(10), 2557–2576 (1993).

[106] Ryen, Ø., Holmedal, B., Nijs, O., Nes, E., Sjölander, E., and Ekström, H.-E. *Metallurgical and Materials Transactions A* **37**(6), 1999–2006 (2006).

[107] Gypen, L. and Deruyttere, A. *Journal of Materials Science* **12**(5), 1028–1033 (1977).

[108] Yan, J. *Strength Modelling of Al-Cu-Mg Type Alloys.* PhD thesis, University of Southampton, (2006).

[109] Deschamps, A. *Influence de la predeformation et des traitements thermique des alliages Al-Zn-Mg-Cu.* PhD thesis, INP Grenoble, (1997).

[110] Ardell, A. *Metallurgical Transactions A* **16**(12), 2131–2165 (1985).

[111] http://en.wikipedia.org/wiki/Strengtheningmechanismsofmaterials.

[112] Myhr, O. R., Grong, Ø., and Pedersen, K. O. *Metallurgical and Materials Transactions A* **41**(9), 2276–2289 (2010).

[113] Dye, D., Stone, H., and Reed, R. *Current Opinion in Solid State and Materials Science* **5**(1), 31–37 January (2001).

[114] Oliver, E. *The generation of internal stresses in single and twp phase materials.* PhD thesis, University of Manchester, (2002).

[115] Davydov, V. *In Situ Neutron Diffraction Analysis of Internal Stresses and Microstructure.* PhD thesis, Czech Technical University in Prague, (2010).

[116] Withers, P. and Bhadeshia, H. *Materials Science and Technology* **17**(4), 366–375 April (2001).

[117] Robinson, J., Hossain, S., Truman, C., a.M. Paradowska, Hughes, D., Wimpory, R., and Fox, M. *Materials Science and Engineering: A* **527**(10-11), 2603–2612 April (2010).

[118] Daymond, M. R., Hartig, C., and Mecking, H. *Acta materialia* **53**(9), 2805–2813 (2005).

[119] Chobaut, N. *Measurements and modelling of residual stress during quenching of thick heat treatable aluminium components in relation to their precipitation state.* PhD thesis, EPFL, THE N 6559 (2015).

[120] Tanner, D. and Robinson, J. *Journal of Materials Processing Technology* **153-154**, 998–1004 November (2004).

[121] Chobaut, N., Carron, D., Ars, S., Schloth, P., and Drezet, J.-M. *submitted to Journal of Materials Processing and Technology* (Nov. 2014).

[122] Van Swygenhoven, H. and Van Petegem, S. *Materials Characterization* **78**, 47–59 (2013).

[123] Clausen, B. and Lorentzen, T. *Metallurgical and Materials Transactions A* **28**(December), 2537–2541 (1997).

[124] Balagurov, A., Bokuchava, G., Schreiber, J., and Taran, Y. V. *Physica B: Condensed Matter* **234**, 967–968 (1997).

[125] Clausen, B., Lorentzen, T., Bourke, M. A., and Daymond, M. R. *Materials Science and Engineering: A* **259**(1), 17–24 (1999).

[126] Lin Peng, R., Odén, M., Wang, Y., and Johansson, S. *Materials Science and Engineering: A* **334**(1), 215–222 (2002).

[127] Clausen, B. and Bourke, M. A. M. **32**(March), 691–694 (2001).

[128] Pang, J., Holden, T., and Mason, T. *Acta Materialia* **46**(5), 1503–1518 March (1998).

[129] Chladil, H. F., Clemens, H., Zickler, G. A., Takeyama, M., Kozeschnik, E., Bartels, A., Buslaps, T., Gerling, R., Kremmer, S., Yeoh, L., et al. *International Journal of Materials Research* **98**(11), 1131–1137 (2007).

[130] Liss, K.-D., Whitfield, R. E., Xu, W., Buslaps, T., Yeoh, L. A., Wu, X., Zhang, D., and Xia, K. *Journal of synchrotron radiation* **16**(6), 825–834 (2009).

[131] Liss, K.-D. and Yan, K. *Materials Science and Engineering: A* **528**(1), 11–27 November (2010).

[132] Dehmas, M., Weisbecker, P., Geandier, G., Archambault, P., and Aeby-Gautier, E. *Journal of Alloys and Compounds* **400**(1-2), 116–124 September (2005).

[133] Tao, K., Choo, H., Li, H., Clausen, B., Jin, J.-E., and Lee, Y.-K. *Applied Physics Letters* **90**(10), 101911 (2007).

[134] Asoo, K., Tomota, Y., Harjo, S., and Okitsu, Y. *ISIJ international* **51**(1), 145–150 (2011).

[135] Hedström, P., Lienert, U., Almer, J., and Odén, M. *Scripta materialia* **56**(3), 213–216 (2007).

[136] Clarke, E. *Internal stresses and dislocation densities generated by phase transformations in steel.* PhD thesis, University of Oxford, (2008).

[137] Schloth, P., Weisser, M., Swygenhoven, H. V., Petegem, S. V., Susila, P., Sarma, V. S., Murty, B., Lauterbach, S., and Heilmaier, M. *Scripta Materialia* **66**(9), 690 – 693 (2012).

[138] Pang, J., Holden, T., and Mason, T. *The Journal of Strain Analysis for Engineering Design* **33**(5), 373–383 (1998).

[139] Johansson, J., Odén, M., and Zeng, X.-H. *Acta materialia* **47**(9), 2669–2684 (1999).

[140] Oliver, E., Daymond, M., and Withers, P. *Acta Materialia* **52**(7), 1937–1951 April (2004).

[141] Davydov, V., Lukáš, P., Strunz, P., and Kužel, R. *Journal of physics. Condensed matter : an Institute of Physics journal* **21**(9), 095407 March (2009).

[142] Young, M., Almer, J., Daymond, M., Haeffner, D., and Dunand, D. *Acta Materialia* **55**(6), 1999–2011 April (2007).

[143] Harjo, S., Tomota, Y., Neov, D., Lukas, P., Vrana, M., and Mikula, P. *ISIJ international* **42**(5), 551–557 (2002).

[144] Jia, N., Lin Peng, R., Wang, Y., Johansson, S., and Liaw, P. *Acta Materialia* **56**(4), 782–793 (2008).

[145] Weisser, M., Evans, A., Van Petegem, S., Holdsworth, S., and Van Swygenhoven, H. *Acta Materialia* **59**(11), 4448–4457 June (2011).

[146] Prangnell, P., Barnes, S., Roberts, S., and Withers, P. *Materials Science and Engineering: A* **220**(1), 41–56 (1996).

[147] Clausen, B. *Characterisation of Polycrystal Deformation.* PhD thesis, Riso National Laboratory, (1997).

[148] Milkereit, B. *Kontinuierliche Zeit-Temperatur-Ausscheidungs-Diagramme von Al-Mg-Si-Legierungen.* PhD thesis, Universitostock, (2011).

[149] Starink, M. *International Materials Reviews* **49**(3), 191–226 June (2004).

[150] Kissinger, H. E. *Analytical chemistry* **29**(11), 1702–1706 (1957).

[151] Donoso, E. *Materials Science and Engineering* **74**(1), 39–46 (1985).

[152] Garcia-Cordovilla, C. and Louis, E. *Materials Science and Engineering: A* **132**, 135–141 (1991).

[153] Dorward, R. *Materials science and technology* **15**(10), 1133–1138 (1999).

[154] Genevois, C., Deschamps, a., Denquin, a., and Doisneaucottignies, B. *Acta Materialia* **53**(8), 2447–2458 May (2005).

[155] Dumont, M., Steuwer, a., Deschamps, a., Peel, M., and Withers, P. *Acta Materialia* **54**(18), 4793–4801 October (2006).

[156] Deschamps, a., Lae, L., and Guyot, P. *Acta Materialia* **55**(8), 2775–2783 May (2007).

[157] Sullivan, a. and Robson, J. *Materials Science and Engineering: A* **478**(1-2), 351–360 April (2008).

[158] Staron, P., Vaidya, W., and Koçak, M. *Materials Science and Engineering: A* **525**(1), 192–199 (2009).

[159] Deschamps, A., Bley, F., Livet, F., and Fabregue, D. (June 2011), 37–41 (2010).

[160] Banhart, J., Chang, C. S. T., Liang, Z., Wanderka, N., Lay, M. D., and Hill, A. J. *Advanced engineering materials* **12**(7), 559–571 (2010).

[161] Deschamps, A., Bastow, T., de Geuser, F., Hill, A., and Hutchinson, C. *Acta Materialia* **59**(8), 2918–2927 May (2011).

[162] Deschamps, A. and Geuser, F. *Metallurgical and Materials Transactions A* **44**(1), 77–86 October (2012).

[163] De Geuser, F. and Deschamps, A. *Comptes Rendus Physique* **13**(3), 246–256 (2012).

[164] Dumont, M., Lefebvre, W., Doisneau-Cottignies, B., and Deschamps, A. *Acta Materialia* **53**(10), 2881–2892 (2005).

[165] https://www.sni portal.de/kfs/Methoden/smallanglescattering.php.

[166] Kohlbrecher, J. and Wagner, W. *Journal of applied crystallography* **33**(3), 804–806 (2000).

[167] Fife, J. L., Rappaz, M., Pistone, M., Celcer, T., Mikuljan, G., and Stampanoni, M. *Journal of synchrotron radiation* **19**(3), 352–358 (2012).

[168] Pauw, B. R. *Journal of Physics: Condensed Matter* **25**(38), 383201 (2013).

[169] Zhang, F., Ilavsky, J., Long, G. G., Quintana, J. P. G., Allen, A. J., and Jemian, P. R. *Metallurgical and Materials Transactions A* **41**, 1151–1158 (2010).

[170] http://www.ill.eu/instruments-support/instruments groups/groups/lss/-grasp/.

[171] Deschamps, A. and De Geuser, F. *Journal of Applied Crystallography* **44**(2), 343–352 (2011).

[172] https://kur.web.psi.ch/sans1/SANSSoft/sasfit.html.

[173] Al-DATA, ThermoTech Ltd., S. G. Y. U.

[174] Taylor, J. *Introduction to error analysis, the study of uncertainties in physical measurements*, volume 1. (1997).

[175] Yu, X. and Robinson, J. Technical report, COMPACT project, University of Limerick, (2007).

[176] Thermo-Calc version N, Foundation for Computational Thermodynamics, S.

[177] Kattner, U. R. *JOM* **49**(12), 14–19 (1997).

[178] Serriere, M. *Etude de la precipitation de dispersoides au cours du traitement d'homogenisation d'un alliage d'aluminium 3003.* PhD thesis, INPL Nancy, (2004).

[179] Fabian, H.-G. and Wolter, R. *Crystal Research and Technology* **26**(1), 93–102 (1991).

[180] Warren, B. *X-ray Diffraction.* (1990).

[181] http://www.microscopy.ethz.ch/bragg.htm.

[182] Stuhr, U. *Nuclear Instruments and Methods in Physics Research Section A: Accelerators, Spectrometers, Detectors and Associated Equipment* **545**(1-2), 319–329 June (2005).

[183] Stuhr, U., Spitzer, H., Egger, J., Hofer, A., Rasmussen, P., Graf, D., Bollhalder, A., Schild, M., Bauer, G., and Wagner, W. *Nuclear Instruments and Methods in Physics Research Section A: Accelerators, Spectrometers, Detectors and Associated Equipment* **545**(1-2), 330–338 June (2005).

[184] http://www.esrf.eu/computing/scientific/FIT2D/.

[185] Weisser, M. A. *Effect of different loading conditions on the accumulation of residual strain in a creep resistant 1diffraction study.* PhD thesis, ole Polytechnique Frale De Lausanne, (2013).

[186] http://terpconnect.umd.edu/toh/spectrum/peakfit.m.

[187] Rajek, H. *Computer simulation of precipitation kinetics in solid metals and application to the complex power plant steel CB8.* PhD thesis, Graz University of Technology, (2005).

[188] Milkereit, B., Kessler, O., and Schick, C. *Thermochimica Acta* **492**(1-2), 73–78 August (2009).

[189] Peterson, N. and Rothman, S. *Physical Review B* **1**(8), 3264 (1970).

[190] Hirosawa, S., Sato, T., Yokota, J., and Kamio, A. *Materials Transactions, JIM* **39**(1), 139–146 (1998).

[191] https://www.ill.eu/sites/fullprof/.

[192] Altenkirch, J., Steuwer, a., Peel, M., Richards, D., and Withers, P. *Materials Science and Engineering: A* **488**(1-2), 16–24 August (2008).

[193] Svoboda, J., Fischer, F., Fratzl, P., and Kozeschnik, E. *Materials Science and Engineering: A* **385**(1-2), 166–174 November (2004).

[194] Kozeschnik, E., Svoboda, J., Fratzl, P., and Fischer, F. *Materials Science and Engineering: A* **385**(1), 157–165 (2004).

[195] Auld, J. and Mck Cousland, S. *Scripta Metallurgica* **5**(9), 765–769 (1971).

[196] Hono, K., Sano, N., and Sakurai, T. *Surface science* **266**(1), 350–357 (1992).

[197] Deschamps, A., Bigot, A., Livet, F., Auger, P., Brechet, Y., and Blavette, D. *Philosophical Magazine A* **81**(10), 2391–2414 (2001).

[198] Engdahl, T., Hansen, V., Warren, P., and Stiller, K. *Materials Science and Engineering: A* **327**(1), 59–64 (2002).

[199] Sha, G. and Cerezo, A. *Acta materialia* **53**(4), 907–917 (2005).

Acronym	**Definition**
AQ	As-quenched
APT	Atom probe tomography
CALPHAD	Calculation of Phase Diagrams
CCP	Continuous cooling precipitation
CRSS	Critical resolved shear stress
DSC	Differential scanning calorimetry
EBSD	Electron back scattered diffraction
EDM	Electrical discharge machining
EDX	Energy dispersive X-ray spectroscopy
EMPA	Electron micro probe analyzer
EPSC	Elasto-plastic self-consistent modelling
EsB	Energy selective backscattered electron
ESRF	European Synchrotron Radiation Facility
ETMT	Electro-thermo mechanical testing
FE	Finite element
FSW	Friction stir welding
FWHM	Full width half maximum
GP	Guinier Preston
HAADF	High angle annular dark field
(HR)SEM	(High resolution) Scanning electron microscopy
HTC	Heat transfer coefficients
NA	Natural aging
ND	Neutron diffraction
PAS	Positron annihilation spectroscopy
PFZ	Precipitate free zone
PSD	Particle size distribution
PSI	Paul Scherrer Institut
QFA	Quench factor analysis
RS	Residual stresses
SAED	Selected area diffraction patterns
SANS	Small angle neutron scattering
SAS	Small angle scattering
SAXS	Small angle X-ray scattering
SHT	Solutionizing heat treatment
SIMAP	Science et Ingénierie des Matériaux et Procédés
SINQ	Swiss Spallation Neutron Source

SLS	Swiss Light Source
SLD	Scattering length density
SS	Supersaturated solid solution
TEM	Transmission electron microscopy
ToF	Time-of-flight
VRC	Vacancy rich clusters
XRD	X-ray diffraction

Latin symbols

b	Burgers vector
D	Diffusion
d	Grain size
ΔG	Free energy change
ΔG^*	Energy barrier for nucleation
ΔG_s	Misfit strain energy
ΔG_v,	Volume free energy
ΔG_m	Activation energy for atomic migration
f_v	Volume fraction of precipitates
k_0 & k_1	incoming and scattered wave
$D_{0,eff}$	Effective diffusion constant
$F(q, R)$	Form factor
h	Heating rate
ΔH^0	Enthalpy of formation
H_f	Formation energy of vacancies
H_m	Migration energy of vacancies
I	Intensity
K	Solute strengthening coefficient
k	Boltzmann constant
k_{GB}	Materials constant
l	Distance between vacancy sinks
M	Taylor factor
$N(R)$	Size distribution
N_{atoms}	Number of atoms
N_{max}	Nucleation sites
n	Exponent of grain boundary strengthening
p	Shape parameter of a particle size distribution
Q	Scattering invariant
q	scattering vector
Q_{eff}	Effective activation energy
$\overline{R}$	Universal gas constant
R	Precipitate radius
R_a	Atomic radius
R_g	Guinier radius
R_{max}	Pseudo Guinier radius
S	Supersaturation of vacancies

$S(q, R, f_v)$	Structure factor
s	Dispersion parameter of a particle size distribution
ΔS^0	Entropie of formation
SF	Shape factor for nucleation
T	Temperature
t	Time
T_p	Peak temperature
V	Volume
v	Growth rate
V_m	Molar volume
V_p	Precipitate volume

Greek symbols

α	Constant
$\Delta\epsilon_{hkl}$	hkl residual lattice strain
γ	Interfacial energy
λ	Wavelength
μ_0	Location parameter
μ	Shear modulus
ω	Vibration energy of atoms
ϕ	Angle between the normal of the slip plane and the direction of the applied stress
ρ_D	Dislocation density
ρ_{GB}	Grain boundary strengthening
ρ_p, ρ_m	Scattering factor density in the precipitate and matrix
$\Delta\rho$	Difference in scattering factor density of the matrix and precipitate
ρ_{NS}	Nucleation sites density
σ_{ys}	Yield strength
τ_c	Critical resolved shear stress
τ_ρ	Dislocation strengthening
τ_{SS}	Solid solution strengthening
τ_{pure}	Flow stress of pure metal
τ_{shear}	Strengthening due to shearable precipitates
τ_{Orowan}	Strengthening due to bypassing of precipitates
θ	Scattering angle
θ_w	Wetting angle
φ	Angle between the slip plane direction and the direction of the applied stress

List of Figures

2.1 Application of AA7xxx alloys in aerospace industry. 8

2.2 Typical thermomechanical treatment for 7xxx aluminium alloys (taken from [18]). 9

2.3 Schematic of the age hardening treatment consiting of (1) solutionizing heat treatment, (2) quench and (3) age hardening heat treatment, exemplarily for the Al-Cu system (pictures are taken from [31]). . . 10

2.4 Schematic of the free energy change ΔF as a function of the critical nucleus radius r due to the presence of vacancies in solute clusters [64]. 15

2.5 (a) Quench-induced η precipitates sourrounded by the characteristic precipitate free zone (PFZ) in a T6 sample [71] and (b) CCP diagram of the AA7150 alloy obtained by DSC experiments [15]. 17

2.6 (a) Free energy change ΔG associated with the nucleation of a homogeneous spherical nucleus as a function of radius r (b) Concentration profile at the interface of the precipitate and matrix [31]. 20

2.7 Schematic of an Euler-like (left) and Lagrange-like multi-class model. Step 1 and 4: disappearance of a class below the critical radius of nucleation. Step 2: flux of precipitates between neighbouring classes. Step 3 and 5: Creation of new classes. Step 6: Growth of present classes. Step 7: Reduction of interclass distance by introducing a new class. (taken from [18]). 22

2.8 Illustration of the two dislocation precipitate interaction mechanisms: precipitate shearing and precipitate bypassing (Orowan). [111]. . . . 26

2.9 Illustration of macrostresses (σ_I), intergranular microstresses (σ_{II}) and intragranular microstresses (σ_{III}) in a randomly orientated polycrystalline material [113]. 29

2.10 Residual stress in several AA7xxx thick plates measured by neutron diffraction [119]. 30

2.11 Schematic illustration of (a) intergranular microstrain evolution in a single crystalline polycrystal and (b) intergranular and interphase microstrain in a two-phase material [taken from [113]] 31

2.12 Deviations from linearity during plastic deformation of a Aluminium polycrystal in the (a) axial and (b) transverse direction [taken from [103]] 32

3.1 Schematic illustration of a SAXS [taken from [165]] 40

3.2 Schematic of the set-up used to perform the in situ SAXS experiments at the cSAXS beamline (adapted from [167]) 43

3.3 Necessary amount of corrections for SAXS raw data when the samples are without a strongly absorbing container, the X-ray beam is stable, a good detector is used and low dark current and/or natural background is present [168] 45

3.4 The influence of the dispersion s of the particle size distribution on the measured Guinier and pseudo Guinier radius (taken from [171]). 48

3.5 (a) SAXS signal in Kratky representation and (b) Evolution of the chemical composition is shown as a function of the precipitate size. 49

3.6 Influence of the sample-to-detector distance (7m and 2m) for the scattering due to large η precipitates ($R_g \approx 60$ nm) at a distance of 7m. The lowest q-value for the 2 m distance is indicated by the vertical line. 52

3.7 (a) Volume fraction, (b) Guinier radius, (c) cooling rates and (d) calculated density as function of temperature for two similar cooling conditions performed at the cSAXS beamline. 53

3.8 Scattering curves and the corresponding error for (a) two SANS experiments with a 75 mm AA7449 plate on samples with 1 mm and 19.1 mm distance to the surface and (b) SAXS during cooling performed at the cSAXS beamline for scattering spectras taken at 343, 162 and 32°C. 54

3.9 Calculated yield strength for the AA7449 and AA7040 is compared to the measured yield strength in the Gleeble machine [121] for different cooling conditions. The root mean square deviation (RMSD) is 9.6 MPa. 64

3.10 Schematic illustration of Bragg's law: constructive interference of incoming waves k_0 after diffraction at a particular set of lattice planes (hkl) under a diffraction angle θ fulfilling Bragg's law. The scattering vector q is defined as k_0-k_1. (Image adapted from [181]) . 65

3.11 Illustration of the tensile samples used for the (a) neutron diffraction and (b) X-ray diffraction experiments. 67

3.12 (a) Stress-strain curve of a T4 sample investigated at the POLDI beamline. The inset shows the stress relaxation during holding time for the diffraction measurement. 68

3.13 The (111) diffraction peak (blue points) measured at the ID15B beamline is shown together with the peak fit (red line) and the fitted results in the upper part. The lower part shows the residuals of the fit. 69

4.1 (a) EBSD image showing the heterogeneous grain microstructure with unrecrystallized and recrystallized grains (black lines = large angle boundaries), which show no subgrains (grey lines= low angle boundaries) structure. (b) HR-SEM image in EsB mode illustrating the presence of intermetallic Al_7Cu_2Fe, (white) and Mg_2Si (black) phases in the AA7449 alloy. Both samples were taken from the quarter thickness of the plate and L defines the rolling direction. . . 72

4.2 High resolution SEM image of the AA7449 material taken from the center of the 75mm plate evidences phase contrast at grain boundaries and inside the grains. The size of that phase is much smaller in comparison with the intermetallic phases. 73

4.3 (a) HAADF-TEM image showing GP(I) zones (white contrast) and their characteristic diffuse spots in the (b) selected area diffraction pattern in Al $\langle 100 \rangle$ projection. 75

4.4 (a) Kratky plots of the T4 state for two sample-to-detector distances and (b) the Guinier radius and volume fraction measured in 1 mm steps through the half plate thickness of the 75 mm AA7449 plate. . 76

4.5 TEM images revealing η precipitation on (a) grain and subgrain boundaries and on (b) Al_3Zr or $Al_3(Cr,Ti)$ dispersoids. The TEM-EDX reveals that the $Al_3(Cr,Ti)$ dispersoids are more effective nucleation sites inside the grain. 77

4.6 (a) TEM images illustrating the position of the EDX map across a η precipitate. (b) The concentration profiles of Zn, Mg, Cu and Al evidence the different solute content in the matrix and the precipitate and the solute depletion around the precipitate. 78

4.7 (a) Guinier radius and volume fraction of the precipitates in the T6 and perfect T6 state as a function of the distance to plate surface. (b) The volume fraction of heterogenous η precipitates through the plate thickness. 79

4.8 (a) SANS curves due to heterogeneous η precipitates is represented by Kratky plots for different positions in the plate, where 0 mm presents the plate surface and 37.5 mm the plate center. (b) Guinier radius and volume fraction of the heterogenous η precipitates as a function of the position in the 75 mm AA7449 plate. 80

4.9 (a) The scattering curves are shown as a function of the different positions in the plate, where 71 mm represents the plate center. (b) The Guinier radius and volume fraction of the η precipitates is shown as function of the position in the 142 mm AA7040 plate. . . 81

4.10 Kratky plot (Iq^2 vs. q) as a function of temperature for the fastest quench (FQ). The Iq^2 scale in the Kratky plot was set to a value of 0.25 in order to better observe the evolution at high-q. 83

4.11 (a) The cooling rates of 5 different coolings (the fastest Q1 to the slowest Q5) for the AA7449 are illustrated along with the measured (b) Guinier radius and (c) volume fraction. (d) The calculated precipitate density during cooling is shown. 84

4.12 (a) The cooling rates of 6 different coolings (the fastest Q11 to the slowest Q16) for the AA7040 (b) Guinier radius, (c) volume fraction and (d) precipitate density. 86

4.13 (a) Cooling curves of Q12 and Q14 for the AA7040 with the corresponding (b) Guinier radius, (c) volume fraction and the (d) calulated precipitate density during cooling and natural aging. The vertical dashed lines show the beginning of the natural aging. 88

4.14 Cooling curves and corresponding evolution of the η volume fraction for the AA7449(a,c) and AA7040 (b,d). 90

4.15 (a) DSC heat flow curves with varying cooling rates from 2 to 80 K/min for the 7449 alloy. (b) Precipitation heat for the two precipitation reactions as a function of the the cooling rate. 91

4.16 (a) cooling rates, (b) volume fraction, (c) Guinier radius and (d) precipitate density as a function temperature for selected AA7449 and AA7040 coolings. 93

4.17 Comparison of the (a) cooling curves and the (b) evolution of volume fraction of η during cooling for the AA7449 (solid lines) and AA7040 (dashed lines). 94

4.18 Continuous cooling precipitation diagram using cooling rates in the DSC (dashed grey lines) and SAXS (dashed black lines). The start and end temperature of η are indicated by full and open black squares. The η' phase is described by full and open red circles and the clusters by blue triangles that are full and open. The full black, red and blue lines serve as guide to the eyes for the temperature regime, where the η, η' and clusters are forming. 96

4.19 (a) Calculated yield strength of the AA7449 for the coolings Q1 to Q5 together with the yield strength measured with the Gleeble machine (crossed points) using the cooling paths Q1 and Q3. (b) Calculated yield strength of the AA7040 for the coolings Q11 to Q16 together with the measured yield strength using the cooling paths Q16 and at the surface of a 75 mm AA7040 plate(crossed points). . 97

5.1 (a) Heat treatment details with corresponding heating and cooling rates applied to the AA7449 sample. Evolution of the scattering signal upon heating after (b) natural aging and (c) directly after the cooling Q1. Kratky plots are shown as function of temperature, where the intensity (scale bar) scales in z-direction. The intensity was scaled to a value of 0.25, which presents the intensity maximum of the high-q peak in (c). 105

5.2 Evolution of the Guinier radius (black) and volume fraction (blue) upon heating is shown for the T4 state (full symbols) and the as-quenched Q1 state (open symbols). The size of the smaller precipitates is also shown as red symbols without line. 106

5.3 Evolution of the scattering signal upon heating is shown starting with an initial microstructure of (a) GP(I) zones that formed during 4 days of natural aging and (b) AQ clusters that formed during cooling. The intensity is scaled to a value of 0.12 in order to observe better the scattering peak in (b). 107

5.4 The changes of the Guinier radius (black) and volume fraction (blue) during heating to the solutionizing temperature are presented for the T4 state (full symbols) and the as-quenched Q13 state (open symbols). 108

5.5 (a) Kratky plot at selected temperatures during heating of the surface sample at 5 K/min. (b) Evolution of the Guinier radius and volume fraction during heating with 1K/min (red) and 5K/min (black) of a quarter thickness sample in the T4 state. 111

5.6 The evolution of the Guinier radius and the volume fraction during heating with (a) 5 K/min and (b) 1 K/min is compared for the surface (black), quarter (red) and center (green) position. 112

5.7 Normalised volume fraction evolution during several reversion heat treatments for the (a) AA7449 and (b) 7040 alloy. The normalized equilibrium volume fraction calculated with the solubility product is also shown (black line) and the influence of the curvature effect of the solvus boundary is emphasized (red line). 113

5.8 Peak temperature analysis applied to GP(I) zones (a) dissolution after natural aging and (b) formation directly after quenching . . . 116

6.1 (a) Calculated supersaturation of vacancies S (solid points) together with the specific cooling rates (solid lines) of Q1, Q3 and Q4. (b) Fitted diffusion coefficients (dashed lines), calculated effective diffusion coefficients (solid lines) and the diffusion of Mg (blue line) for the three coolings Q1, Q3 and Q4. 121

6.2 Comparison of the (a) volume fraction and (b) average radius evolution during the rapid coolings Q1, Q3 and Q4 obtained from in situ SAXS experiment (points) and precipitation modelling (solid lines). In addition, the equilibrium volume fraction of the GP(I) zones is shown as dashed black line in (a). 123

6.3 Comparison of the (a) the measured and fitted scattering signal for Q1, Q3 and Q4 at the end of the cooling. The simulated and fitted PSD's for (b) Q1, (c) Q3 and (d) Q4. 125

6.4 (a) Temperature vs time for the Q1 cooling and the subsequent heat up of the sample. In addition the vacancy supersaturation S is shown on the right. Evolution of (b) volume fraction, (c) average radius and (d) density of GP(I) zones during the cooling Q1 and the following heat up. The dashed black lines serve as guide to the eyes for the beginning and end of the cooling. 127

6.5 Comparison of the (a) volume fraction and (b) average radius evolution during the rapid coolings Q11, Q13, Q15 and Q16 obtained from in situ SAXS experiment (points) and precipitation modelling (solid lines). In addition, the equilibrium volume fraction of the GP(I) zones is shown as dashed black line in (a). 129

6.6 Simulated and fitted PSD's for (a) Q11 (b) Q13, (c) Q15 and (d) Q16 cooling conditions. 131

6.7 Evolution of (a) GP(I) zones volume fraction and (b) average radius as function of temperature for the surface, quarter and center position of a 75 mm thick plate of AA7449. The influence of macrosegregation is shown with dashed lines. 133

6.8 The calculated yield strength for the surface, quarter and center position during quench in the 75 mm AA7449 thick plate. The solid lines present the prediction for a constant chemical composition, whereas the dashed lines take into account the macrosegregation in the plate. 134

6.9 Simulated (a) volume fraction, (b) average radius and density of GP(I) zones as function the distance the plate surface at the end of the quench by taking into account macrosegregation. (d) Calculated yield strength through half-thickness of the 75mm AA7449 plate. . . 136

6.10 The simulated and measured yield strength at the surface of two AA7449 plates with 20 and 75 mm thickness and two AA7040 plates with with 75 and 140 mm thickness. 137

7.1 (a) X-ray diffraction pattern of the T4, T6x and T7x microstructure with the high intensity (111), (200), (220) and (311) aluminium peaks. The intensity is in log-scale to emphasize to low intensity peaks of the secondary phases such as the (111), (002) and (101) η peaks. (b) Typical stress-strain curves for the T4, T6x and T7x samples. 145

7.2 Lattice strain evolution as a function of applied stress of the (111), (200), (220) and (311) reflections of the T4 sample. 146

7.3 Lattice strain evolution as function of plastic deformation of the (111), (200), (220) and (311) reflections for the (a) axial and (b) transverse directions of the T4 sample. The open crossed points represent the residual lattice strain after unloading. 148

7.4 Lattice strain evolution as function of plastic deformation of the (111), (200), (220) and (311) reflections for the (a) axial and (b) transverse reflections of the T6x sample. The open points refer to the residual lattice strain after unloading. 149

7.5 Residual lattice strain evolution as function of plastic deformation of the (111), (200), (220) and (311) reflections for the (a) axial and (b) transverse direction of the T4 sample. The X-ray diffraction (solid lines and points) and neutron diffraction (open points) results are shown. 150

7.6 Residual lattice strain evolution as function of plastic deformation of the (111), (200), (220) and (311) reflections for the (a) axial and (b) transverse direction of the T6x sample. The X-ray diffraction (solid lines and points) and neutron diffraction (open points) results are shown. 151

7.7 Applied stress as a function of the lattice strain of the (111), (200), (220) and (311) aluminium reflections for the axial direction of the T7x sample. In addition, the (100), (002) and (101) reflections of the η precipitates are shown. 152

7.8 Residual lattice strain evolution as function of plastic deformation of the (111), (200), (220) and (311) aluminium and (100), (002) and (101) η reflections for the axial (a) and transverse (b) direction of the T7x sample. 153

7.9 (a) Residual lattice strain as function of applied strain of the (111), (200), (220) and (311) aluminium reflection in the T4, T6x and T7x samples measured by XRD. (b) Residual lattice strains versus the precipitation state after 3.3 % plastic deformation. 155

C.1 Lattice strain evolution as function of plastic deformation of the (111), (200), (220) and (311) reflections for the (a) axial and (b) transverse direction of the T4 sample. The X-ray diffraction (solid lines and points) and neutron diffraction (open points) results are shown. 174

C.2 Lattice strain evolution as function of plastic deformation of the (111), (200), (220) and (311) reflections for the (a) axial and (b) transverse direction of the T6x sample. The X-ray diffraction (solid lines and points) and neutron diffraction (open points) results are shown. 174

C.3 Lattice strain evolution as function of plastic deformation of the (111), (200), (220) and (311) aluminium and (100), (002) and (101) η reflections for the (a) axial and (b) transverse direction of the T7x sample. 175

List of Tables

3.1 Nominal composition (in wt.%) of the AA7449 and AA7040 36

3.2 Laboratory heat treatment performed for this study 36

6.1 Model parameters 120

6.2 Fitted effective Mg diffusion parameters of Mg for the coolings Q1, Q3 and Q4 122

6.3 Fitted PSD parameter for Q1,Q3 and Q4 (lognormal distribution with constant shape parameter p=1) 124

6.4 Fitted effective diffusion parameter for the coolings Q11, Q13, Q15 and Q16 128

6.5 Fitted PSD parameter for Q11, Q13, Q15 and Q16 (lognormal distribution with constant shape parameter p=1) 130

6.6 Fitted effective diffusion parameter of Mg for the cooling conditions at the surface, quarter and center position of a 75 mm AA7449 plate 132

7.1 Precipitate characteristics for the T4, T6x and T7x microstructure . 144

7.2 Calculated stress using equation 3.53 and a Young's modulus of 71 GPa and a Poisson's ratio of 0.3 in the axial and transverse direction for an applied plastic strain ϵ_{pl} of 3.3% from the XRD and ND experiments. 157

A.1 Chemical composition of Guinier Preston zones 168

A.2 Chemical composition of η' phase 169

A.3 Chemical composition of η phase 170

A.4 Chemical composition of heterogeneous η phase 170

B.1 Axial and transverse diffraction elastic constants for the T4 and T6x state from neutron diffraction 171

B.2 Axial diffraction elastic constants 171

C.1 Residual lattice strain (in 10^{-6}) after $\approx 3.4\%$ plastic deformation for the T4, T6x and T7x microstructure 175

Patrick Schloth

Allschwilerstrasse 106
4055 Basel, Switzerland

German, 13.05.1984
Email: patrick.schloth@ingenieur.de

Education

2011- 2015	PhD thesis in Materials Science and Engineering Ecole Polytechnique Fédérale de Lausanne (EPFL), Lausanne, Switzerland.
2005- 2010	Diploma in Mechanical Engineering Otto-von-Guericke University Magdeburg (OvGU), Magdeburg, Germany

Publications

- P. Schloth et. al. "Early cluster formation during rapid cooling of an Al-Cu-Mg alloy: in situ small-angle X-ray scattering", submitted to Scripta Materialia.
- N. Chobaut, D. Carron, S. Arsène, P. Schloth and J.-M. Drezet. "Quench induced residual stress prediction in heat treatable 7xxx aluminium alloy thick plates using Gleeble interrupted quench tests", submitted to *Journal of Materials Processing Technology*
- P. Schloth et. al. "Early precipitation during cooling of an Al-Zn-Mg-Cu alloy revealed by in situ small angle X-ray scattering". *Applied Physics Letters* 105, 101908 (2014).
- P. Schloth et. al. "Two strain-hardening mechanisms in nanocrystalline austenitic steel: An in situ synchrotron X-ray diffraction study", *Scripta Materialia* 66, 690 (2012).
- M. Krüger, G. Dietze, D. Sturm, P. Schloth, "Vergleichende Untersuchungen zum Rissausbreitungsverhalten von intermetallischen Werkstoffen für

Hochtemperaturanwendungen", *Fortschritte in der Metallographie, DGM*, S. 161-166, 2012.

Awards

- *CCMX poster prize*, 30.05.2014, Bern, Switzerland.
- *THERMEC'2013 student grant recipient*, 02-06.12.2013, Las Vegas, USA.
- *MDZWP graduate award 2011*, 01.04.2011, Magdeburg, Germany.